UNIVERSIDADE ESTADUAL PAULISTA
"JÚLIO DE MESQUITA FILHO"
Campus de Botucatu

UNIVERSIDADE ESTADUAL PAULISTA

"Júlio de Mesquita Filho"

INSTITUTO DE BIOCIÊNCIAS DE BOTUCATU

Síntese e caracterização de fosfatos de cálcio dopados com cobalto: Potencial biomimético para regeneração óssea

GERSON SANTOS DE ALMEIDA

Tese apresentada ao Instituto de Biociências, Campus de Botucatu, UNESP, para a obtenção do título de Doutor pelo Programa de Pós-Graduação em Biologia Geral e Aplicada, Área de concentração Biologia Celular, Estrutural e Funcional (BCEF)

Orientador: *Prof. Dr. Willian Fernando Zambuzzi*

BOTUCATU – SP
2024

UNIVERSIDADE ESTADUAL PAULISTA

"Júlio de Mesquita Filho"

INSTITUTO DE BIOCIÊNCIAS DE BOTUCATU

Síntese e caracterização de fosfatos de cálcio dopados com cobalto: Potencial biomimético para regeneração óssea

GERSON SANTOS DE ALMEIDA

Tese apresentada ao Instituto de Biociências, Campus de Botucatu, UNESP, para a obtenção do título de Doutor pelo Programa de Pós-Graduação em Biologia Geral e Aplicada, Área de concentração Biologia Celular Estrutural e Funcional (BCEF)

Orientador: *Prof. Dr. Willian Fernando Zambuzzi*

BOTUCATU – SP
2024

A447s

Almeida, Gerson Santos de
Síntese e caracterização de fosfatos de cálcio dopados com cobalto: Potencial biomimético para regeneração óssea / Gerson Santos de Almeida. -- Botucatu, 2024
226 p.

Tese (doutorado) - Universidade Estadual Paulista (Unesp), Instituto de Biociências, Botucatu
Orientador: Willian Fernando Zambuzzi
Coorientador: Margarida Juri Saeki

1. Monetita Dopada com Cobalto. 2. Biomimético. 3. Regeneração Óssea. 4. Biomaterial. I. Título.

Sistema de geração automática de fichas catalográficas da Unesp. Biblioteca do Instituto de Biociências, Botucatu. Dados fornecidos pelo autor(a).

Essa ficha não pode ser modificada.

UNIVERSIDADE ESTADUAL PAULISTA

Câmpus de Botucatu

CERTIFICADO DE APROVAÇÃO

TÍTULO DA TESE: Síntese e caracterização de fosfatos de cálcio dopados com cobalto: Potencial biomimético para regeneração óssea

AUTOR: GERSON SANTOS DE ALMEIDA
ORIENTADOR: WILLIAN FERNANDO ZAMBUZZI
COORIENTADOR: PAULO NORONHA LISBOA FILHO
COORIENTADORA: MARGARIDA JURI SAEKI

Aprovado como parte das exigências para obtenção do Título de Doutor em Biologia Geral e Aplicada, área: Biologia Celular Estrutural e Funcional pela Comissão Examinadora:

Prof. Dr. WILLIAN FERNANDO ZAMBUZZI (Participaçao Presencial)
Departamento de Ciencias Quimicas e Bioquimicas / Instituto de Biociencias de Botucatu Unesp

Profa. Dra. CARLA DOS SANTOS RICCARDI (Participaçao Presencial)
Departamento de Bioprocessos e Biotecnologia / Faculdade de Ciencias Agronomicas UNESP

Prof. Dr. RODRIGO CARDOSO DE OLIVEIRA (Participaçao Presencial)
Departamento de Ciências Biológicas / Faculdade de Odontologia de Bauru - USP

Prof. Dr. VLADIMIR ELIODORO COSTA (Participaçao Presencial)
Departamento de Biofisica e Farmacologia / Instituto de Biociencias de Botucatu Unesp

Profa. Dra. CARMEN VERÍSSIMA FERREIRA HALDER (Participaçao Presencial)
Departamento de Bioquímica e Biologia Tecidual / Universidade Estadual de Campinas

Botucatu, 23 de fevereiro de 2024

Maria Victória Ramalho da Cunha
Assistente Administrativo II da Seção Técnica de Pós-Graduação
Instituto de Biociências de Botucatu

Instituto de Biociências - Câmpus de Botucatu -
Rua Doutor Antonio Celso Wagner Zanin, s/nº, 18618689
http://www.ibb.unesp.br/#!/pos-graduacao/biologia-geral-e-aplicada/CNPJ: 48031918002259.

Dedicatória

A minha filha Catarina e minha esposa Ana Carolina

Agradecimentos

Agradeço a minha esposa Ana Carolina por estar sempre ao meu lado, por ser meu porto seguro, por todo o amor, confiança e respeito, obrigado por ser meu sol. Não tenho palavras para demonstrar minha gratidão, eu jamais poderia imaginar o quanto minha vida mudaria e o quanto eu sou feliz desde o momento que te conheci.

Agradeço a minha filha Catarina, você iluminou tudo desde o momento que soubemos da sua vinda, obrigado por ser minha inspiração diária.

Agradeço a minha família por me fornecerem a oportunidade de estudar, por tudo que fazem por mim, por todos os sacrifícios, por todas as lutas e por todo o apoio.

Agradeço a minha segunda família por me receberem e pelo enorme carinho, agradeço aos meus sogros Sandro e Marli e a minha cunhada e amiga Gabriela. Vocês são essenciais em minha vida.

Agradeço ao meu orientador Professor Willian por ter me aceito como seu aluno e por não medir esforços para ajudar não só aos que conhece, mas a todos aos que recorrem a ele. Agradeço seus conselhos, por ser um exemplo de profissional e por sempre tentar extrair o melhor de nós. Obrigado pela oportunidade e por sempre acreditar em nosso potencial, tornando-se um amigo além de orientador.

Agradeço aos meus amigos de laboratório por toda a ajuda, troca de experiências e por terem me acolhido, em especial ao Célio, Geórgia, Marcel e Thais, sem vocês esse trabalho não seria possível.

Agradeço a Professora Margarida pelo auxilio durante meu mestrado e doutorado. Sua disposição em sempre ajudar, suas dicas e por abrir as portas de seu laboratório, sua colaboração foi essencial para o desenvolvimento deste trabalho e para o meu crescimento como cientista.

Agradeço ao Professor Paulo Noronha por toda ajuda durante o doutorado, por sua coorientação e por todas as análises e colaboração na caracterização dos materiais, e por todo o empenho em me ajudar no CapesPrInt.

Agradeço ao Professor Vladimir por estar sempre com suas mãos estendidas e disposto a ajudar a todos, por sua empatia e por sua vontade de ensinar.

Agradeço ao Professor Diego pelas análises de DRX e toda colaboração no projeto, sua ajuda foi muito importante.

Agradeço a Professora Elidiane e Professor Nilson, e aos alunos Gabrielly e João pela disposição nas análises de MEV, pela parceria e toda a disposição em ajudar.

Agradeço ao Professor Gustavo por toda a ajuda na síntese de materiais e por ceder seu laboratório sempre que precisamos.

Agradeço ao Professor Rodrigo Cardoso, por todas as reuniões, por ter se disponibilizado a ensinar as técnicas cirúrgicas, e por tudo que nos ajudou nesse trabalho.

Agradeço as alunas Luísa, Julia M, Paula, Júlia B e Maria Gabriela, obrigado pela confiança em tentar coorientá-las durante esse período e por todo o auxílio que me deram, pude aprender muito com vocês.

Agradeço ao Dr. Alaor Almeida por ter sido a primeira pessoa a me proporcionar uma oportunidade na universidade, com o projeto de extensão pude crescer e aprender muito.

Agradeço ao Orisson e Nicolas por toda a parceria durante o intercambio, por toda a ajuda e amizade durante essa experiência.

Agradeço ao Ariel Colaço e Vinicius Fidelis por toda a sua ajuda durante meu tempo em Quebec e no LBB, obrigado por sua amizade, por suas dicas e toda a colaboração.

Agradeço a todos os meus amigos e amigas que estiveram e estão ao meu lado nessa caminhada.

Agradeço ao Prof. Diego Mantovani, pela oportunidade de estar em seu laboratório e proporcionar a experiência de conhecer outra cultura e diferentes técnicas, pude crescer e aprender muito durante meu tempo em sua equipe.

Agradeço a Dra. Pascale, pela supervisão e direcionamento durante meu estágio.

Agradeço a Professora Carla Riccardi, Professor Luís Justulin, e Prof. Carlos Grandini por terem feito parte da minha banca de qualificação, por todas as considerações, discussões e dicas, suas colaborações foram essências para melhorar o trabalho.

Agradeço aos membros da banca de defesa do doutorado pela avaliação, correção, discussões e toda a colaboração para que este trabalho fosse aprimorado, agradeço a Professora Carmem Halder, Professora Carla Riccardi, Professor Rodrigo Cardoso e Professor Vladimir Eliodoro.

Agradeço a equipe da Pós-graduação por sua disposição em sanar as dúvidas e colaborar no que for possível.

Agradeço aos meus amigos de longa data, por mais que nossos encontros sejam raros, carrego vocês comigo, obrigado por existirem, Sabrina, Gabriel, Itamar e Rodrigo.

Agradeço a Professora Vera e a Dra. Stéfani pelas análises de antibiograma.

Agradeço ao LNNano/CNPEM pelas análises de XPS.

Agradeço a todos os brasileiros que por meio de seus impostos puderam proporcionar toda a minha formação.

Agradeço a Capes pelo financiamento.

Epigrafe

“Talvez não tenhamos conseguido fazer o melhor, mas lutamos para que o melhor fosse feito!*”*
Martin Luther King Jr.

Resumo

A síntese de monetita dopada com cobalto (CoCaP) foi realizada pelo método de co-precipitação, com um teor nominal de cobalto entre 2 a 20%. As amostras foram submetidas a uma caracterização estrutural por meio de difração de raios-X (DRX), espectroscopia de infravermelho por transformada de Fourier (FTIR), microscopia eletrônica de varredura (MEV) e espectroscopia de raios-X por dispersão de energia (EDS). Análises estruturais detalhadas confirmaram o sucesso da síntese e revelaram alterações estruturais distintas devido à dopagem com cobalto. Os resultados de DRX mostraram que as amostras dopadas com Co exibiam uma fase única de monetita, com parâmetros de célula e tamanho de cristalito dependentes da quantidade de cobalto incorporada. Ensaios de viabilidade e adesão celular não mostraram toxicidade, enquanto a análise de expressão gênica por RTqPCR indicou diferenças significativas nos genes associados ao fenótipo osteoblástico, sugerindo um potencial para regeneração óssea. Posteriormente, avançamos na resposta biológica da CoCaP e mostramos seu desempenho na migração de osteoblastos, indicando um potencial para acelerar a cicatrização óssea, enquanto uma regulação positiva de genes relacionados a quinases dependentes de ciclinas (CDKs) foi observada. Por fim, para seu uso como recobrimento de titânio, investigamos os revestimentos de monetita e CoCaP em titânio comercialmente puro (Ti-c.p.). Os revestimentos apresentaram rugosidade superficial pronunciada e hidrofilia inerente à biocompatibilidade, influenciando positivamente a morfologia celular e a qualidade desta interação célula-material, o que pode ser confirmado através de análises de expressão gênica requerendo genes distinguidos à osteogênese e remodelação da matriz extracelular. Em suma, esta tese demonstra o potencial da monetita dopada com cobalto como um material biomimético para regeneração óssea, destacando sua capacidade de imitar o ambiente de cicatrização do osso, promover a diferenciação e atividade osteoblástica, e melhorar a osseointegração de dispositivos médicos. Esses resultados oferecem perspectivas promissoras para futuras aplicações clínicas e avanços na engenharia de biomateriais para medicina regenerativa.

Palavras-chave: Monetita Dopada com Cobalto; Biomimético; Regeneração Óssea.

Abstract

The synthesis of cobalt-doped monetite (CoCaP) was performed by the co-precipitation method, with a nominal cobalt content ranging from 2 to 20%. The samples underwent structural characterization through X-ray diffraction (XRD), Fourier transform infrared spectroscopy (FTIR), scanning electron microscopy (SEM), and energy dispersive X-ray spectroscopy (EDS). Detailed structural analyses confirmed the success of the synthesis and revealed distinct structural alterations due to cobalt doping. XRD results showed that Co-doped samples exhibited a single phase of monetite, with cell parameters and crystallite size dependent on the amount of incorporated cobalt. Viability and cell adhesion assays showed no toxicity, while RT-qPCR analysis indicated significant differences in genes associated with the osteoblastic phenotype, suggesting potential for bone regeneration. Subsequently, we further explored the biological response of CoCaP, demonstrating its performance in osteoblast migration, indicating potential for accelerating bone healing, while a positive regulation of cyclin-dependent kinase (CDK)-related genes was observed. Finally, for its use as a coating on titanium, we investigated the coatings of monetite and CoCaP on commercially pure titanium (Ti-c.p.). The coatings exhibited pronounced surface roughness and inherent hydrophilicity conducive to biocompatibility, positively influencing cellular morphology and the quality of this cell-material interaction, as confirmed through gene expression analyses requiring genes distinguished in osteogenesis and extracellular matrix remodeling. In summary, this thesis demonstrates the potential of cobalt-doped monetite as a biomimetic material for bone regeneration, highlighting its ability to mimic the bone healing environment, promote osteoblastic differentiation and activity, and improve the osseointegration of medical devices. These results offer promising prospects for future clinical applications and advancements in biomaterial engineering for regenerative medicine.

Keywords: Cobalt Doped Monetite; Biomimetic; Bone Regeneration.

Sumário

Lista de Figuras

Capítulo 1

Capitulo 2

CoCaP10 ($^{*}p = 0.0137$) and CoCaP20 ($^{**}p = 0.0024$). There were also significant differences in expression between the CaP and CoCaP1 groups, with CoCaP showing an increase compared to CaP ($^{++++}p = 0.0001$). (**c**) The BSP gene expression was increased in the groups CaP ($^{*}p = 0.0147$) and CoCaP2 ($^{****}p = 0.0001$), and decreased in CoCaP20 ($^{*}p = 0.0499$) when compared to the control group. Higher expression: the expression was higher in the CaP and CoCaP groups compared to the other treatments, CoCaP5 ($^{+++}p = 0.0002$, $^{¢¢¢¢}p = 0.0001$) CoCaP10 ($^{+++}p = 0.0001$, $^{¢¢¢¢}p = 0.0001$) and CoCaP20($^{++++}p = 0.0001$, $^{¢¢¢¢}p = 0.0001$). Between the CaP and CoCaP groups, in the CoCaP2 ($^{++++}p = 0.0001$) group there is an increase in expression when compared to CaP. (**d**) Higher expression of Osteocalcin: CoCaP2 ($^{**}p = 0.0013$); Lower expression: CoCaP5 ($^{**}p = 0.0029$), CoCaP10 ($^{*}p = 0.0043$) and CoCaP20 ($^{**}p = 0.0012$). When comparing the treated groups, each other, the expression was higher in the CaP and CoCaP groups compared to the other treatments, CoCaP5 ($^{+++}p = 0.0007$, $^{¢¢¢¢}p = 0.0001$) CoCaP10 ($^{+++}p = 0.0010$, $^{¢¢¢¢}p = 0.0001$) and CoCaP20($^{+++}p = 0.0004$, $^{¢¢¢¢}p = 0.0001$). Between the CaP and CoCaP group, in the CoCaP2 group ($^{+}p = 0.0228$) there is an increase in expression when compared to CaP. All groups of samples n=3.....55

Figure 8. Osteoclastoegenesis-related gene (RANKL) and hypoxia biomarker were investigated in this study. (a) Higher expression of RANKL: CaP ($^{*}p = 0.0125$) and CoCaP2 ($^{****}p = 0.0001$) treatments there was an increase in its expression when compared with the control. When comparing the treated groups, the expression was higher in the CoCaP2 groups compared to the other treatments, CaP ($^{++}p = 0.0022$), CoCaP5 ($^{¢¢¢}p = 0.0003$) CoCaP10 ($^{¢¢¢¢}p = 0.0001$) and CoCaP20 ($^{¢¢¢¢}p = 0.0001$); (**b**) In order to analysis the effect of hypoxia in response to the treatments, the Hif1α gene was evaluated. The gene expression also revealed significant modulation in response to treatment in CaP ($^{***}p = 0.0005$) and CoCaP2 ($^{**}p = 0.0001$) when compared with the control and in the other treatments it was not statistically significant. When comparing the treated groups, the expression was higher in the CaP and CoCaP2 groups compared to the other treatments, CoCaP5 ($^{++++}p = 0.0001$, $^{¢¢¢¢}p = 0.0001$) CoCaP10 ($^{++++}p = 0.0001$, $^{¢¢¢¢}p = 0.0001$) and CoCaP20 ($^{++++}p = 0.0001$, $^{¢¢¢¢}p = 0.0001$). Between the CaP and CoCaP2 groups, in the CoCaP2 group ($^{++++}p = 0.0001$) there is an increase in expression when compared to CaP. All groups of samples n=3.....56

Figure 9. Molecular machinery related with cell adhesion and cytoskeleton rearrangement. (**a**) α1-integrin gene was higher in the groups: CaP ($^{***}p = 0.0009$), CoCaP2 ($^{****}p = 0.0001$), and CoCaP20 ($^{*}p = 0.0347$) when compared with control. Among the treatments, there were statistically significant differences, with a lower expression in the CoCaP2.5 group when compared with CaP ($^{++++}p = 0.0001$), CoCaP2 ($^{¢¢¢¢}p = 0.0001$), and CoCaP20 ($^{\&\&}p = 0{,}0091$). Among the groups, the expression was higher in the CaP and CoCaP2 groups compared to the other treatments, CoCaP5 ($^{+++}p = 0.0003$, $^{¢¢¢¢}p = 0.0001$) CoCaP10 ($^{+}p = 0.00326$, $^{¢¢¢¢}p = 0.0001$) and CoCaP20 ($^{¢¢¢¢}p = 0.0001$). Between the CaP and CoCaP2 groups, in the CoCaP2 group ($^{++++}p = 0.0001$) was higher in expression when compared to CaP; (**b**) β1-integrin expression was lower in response to CoCaP5 ($^{***}p = 0.0008$), CoCaP10 ($^{*}p = 0.0007$) and CoCaP20 ($^{***}p = 0.0007$). When comparing the treated groups, the expression was higher in the CaP and CoCaP2 groups compared to the other treatments, CoCaP5 ($^{+++}p = 0.0003$, $^{¢¢¢¢}p = 0.0001$) CoCaP10 ($^{+++}p = 0.0002$, $^{¢¢¢¢}p = 0.0001$) and CoCaP20($^{+++}p = 0.0003$, $^{¢¢¢¢}p = 0.0001$). Between the CaP and CoCaP2 genes, in the CoCaP2 group ($^{+}p = 0.0479$) there is an increase on expression when compared to CaP; (**c**) FAK gene expression was considered and it was higher in response to CoCaP2 ($^{**}p = 0.0069$),

CoCaP10 (*p = 0.0154) and CoCaP20 (****p = 0.0001) when compared with the control, while CaP and CoCaP5 treatments it was not statistically significant. The other groups had statistically significant differences when compared among themselves, with increased expression in CoCaP2 and CoCaP20, the statistical differences were: CoCaP5 ($^{¢}$p = 0.0210, $^{+++}$p = 0.0001), CoCaP10 ($^{¢¢¢}$p = 0.0010) and CoCaP20 ($^{++++}$p = 0.0001, $^{¢¢¢¢}$p = 0.0001, $^{\&\&\&}$p = 0.0002, $^{££££}$p = 0.0010); (**d**) Src gene expression was higher in the groups: CaP (****p = 0.0001), CoCaP10 (***p = 0.0007) and CoCaP20 (***p = 0.0001) when compared with control, between CoCaP2 and CoCaP5 treatments was not statistically significant. The other groups showed statistically significant differences when compared among themselves, with higher expression in response to CaP, CoCaP10 and CoCaP20. The statistical differences were: CoCaP2 ($^{+++}$p = 0.0001), CoCaP5 ($^{+++}$p = 0.0001), CoCaP10 ($^{¢¢¢}$p = 0.0010, $^{\&\&\&}$p = 0.0010) and CoCaP20 ($^{¢¢¢}$p = 0.0002, $^{\&\&\&}$p = 0.0002); (**e**) Cofilin gene expression was higher in the groups as follows: CaP (**p = 0.0034), CoCaP2 (****p = 0.0001), CoCaP10 (**p = 0.0024) and CoCaP20 (**p = 0.0037) when compared with control, in the CoCaP5 it was not statistically significant. The other groups had statistically significant differences when compared among themselves, with higher expression in CaP, CoCaP2, CoCaP10 and CoCaP20, the statistical differences were: CoCaP2 ($^{+++}$p = 0.0001), CoCaP5 ($^{+}$p = 0.0207, $^{¢¢¢¢}$p = 0.0001), CoCaP10 ($^{¢¢¢}$p = 0.0002, $^{\&}$p = 0.0134) and CoCaP20 ($^{¢¢¢}$p = 0.0001, $^{\&}$p = 0.0229. All groups of samples n=3. 57

Complementary assays

Capítulo 5

Fig.3. SEM micrographs of cobalt-doped monetite, obtained by coprecipitation method and semiquantitative analysis and elemental distribution of cobalt-doped apatite by EDS. **a.** Monetite; **b.** Co-doped Monetite. **Cytotoxicity Assays. c.** The cells showed no reduction in viability when compared to Ctrl. The CaP and CoCaP groups showed a statistically significant increase when compared to (****p = <0.0001and $^{++++}$p = < 0.0001) and O.M ($^{¢¢¢¢}$p = <0.0001and ($^{\$\$\$\$}$p = <0.0001) in both treatment times and the CoCaP ($^{£££}$p = 0.0001) group showed a difference when compared to CaP. CaP (^{cccc}p = <0.0001) and CoCaP (^{bb}p = 0.0042) also showed differences when compared to their respective treatments with time. **d.** All groups showed no reduction in Crystal Violet staining. CaP-3 days showed a statistically significant increase when compared to Ctrl (***p = 0.0001), O.M ($^{¢¢¢¢}$p = <0.0001, and CoCaP ($^{\&\&\&}$p = 0.0003). When compared to the 7-day treatment, a significant difference was also found in CaP (^{cp} = 0.0003). All sample groups n = 6.....83

Fig.4. a. The cell regeneration effect of treatments with Ctrl (conventional medium), O.M (osteogenic-inducing medium), CaP (Monetite), and CoCaP (Co-doped Monetite) was measured by a wound-healing assay. **b. Quantification Wounding area**. The wound area was estimated by calculating the cell-free area in captured images using the ImageJ software (NIH, Bethesda, MD)**.** The migration rate is expressed in percentage as the change in the wound area over time, the scratch area at time point 0 hours was set to 100%, and the other ones are represented as wound closure expressed as the remaining area uncovered by the cells in percentage. At 12 hours' treatment: The CaP (***p = 0.0001) and CoCaP (**p = 0.0017) groups showed a reduction when compared to Ctrl, O.M. did not show the same profile. At 16 hours' treatment: Only CoCaP ($^{++++}$p = <0.0001) showed a statistically significant reduction when compared to Ctrl. **c. Cdk2** there were no statistically significant differences in the 3-day treatment. In the 7-day treatment, the CoCaP group showed an increase in expression compared to Ctrl ($^{++++}$p = <0.0001), O.M ($^{\$\$\$\$}$p = <0.0001) and CaP ($^{££££}$p = <0.0001). d**. Cdk4**, in the 3-day treatment there were differences in the expression in CaP (*p = 0.0115) and CoCaP (*p = 0.0326) groups when compared to the Ctrl group. In the 7-day treatment, no group showed statistically significant differences. e**. Cdk6**, 3-day treatment, only CaP (****p = <0.0001) showed statistically significant differences when compared to Ctrl. At 7-day treatment, CoCaP showed increased expression when compared to Ctrl ($^{++++}$p = <0.0001), O.M ($^{\$\$\$\$}$p = <0.0001) and CaP ($^{££££}$p = <0.0001. All sample groups n = 3.....86

Fig.5. Cytokines were changes by CoCaP: **a.** RANKL, in the 3-day treatment showed an increase in its expression in the CaP (****p <0.0001 and $^{¢¢¢}$p = 0.0007) and CoCaP (****p <0.0001 and ($^{¢¢¢¢}$p <0.0001) groups when compared to Ctrl and O.M, respectively. The CoCaP group ($^{\&\&\&}$p = 0.0001) showed an increase when compared to the CaP group. In the treatment for 7 days, the O.M ($^{++++}$p <0.0001) and CoCaP ($^{++++}$p <0.0001) show increases when compared to the Ctrl group. The O.M and CoCaP ($^{££££}$p <0.0001) also show increases in expression when compared to the CaP ($^{\$\$\$\$}$p <0.0001). **b.** OPG, in the 3-day treatment, only the CaP (*p = 0.0419 and $^{¢¢}$p = 0.0048) showed an increase when compared to the Ctrl and O.M. groups. In the 7-day treatment, the CoCaP group showed an increase in its expression when compared to the Ctrl ($^{++++}$p <0.0001), O.M ($^{\$\$\$\$}$p <0.0001), and CaP ($^{££££}$p <0.0001). **c.** RANKL/OPG, in the 3-day treatment the CaP (*p = 0.0351) and CoCaP (****p <0.0001) was higher than the Ctrl. The CoCaP group also showed differences concerning the O.M ($^{¢¢¢¢}$p <0.0001) and CaP ($^{¢¢¢¢}$p <0.0001). In the 7-day treatment, only the O.M group ($^{+++}$p = 0.0001) showed an increase compared to Ctrl, CaP ($^{\$\$\$\$}$p <0.0001), and CoCaP ($^{\$\$\$\$}$p

Capítulo 7

Suplementary material

Lista de Tabelas

Capítulo 1

Capítulo 2

Capítulo 4

Capítulo 5

Capítulo 6

SUPPLEMENTARY DATA

Capítulo 7

Lista de Anexos

Atividades Desenvolvidas no período

Lista de Abreviaturas e Siglas

α-TCP	α-Fosfato tricálcico
β-TCP	β-Fosfato tricálcico
β-CPP	β-pirofosfato de cálcio
γ-CPP	γ-pirofosfato de cálcio
µL	Microlitro
3D	Três dimensões
18S	RNA ribossomal
ACP	Fosfato de cálcio amorfo
ADP	Adenosina difosfato
Ag	Prata
AKT	Proteína quinase B
Al	Alumínio
ALP	Fosfatase alcalina
ANOVA	Análise de Variância
Au	Ouro
BCL2	Regulador de apoptose BCL2
BCP	Bifosfato de Cálcio
BGLAP	Osteocalcina
BMP's	Proteínas morfogenéticas ósseas
BMP2	Proteína morfogenética óssea 2
BMPR1	Receptor da proteína morfogênica óssea do tipo 1
BMPR2	Receptor da proteína morfogênica óssea do tipo 2
BMPs	Proteína morfogenética óssea
C	Carbono
C_0	Concentração inicial
$CaCl_2$	Cloreto de Cálcio
CAGR	Taxa anual de crescimento composta
CaP	Fosfatos de Cálcio ou *calcium phosphate*
CaPs	Ortofosfatos/fosfatos de cálcio ou Calcium orthophosphates/phosphates
CDK2	Quinase 2 dependente de ciclina
CDK4	Quinase 4 dependente de ciclina
CDK6	Quinase 6 dependente de ciclina
cDNA	Ácido Desoxirribonucleico Complementar
cm	Centímetros
Co	Cobalto
CO_2	Dióxido de carbono
CoCaP	Fosfato de Cálcio dopado com Cobalto
$CoCl_2$	Cloreto de Cobalto
CPC	Cimentos de CaPs
CPP	calcium pyrophosphate ou pirofosfato de cálcio
Cu	Cobre
DCPA	Monetita ou *Monetite*
DCPD	Brushita ou *Brushite*

DMEM	Duldecco’s Modified Eagle Medium
DMSO	Dimetilsulfóxido
DRX	Difratrometria de Raios X
EDX e EDS	Espectroscopia de raios X por dispersão em energia
EG	Ethylene glycol
ERK	Quinases reguladas por sinal extracelular
FAK	Proteína tirosina quinase de adesão focal
FGF	Fator de crescimento do fibroblasto
FTIR	Espectroscopia no Infravermelho com Transformada de Fourier
g	Grama
GAPDH	Gliceraldeído 3-fosfato desidrogenase
h	horas
H	Hidrogênio
H_2O	Água
HA	Hidroxiapatita
HB	Hidroxiapatita bovina
HPO_4^{2-}	hidrogenofosfato
IGF1	Fator de crescimento semelhante à insulina tipo 1
IGFR1	Receptor de fator de crescimento semelhante à insulina 1
IL1	Interleucina 1
IL18	Interleucina 18
IL18R1	Receptor de interleucina 18 do tipo 1
Il1r1	Receptor de interleucina-1 tipo 1
Il1R1	Receptor de interleucina 1 do tipo 1
IL1β	Interleucina 1 beta
IL33	Interleucina 33
IL6	Interleucina 6
iNOS	Óxido nítrico sintase induzível
ISO	Organização Internacional de Normalização
ITGB1	Integrina subunidade beta 1
JAK	Janus quinase
JNK	c-Jun quinases terminais N
KBr	Brometo de potássio
kV	Quilovolts
L	Litro
mA	Miliamperes
MAPK	Proteína-quinases ativadas por mitógenos
MAPK3	Proteína mitogênica-ativada 3
MC3T3	Pré-osteoblastos de Camundongo
MEC	Matriz Extracelular
MEM	Meio Mínimo Essencial (Minimum Essential Medium)
MEV	Microscopia Eletrônica de Varredura
mg	Miligrama
Mg	Magnésio
min	Minutos

Mn	Manganês
mRNA	Ácido Ribonucleico Mensageiro
miRNAs	Micro RNA
mL	Mililitro
mM	Milimolar
Mn	Manganês
MO	Meio osteoindutor
MTT	Brometo de 3-4,5-dimetil-tiazol-2-il-2,5-difeniltetrazólio
N	Nitrogênio
Na_2HPO_4	Fosfato de sódio dibásico
NaCl	Cloreto de sódio
NFκB	Factor nuclear kappa B
Ni	Níquel
NLRP3	Proteína 3 contendo os domínios NACHT, LRR e PYD
nm	Nanometro
nNOS	Óxido nítrico síntase
NO	Óxido nítrico
OCP	Fosfato octacálcico
OCT ou OCN	Osteocalcina
OD	Densidade ótica
OH	Hidroxila
ON	Osteonectina
OPG	Osteoprogeterina
OPN	Osteopontina
OTX	Osterix
P15	Inibidor de quinase dependende de cíclica 2B
P21	Inibidor da cinase dependente de ciclina 1
P_2O_7	Pirofosfato
P38	Proteína quinase ativada por mitógeno p38
PBS	Tampão fosfato-salino
PCR	Reação de cadeia polimerase
PDGFs	Fatores de crescimento derivados de plaquetas
pg	Picograma
pH	Potencial (ou potência) hidrogeniônico
PMNs	neutrófilos polimorfonucleares
PO_4	Fosfato
Raman	Espectroscopia de espalhamento Raman com microscopia óptica
RANKL	Ativador de receptor do fator nuclear κ B
RNA	Ácido Ribonucleico
RNA-seq	Sequenciamento de Ácido Ribonucleico
RPM	Rotações por minuto
RT-qPCR	Transcriptase reversa seguida de quantificação utilizando a técnica da reação em cadeia da polimerase
Runx2	Fator de Transcrição relacionado ao RUNT2
SA	Alginato de sódio

Se	Selênio
SFB	Soro Fetal Bovino
Si	Silício
SP7	Fator de transcrição Sp7
SRC	Proteína tirosina quinase SRC
STAT	Membros do transdutor de sinal e ativador da família das proteínas de transcrição
TCP	Fosfato Tricálcio ou Tricalcium phosphate
TFT	Alvos de Fatores de Transcrição
TGA	Análise por Termogravimetria
TGFs	Fatores de crescimento transformadores
TGFBR1	Receptor 1 do fator de crescimento transformador
TGF-β1	O fator de crescimento transformador beta 1
TNFα	Fatores de Necrose Tumoral Alfa
TTCP	Fosfato tetracálcico
UV	Ultravioleta
VEGF	Fator de crescimento endotelial vascular
VEGFR1	Receptor tirosina quinase 1 Relacionado a Fms
VEGFR2	Receptor de domínio de inserção de quinase
VN	Vermelho Neutro
Zn	Zinco

Capitulo 1

Introdução – Revisão de Literatura

1. Introdução – Revisão de Literatura

1.1 O tecido ósseo

Os ossos constituem a base mecânica e de sustentação para os vertebrados e possuem a maior proporção da massa tecidual conectiva do corpo. Entre os tecidos vitais, o osso é um tecido distinto que tem características de renovação e auto reparo. O processo de remodelação óssea é baseado na cooperação contínua entre dois tipos de células, osteoclastos e osteoblastos, que por meio de uma eficiente homeostase, mantêm o tamanho, forma e função óssea (GAO et al., 2017). Na estrutura complexa e hierárquica dos ossos, junta-se à porção mineralizada, componentes de uma matriz orgânica (osteóide), majoritariamente formada por colágeno, além de outras proteínas não colagênicas, como é o caso de vimentina e fibronectina. Sabe-se também que proteoglicanos são decisivos para manutenção da hidratação do tecido, conferindo-lhe propriedades físico-químicas distintas (FLORENCIO-SILVA et al., 2015; PREETHI SOUNDARYA et al., 2018).

Além de seus componentes minerais e proteicos, o osso também é histologicamente composto por células, macromoléculas e vasos sanguíneos, dos quais angiogênese e osteogênese estão acoplados (KARSENTY; FERRON, 2012). O tecido ósseo é um sistema altamente vascularizado e complexo que fornece uma estrutura externa, bem como uma estrutura de suporte e proteção para os tecidos e órgãos internos, como o cérebro, o coração e os pulmões. Este tecido tem uma capacidade de carga e, em colaboração com o sistema muscular, é o principal responsável pela ação do movimento e, naturalmente, é classificado como uma composição vital, encontrada apenas em vertebrados (KARSENTY, 2000a; VAN DER EERDEN; TETI; ZAMBUZZI, 2014). Além disso, o osso é caracterizado por suas propriedades mecânicas únicas, que lhe permitem absorver a força externa e depois distribuí-lo igualmente sobre o tecido, evitando danos e permitindo a execução de diferentes atividades (VAN DER EERDEN; TETI; ZAMBUZZI, 2014).

O tecido ósseo também atua como reservatório de vários minerais, principalmente cálcio e fosfato, e também armazena fatores de crescimento, ácidos graxos, além de possuir a capacidade de absorver toxinas e metais pesados para minimizar os efeitos em outros órgãos. Além da função de absorção e liberação de sais, responsáveis por eventos de tamponamento do sangue e prevenção de grandes variações de pH (HAIDER et al., 2017; SADOWSKA et al., 2019; SUNTERS et al., 2010).

Devido a seu microambiente intrínseco, o osso saudável é capaz de adaptar sua massa e se reparar continuamente durante toda a vida. Outra característica distinta, o estroma da medula óssea contém células-tronco mesenquimais, que podem se diferenciar em uma variedade de tipos de células, incluindo glóbulos vermelhos e glóbulos brancos.

Células ósseas: Três tipos de células representam a construção principal do osso, e cada uma está igualmente envolvida no processo de desenvolvimento e remodelação, a **Figura 1** ilustra essas células. **Os osteoblastos**, são células mononucleares de origem mesenquimal, que são estimuladas por uma variedade de fatores de crescimento para se diferenciarem em células osteoprogenitoras e ocupam cerca de 4-6% do total de células no osso. Os osteoblastos ficam na superfície óssea e produzem estrutura não-mineralizada durante o processo de formação e mineralizando-os em seguida (HARADA; RODAN, 2003). **Os osteócitos**, células de origem mesenquimal, embebidas na matriz óssea mineralizada, constituem o maior volume de células ósseas em um esqueleto maduro, e também possuem a capacidade de se comunicar com outras células através da junção de fendas. As funções dos osteócitos são manter a matriz celular, regular as concentrações de cálcio/fósforo no osso e desempenhar um papel na mecano-sensibilidade do osso por orquestrarem a remodelação, sendo reservas importantes de RANKL (BOSKEY; ROBEY, 2018). **Os osteoclastos**, células multinucleadas encontradas na superfície óssea e são as únicas células ósseas capazes de se dividir. Eles são derivados de células-tronco hematopoiéticas, e realizam função inversa àquelas exercida pelos osteoblastos, visto que degradam a matriz óssea favorecendo reabsorção de minerais e proteínas (MANOLAGAS, 2000; XIONG et al., 2011). Os três tipos celulares se comunicam através de moléculas de sinalização, cujas vias de participação são complexas (ZAMBUZZI; MILANI; TETI, 2010) e tem papel fundamental para a eficiência do mecanismo de regeneração e vascularização óssea (SARAN; GEMINI PIPERNI; CHATTERJEE, 2014).

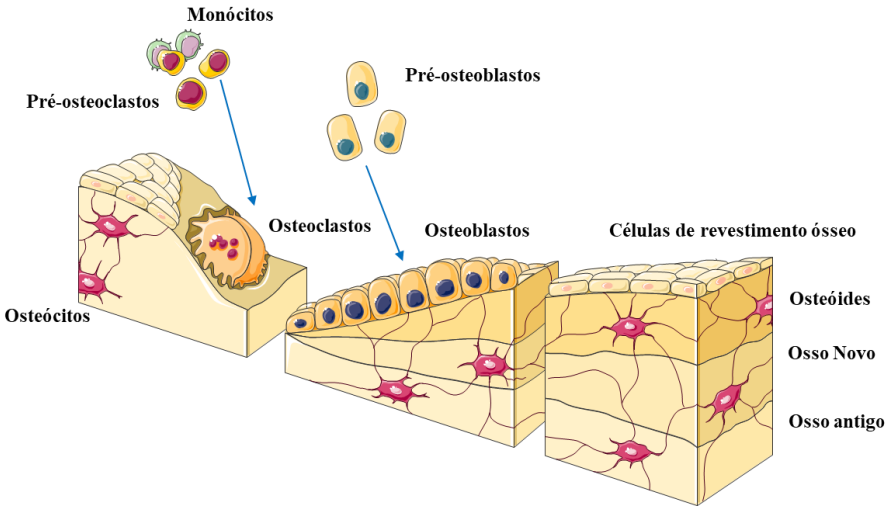

Figura 1: Esquema ilustrado dos diferentes tipos de células do osso. Elementos gráficos foram obtidos em https://smart.servier.com/.

Composição óssea: O osso é um tecido conjuntivo distinto com sua estrutura arquitetônica única, visto que lhe proporciona rigidez e flexibilidade ao mesmo tempo, proporcionado a capacidade de absorver e suportar e distribuir o estresse recebido, evitando danos a sua estrutura. A composição

do osso é basicamente água (10%), hidroxiapatita mineral inorgânica (60-70%), e o restante apresenta-se como colágeno de fase orgânica (CARREIRA et al., 2014). A combinação de colágeno e cristais minerais forma a matriz celular, que proporciona suas propriedades ser regido e flexível (WARDEN et al., 2005).

Estrutura óssea: Unidos por tecido conjuntivo, o sistema esqueleto dos adultos possui mais de 200 ossos. Apesar de compartilharem uma composição sólida, os ossos diferem em termos de função e estrutura. No nível macroscópico, o tecido ósseo pode ser dividido em dois tipos: osso cortical (compacto) e osso trabecular (WARDEN et al., 2005).

O osso cortical é uma camada externa sólida que ocupa aproximadamente 80% do volume total do esqueleto. O osso cortical é uma estrutura densa que se forma na superfície e tem uma baixa porosidade (5-10%), o que reflete sua resistência à compressão (COWIN, 1999). O osso poroso está localizado principalmente na área interna das regiões epifisárias e metafisárias. O osso poroso é de natureza esponjosa, que ocupa apenas 20% da massa óssea total, mas 75% da área total da superfície óssea (COWIN, 1999).

O osso trabecular proporciona uma capacidade de suporte indireta absorvendo energia e distribuindo a carga para manter o osso cortical (AERSSENS et al., 1997). No nível microscópico, os ossos corticais e trabeculares contêm o osso lamelar. O osso primário é um osso primitivo ou imaturo encontrado principalmente durante a ontogênese rápida do esqueleto, crescimento longitudinal do osso, fraturas do estágio inicial e remodelação óssea ou formação de células ósseas insalubres (AERSSENS et al., 1998). O osso lamelar é um osso maduro que precisa de mais tempo para ser formado, em comparação com o osso primário. As fibras de colágeno seguem um padrão arranjado no osso lamelar durante a formação com deposição aleatória de fibras, e isto leva a um aumento da resistência mecânica em comparação com o osso trabecular (BECK et al., 2001; SPANGENBERG et al., 2016).

Formação e desenvolvimento ósseo: O mecanismo osteogenético segue dois processos essenciais de desenvolvimento, que são diretos (intramembranosos) ou indiretos (endocondral). O sucesso da elaboração da matriz extracelular (MEC) e sua mineralização depende também de um suprimento vascular adequado. Qualquer deficiência resultará em uma imperfeição durante a fase de diferenciação (RUNYAN; GABRICK, 2017).

Ossificação intramembranosa: O principal diferencial desse processo de formação é a não dependência de um precursor cartilaginoso e está relacionado com a diferenciação de células mesenquimais em osteoblastos (PALUMBO; FERRETTI; DE POL, 2003; PERCIVAL; RICHTSMEIER, 2013; YANG et al., 2012). Este processo pode ser resumido na diferenciação de

células mesenquimais em osteoblastos e está ilustrado na **Figura 2**, esses que por sua vez iniciam a síntese de matriz do osteóide, essa matriz recém sintetizada e rica em proteínas, para sua mineralização, mecanismos endócrinos hormônios e vitaminas necessitam estar em equilíbrio (PALUMBO; FERRETTI; DE POL, 2003). Conforme os osteoblatos produzem e depositam essa matriz óssea de forma não ordenada, estes acabando aprisionados dentro da matriz por ele secretados. Este aprisionamento dos osteoblastos à MEC, fator que influencia para mudança fenotípica dessas células, se diferenciando em osteócitos (ZAMBUZZI, 2008). Estes osteócitos envoltos na matriz extracelular iniciam uma comunicação com células adjacentes via dendritos formando uma forte rede através das lacunas ósseas (RUTKOVSKIY; STENSLØKKEN; VAAGE, 2016; YANG et al., 2012). Essa comunicação ocorre inclusive com tecido endotelial promovendo a nutrição do tecido gerado e podendo carregar fatores produzidos por osteócitos. A combinação das lacunas ósseas, vasos sanguíneos, células osteoprogenitoras e mesenquimais formam uma estrutura esponjosa no osso e a formação por células mesenquimais e vasos sanguíneos de medula óssea (CHOI et al., 2002). Diferentes centros de ossificação com seu crescimento radial, acabam se fundindo e substituindo a membrana conjuntiva preexistente.

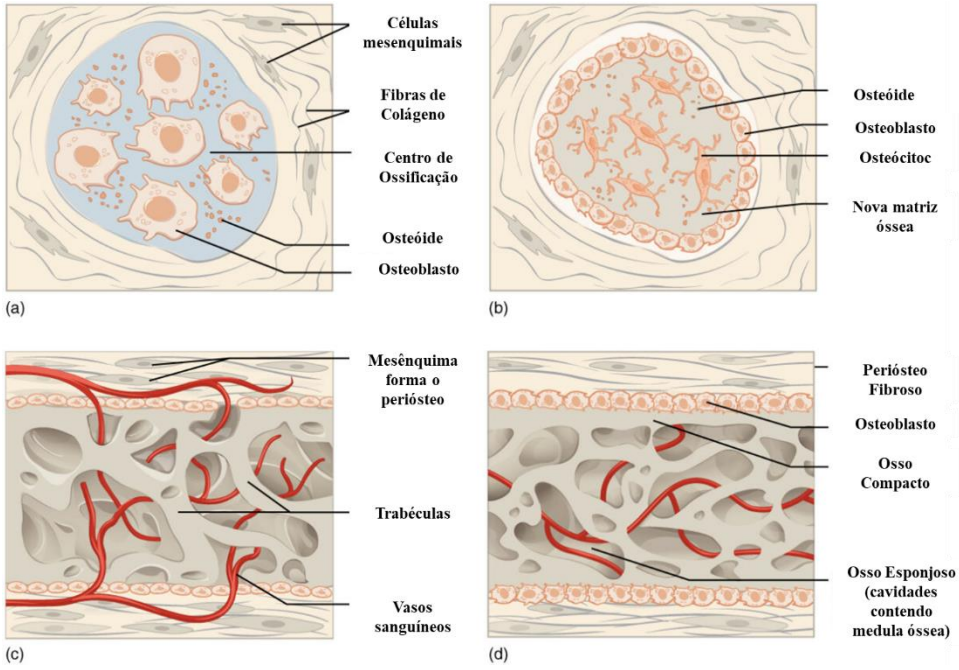

Figura 2: Processo de ossificação intramembranosa. A ossificação intramembranosa segue quatro etapas. **(a)**. As células mesenquimais se agrupam em grupos, e se formam centros de ossificação. **(b).** Osteoblastos ficam aprisionados na matriz e se transformam em osteócitos. **(c).** Mesequima forma o periósteo, a matriz trabecular é formada e vasos a invadem. **(d).** Osso compacto se desenvolve superficial ao osso trabecular, e vasos sanguíneos apinhados se condensam em medula óssea. Figura adaptada de OpenStax College, Anatomy and Physiology. OpenStax CNX. http://cnx.org/contents/14fb4ad7-39a1-4eee-ab6e-3ef2482e3e22@11.1. (SCHATZ, 2016).

Ossificação endocondral: A ossificação endocondral diferente do processo intramembranoso, é um processo pelo qual os ossos da cartilagem, associados às articulações e ossos longos, se

formam. Em eventos de cicatrização do tecido ósseo, é possível que os 2 eventos aconteçam, participando de modo combinado na regeneração do tecido. As células mesenquimais sob condensação se diferenciam em condrócitos para formar um modelo hialino com ossificação primária ocorrendo na zona média (MAES et al., 2010). A atividade dos osteoblastos e a formação vascular ocorrem durante a ossificação primária, enquanto que uma ossificação secundária ocorre mais tarde no centro das regiões epifisárias. Ao longo da haste do osso, a área de cartilagem desenvolvida se estende através da região de crescimento entre (diáfise) e ambas as extremidades (epífise) (RUNYAN; GABRICK, 2017). A ossificação endocondral promove o crescimento longitudinal dos ossos que no final do desenvolvimento requer a substituição do tecido jovem por tecido ósseo lamelar duro (DIRCKX; VAN HUL; MAES, 2013). A **Figura 3** ilustra todo o processo e este geralmente ocorre até a o início da idade adulta (18-25 anos) e conforme o crescimento do indivíduo esse processo acaba sendo comprometido (JACOBSEN et al., 2008; MAIA et al., 2022).

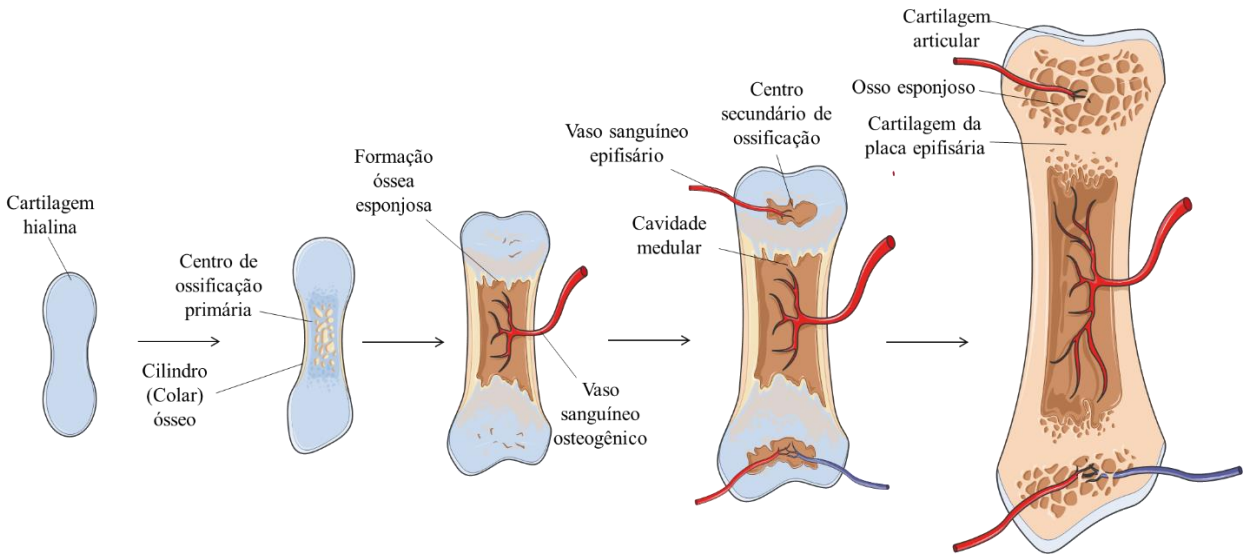

Figura 3: Esquema de ossificação endocondral com crescimento longitudinal do tecido ósseo a partir de um molde cartilaginoso. A partir de um molde de cartilagem forma-se o centro primário de ossificação com invasão de vasos na porção central do osso. Nas extremidades formam-se os centros secundários de ossificação que depois de vascularizado, irá promover a substituição completa de cartilagem por osso com auxílio de condroclastos trazidos pela corrente sanguínea. **Fonte.** Adaptado de Histologia Básica, L.C. Junqueira e José Carneiro. - [12ª Edição] - Rio de Janeiro: Guanabara Koogan, 2013.

Fratura e reparo ósseo: O sistema de reparo de um osso lesionado inicia imediatamente o recrutamento de células ósseas para reparar qualquer dano. Este processo passa por uma complexa e coordenada cascata de ações. Muitos componentes estão envolvidos no processo de restauração, incluindo citocinas e seus receptores. Com base na natureza da fratura, o processo de cicatrização pode ser dividido em cicatrização óssea primária e cicatrização óssea secundária (CARREIRA et al., 2014).

Cura óssea primária: No caso de lesões superficiais, pode ocorrer uma formação óssea primária. A área entre as bordas da fratura é preenchida diretamente com osso recém-formado e a formação do calo é reprimida. Nem o tecido conjuntivo nem o tecido fibrocartilaginoso estão envolvidos neste processo de cicatrização (LIEBERMAN; FRIEDLAENDER, 2005). A cicatrização óssea primária pode ser ainda subdividida em cicatrização de fendas e cicatrização de contato. Na cicatrização de fendas, a cavidade é preenchida diretamente com osso produzido pelos osteoblastos, onde um andaime de tecido ósseo é criado e apoiado pela estrutura óssea lamelar (LAD; MCGRAW; DAEGLING, 2019). Após várias semanas, a extremidade necrótica é reconstruída pela remodelação Haversian e substituída por camadas não mineralizadas de osso (osteons) (CHANG; LIU, 2022; LAD; MCGRAW; DAEGLING, 2019). Na cicatrização por contato, ao contrário, os osteons são capazes de crescer em todo o local da fratura devido à ausência de um espaço (SHEEN; GARLA, 2019). O túnel é feito por osteoclastos cortando cones através da linha de fratura. Um laço capilar de parede fina segue os osteoclastos suportados por células mesenquimais e células osteoprogenitoras para estabelecer camadas não mineralizadas de osso (osteons) (BIGHAM-SADEGH; ORYAN, 2015).

Cura óssea secundária: Uma fratura com um padrão complexo e uma falta de estabilidade biomecânica é classificada como uma formação óssea secundária. Tanto a ossificação intramembranosa quanto a endocondral estão envolvidas no processo, e a formação de um calo também ocorrerá. Normalmente, o termo está associado a um tratamento conservador que inclui possível micromoção dentro da fratura. Três fases sobrepostas ocorrem no processo secundário de cura óssea: inflamação, reparação e remodelação e são ilustradas na **Figura 4**:

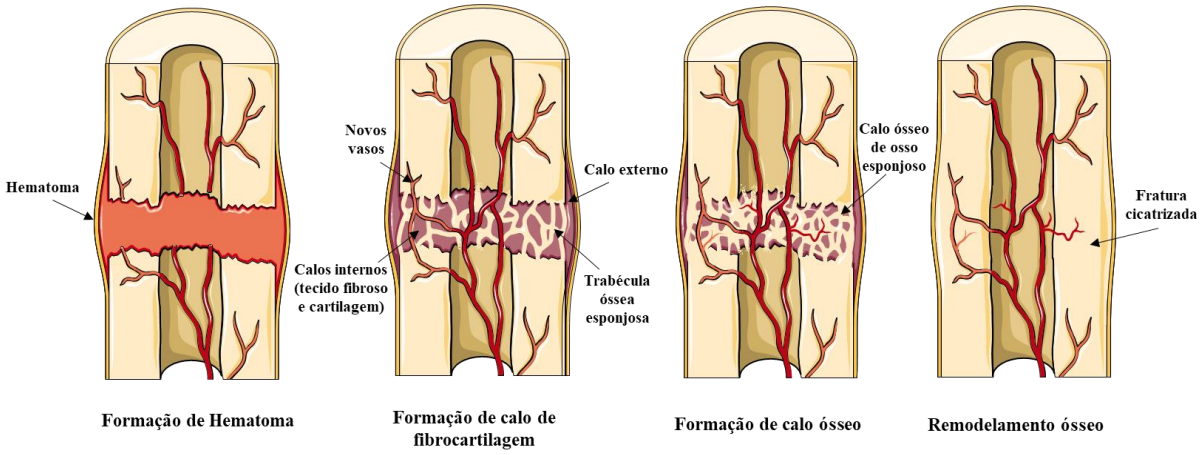

Figura 4: O esquema de formação óssea secundária ilustra os processos de cura, em ordem: Formação de hematoma, Fase de inflamação, Fase de reparo, Fase de remodelação. Elementos gráficos foram obtidos em https://smart.servier.com/.

Fase de inflamação: Uma fratura óssea leva a uma menor tensão de oxigênio no local da lesão devido à interrupção do fluxo vascular e da arquitetura da medula óssea. Uma resposta inflamatória

atinge seu pico após 48 horas e se estende por até 1 semana, e esta resposta é iniciada pela formação de um coágulo sanguíneo para recrutar moléculas bioativas, bem como precursores de osteoblastos e condroblastos. Uma cascata regulada de fatores de crescimento (fator de crescimento do fibroblasto [FGF], fator de necrose tumoral-α [TNF-α], PDGF e TGF-b) e uma variedade de citocinas são secretadas para encorajar as células mesenquimais a proliferar e diferenciar-se nas linhagens condrogênicas e osteogênicas (KOMORI, 2019; SHEEN; GARLA, 2019).

Fase reparadora: Tanto ossificações intramembranosas quanto endocondral estão envolvidas nesta fase, e ela começa dentro de poucos dias após a lesão, até que a fase inflamatória desapareça. O período endocondral pode durar até 28 dias. O objetivo desta fase é desenvolver um calo duro ao redor da área lesada para proporcionar suporte e estabilidade, e este será posteriormente substituído pelo osso. Fibroblastos, condroblastos e osteoblastos são formados por células mesenquimais no local da fratura. A migração de outras células com vasos sanguíneos também ocorre para produzir tanto osso compacto quanto trabecular. A mineralização do calo provavelmente ocorre com a mudança do pH, e a formação do osso ocorre como resultado da diferenciação dos osteoblastos. O calo mole é um resultado de células indiferenciadas. Trata-se de uma cartilagem desenvolvida que está associada à formação do osso endocondral, e eventualmente, após 4-5 semanas, a cartilagem calcificada será substituída por tecido fibroso (BAHNEY et al., 2019; KOSTENUIK; MIRZA, 2017; SCOTLANDI et al., 2000).

Fase de remodelação: A remodelação é a etapa final do processo de cura. Esta fase envolve a colaboração entre osteoblastos e osteoclastos para converter tecido mole em uma estrutura óssea capaz de suporte mecânico. Sob tensões fisiológicas, o tecido ósseo é substituído pelo osso lamelar, e o osso trabecular é reabsorvido pelos osteoclastos, o que cria pequenas cavidades conhecidas como lacunas da Howship. As células osteoblastos entram nestas cavidades e produzem novas matrizes, que prendem as células que depois se desenvolvem em osteócitos (ARO et al., 1990; SHEEN; GARLA, 2019).

Considerando esse repertório de informações, o osso demonstra ter capacidade de regenerar-se, resultando em tecido de reparação com propriedades anatômico-funcionais semelhantes aos originais. Outrossim, há ocasiões em que o tecido ósseo sofre lesões de tamanho crítico, nas quais seu processo cicatricial exige processos clínicos intervencionistas. Em auxílio ao procedimento de regeneração deste tipo de injúria, a aplicação de biomateriais no campo da engenharia de tecidos permite uma recuperação mais eficiente da lesão, trazendo o restabelecimento ao indivíduo. Diante deste fato, o desenvolvimento de novas estratégias com capacidade osteointegrativa aptos a prover um microambiente adequado à adesão, proliferação e diferenciação celulares com o intuito de ofertar as condições necessárias para a regeneração óssea

1.2 Circulação sanguínea, angiogênese e osteogênese: um acoplamento necessário

Vascularização é essencial para o desenvolvimento do esqueleto, sobretudo em eventos biológicos referente ao crescimento e remodelação do osso (BRANDI; COLLIN-OSDOBY, 2006; CHIM et al., 2013; DIRCKX; VAN HUL; MAES, 2013; HE et al., 2013), abastecendo o tecido com nutrientes, fatores de crescimento, hormônios, citocinas e quimiocinas, de acordo com as necessidades; além da importante função de remoção de metabólitos residuais (BRANDI; COLLIN-OSDOBY, 2006; KANCZLER; OREFFO, 2008). Dependendo de sua origem, o desenvolvimento ósseo ocorre por meio de dois modos distintos de ossificação: **1-** intramembranosa: (ossos chatos, como crânio e clavícula) e **2 -** Endocondral (como o fêmur). Apesar de suas diferenças, no entanto, vascularização é um pré-requisito para os dois tipos de ossificação (DIRCKX; VAN HUL; MAES, 2013; GERBER; FERRARA, 2000; YE et al., 2012), destacando-se como ponto comum aos eventos diferenciais de ossificação. Na verdade, o desenvolvimento da rede vascular desempenha um papel essencial na orientação e morfogênese de membros, durante a organogênese (BRANDI; COLLIN-OSDOBY, 2006). A vascularização é necessária para que ocorra a osteogênese: exercendo papel vital durante o processo de ossificação e remodelação óssea (CHIM et al., 2013; DIRCKX; VAN HUL; MAES, 2013; MAES, 2013), como também componentes-chave durante sua reparação do tecido lesado. Angiogênese no calo ósseo garante o fornecimento necessário de moléculas vitais como nutrientes, oxigênio, fatores de crescimento, citocinas, além de células osteo-precursoras (BORD et al., 1996). Assim, a associação espacial e temporal da formação óssea com vascularização já tem sido denominado como "acoplamento angio-osteogênico" (DIRCKX; VAN HUL; MAES, 2013; MAES, 2013; SCHIPANI et al., 2009).

Anatomicamente, a vasculatura dos ossos longos é constituída por 4 artérias, destacando as metafisárias, epifisárias e artérias do periósteo (ITKIN et al., 2016). Estas artérias adentram os ossos e atingem a cavidade medular, onde se dividem formando as corticais e microcirculações da medula (SANTOS; REIS, 2010). No osso cortical, os vasos alimentam os capilares Haversianos e canais de Volkmann (LAROCHE, 2002), enquanto que na medula, os capilares drenam para sinusóides (WILSON; TRUMPP, 2006). Estes capilares, unem-se para formar uma única vénula que segue o percurso da arteríola e volta para o plexo pericondral (HAYASHI, 1992). Somando-se, um dos componentes histológicos mais importantes dos vasos sanguíneos é o endotélio, o que desempenha um papel fundamental na manutenção da homeostase óssea, não só ao funcionar como uma barreira, mas também altamente permeável, segregando fatores capazes de recrutar células especiais ao osso (BRANDI; COLLIN-OSDOBY, 2006; IMAI et al., 1999).

Em ossos adultos, sabemos que são submetidos continuamente a remodelação, a fim de manter a sua integridade e estabilidade biomecânica (CHIM et al., 2013; DIRCKX; VAN HUL; MAES, 2013). A remodelação óssea ocorre em duas fases importantes: a reabsorção óssea mediada pelos osteoclastos e a formação do osso novo, mediada pelos osteoblastos (BAROU et al., 2002; KARSENTY, 2000b; SANTOS; REIS, 2010). Este processo ocorre em estruturas especiais chamadas de unidades remodelação óssea (BRUs) (DIRCKX; VAN HUL; MAES, 2013; HAUGE et al., 2001). A BRU facilita a interação celular entre osteoblastos e precursores de osteoclastos: onde ocorre a secreção do Ligante ativador de receptor de NF-kB (RANKL), modulando a ativação de células mononucleares a se diferenciarem em osteoclastos (HENRIKSEN et al., 2009; MARTIN; SEEMAN, 2008; SIMS; GOOI, 2008; YASUDA et al., 1998), onde osteócitos desempenham papel crucial, já que representam a maior fonte de RANKL no organismo.

Estudos sugerem que o desenvolvimento de vasos sanguíneos nos ossos e osteogênese sejam eventos acoplados, o que é indicativo da presença de um *crosstalk* molecular entre as células endoteliais e osteoblásticas (ESHKAR-OREN et al., 2009; MAES et al., 2010). Kusumbe et al. (2014) (KUSUMBE; ADAMS, 2014) identificaram um novo subtipo de capilar presente na biologia do sistema esquelético, com propriedades morfológicas, moleculares e funcionais distintas. Eles demonstraram que estes vasos sanguíneos, foram capazes de gerar um metabolismo distinto capaz de mediar o crescimento vascular do osso, mantendo osteoprogenitores perivasculares, acoplando angiogênese e a osteogênese. Estes autores também demonstraram que a este acoplamento estava reduzido com a idade (KUSUMBE; ADAMS, 2014; KUSUMBE; RAMASAMY; ADAMS, 2014). Além disso, um segundo estudo realizado pelo mesmo grupo de pesquisa foi capaz de estabelecer uma ligação molecular entre angiogênese, sinais angiocrinos e osteogênese (KUSUMBE; RAMASAMY; ADAMS, 2014): eles demonstraram que a atividade de Notch endotelial desempenha um papel crucial na promoção do acoplamento entre angiogênese e osteogênese. A ruptura de sinalização Notch não só prejudica morfologia e crescimento dos vasos nos ósseos, mas também leva a uma diminuição da osteogênese (RAMASAMY et al., 2016b). Diante desta literatura atual, temos a clareza de que angiogênese e osteogênese são eventos fisiológicos acoplados, como ilustrado na **Figura 5**, onde a hipóxia parece exercer papel importante.

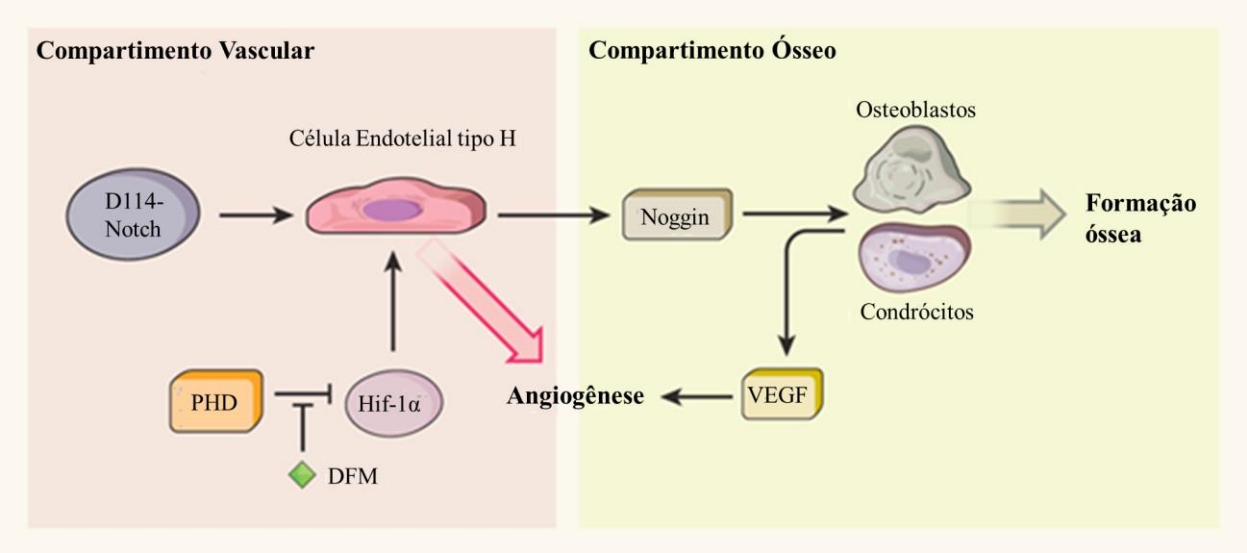

Figura 5*:* Kusumbe et al. e Ramasamy et al. definiram o tipo H de células endoteliais como uma população vascular no tecido ósseo, satisfazendo angiogênese em condições fisiologicamente normais. Nestes trabalhos, os autores mostraram que células endoteliais do tipo H são capazes de secretarem a proteína Noggin, a qual conhecidamente regula o metabolismo de osteoblastos e condrócitos. Além da Noggin, mostraram o envolvimento de VEGF, Hif-1α e da sinalização Dll4–Notch neste cenário. Porém, trata-se de uma sinalização parácrina complexa, onde os envolvimentos de moléculas efetoras ainda necessitam de maiores esclarecimentos. **Fonte:** Adaptado de Noble e colaboradores (LE NOBLE; LE NOBLE, 2014).

Somado ao recente progresso, acreditamos que este acoplamento entre as duas linhagens celulares é regido por um repertório de moléculas e vesículas, as quais, ainda, não tem sido documentado e que poderia ser regulado pela difusão de oxigênio molecular no tecido. Portanto, explorar o efeito cruzado dos mecanismos parácrinos envolvidos entre células ósseas e endoteliais e validar seus efeitos em modelos funcionais de hipóxia trarão informações valiosas na busca por novas terapias, uma necessidade emergente no campo da medicina regenerativa.

1.3 Mecanismos biológicos envolvidos com a hipóxia

Em contextos patológicos, como câncer e isquemia, bem como durante o desenvolvimento através da diferenciação celular, a capacidade de uma célula se adaptar a condições de hipóxia é crítica e sempre despertou interesse na área acadêmica. Como sabemos, o oxigênio pode ser considerado um substrato metabólico importante e indispensável em várias reações enzimáticas, incluindo a respiração mitocondrial, servindo como aceptor final de elétrons no final da cadeia respiratória - durante o desenvolvimento embrionário, por exemplo, acredita-se que a diferenciação celular, e consequente morfogênese dos tecidos, sejam modulados por gradientes de oxigênio que, pelo menos em parte, dependem da via de sinalização do fator induzível por hipóxia (HIF) para mediar seus efeitos (DUNWOODIE, 2009). Os fatores de transcrição HIF-1 e HIF-2 são mediadores centrais das respostas fisiológicas que permitem que as células hipóxicas sobrevivam e se diferenciem (GIACCIA; SIMON; JOHNSON, 2004). Essas

proteínas desencadeiam uma série de efeitos autônomos, autócrinos, parácrinos e endócrinos com o objetivo central de aumentar a entrega de oxigênio aos tecidos enquanto diminui seu consumo de oxigênio (SEMENZA, 2012).

Neste cenário, HIF-1α é ativado quando os níveis de oxigênio caem, o que é detectado por uma classe de prolil hidroxilases dependentes de 2-oxoglutarato (PHDs) e dependentes de Fe^{2+} (**Figura 6**) (IVAN et al., 2001; JAAKKOLA et al., 2001; POUYSSEGUR; DAYAN; MAZURE, 2006; WANG; SEMENZA, 1993). Por outro lado, O HIF-1β é expresso constitutivamente de maneira independente de oxigênio. A atividade de HIF-1α é determinada pela tensão do oxigênio, sendo que em condições acima de 5%, sua meia-vida é muito curta, sendo então degradado pela via protessômica (**Figura 6**). Por outro lado, em condições hipóxicas, a proteína HIF-1α se acumula, transloca-se para o núcleo, dimeriza com HIF-1β e, mediante o recrutamento de vários outros co-ativadores transcricionais, liga-se a elementos de resposta à hipóxia nos promotores de genes específicos (KEITH; JOHNSON; SIMON, 2011). Sabe-se que esta via de sinalização de HIF está envolvida com feedback tecidual direto, necessitando o aumento de número de vasos sanguíneos, destacando-se assim como fator importante no estimula da angiogênese, como ilustrado na **Figura 6**. Como angiogênese é necessária a eventos teciduais requeridos na regeneração funcional de tecidos, destaca-se a importância desta via como ferramenta a ser explorada em bioengenharia de tecidos, como o tecido ósseo.

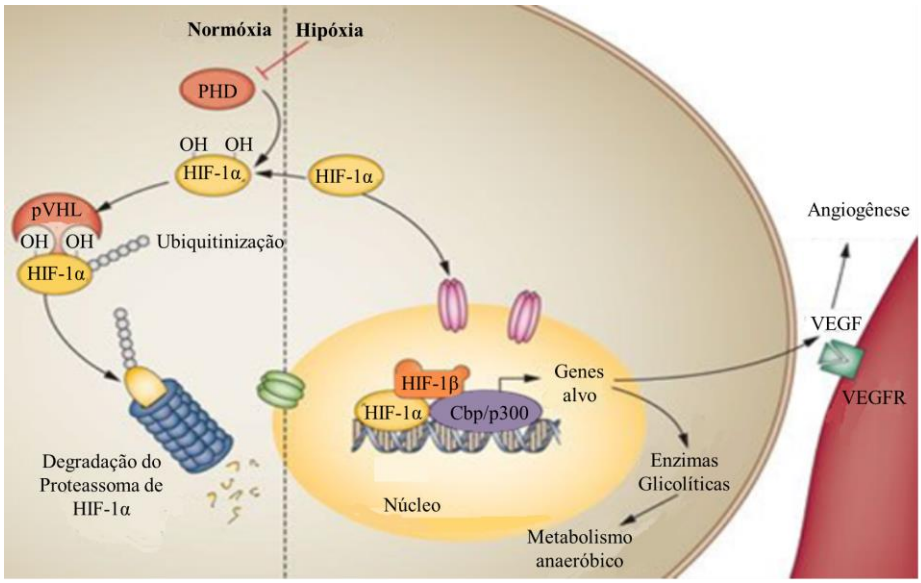

Figura 6*:* Sinalização de HIF-1α. Na normoxia, os sensores celulares de oxigênio (PHDs) hidroxilam resíduos prolina específicos (Pro402 e Pro564) do HIF-1α, levando à sua degradação proteossômica mediada por pVHL, uma ubiquitina ligase E3. Durante a hipóxia, o HIF-1α não é ubiquitinilado, consequentemente não é degradado, atuando como um fator de transcrição de genes, incluindo o VEGF, que promove a angiogênese e genes envolvidos no metabolismo anaeróbico. **Fonte:** Adaptado de MAES (MAES; CARMELIET; SCHIPANI, 2012).

1.4 Hipóxia e homeostase óssea

O osso adulto é submetido continuamente ao remodelamento, o que possibilita a manutenção da homeostase esquelética e mineral (TAKUBO et al., 2010). O equilíbrio entre a formação óssea pelos osteoblastos (de origem mesenquimal) e a reabsorção óssea pelos osteoclastos (de origem hematopoiética) é fundamental na remodelação óssea e, quando em desequilíbrio desta coordenação, resulta em um osso poroso (KARSENTY; KRONENBERG; SETTEMBRE, 2009). Ao contrário da cartilagem, a medula óssea é altamente vascularizada e, embora o papel desse abundante suprimento sanguíneo na remodelação óssea seja mal definido, é provável que vá além de ser uma mera fonte de nutrientes (SCHIPANI et al., 2009). De fato, já se discutia que esses vasos sanguíneos entregam precursores de osteoblastos e osteoclastos ao osso (MAES et al., 2010).

A modulação da via HIF em osteoblastos revelou que essa via exerce papel importante na formação óssea (WANG et al., 2007b). A perda de HIF1α ou HIF2α em osteoblastos de camundongos causa uma diminuição considerável no volume ósseo (SHOMENTO et al., 2010), enquanto níveis aumentados destes genes levam ao seu aumento (WANG et al., 2007b). Notavelmente, as alterações no volume ósseo correlacionam-se positivamente com alterações na vascularização óssea e na expressão de VEGF, reforçando uma possível ligação entre angiogênese e osteoblastogênese (SCHIPANI et al., 2009). Apesar da crescente evidência de um papel importante da angiogênese na aumentando o volume ósseo via regulação positiva da via do HIF, mecanismos celulares autônomos a via de HIF, como a regulação do metabolismo anaeróbico, também podem ser importantes, pois o metabolismo anaeróbico é um dos principais alvos do HIF.

A regulação da angiogênese por VEGF, um importante alvo da via de HIF’s, também já foi criticamente avaliada e uma associação com o remodelamento do osso é proposta, como sugerido na **Figura 7**. Assim, a identificação dos mecanismos moleculares que governam a complexa rede de sinalização celular decorrente aos efeitos biológicos dos HIF’s precisa ser aprofundada e melhor compreendida. Em particular, mecanismos farmacológicos capazes de promover a hipóxia e concomitante aumento da diferenciação de osteoblastos são extremamente necessários para proposição de novas ferramentas clínicas e produtos tecnológicos a serem explorados na prática de reconstrução do osso.

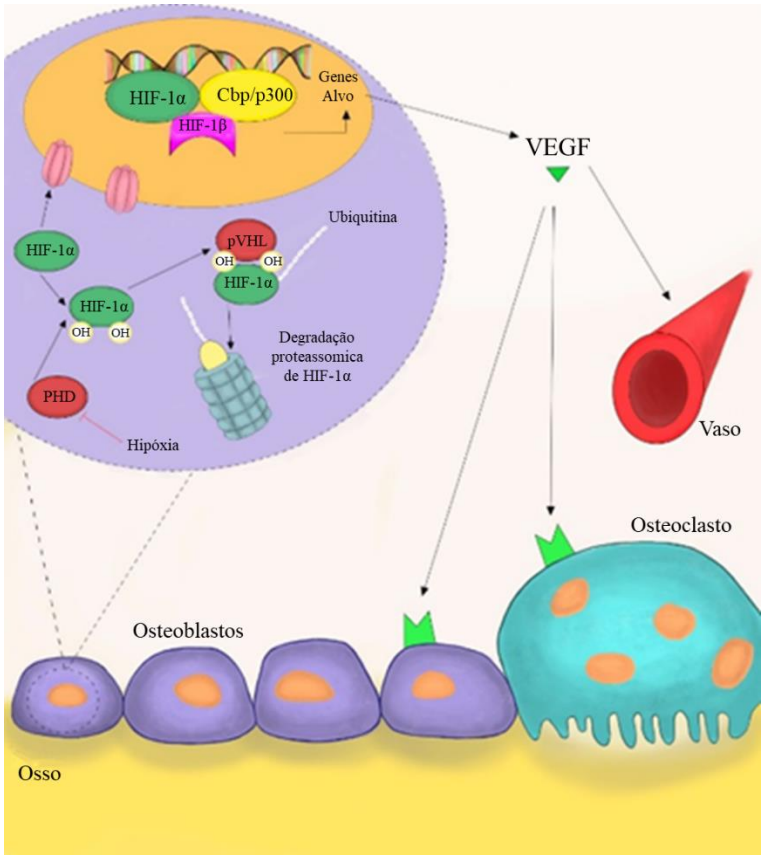

Figura 7: Acoplamento entre as vias de HIF e VEGF no osso. Os osteoblastos expressam ambos HIF-1α e HIF-2α, que modulam o desenvolvimento ósseo, sua homeostase e a angiogênese. Alguns dos efeitos dos HIF's no osso e na angiogênese são mediados pelo VEGF. **Fonte:** Próprio autor e imagem ilustrada por Paula Bertin.

1.5 VEGF na reparação de fraturas

O reparo bem-sucedido da fratura recapitula amplamente os vários estágios do desenvolvimento ósseo; o desenvolvimento adequado dos vasos sanguíneos é, portanto, essencial. Vários fatores angiogênicos, incluindo o VEGF, estão aumentados durante a cicatrização e reparo funcional da fratura (GERSTENFELD et al., 2003). Em camundongos, o tratamento com um receptor solúvel de VEGF (VEGFR) ou antagonista de VEGF resulta em comprometimento da formação óssea, enquanto a administração local de VEGF aumenta com sucesso seu processo de reparo (STREET et al., 2002). VEGFR-1 e VEGFR-2 estão criticamente envolvidos na angiogênese e na formação óssea durante o reparo da fratura (JACOBSEN et al., 2008). Vários tipos de células no microambiente ósseo, incluindo células osteogênicas, macrófagos e osteoclastos, podem secretar moléculas ativas neste contexto e, portanto, participam de mecanismos importantes e integrados no desenvolvimento do osso (FISCHER et al., 2008).

1.6 Princípios Gerais da Regeneração Óssea

Quando lesado o tecido ósseo inicia o processo de cicatrização, uma resposta comum a vários tipos de lesões, com o objetivo de restabelecer sua estrutura e função. A partir de uma cascata de eventos biológicos altamente organizada e modulada por vários mediadores químicos, citocinas e fatores de crescimento, além de fatores ambientais e locais (BLUMENTHAL et al., 2003; WANG et al., 2017), tornando-o um evento multifatorial. A cicatrização óssea pode ocorrer por dois processos: regeneração e reparação. O processo de regeneração ocorre quando o tecido lesado é povoado com base na proliferação e completa diferenciação dos elementos teciduais originais. Assim, a cicatriz do tecido possuí características morfológicas e propriedades funcionais semelhantes à do tecido original. O processo de reparação consiste na substituição do tecido lesado pela formação de um tecido conjuntivo fibroso, resultando num tecido que difere das propriedades originais do tecido lesionado. Considera-se hoje prioritário regenerar e não reparar, reconstruindo a forma e restaurando sua função. Para isso é necessário uma sequência de eventos hierárquicos onde as células progenitoras mesenquimais da medula óssea dão origem a osteoblastos sob a influência de vários sinais osteogênicos específicos para a sua proliferação e diferenciação(MATTA et al., 2019; MOEINZADEH; JABBARI, 2015). A diferenciação de osteoblastos tem seu início pela sinalização de Proteínas Morfogenéticas Óssea (BMP) junto aos seus receptores responsáveis pela ativação de fatores de transcrição (Runx2 e Osterix), e subsequente expressão de genes específicos de osteoblastos tais como: fosfatase alcalina, o colágeno tipo 1, Osteonectina, Osteocalcina e Sialoproteina óssea (BALOUL, 2015; MOEINZADEH; JABBARI, 2015).

O desenvolvimento de estratégias terapêuticas para aplicação em engenharia de tecidos assenta tradicionalmente numa tríade regenerativa constituída por três elementos básicos que se interagem entre si: 1) células competentes capazes de uma resposta eficaz (MINE et al., 2014; PASCHOS et al., 2015), 2) moléculas de sinalização com capacidade de estimular as células no sentido pretendido (CAO et al., 2014) e 3) matrizes de suporte (Biomateriais) capazes de guiar e apoiar a formação do tecido a se regenerar (MOUNTZIARIS; MIKOS, 2008; SALGADO; COUTINHO; REIS, 2004; SHIH et al., 2014). Com os avanços atuais, tem-se enfatizado a inclusão de um quarto elemento de reconhecida relevância à tríade: a estabilidade mecânica. A estabilidade do microambiente onde se localiza o defeito ósseo a ser regenerado parece ser determinante para a resposta biológica dos outros três elementos (células, fatores de crescimento e matrizes) já discutidos anteriormente. Neste contexto, uma boa vascularização local, consequência ainda de uma boa estabilidade, faz toda a diferença sendo também um pré-requisito essencial. Este conceito de quatro faces terá muito mais faces se considerarmos a evolução da nanotecnologia, da genômica e da proteômica, conduzindo ao desenvolvimento, num futuro próximo, de um biorreator capaz

de, a partir de aspirados medulares, regenerar nosso próprio tecido ósseo quando necessário, o que funcionaria posteriormente como um auto-enxerto. Este progresso só se justifica através de uma ação coordenada e multidisciplinar, envolvendo expertises dentro da Biologia, Física, Química, Engenharia e Medicina, criando uma nova área: a Medicina Regenerativa.

Atualmente, a Medicina Regenerativa tem obtido destaque por disponibilizar novas metodologias terapêuticas sofisticadas e multifatoriais, com o objetivo de regenerar o tecido lesado ou totalmente perdido (RAVINDRAN; GEORGE, 2014; REZZA; SENNETT; RENDL, 2014; ROBINTON; DALEY, 2012). Atualmente dependendo do tamanho e tipo de lesão, é requerida a utilização de enxertos ósseos (SANTOS et al., 2013). O enxerto utilizado como padrão ainda é o osso autólogo, porém a utilização deste significa muitas vezes submeter o paciente a outro procedimento cirúrgico, gerando uma significativa morbidade e custos tanto para o paciente, como para o sistema público de saúde. Por estas e outras razões, estudar e desenvolver novas alternativas torna-se imprescindível.

O desenvolvimento e avaliação de protocolos clínicos inteligentes capazes de estimular as células osteoprogenitoras que permitam mimetizar aquelas características osteogênicas do enxerto autógeno, assim criando alternativas como os biomateriais. Por fim, certas características da superfície do biomaterial influenciam enormemente a atividade celular (DA COSTA FERNANDES et al., 2018a, 2018b; ZAMBUZZI et al., 2014) e a integração célula-material (p. ex, formação de componentes de adesão focal e organização do citoesqueleto com efeitos na maturação dos osteoblastos e subsequente mineralização). Desta forma, conhecer os mecanismos moleculares envolvidos neste processo faz-se necessário, visto que parâmetros adicionais agregam novas características durante o desenvolvimento de novos materiais ou superfícies, aumentando o desempenho do material, diminuição do tempo de reabilitação do paciente, etc (GEMINI-PIPERNI et al., 2014a; SARAN; GEMINI PIPERNI; CHATTERJEE, 2014). Este tema tem sido explorado pelo nosso grupo nos últimos anos, buscando conhecer a identidade molecular dos Biomateriais (BEZERRA et al., 2017; KANG et al., 2018; NASCIMENTO et al., 2017).

1.7 Biomateriais

A partir de 2018, a definição de biomaterial pode ser descrita como: “ um material projetado para assumir uma forma que pode direcionar, por meio de interações com sistemas vivos, o curso de qualquer procedimento terapêutico ou de diagnóstico" (ZHANG; WILLIAMS, 2019).

Biomateriais são materiais projetados com a função de substituir partes do corpo e, assim, permitindo a recuperação tecidual e funcional do tecido, por vezes afetados por doenças ou acidentes. Principais diferenciais dos aspectos funcionais dos materiais biomédicos tratam

aspectos de biocompatibilidade e biofuncionalidade, características necessárias para que esses exerçam essas funções diversas. Por definição, biocompatibilidade refere-se à capacidade de um material de funcionar com uma resposta apropriada do hospedeiro em uma aplicação específica, e a biofuncionalidade representa a habilidade do material desempenhar a função desejada, restabelecendo o tecido com suas características anatômico-funcionais (HAIDER et al., 2017; SHIN et al., 2016; WILLIAMS, 2019; ZHANG; WILLIAMS, 2019).

1.7.1 História dos biomateriais

A fabricação de implantes e próteses datam de mais de 7000 anos e é tão antiga quanto o início da invenção de instrumentos e ferramentas, tão antigos quanto o início da ciência dos materiais em cerâmica e metalurgia (RATNER; ZHANG, 2013).

As primeiras evidências do reconhecimento da deformidade e da necessidade de reabilitação pelo homem são difíceis de estabelecer, pois muitas civilizações antigas não tinham registros escritos ou estes se perderam com o tempo. Porém com informações de antropólogos e arqueólogos para interpretar os mitos, obras de arte e restos humanos, informações importantes sobre o desenvolvimento e utilização de próteses e outros dispositivos para auxiliar a vida humana, começaram a ser compreendidas (HILDEBRAND, 2013).

Por conta de acidentes, guerras, batalhas, ataques de outros povos ou mesmo de animais, muitos seres humanos perderam membros como braços, mãos, pernas, pés ou outras partes do corpo, que foram substituídas por "implantes" ou "próteses". Evoluindo juntamente com à prática médica, os primeiros dispositivos protéticos que foram desenvolvidos e que foram encontrados, apresentavam funções eficientes, considerando o acesso a diferentes materiais e tecnologias dos seus respectivos períodos (HILDEBRAND, 2013; RATNER; BRYANT, 2004).

Dos tipos de materiais que foram encontrados, uma variedade tem relação com o osso, utilizando para reparação óssea, substituição de dentes e trepanação da cabeça (craniotomia). Diferentes materiais foram utilizados desde o início: os materiais de primeira aparição de origem natural eram madeira, nácar e marfim, mas também osso alogênico ou mesmo xenogênico para construções ortopédicas. Quanto aos substitutos de dentes, na antiguidade os “profissionais da odontologia” aplicaram diferentes dentes de animais, em particular de cães, bezerros, focas e outros animais (HILDEBRAND, 2013).

Com o progresso da tecnologia, os cirurgiões e estudiosos dos períodos, iniciaram a introdução de metal como prótese e material de implante, em particular ouro, prata, cobre e chumbo com mais ou menos alto grau de pureza. Apesar da falta de conhecimento sobre toxicidades, eles obtiveram sucesso de tais dispositivos médicos, pois múltiplos achados

arqueológicos mostram que os pacientes operados sobreviveram à operação cirúrgica e apresentaram osseointegração (HILDEBRAND, 2013; RATNER; BRYANT, 2004; RATNER; ZHANG, 2013).

1.7.2 Tipos de próteses encontradas

Próteses de membros e pés: No Egito, foram encontradas substituições de dedos dos pés. O dedo do pé do Cairo (

O dedo do Cairo **(Figura 8)** que foi encontrado originalmente em 2000 pelo patologista alemão Andreas Nerlich da Ludwig Maximilian University of Munich, ligado a uma antiga múmia egípcia. Este artefato é datado entre 1550 e 700 AC, foi construído em madeira e couro, permitindo que a utilização com alguma elasticidade oferecendo maior conforto para o amputado (THURSTON, 2007). Artefatos como este, apresentam sinais de desgaste, relatando que ocorreu o contato da pele com o material, assim indicando que foram usados em vida e não podem ser considerados como membros completos para a vida após a morte.

Figura 8: O dedo do Cairo - "The **Cairo Toe**", pertenceu a uma múmia egípcia (entre 1550 e 700 AC).

Entre os séculos XVIII e XIX, portadores famosos de próteses de perna como o antigo governador holandês de Nova Amsterdam (mais tarde Nova York), Pieter Stuyvesant (1592-672) (**Figure 9a**), e Józef Sowiński (1777-1831), general da artilharia polonesa, sua perna de madeira (**Figure 9b** é encontrada no Museu do Exército Polonês em Varsóvia (HILDEBRAND, 2013). O século XIX trouxe inovação aos dispositivos protéticos. A *Anglesey Leg* foi inventada em 1800 por James Potts de Londres e patenteada em 1805 (**Figura9c**). Ela pode ser encontrada no Museu de Ciências em Londres (GUTFLEISCH, 2003).

Figura 9: a. Pieter Stuyvesant (1592–1672) estátua mostrando sua perna de madeira (City of Kinston, New York), **b.** Perna de madeira pertencente ao General ***Józef Sowiński*** (1777–1831) preservada no *Polish Army Museum* em Varsóvia. **c.** A *Anglesey Leg* inventada em Londres por *James Potts* em 1800 e patenteada em 1805. Imagens obtidas e adaptadas de Hildebrand (HILDEBRAND, 2013).

Implantes cranianos: Técnicas de fechamento do crânio por meio de implantes, conhecidas por cranioplastia. Nos achados, em múltiplos casos, foram inseridas placas de cobre, prata ou ouro para proteger o cérebro contra agressões externas. Além disso, o cobre e a prata têm um efeito antisséptico conhecido e certamente desempenharam um papel importante na prevenção de infecções (HAN; CHEN, 2007; HILDEBRAND, 2013; RATNER; ZHANG, 2013). A **Figura10a** demonstra uma placa metálica implantada com indícios de osseointegração.

Restaurações dentárias: Os implantes e próteses mais frequentemente fabricados e usados em todas as culturas e em todos os tempos foram os dentes. Os egípcios e os fenícios, começaram a fabricar próteses dentárias, ancorando dentes instáveis com fios de ouro e substituindo os dentes eventualmente perdidos por dentes de cães (**Figura10b**) (CRUBEZY et al., 1998; HUEBSCH; MOONEY, 2009; MINOZZI et al., 2007). Entre os achados arqueológicos e considerado um exemplar de destaque, está no crânio peruano Mochica (**Figura10c**), uma substituição completa de todos os dentes por esculpidos quartzo rosa (HILDEBRAND, 2013; HUEBSCH; MOONEY, 2009).

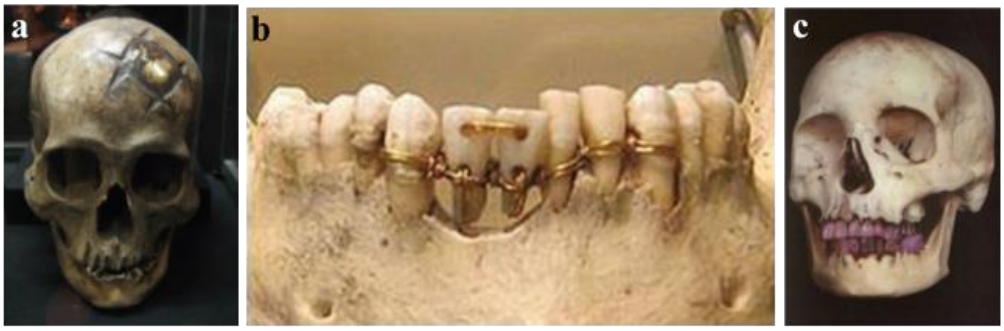

Figura 10: a. Crânio trepanado pertencente a cultura Inca, fechado por ouro e exibindo uma reconstrução óssea, ao artefato está *no Museu del Oro em Lima, Peru.* **b.** Restauração típica realizada pelos fenícios. **c.**

Crânio Peruano, com substituição de todos os dentes por quartzo rosa, em exposição no Museu del Oro, em Lima. Figuras obtidas e adaptadas de Hildebrand (HILDEBRAND, 2013).

1.8 Biomateriais e a Engenharia de tecidos ósseos

A engenharia de tecidos é um campo interdisciplinar que combina conceitos essenciais da engenharia e das ciências da vida para criar bio-substitutos que possam restaurar, manter ou aprimorar a função de tecidos lesionados ou comprometidos por doenças (RATNER; BRYANT, 2004). Ela se baseia na compreensão da configuração de novos tecidos em termos de regeneração. Diferentes áreas da ciência estão envolvidas e são combinadas para o desenvolvimento da engenharia de tecidos, como física, química, engenharia, biologia e medicina.

O processo de remodelação é uma resposta comum baseada em uma harmonia contínua entre as células ósseas para manter o tamanho, forma e função óssea (CARREIRA et al., 2015). Como citado anteriormente o mecanismo de cura óssea envolve uma complexa cascata de ações, que são expressas principalmente por três fases (inflamação, reparação e remodelação) (BAHNEY et al., 2019). A integração das fases de cicatrização leva à restauração dos vasos sanguíneos, estruturas porosas e compactas, e seu correto funcionamento (CARREIRA et al., 2014). Entretanto, defeitos ósseos que causados por trauma, câncer, infecção, ressecção, degeneração patológica e malformação congênita, necessitam de intervenção cirúrgica (ZHANG et al., 2019). Algumas vezes a lesão é classificada como um defeito não cicatrizante (defeito de tamanho crítico) onde os ossos são incapazes de formar um calo e preencher a lacuna da fratura (CAO et al., 2014). Nesses casos, a engenharia de tecidos ósseos desempenha um papel importante para impulsionar a osteogênese óssea e restaurar o tecido lesionado.

Os substitutos ósseos podem ser formados usando materiais tradicionais e sintéticos. A técnica tradicional utiliza osso natural para compensar a área em falta. Uma revolução na engenharia de tecidos ósseos, entretanto, introduziu materiais sintéticos com os quais os tratamentos podem ser aperfeiçoados para superar as complicações associadas aos enxertos naturais. Diferentes tipos de substitutos são utilizados em regeneração óssea, como auto-enxertos, aloenxertos, xenoenxertos, cerâmicas e polímeros, informações básicas sobre as diferenças, vantagens e desvantagens serão abordadas.

1.8.1 Requisitos de substitutos de engenharia de tecidos ósseos:

Biocompatibilidade pode ser definida como a capacidade de um material de funcionar com uma resposta apropriada do hospedeiro em uma aplicação específica (ZHANG; WILLIAMS, 2019). Esta é uma das exigências mais importantes associadas aos materiais implantados (CAPLAN; SHAH, 2009). O substituto ósseo não é um objeto inerte; ele interage com o ambiente circundante

após a implantação. Estas interações devem causar efeitos mínimos ou nenhum efeito tóxico ao tecido adjacente ao implante ou outros órgãos e tecidos do hospedeiro (GOMES et al., 2020).

Biodegradabilidade refere-se à degradação macromolecular por um produto químico passivo ou uma atividade celular para evitar qualquer outra operação cirúrgica (ASLANKOOHI et al., 2019). Os elementos degradados devem ser eliminados do corpo sem nenhum efeito colateral residual. Como um biomaterial *scaffold* ou andaime, o objetivo desejado é fornecer um suporte mecânico de forma coordenada até que o novo tecido seja formado e recupere sua função (GINEBRA et al., 2010). Entretanto, a taxa de degradação é difícil de controlar e pode alterar a abordagem. Portanto, o melhor cenário de degradação é aquele que ocorre simultaneamente com a nova formação do osso (LIU et al., 2017).

Osteocondutividade, na regeneração óssea é a característica de fornecer um suporte (andaime) tridimensional que pode suportar capilares e crescimento celular, bem como isolar o tecido mole circundante de interromper o novo crescimento ósseo (LEI et al., 2019) [39]. Os substitutos ósseos ideais devem permitir que a adesão das células, que elas sobrevivam e proliferem, e devem permitir que as células fabriquem a matriz extracelular na superfície (LE GUÉHENNEC et al., 2007).

Osteoindutividade, refere-se ao recrutamento de células osteoprogenitoras para o local da lesão, estimulando as células pluripotentes a se diferenciarem em células osteogênicas (BOSE; ROY; BANDYOPADHYAY, 2012). Uma cascata regulada de fatores de crescimento, proteínas e receptores são secretados e ativados respectivamente, para encorajar as células mesenquimais a proliferar e se diferenciar em linhagens osteogênicas (GROEN et al., 2015).

A porosidade e a interconectividade têm um efeito a nível celular, induzindo os processos de migração e mineralização. A porosidade também funciona para intertravar o implante no tecido circundante para estabilidade mecânica (TUYEN; LEE, 2011). O osso varia em sua quantidade de porosidade, com aproximadamente de seu volume total em 10% em osso cortical e 50-90% do esponjoso (GALEA et al., 2008). Da mesma forma, os enxertos ósseos devem conter uma taxa consistente de poros entre micro e macro-escalas, e estes devem ser distribuídos de forma homogênea (SIONKOWSKA; KACZMAREK, 2017). A porosidade e a interconectividade também estão associadas à melhoria da osteocondutividade, melhorando a fixação celular, migração, proliferação e diferenciação (KIM et al., 2010). Além disso, os poros interligados podem afetar a osteoindutividade, onde poros abertos totalmente conectados aumentam a taxa de difusão, penetração e migração celular, invasão de vasos sanguíneos, fornecimento de oxigênio e nutrientes, bem como remoção de resíduos metabólicos (GBURECK et al., 2007).

O osso natural combina propriedades que lhe fornecem rigidez e flexibilidade na presença de materiais orgânicos (colágeno) e não orgânicos (hidroxiapatita) (HABIBOVIC; DE GROOT, 2007). Portanto, os substitutos dos enxertos ósseos devem ter a capacidade de imitar a resistência mecânica dos ossos naturais, especialmente no caso de ossos que suportam cargas (HABIBOVIC; DE GROOT, 2007).

1.8.2 Enxertos ósseos-substitutos:

Um enxerto ósseo-substituto é um material biocompatível utilizado para promover a cura óssea, fornecendo uma resposta biológica no local (MOIRANGTHEM et al., 2015). Em cirurgia ortopédica, a exposição a uma lesão grave geralmente requer intervenção cirúrgica para compensar e reparar o defeito. Os enxertos ósseos são frequentemente necessários para substituir a peça perdida, principalmente em defeitos críticos de tamanho ósseo, onde o processo reconstrutivo será aprimorado ao apoiar o crescimento do tecido (SALGADO; COUTINHO; REIS, 2004; ZHANG et al., 2019). As técnicas de substituição variam dependendo se um enxerto convencional é usado ou materiais sintéticos avançados, ou uma combinação de ambos.

Autoenxertos: O autoenxerto é o processo de transplante de medula óssea, osso esponjoso ou cortical, ou enxertos vascularizados, de uma parte do corpo para outra dentro do mesmo indivíduo (LIEBERMAN; FRIEDLAENDER, 2005). Um autoenxerto utiliza material que é conhecido como material osteogênico. Um enxerto ósseo trabecular é uma escolha superior na restauração óssea devido à alta quantidade de células precursoras (GIORI; BEAUPRE, 2011). O enxerto pode ser retirado de um ponto não afetado no corpo, como a crista ilíaca, rádio distal, metáfise femoral, tíbia proximal, fíbula ou costelas (CAMPANA et al., 2014). O autoenxerto é o "padrão ouro" em engenharia de tecidos e regeneração óssea devido a sua osteocondutividade, osteoindutividade e tendência osteogênica (BALDWIN et al., 2019). Entretanto, o processo tem desvantagens associadas, tais como a quantidade limitada de volume ósseo (BALDWIN et al., 2019) . Além disso, a coleta do osso requer uma operação adicional, podendo resultar em dores ao paciente e possíveis e complicações (CAMPANA et al., 2014). Embora a natureza autóloga a torne uma opção favorável, tem sido relatado que entre 8,5-20% das fatalidades associadas à coleta de autoenxerto são formação de hematoma, lesão nervosa, perda de sangue, formação de hérnia, infecção, lesão arterial, lesão ureteral, fratura, instabilidade pélvica, defeitos cosméticos, transplante de tumor e, às vezes, dor crônica no local doador (GARCÍA-GARETA; COATHUP; BLUNN, 2015; GOLDBERG; STEVENSON, 1987).

Aloenxertos: O aloenxerto é a segunda opção. Neste processo, o osso é obtido de um doador e transplantado para outro indivíduo para restaurar um defeito ósseo maciço (VINING; WARME; MOSCA, 2012). O aloenxerto vem em muitas formas, incluindo matrizes ósseas desmineralizadas,

tecidos ósseos esponjosos e corticais, dependendo da necessidade do hospedeiro (BALDWIN et al., 2019). A atribuição osteogênica é reservada para o aloenxerto, enquanto a resposta osteocondutora é mais provável de ser encontrada em autoenxertos. Além disso, na ausência de fatores de crescimento, a osteoindutividade pode parar, devido a um processo de desvitalização via irradiação, congelamento ou liofilização (ALI et al., 2022; CZITROM et al., 1986; ZUNINO et al., 2004). Embora os aloenxertos estejam disponíveis em grandes quantidades, sejam capazes de suportar defeitos significativos e evitar a necessidade de uma segunda operação para o paciente, ainda há preocupações sobre os custos e riscos associados à transmissão de doenças ou rejeição imunológica (APONTE-TINAO et al., 2015; ZUNINO et al., 2004).

Xenoenxertos: O xenoenxerto é outro processo semelhante, embora neste caso os ossos sejam transplantados de animais para humanos a fim de restaurar o funcionamento e acelerar o crescimento dos tecidos (HAUGEN et al., 2019). Clinicamente, o xenoenxerto tem sido utilizado por mais de 100 anos (CUPERSCHMID; CAMPOS, 2007; GOLDBERG, 2003; SANDERS, 2007; YILDIRIM et al., 2000); e recentemente tem sido explorado e estabelecido utilizando osso bovino tratado inorganicamente como um substituto (KAO; SCOTT, 2007; LEDFORD et al., 2013). Independentemente da osteoindutividade e osteogenicidade, a composição do xenoenxerto tem uma estrutura hidroxiapatita semelhante ao osso humano, e pode fornecer uma estrutura de andaime tridimensional para suportar a formação de novos ossos (SHIBUYA; JUPITER, 2015; VALENCIA-LLANO et al., 2022). Os xenoenxertos são diferentes dos autoenxertos e aloenxertos na medida em que tendem a ser materiais frágeis e quebradiços, o que pode retardar o processo de cura (LEE et al., 2019; SHIBUYA; JUPITER, 2015). Apesar do fato de que os xenoenxertos têm uma capacidade de osteocondutividade, existem riscos de doença de zoonose após a transmissão e a possibilidade de rejeição imunológica. Por fim, a matriz bovina demonstrou que pode ser integrada ao osso humano. No entanto, o processo de substituição é muito lento, o que pode impactar a qualidade do osso recém-formado (BOHNER, 2019; ZUNINO et al., 2004).

1.9 Substitutos de Ossos Sintéticos

As limitações e desafios associados ao enxerto convencional levaram ao desenvolvimento da engenharia de tecidos ósseos. Esta abordagem procura superar as limitações do uso de autoenxertos, aloenxertos e xenoenxertos, fabricando substitutos ósseos sintéticos. Os materiais sintéticos geralmente atendem aos requisitos biológicos básicos de biocompatibilidade, biodegradabilidade, osseointegração e osteocondutividade (ASLANKOOHI et al., 2019; CHAI et al., 2011). Entretanto, a osteoindutividade pode ser fornecida indiretamente, encapsulando agentes bioativos com diferentes sistemas de administração de drogas para estimular células

osteoprogenitoras. Além disso, as propriedades mecânicas podem ser modificadas de acordo com a finalidade e o local desejado.

1.9.1 Biocerâmica: À base de fosfato de cálcio (Ca/P)

O primeiro uso clínico de Ca/P como enchimento de defeitos ósseos data dos anos 1920, e seu primeiro uso em odontologia e ortopedia foi em 1980 (ASLANKOOHI et al., 2019; HABRAKEN et al., 2016). Devido a uma estrutura química semelhante ao osso natural, bem como sua compatibilidade biológica e osteocondutividade, materiais à base de Ca/P têm sido usados por décadas e se tornaram uma das opções mais atraentes para a reparação e regeneração óssea (ASLANKOOHI et al., 2019; CHAI et al., 2011). Os ortofosfatos/fosfatos de cálcio (CaPs) são minerais encontrados em calcificações normais (ossos, dentes, tendões) e também em formações de calcificações patológicas. Os CaPs estão presentes em diferentes tipos de aplicações, incluindo medicina, tratamento de água, catálise e agricultura (BROWN et al., 2010; HABRAKEN et al., 2016). Diferentes formas de CaPs ocorrem em vários compostos com diferentes solubilidades, formas e aplicações. A **Tabela 1**, apresenta alguns exemplos de fosfatos de cálcio (CARRODEGUAS; DE AZA, 2011; DOROZHKIN, 2014; GHINA IMANIYYAH; SUNARSO; HERDA, 2022; HABRAKEN et al., 2016).

Tabela 1: Exemplos de fosfatos de cálcio e sua fórmula química.

Composto	**Fórmula**	**Relação Ca/P**
Brushita (DCPD)	$CaHPO_4.2H_2O$	1.0
Monetita (DCPA)	$CaHPO_4$	1.0
Fosfato octacálcico (OCP)	$Ca_8H_2\ (PO_4)_6.5H_2O$	1.33
α-Fosfato tricálcico (α-TCP)	$\alpha\text{-}Ca_3(PO_4)_2$	1.5
β-Fosfato tricálcico (β-TCP)	$\beta\text{-}Ca_3(PO_4)_2$	1.5
Pirofosfato de cálcio	$Ca_2P_2O_7$	1.0
Pirofosfato de cálcio di-hidratado	$Ca_2P_2O_7.\ 2H_2O$	1.0
Fosfato de cálcio amorfo (ACP)	$Ca_xH_y(PO_4)_z{\bullet}nH_2O$	0.67 – 1.5
Hidroxiapatita (HA)	$Ca_{10}(OH)_2(PO_4)_6$	1.67
Fosfato tetracálcico (TTCP)	$Ca_4(PO_4)_2O$	2.0

As cerâmicas bioativas são conhecidas por ter uma alta resistência à compressão. Entretanto, em termos de fratura e fadiga, sua natureza frágil significa que podem falhar facilmente, e por isso seu uso deve ser limitado em áreas de torção e grandes defeitos. Para isso, uma combinação de diferentes materiais poderia aliviar a tensão e reduzir a fragilidade

(BHATTACHARJEE et al., 2020; HENCH, 1991). Além disso, a biocerâmica funciona como cimentos bioativos, e estes podem ser divididos em tipos não reabsorvíveis ou reabsorvíveis (ASLANKOOHI et al., 2019). Estes podem ser usados em muitas formas, incluindo partículas, camadas de revestimento, pastas injetáveis e andaimes.

Entre os CaP's, a hidroxiapatita (HAp, $Ca_{10}(OH)_2(PO_4)_6$) e o fosfato tricálcico (TCP, $Ca_3(PO_4)_2$) têm sido as fases mais pesquisadas em ortopedia e odontologia (EBRAHIMI; BOTELHO, 2017; HABRAKEN et al., 2016), principalmente com sua semelhança com a fase mineral óssea. A principal diferença entre os dois é a capacidade de reabsorção; enquanto o primeiro permanece sem ser absorvido durante anos, o segundo ganhou destaque devido à sua melhor reabsorvibilidade (CARRODEGUAS; DE AZA, 2011; HABRAKEN et al., 2016; HENCH, 1991). Além dessas duas fases do CaP's , pesquisadores vem buscando explorar as aplicações dos outras fases, principalmente devido a capacidade de reabsorção e outras propriedades tão interessantes quanto o TCP, visando aplicações ortopédicas e odontológicas e outras aplicações de biomateriais (ASLANKOOHI et al., 2019; DOROZHKIN, 2007; EBRAHIMI; BOTELHO, 2017). Por exemplo, fosfato de cálcio dibásico anidro (DCPA, monetita, $CaHPO_4$), juntamente com sua contraparte hidratada fosfato de cálcio dibásico di-hidratado (DCPD, brushita, $CaHPO_4.\ 2H_2O$) tem sido alvos de pesquisadores (BOANINI et al., 2022; SHEIKH et al., 2015c; TORRES et al., 2015). Com destaque para a monetita, seu comportamento de reabsorção *in vivo* tem sido superior quando comparado com a brushita (TAMIMI; SHEIKH; BARRALET, 2012), Tamimi et al destacou sua capacidade de fornecer de reabsorção do implante de monetita para a formação de osso novo sem comprometer a estabilidade mecânica do material (TAMIMI et al., 2010). Outros estudos sustentam o uso da monetita como um biomaterial para aplicações ósseas e em muitos casos, é preferível a brushita, HAp e TCP (GBURECK et al., 2007; TORRES et al., 2015).

1.10 Dopagem de materiais

A dopagem de fosfatos de cálcio e outros biomateriais com elementos químicos adicionais é uma prática comum e significativa na engenharia de biomateriais, principalmente devido à sua influência nas propriedades físico-químicas e biológicas dos materiais resultantes. Este procedimento é realizado visando otimizar as características do material para aplicações específicas em medicina regenerativa, odontologia, ortopedia, entre outras áreas biomédicas (CARREIRA et al., 2015; GRIFFONI et al., 2022; RAU et al., 2019; XUE et al., 2008; YOSHIDA et al., 2005).

As razões para a dopagem são diversas e abrangentes. Em primeiro lugar, a adição de outros elementos pode modular as propriedades mecânicas do material, como a resistência à compressão

e à tração, bem como a sua tenacidade (RAHMAN, 2023; TARASOVA; BEDARKOVA, 2022; ZDOROVETS; PRMANTAYEVA; KOZLOVSKIY, 2021). Além disso, a dopagem pode influenciar a biocompatibilidade do biomaterial, tornando-o mais aceitável para o ambiente biológico circundante. Elementos como íons de prata podem ser incorporados para conferir propriedades antibacterianas, enquanto elementos como íons de zinco podem promover a atividade osteogênica (ADAWY; DIAZ, 2022; XUE et al., 2008). A dopagem também pode afetar a degradação do material, controlando sua taxa de absorção no corpo humano (BANTAWAL; SHENOY; BHAT, 2020; KRAMER; ITZKOWITZ; WEI, 2014).

As vantagens da dopagem incluem a capacidade de personalizar as propriedades dos biomateriais de acordo com requisitos específicos de uma aplicação clínica. Isso possibilita o desenvolvimento de implantes mais eficazes, duráveis e seguros, reduzindo assim a probabilidade de rejeição ou complicações pós-implantação. Além disso, a dopagem pode permitir a incorporação de funcionalidades adicionais, como a liberação controlada de fármacos ou a promoção direcionada da regeneração tecidual (GRIFFONI et al., 2022; RYU et al., 2002; ZHOU et al., 2021c).

Entretanto, é crucial considerar os limites de dopagem para garantir a integridade estrutural e funcional do material. O limite de adição de outros elementos depende de vários fatores, incluindo a natureza do biomaterial de base, o método de dopagem empregado e as propriedades desejadas do material final. Um excesso de dopagem pode levar à instabilidade estrutural, comprometendo a integridade do biomaterial e potencialmente resultando em falha do implante ou respostas adversas no hospedeiro (BANTAWAL; SHENOY; BHAT, 2020; KULANTHAIVEL et al., 2015). Portanto, é essencial realizar estudos abrangentes para determinar os limites ideais de dopagem, levando em consideração aspectos como a toxicidade dos elementos adicionais, a cinética de liberação e a resposta biológica associada.

Capitulo 2

Monetita

2 Monetita

A ocorrência natural de monetita pura na natureza é rara, pois é encontrada principalmente como componente acompanhante de outros materiais (ZHOU et al., 2020). Para aplicações biomédicas, a Monetita pode ser aplicada como componente principal ou pode ser acompanhada por outras fases de fosfatos de cálcio. Nos últimos anos diferentes pesquisadores vem contribuindo com as promissoras aplicações biomédicas da Monetita, como revestimentos em próteses metálicas, cimento ósseo injetável autofixante e andaimes biodegradáveis. Em 2012 Tamimi et al. e em 2020 Zhou et al. publicaram importantes artigos de revisão sobre o tema, com ênfase em cimentos de fosfato bicálcicos, as rotas de síntese, aplicações e perspectivas foram abordadas, mostrando as diferentes propriedades dos materiais e os principais estudos publicados (TAMIMI; SHEIKH; BARRALET, 2012; ZHOU et al., 2020).

2.1 Sínteses de Monetita

A obtenção de Monetita ocorre por diferentes métodos, com a utilização de diferentes reagentes e configurações experimentais. Diferentes estudos relatam as diferentes rotas de síntese de monetita e também o efeito dessas rotas na morfologia do material. Adaptando de Zhou e colaboradores, a **Tabela 1**, resume os reagentes usados e o método de síntese (ZHOU et al., 2020).

Tabela 1: Resumo de sínteses de monetita: seus reagentes e método de obtenção, adaptado de Zhou 2020.

Reagentes	**Método de Síntese**
$CaHPO_4.2H_2O$	Desidratação a 220°C
$CaHPO_4.2H_2O$	Desidratação por aquecimento a seco a 250°C ou autoclavagem a 121°C
$CaHPO_4.2H_2O + H_3PO_4 + H_2O$	Desidratação por fervura
$CaHPO_4.H_2O$	Desidratação na presença de uma mistura de metanol e água, ou em ar úmido
$Ca(H_2PO_4)_2.H_2O + H_2O$	Autoclavagem a 200°C
$Ca(H_2PO_4)_2.H_2O + H_2O + Ca(OH)_2$	Autoclavagem a 160°C
$Ca(OH)_2 + H_3PO_4 + H_2O$	Aquecimento a 85°C
$Ca(OH)_2 + H_3PO_4 + NaHCO_3 + H_2O$	Mistura de reagentes
$CaCl_2 + Na_2HPO_4 + H_2O$	Aquecimento a 95°C
$Ca(NO_3)_2 .4H_2O + (NH_4)_2HPO_4$ + ureia + H_2O	Refluxo da solução a 90°C
$Ca(NO_3)_2 + (NH_4)_2 HPO_4$ + EDTA/MEA	Tratamento hidrotérmico a 200°C
$CaCl_2 + KH_2PO_4$ + CTAB + H_2O	Refluxo da solução a 120°C + Autoclavagem a 90–150°C
$CaCl_2$ $6H_2O$ + cloreto de colina + $(NH_4)_2HPO_4$ + H_2O	Aquecimento a 120°C
$CaHPO_4$ + ácido acético	Secagem por pulverização
$CaCO_3 + H_3PO_4 + H_2O$ + etanol	Agitação à temperatura ambiente
$Ca(NO_3)_2 + H_3PO_4 + H_2O$ + acetona	Troca de solvente
$CaCl_2$•$2H_2O + H_3PO_4$ + óxido de propileno + H_2O + metanol	Reação sol-gel
$Ca(H_2PO_4)_2.H_2O + Ca_3(PO_4)_2.1/6H_2O$	Moagem
$Ca(H_2PO_4)_2.H_2O + Ca_{10}(PO_4)_6(OH)_2$ + acetona	Moagem
$CaCl_2 + NaH_2PO_4 + Na_2H_2$ EDTA•$2H_2O + H_2O$	Eletroquímica
$Ca(NO_3)_2 + NH_4H_2PO_4 + H_2O$	Aquecimento por indução eletromagnética
$CaCl_2 + NaH_2PO_4 + H_2O$ + DMF+ EG	Ultrasonicação
$CaCl_2.5H_2O + NaH_2PO_4$ + SDS + H_2O + EG	Microondas

2.2 Características Estruturais

2.2.1 Difração por raios-X

O primeiro trabalho que relatou a estrutura cristalina da Monetita foi publicado em 1955, por MacLennan & Beevers (MACLENNAN; BEEVERS, 1955). A **Figura 1**, ilustra um padrão de difração de raios-X (DRX) típico de monetita, com picos de difração vistos em valores 2θ, 26.42°, 26.58° e 30.18° com índices de Miller correspondentes (hkl) como (0 2 0), (-2 2 0) e (-1 1 2) respectivamente. Refinamentos estruturais de monetita foram realizados e relatados por vários grupos (CATTI; FERRARIS; FILHOL, 1977; CATTI; FERRARIS; MASON, 1980; DENNE; JONES, 1971; HLEL; KAMOUN; GUIDARA, 2006; JONES; CRUICKSHANK, 1961;

YASHIMA et al., 2003). Os artigos concordam-se que a monetita pertence a um sistema cristalino triclínico com grupo espacial P1, com os seguintes parâmetros de célula unitária a = 6.910, b = 6.627, c = 6.998 Å, α = 96.34°, β = 103.82°, γ = 88.33° a 25°C (DICKENS; BOWEN; BROWN, 1972). Outras características são distintivas da estrutura monetítica. Primeiro, consiste em uma rede tridimensional de tetraedros de íons de fosfato (PO_4^{3-}) com íons de cálcio (Ca^{2+}) em interstícios, mantendo os ânions juntos por ligações altamente iônicas com oxigênio (O_2^-) (MACLENNAN; BEEVERS, 1955). A segunda característica importante é a presença de três tipos de ligações de hidrogênio , com comprimentos de 2.565Å, 2.458Å e 2.669Å (HLEL; KAMOUN; GUIDARA, 2006). Devido a esta estrutura, a monetita exibe um efeito piezoelétrico fraco (DENNE; JONES, 1971).

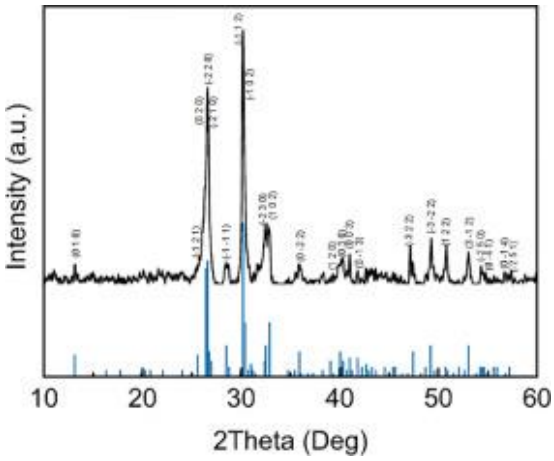

Figura 1: Pico de difração DRX de monetita. A amostra de monetita foi preparada por meio da reação de $Ca(OH)_2$ e H_3PO_4 na razão molar Ca/P de 1. Todos os picos correspondem à fase monetita e o padrão típico é derivado do PDF# 09-0080 conforme obtido do Centro Internacional de Dados de Difração, Figura obtida em Zhou e colaboradores e referenciada de Desai 2008 (DESAI; BHADURI; TAS, 2008).

2.2.2 Espectros Vibracionais

A tabela foi adaptada de Zhou e colaboradores, onde é possível observar as localizações de bandas características de picos observados para os modos de alongamento e flexão PO da monetita, conforme relatado na literatura (ZHOU et al., 2021a). A estrutura da monetita depende de dois conjuntos de unidades de PO_4 na célula primitiva. Como consequência de sua existência, ocorre a divisão do grupo de fatores. Isso resulta na observação de dois conjuntos de modos de alongamento simétrico v_1 e três conjuntos de vibrações de alongamento antissimétrico v_3. Os dois conjuntos de tetraedros PO_4 também são refletidos no PO_4 modos de dobra, exibindo dois conjuntos de modos de dobra v_2 e três conjuntos de modos de dobra v_4. Além disso, devido à presença de um centro de simetria, não são esperadas coincidências entre as bandas observadas nos espectros Raman e infravermelho, conforme mostrado na **Tabela 2.**

Tabela 2: Frequências características (cm^{-1}) e atribuições de bandas para monetita relatadas no espectro Raman e infravermelho.

Banda Raman (cm^{-1})				**Banda infravermelho (cm^{-1})**		**Atribuição**
1140 1126	1129	1133	1170 1130	1132	1176 1132	Alongamento PO (v_3')
1086 1060	1089	1095	1070	1070	1070	Alongamento PO (v_3'')
983 946	980	988v	1000	-	996	Alongamento PO (v_1)
895	898	901	900	898	893	PO(H) Alongamento (v_3''')
583	585	591	581	583	584	Flexão PO (v_4')
569	566	-	566	566	-	Flexão PO (v_4'')
553 539	529	562	530	529	531	Flexão PO (v_4''')
423 413	411	420	428	406	430	Flexão PO (v_2')
390	389	395	405 398	-	405	Flexão PO (v_2'')

Além disso, a monetita pode ser facilmente distinguida de outras fases de CaP como HA, TCP, γ-pirofosfato de cálcio (γ-CPP, γ-$Ca_2P_2O_7$), brushita, whitlockita ($Ca_{18}Mg_2(HPO_4)_2(PO_4)_{12}$, a fase inorgânica secundária no osso) por picos detectados pela espectroscopia Raman , devido à sua estrutura cristalina única (WOPENKA; PASTERIS, 2005). A **Figura 2a-b** ilustra as diferenças dos espectros Raman de monetita e outras fases de CaP's. Diferentemente da HA, a monetita não possui íon hidroxila, e como observado na brushita, a monetita também não apresenta H_2O em sua estrutura cristalina, nenhum pico em aproximadamente 3500Δcm^{-1} causado por vibrações de O-H é observado. Além disso, os espectros Raman também mostram uma distinção clara de monetita e outras fases CaP que contêm o grupo HPO_4^{2-} (hidrogenofosfato) (**Figura** 2**b**). Um forte pico em 966Δcm^{-1} de ligação tetraédrica P-O e um pico em 900 Δcm^{-1} devido a ligações P-O que estão na configuração P-O-H^+ e só podem ser vistos em monetita.

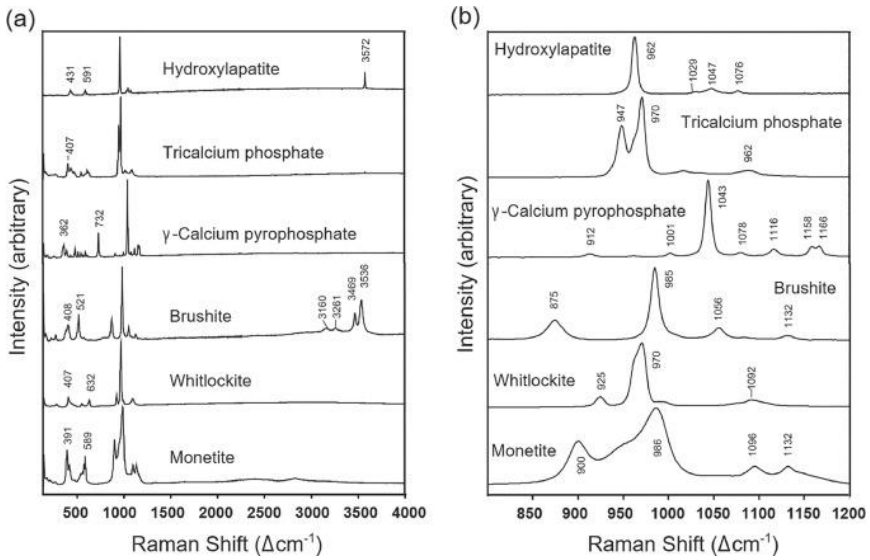

Figura 2: (a) Espectros Raman de alguns CaPs como HA, TCP, γ-pirofosfato de cálcio (γ-CPP, γ-$Ca_2P_2O_7$), brushita, whitlockite ($Ca_{18}Mg_2(HPO_4)_2(PO_4)_{12}$), e monetita, na qual a monetita tem picos causados pelos modos de alongamento e flexão do P-O abaixo de 1400 Δcm^{-1}, mas não apresenta pico acima de 3000 Δcm^{-1} causado por vibrações do O-H. **(b)** Ampliação da região espectral Raman de 800 para 1200 Δcm^{-1} das fases acima mencionadas mostrando P –O vibrações de estiramento em todas as fases, dentre as quais a monetita apresenta fortes picos em 966 e 900 Δcm^{-1}. Figura obtida em Zhou e colaboradores e referenciada de Desai 2008 (DESAI; BHADURI; TAS, 2008).

2.2.3 Decomposição termal

Por ser utilizada na composição de outros CaPs, entender a decomposição térmica da monetita é importante. A conversão térmica de monetita em pirofosfato de cálcio foi documentada em vários estudos. Por exemplo, Hlel e colaboradores em um estudo com espectroscopia ^{31}PMAS-NMR de monetita, observou que os ânions HPO_4^{2-} que são abundantes na estrutura da monetita foram progressivamente transformados em $P_2O_7^{4-}$ quando a temperatura de recozimento aumentou de 100°C para 450°C (HLEL; KAMOUN; GUIDARA, 2006). Um outro estudo calorimétrico da monetita realizado entre 27°C e 477°C revelou uma região endotérmica. Este resultado pode ser explicado pela ocorrência de transformação de estado sólido da amostra recém-preparada em cerca de 369°C e 405°C (LOUATI et al., 2005). Com o aumento da temperatura, a reação de desidratação produz γ-CPP, com posterior conversão de γ-CPP em β-CPP (WIKHOLM; BEEBE; KITTELBERGER, 1975).

2.3 Propriedades biológicas da monetita

A monetita pode ser utilizada em aplicações ortopédicas e odontológicas como uma fase única ou pode ser acompanhada por outras fases de CaPs. Ela pode ser aplicada como revestimento de próteses metálicas, cimento ósseo injetável autofixante e enxertos ósseos (IDOWU et al., 2014; KO et al., 2015). *Estudos in vitro* usando células osteoblásticas e células da medula óssea revelaram que a monetita pode promover a proliferação celular e aumentar os níveis de genes

osteogênicos, como fator de transcrição relacionado a Runt 2 (Runx2), osteopontina (OPN) e fosfatase alcalina (ALP) (DE ALMEIDA et al., 2023; TAMIMI et al., 2012; TORRES et al., 2015). Além disso, Torres 2015 avaliou o potencial *in vitro* da monetita para induzir a diferenciação osteogênica em células-tronco mesenquimais humanas usando HA como comparação. No dia 14, foi observado um aumento acentuado das expressões de marcadores específicos de osso ALP, osteocalcina (OCN) e osteonectina (ON) em células-tronco (TORRES et al., 2015). Esses modelos *in vitro* fornecem evidências de que a monetita é um promissor material regenerativo ósseo. Além disso, Fine e colaboradores, revelou que os neutrófilos polimorfonucleares (PMNs) e monócitos derivados do sangue humano são altamente ativados após a exposição à monetita, indicando a capacidade da monetita de desencadear uma resposta inflamatória aguda inicial após a implantação (FINE et al., 2020).

Em estudos com modelos animais e alguns estudos com humanos, a monetita foi implantada visando observar a sua capacidade de regeneração óssea, os estudos foram observados na calvária (TAMIMI et al., 2008), área craniofacial (TAMIMI et al., 2009), osso alveolar (TAMIMI et al., 2010), côndilo do fêmur (SHEIKH et al., 2017) e platô tibial proximal (TAMIMI et al., 2012). Os resultados destes estudos *in vivo* confirmaram o potencial do material para ser osteocondutor, induzindo a formação óssea no implante) (BABILOTTE et al., 2021; GUO et al., 2020; KLAMMERT et al., 2009) e efeito osteoindutor, induzindo a formação óssea através do implante (HABIBOVIC et al., 2008).

A reabsorção da monetita após a implantação pode ocorrer por dois processos diferentes: dissolução passiva e reabsorção celular ativa. Enquanto o primeiro depende de sua solubilidade, porosidade, área de superfície e da taxa de troca de água no local do implante (TAMIMI et al., 2010), o último está associado à atividade dos osteoclastos (MONTAZEROLGHAEM et al., 2015). No caso de produtos densos de monetita, os mecanismos de reabsorção geralmente envolvem dois componentes – degradação ativa e passiva. Enquanto a degradação ativa foi predominante com uma liberação cumulativa de Ca^{2+} de 1.20 µmol durante os primeiros 13 dias, a degradação passiva liberou apenas 0,04 µmol de íons Ca^{2+} no meio de cultura (GROSSARDT et al., 2010). Para uma avaliação completa dos efeitos da reabsorção passiva e ativa, Sheikh e colaboradores realizaram um estudo para investigar os efeitos da porosidade, área de superfície e fase do material no comportamento de degradação *in vitro* e na extensão da reabsorção. Duas fases materiais foram escolhidas para o estudo - brushita e monetita (SHEIKH et al., 2015a). Alguns dos resultados do estudo são mostrados na **Figura 3**, a monetita exibiu reabsorção mais rápida do que a brushita *in vivo*. Em uma comparação entre blocos de monetita e enxertos autólogos com base na eficiência da cicatrização óssea, os resultados da histomorfometria revelaram que 42% da monetita foi reabsorvida e que o novo osso formado dentro do implante ocupou 43% do seu

volume (SHEIKH et al., 2015a). Isso indicou que a reabsorção de monetita pode potencialmente fornecer um equilíbrio bem adaptado entre a reabsorção do implante e a formação de osso novo sem comprometer a estabilidade mecânica, uma vantagem que diferencia a monetita de HA e brushita.

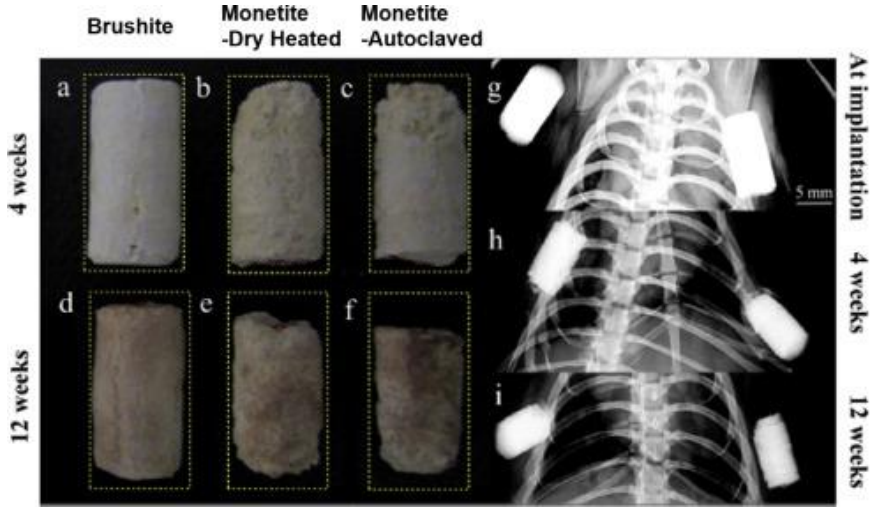

Figura 3: Imagens dos enxertos de brushita, monetita (formado através de brushita de aquecimento a seco, referido como monetite-dry heated) e monetita (formado por meio de brushita autoclavado, referido como monetite-autoclaved) após 4 semanas (a-c) e após 12 semanas (d –f) de implantação subcutânea em ratos (as linhas pontilhadas amarelas indicam as dimensões iniciais dos enxertos de 6×12 mm). Radiografias de brushita implantado (esquerda) e enxertos autoclavados com monetita (direita), (g) após a implantação, (h) após 4 semanas e (i) após 12 semanas *in vivo*, os enxertos autoclavados com monetita eram de cor mais escura em comparação com brushita enxertos indicando maior quantidade de adsorção de proteínas. Imagem obtida de Sheikh e colaboradores (SHEIKH et al., 2015a).

2.4 Aplicações ortopédicas

Os fosfatos de cálcio têm uma longa história como materiais regenerativos ósseos na forma de grânulos, andaimes, cimento e revestimentos. A maioria dessas aplicações está relacionada a HA e TCP com ainda pouco destaque para a monetita. Um dos principais motivos é o processo de obtenção que geralmente se utiliza alta temperatura para produzir monólitos cerâmicos, o que não se à monetita devido à formação de pirofosfato de cálcio a temperaturas relativamente baixas. Portanto, é necessário aplicar regimes de processamento de baixa temperatura para a fabricação de cerâmica de monetita, enquanto a fase de monetita é frequentemente formada diretamente dentro da estrutura cerâmica por uma reação cimentícia em condições ácidas.

2.4.1 Cimentos ósseos

Os cimentos ósseos são um material autoendurecível moldável que pode ser aplicado manualmente ou injetado com uma seringa para reparo de tecidos duros. Eles geralmente passam por uma transição de um estado viscoso que pode ser prontamente implantado para o estado solidificado que possui uma geometria fixa com maior resistência mecânica e estabilidade. O principal mecanismo de obtenção dos cimentos de Ca/P (CPC) é uma reação de dissolução-

precipitação de precursores em pó em meio aquoso e o entrelaçamento do cristal precipitado para formar uma matriz rígida no espaço limitado da pasta de cimento (APELT et al., 2004; BOHNER et al., 2003; CONSTANTZ et al., 1998; KO et al., 2015; MIRTCHI; LEMAITRE; TERAO, 1989; TAMIMI et al., 2008; THEISS et al., 2005; TORRES et al., 2015).

2.4.2 Revestimentos

Os revestimentos bioativos desempenham um papel importante na melhoria da osseointegração do implante com o osso (KOJU et al., 2017; KURODA et al., 2002). Devido à sua degradabilidade em pH fisiológico, a monetita e a brushita podem fornecer supersaturação de Ca^{2+} e PO_4^{3-} na interface do implante, resultando em melhor osseointegração (DIVYA RANI et al., 2012; HAMADA et al., 2002). Dos dois fosfatos dicálcicos, a monetita ganhou maior atenção do que a brushita. Vários relatórios abordam o sucesso de revestimentos de monetita em diferentes tipos de substratos de implantes, como titânio (Ti), compósitos de carbono/carbono e magnésio biodegradável (Mg) e suas ligas (AZ31), estão disponíveis na literatura as tecnologias de revestimento, e estas incluem as técnicas de secagem por pulverização (SHI et al., 2017), deposição por aquecimento por indução (XIONG et al., 2013), deposição por aquecimento por indução ultrassônica (XIONG et al., 2014), deposição eletroforética (DJOŠIĆ et al., 2009; LIN et al., 2018), hidrotérmica (ALI et al., 2019) e outros métodos químicos (ZAVGORODNIY et al., 2012).

2.4.3 Grânulos

Em comparação com outras formas de aplicações de monetita, os grânulos de monetita não foram explorados extensivamente. A literatura possui alguns casos que indicam aplicações de grânulos. Tamimi e colaboradores em um trabalho com grânulos de monetita em defeitos de tamanho crítico na calvária de ratos para induzir a regeneração óssea (TAMIMI et al., 2008). Os grânulos foram fabricados por autoclavagem de grânulos de cimento brushita pré-preparados. As observações histológicas mostraram sinais de reabsorção do enxerto e, mais importante, descobriu-se que tecido ósseo recém-formado circundava e penetrava através dos grânulos implantados. Em outro estudo do mesmo grupo, grânulos de monetita foram inseridos em defeitos ósseos alveolares de pacientes humanos. A hidroxiapatita bovina (HB), um grânulo de apatita porosa amplamente utilizado, foi usada para comparação (TAMIMI et al., 2010). Após seis meses, a análise histomorfométrica das biópsias revelou que a quantidade de osso regenerado com monetita foi significativamente maior do que a obtida com HB. Além disso, a quantidade de enxerto não reabsorvido foi maior nos alvéolos tratados com HB do que naqueles implantados com monetita. A maior quantidade de osso neoformado foi atribuída ao fato de que a monetita é mais reabsorvível que a HB. Portanto, ao ser reabsorvido ao longo do tempo, forneceu espaço e íons (Ca^{2+} e PO_4^{3-})

para a formação de osso novo. Em um estudo subsequente, uma comparação entre grânulos de monetita e osso autólogo particulado foi realizada usando defeitos cranianos bicorticais em coelhos, conforme mostrado na **Figura 4**. O exame histológico das amostras retiradas dos locais experimentais revelou que o osso havia crescido das bordas dos defeitos e para dentro, formando uma ponte óssea completa do defeito. Defeitos tratados com monetita exibiram alta infiltração de novo osso e apenas 13.4 ± 8.4% do total de grânulos permaneceram após 8 semanas da intervenção cirúrgica. A quantidade de tecido mineralizado aumentado nos defeitos ósseos obtidos com grânulos de monetita não foi significativamente diferente da obtida com osso autólogo, confirmando o potencial dos biomateriais à base de monetita como alternativa ao enxerto ósseo autólogo (TORRES et al., 2015).

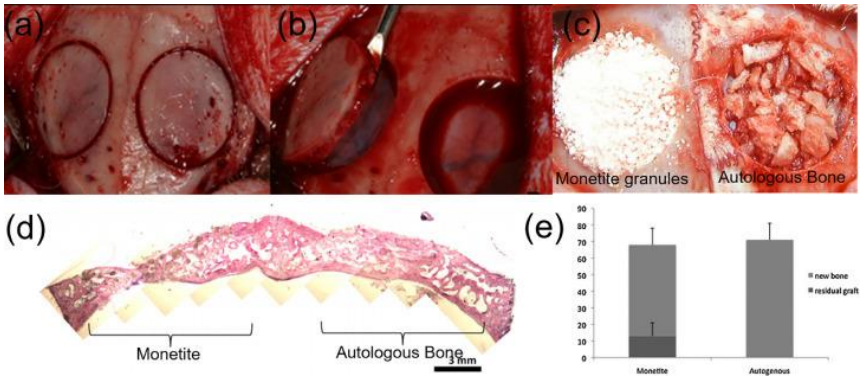

Figura 4: Grânulos de monetita e partículas ósseas autólogas foram implantados em defeitos cranianos bicorticais de coelhos para comparar a capacidade de regeneração óssea: **(a)** defeitos cranianos bicorticais circulares (10.0 mm de diâmetro) foram feitos com trefina; **(b)** dois tampões ósseos foram removidos e usados para criar partículas de autoenxerto por moagem; **(c)** os defeitos foram preenchidos com grânulos de monetita e partículas de autoenxerto separadamente; **(d)** micrografia óptica de seção coronal de defeitos tratados com monetita e tratados com osso autólogo, nos quais os grânulos de monetita não reabsorvidos restantes pareciam de cor escura e foram encapsulados por osso novo em todo o defeito; **(e)** a quantidade de tecido mineralizado aumentado nos defeitos ósseos obtidos com grânulos de monetita foi comparável ao osso autólogo. Figura obtida em Torres et al (TORRES et al., 2015).

2.4.4 *Scaffolds*

A fabricação de andaimes de monetita envolveu principalmente a conversão hidrotérmica de precursores de CaP. Sheikh et al produziu enxertos de discos de monetita preparados via autoclave ou enxertos de discos de brushita com aquecimento a seco (SHEIKH et al., 2015a). Para a conversão de calor seco, os discos brushita foram aquecidos a 250°C por 30 min sob vácuo. A densidade do suporte foi semelhante para os enxertos de disco de brushita aquecidos e autoclavados. A área de superfície específica (SSA) foi aproximadamente 12 vezes maior e a porosidade total foi aproximadamente 10% menor nos enxertos aquecidos a seco quando comparados aos autoclavados. Observou-se que a maior porosidade dos enxertos autoclavados aumentou a capacidade de reabsorção e aumentou a porcentagem de volume ósseo da área do

implante, sendo possível observar na **Figura 3**. Já os enxertos aquecidos a seco que apresentaram menor porosidade, porém maior SSA apresentaram maior resistência mecânica. A parte *in vivo* deste trabalho comparou o desempenho dos dois tipos de monetita mencionados acima (aquecido a seco e autoclavado) e brushita, a **Figura 5** ilustra esses resultados (SHEIKH et al., 2015a, 2015b). Os resultados do modelo animal revelaram que ambos os materiais de enxerto de monetita foram reabsorvidos mais rapidamente do que brushita e mais formação óssea foi alcançada. No entanto, não houve diferença significativa na quantidade de osso formado entre os dois tipos de enxertos de monetita.

Uma possível explicação afirmava que os enxertos de brushita sofreram transformação de fase para formar HA, o que acabou limitando a reabsorção. Pelo contrário, HA não foi formado no caso de monetita. Tais estudos confirmam as propriedades únicas da monetita que devem destacar as aplicações do material na regeneração óssea. Os resultados também devem indicar a superioridade da monetita no campo da medicina regenerativa sobre suas contrapartes bem conhecidas - brushita e HA, proporcionando assim um equilíbrio muito melhor entre a reabsorção substituta e a formação de osso novo (SHEIKH et al., 2015c, 2016; TAMIMI et al., 2012).

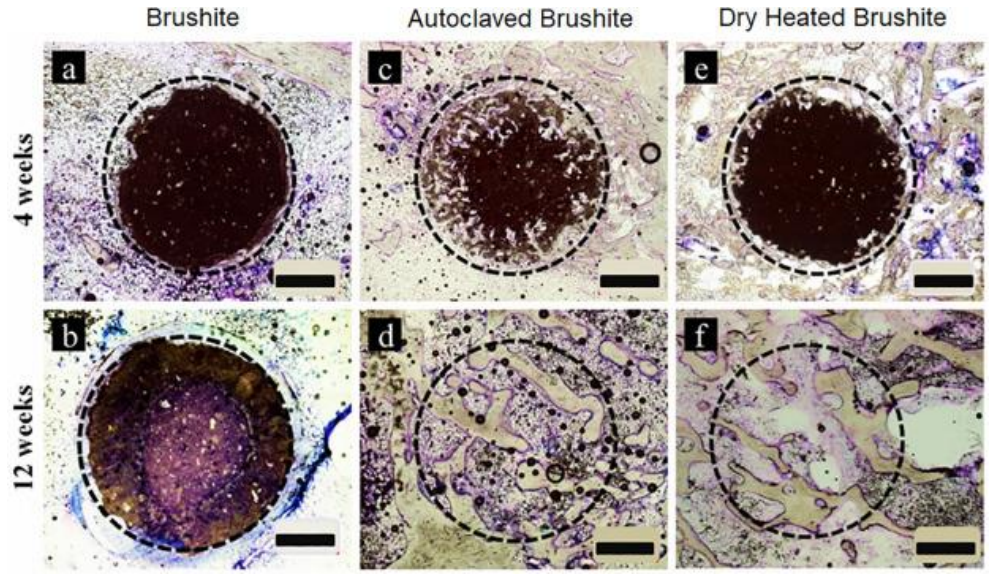

Figura 5: Cortes histológicos (coloração H&E) de brushita (a & b), brushita autoclavado (c & d) e brushita seco aquecido (e & f) após 4 e 12 semanas de implantação (as áreas pontilhadas representam o diâmetro original do enxerto de 3 mm, escala barra representa 1 mm). Figura obtida em (SHEIKH et al., 2015a).

2.5 Um olhar translacional e direções futuras da monetita

A pesquisa sobre aplicações biomédicas de monetita aumentou durante os últimos 20 anos, resultando em dezenas de estudos e produtos. A monetita ainda está em estágio inicial para a aplicação clínica, embora animadores resultados *in vivo* indiquem os benefícios do uso de monetita em vez de HAp, brushita e autoenxertos. Os testes em animais ainda são escassos quando

comparados a estudos com outros CaP's como β-TCP ou BCP (fosfato de cálcio bifásico, HAp+βTCP).

Os estudos sobre monetita têm sido associados principalmente ao fornecimento de uma matriz regenerativa para defeitos ósseos. O crescente conhecimento e tecnologia em ciências biomédicas e de materiais trazem oportunidades interessantes para o desenvolvimento de monetita. Utilizando combinações seletivas de íons efetivos e/ou moléculas terapêuticas com matrizes de CaP têm sido relatadas como uma forma eficiente de estimular atividades celulares e aumentar a regeneração óssea (NAVARRO DA ROCHA et al., 2019; ZHOU et al., 2019). Íon como Mg, Si, Zn, Sr, Se, Mn, Cu e Co, podem desempenhar papéis essenciais na regulação da migração, proliferação e diferenciação das células ósseas, bem como na angiogênese (GHINA IMANIYYAH; SUNARSO; HERDA, 2022; HURLE et al., 2021; SHADANBAZ et al., 2014). No entanto, uma vez que uma mudança na composição da monetita geralmente leva a uma mudança de solubilidade e estrutura, as composições finais devem ser verificadas quanto aos atributos de reabsorção e liberação de íons. Outras moléculas vêm sendo incorporados, como proteínas morfogenéticas ósseas (BMPs), fator de crescimento endotelial vascular (VEGFs), fatores de crescimento transformadores (TGFs), fatores de crescimento de fibroblastos (FGFs), fatores de crescimento derivados de plaquetas (PDGFs) e vários peptídeos e drogas, como gentamicina e bisfosfonatos, são potenciais moléculas terapêuticas que podem ser introduzidas para melhor desempenho biológico da monetita (GHINA IMANIYYAH; SUNARSO; HERDA, 2022; ZHOU et al., 2020) . A atividade e o destino dos agentes após a exposição ao complicado ambiente corporal devem ser um importante campo de pesquisa.

Alguns estudos têm abordado os efeitos e propriedades da monetita quando dopada com outros elementos, Chen e colaboradores utilizaram a dopagem com prata buscando a atividade antimicrobiana em cimentos para aplicações dentárias. A monetita dopada com prata foi comparada com a hidroxiapatita também dopada, eles concluíram que a dopagem melhora o potencial antibacteriano, porém não altera a resistência a compressão dos materiais testados (CHEN et al., 2016). Outro interessante estudo foi desenvolvido por Adawy & Diaz, a dopagem de monetita foi realizada com os elementos prata, estrôncio e zinco, eles identificaram que cada elemento modificou a morfologia dos cristais de monetita, zinco foi o elemento mais incorporado na fase de monetita e o estrôncio foi o elemento menos incorporado. Os estudos microbiológicos revelaram que a prata é um agente antimicrobiano muito eficaz em baixas concentrações, mas inadequado em altas concentrações, pois apresentou citotoxicidade em células Saos2. A dopagem com zinco levou a uma atividade antimicrobiana sem comprometer a viabilidade celular. O estudo também destaca que o estrôncio, amplamente conhecido por sua osteoindutividade, tem um efeito antimicrobiano em altas concentrações (ADAWY; DIAZ, 2022).

Kaygili e colaboradores realizaram a dopagem com níquel/alumínio, níquel/manganês, o estudo demonstrou que a síntese foi efetiva, os elementos foram incorporados nos cristais de monetita, parâmetros observados na técnica de DRX apresentam diferenças, a morfologia dos cristais não aparentou mudanças com os dopantes, porém no estudo não foram abordados ensaios in vitro ou microbiológicos, não sendo possível avaliar seus efeitos ainda (KAYGILI et al., 2017).

Hurle e colaboradores realizaram a dopagem de brushita com lítio, o estudo demonstrou que a presença do dopante favorece a formação de monetita. O lítio é um elemento promissor para estimular a migração e a proliferação de células-tronco derivadas do tecido adiposo (hASCs) e a expressão de genes relacionados à diferenciação osteogênica e a expressão de genes relacionados à diferenciação osteogênica, essenciais para a osteogênese. O DRX mostrou a precipitação de brushita, como fase principal, e monetita. Os cimentos apresentaram resistência mecânica à compressão dentro das faixas relatadas para osso esponjoso. Os ensaios *in vitro* usando hASCs mostraram níveis proliferativos normais. O perfil de expressão genica dos marcadores relacionados à osteogênese destacam um potencial osteogênico dos cimentos de brushita dopados com Li para futuras aplicações em defeitos ósseos (HURLE et al., 2021).

Este capítulo apresenta uma base de conhecimento sobre a monetita. Fornecendo informações sobre técnicas de preparação, propriedades físico-químicas e das aplicações biomédicas da monetita. Os estudos *in vitro* e *in vivo* comprovaram que a monetita apresenta interessantes propriedades osteocondutoras e biodegradáveis do que suas conhecidas contrapartes de fosfatos de cálcio, como hidroxiapatita e brushita. Tais resultados destacam o potencial da monetita para ser um material ortopédico sintético.

Capitulo 3: Justificativa e Objetivos

3. Justificativa e Objetivos

3.1. Justificativa

Compreender a importância dos fosfatos de cálcio na integração do tecido ósseo e a necessidade de otimizar essa interação, esta tese buscou explorar em profundidade os aspectos biológicos envolvidos nas respostas a monetita, por vezes dopada com cobalto. Sabemos que o esqueleto dos mamíferos, uma estrutura complexa e dinâmica, abriga uma série de células que mantêm a formação óssea durante toda a vida de maneira hierarquizada. A osteogênese, processo vital para a renovação e reparação óssea, é particularmente crítica na consolidação de fraturas e regeneração adequada do novo osso.

No entanto, com o avanço da idade, a capacidade regenerativa do osso tende a diminuir, resultando na perda de massa óssea e no aumento de incidência de fraturas. Esta realidade apresenta um desafio substancial na medicina regenerativa, ortopédica e odontologia, exigindo avanços significativos no desenvolvimento de biomateriais que possam efetivamente atender às demandas de um organismo em envelhecimento, ou mesmo tecidos lesados em extensões críticas. Assim, esta tese justifica-se pela urgente necessidade de compreender e aprimorar os mecanismos pelos quais os biomateriais podem melhorar a regeneração tecidual, visando oferecer soluções inovadoras e eficazes para a restauração da integridade estrutural óssea, principalmente em populações mais velhas, onde tal necessidade é mais premente.

Cumpre destacar que nosso grupo vem contribuindo com resultados importantes acerca dos mecanismos biológicos acerca das interações de células ósseas e endoteliais durante interações com biomateriais e biomarcadores destes eventos foram revelados (DA COSTA FERNANDES et al., 2021a; DE ALMEIDA et al., 2023; FERNANDES et al., 2023; PINTO et al., 2022; WOOD et al., 2023).

Com base no conhecimento avançado adquirido nos últimos anos, esta tese desenvolve a síntese de um novo material biomimético, inspirado na hipoxia como um mecanismo essencial para a integração tecidual. Utilizando o cobalto, um agente hipoxiante conhecido, propomos aplicações deste material em casos que demandem enxertos ósseos. Este avanço abre caminho para o preenchimento de lesões ósseas, revestimento de estruturas metálicas e na formulação de géis ou pastas otimizados para a impressão 3D, potencializando a regeneração óssea e a osteointegração.

3.2. Objetivos

O objetivo geral dessa tese foi desenvolver e caracterizar um biomaterial inovador capaz de mimetizar um ambiente hipóxico a fim de aprimorar a regeneração óssea e a osteointegração, utilizando o cobalto como agente hipoxiante. Os objetivos específicos estão agrupados nas Etapas I-IV, abaixo:

Etapa I: Síntese e Caracterização de Monetita dopada com Cobalto

I. Revisão de literatura e planejamento das sínteses e sua padronização; Realização das sínteses em diferentes concentrações de cobalto;
II. Ensaios de caracterização físico-químicas;
III. Estabelecer aspectos de citotoxicidade, bem como marcadores do remodelamento da matriz extracelular (Integrina-α1, Integrina-β1, SRC, FAK e Cofilina), específicos osteogênicos (Runx2, Osterix, BSP e Osteocalcina) e do gene HIF1α;
IV. Definição da concentração ideal para seguimentos das próximas etapas.

Etapa II: Avaliar os efeitos da Monetita e Monetita dopada com Cobalto (2% mmol) em pre-osteoblastos

I. Ensaios complementares de caracterização físico químicas;
II. Ensaios de citotoxicidade e regeneração celular (Wounding Healing);
III. Avaliação dos marcadores de remodelamento da MEC, fenótipo osteogênico, angiogênicos (VEGF e eNOS), HIF1α e metaloproteinases;
IV. Avaliação da atividade de MMP9 e MMP2 por Zimografia;
V. Avaliação das espécies reativas de oxigênio por meio do ensaio de carbonilação de proteínas.

Etapa III: Tratamentos térmicos nos biomateriais

I. Realização de tratamentos térmicos nas temperaturas 700, 900 e 1050ºC;
II. Ensaios de caracterização;
III. Ensaios de citotoxicidade, regeneração celular, expressão gênica e carbonilação de proteínas.

Etapa IV: Revestimentos de titânio

I. Revisão de literatura e planejamento das sínteses;
II. Realização do método hidrotérmico para revestimentos de ligas de titânio;
III. Ensaios de caracterização físico-químicas;
IV. Avaliação da citotoxicidade em células pre-osteoblastos;

Capítulo 4

Artigo 1: Development of cobalt (Co)-doped monetites for bone regeneration

de Almeida GS, Ferreira MR, da Costa Fernandes CJ, Suter LC, Carra MGJ, Correa DRN, Rangel EC, Saeki MJ, Zambuzzi WF. **Development of cobalt (Co)-doped monetites for bone regeneration.** Journal of Biomedical Materials Research Part B: Applied Biomaterials, 112, 1, 1 2024. doi: 10.1002/jbm.b.35319.

Development of cobalt (Co)-doped monetites for bone regeneration

Gerson Santos de Almeida[1], Marcel Rodrigues Ferreira[1], Célio Junior da Costa Fernandes[1], Luísa Camilo Suter[1], Maria Gabriela Jacheto Carra[1], Diego Rafael Nespeque Correa[2], Elidiane Cipriano Rangel[3], Margarida Juri Saeki[1], Willian Fernando Zambuzzi[1]*

[1]Laboratory of Bioassays and Cellular Dynamics, Department of Chemical & Biological Sciences, Institute of Biosciences, São Paulo State University - UNESP, Botucatu, São Paulo, 18618-970, Brazil

[2]Laboratory of Anelasticity and Biomaterials, Department of Physics and Meteorology, School of Sciences, São Paulo State University - UNESP, Bauru, São Paulo, 17033-360, Brazil

[3]Laboratory of Technological Plasmas (LaPTec), Institute of Science and Technology, Sao Paulo State University (UNESP), Sorocaba, Sao Paulo, 18087-180, Brazil

[#]Corresponding author:
Prof. Dr. Willian F Zambuzzi
UNESP - Campus de Botucatu - Instituto de Biociências
Rua Profª. Drª. Irina Delanova Gemtchujnicov, s/nº
18618-693 – Botucatu-SP - Brazil

e-mail: w.zambuzzi@unesp.br
Phone: +55-14 38800599
Fax: +55-14 3880 0573

ABSTRACT

Cobalt-doped monetite powders were synthesized by coprecipitation method under a cobalt nominal content between 2 to 20 mol% of total cation. Structural characterization of samples was performed by using X-ray diffraction (XRD), Fourier transform infrared spectroscopy (FTIR), scanning electron microscopy (SEM) and energy dispersive X-ray spectroscopy (EDS). XRD results indicated that the Co-doped samples exhibited a monetite single-phase with the cell parameters and crystallite size dependent on the amount of substitutional element incorporated into the triclinic crystalline structure. Cell viability and adhesion assays using pre-osteoblastic cells showed there is no toxicity and the RTqPCR analysis showed significant differences in the expression for osteoblastic phenotype genes, showing a potential material for the bone regeneration.

Keywords: biomaterial; bioceramics; bioengineering; tissue regeneration; bioactive.

INTRODUCTION

Calcium phosphates are considered promising materials for the regenerative medicine, especially in bone replacement or regeneration because of their bone-like composition [1–6]. Among the calcium phosphates, the gold-standard are hydroxyapatite ($Ca_{10}(PO_4)_6(OH)_2$) and tricalcium phosphate ($Ca_3(PO_4)_2$), due to their biocompatibility, biological activity and osteoinduction properties [7–9]. Nevertheless, monetite or calcium biphosphate ($CaHPO_4$) has attracted significant interest in recent years. It is a ceramic amongst calcium phosphate family, possessing calcium ions (Ca^{2+}) and phosphate anions under the same molar amount [10], and as it is more rapidly resorbed in vivo than other types of calcium phosphates [10,11] it can also be used in bone regeneration.

Tamimi and collaborators focused their studies on the monetite, performing in vitro and in vivo assays [12–14]. They observed different effects of this material compared to those of hydroxyapatite in vivo assay. The patient presented bone formation as well as the material was absorbed, while hydroxyapatite did not perform similar results [12] reinforcing potential for the regenerative application.

In turn, cobalt (Co) presents important physicochemical characteristics that confer mechanical strength and greater biocompatibility to implants [15–17]. In the human body, cobalt performs important functions as the micronutrient in the form of cobalamin ($C_{63}H_{88}CoN_{14}O_{14}P$), also known as vitamin B12 [18]. Among its several activities in the human metabolism, vitamin B12 has two crucial functions: acting in DNA synthesis and in the conversion of L-methylmalonyl Coenzyme A to succinyl coenzyme A, which is essential for energy generation in the Krebs Cycle [18].

Co has been used since the 1930s, being initially applied in a dental implant and later in orthopedic and cardiology areas. Currently it has been associated with other materials to compose specific alloys presenting interesting results [19–21]. In addition, we have shown that Cobalt affects the metabolism of cells when available in the cell medium. We attributed this effect to the hypoxia induced in the cells which, by increasing the activity of HIF1α, it stimulates the angiogenesis. This process may contribute to the bone regeneration, since these two processes are correlated [17,22,23] as showed by Wang and co-workers. They observed that higher levels of HIF-1α or HIF-2α in osteoblasts lead to increase the bone volume [23].

In this work, we considered the combination of the hypoxia effect, induced by cobalt, with osteogenesis properties promoted by monetite, proposing a new material that indeed might be used in regenerative medicine and dentistry.

METHODS

Synthesis of materials

The coprecipitation method was used for the syntheses starting from the following reagents: Dibasic Sodium Phosphate (Na_2HPO_4, Sigma-Aldrich, 99%), Calcium Chloride ($CaCl_2$, Sigma-Aldrich, 97%) and Cobalt Chloride ($CoCl_2$, Sigma-Aldrich, 99%). Firstly, the Calcium Chloride and Cobalt Chloride were dissolved at 50 mmol/L under $Co^{2+}/(Co^{2+}+Ca^{2+})$ nominal ratio of 2, 5, 10 and 20 mol% in the water (18.2 mΩ cm) and added at a rate of 1 drop per second into the Dibasic Sodium Phosphate aqueous solution. The pH at the end of precipitation was $5.8 \leq pH \leq 6.5$. After dripping, the suspension was homogenized for 30 minutes in a magnetic stirrer and centrifuged for 15 minutes at 4000 rpm. The solid was suspended in water, then stirred on an orbital tube shaker for one hour, centrifuged again and finally dried in an oven at 80ºC, and monetite powders are obtained.

The samples will be named CaP, CoCaP 2, CoCaP 5, CoCaP 10 and CoCaP 20 here in after.

Fourier transform infrared spectroscopy (FTIR)

The infrared spectroscopy technique was employed to identify the functional groups of the material using a Nicolet Nexus 670 (Thermo, USA) spectrometer. The samples were prepared as 200 mg KBr pellets containing 2% sample. The analysis was carried out in the transmittance mode with 4 cm^{-1} of resolutions and the spectra are averages of 200 scans.

X-ray diffraction (XRD)

XRD patterns were collected using a Rigaku diffractometer (DMax 2100PC), employing Ni-filtered CuK_α radiation (λ = 1.5406 Å; 40 kV; 15 mA), in Bragg-Brentano configuration, continuous scan mode, at 4º for min^{-1} and a step size of 0.04º. The peaks were indexed using Search-Match software (Malvern Panalytical) and PDF-2 database (ICSD, 2003) [24–27]. Rietveld method (GSAS software) with the EXPGUI interface was used for the structural refinement to obtain cell parameters and crystalline information's. The refinements were carried out with a standard Y_2O_3 sample for instrumental contribution, using the Pseudo-Voigt, Chebyshev, and March-Dollase functions for profile, background, and preferred orientation adjustments, respectively. The crystallite size was calculated using Scherrer and Williamson-Hall equations from the FHWM (Full Width at Half Maximum) of the diffracted peaks, as detailed by Kaygili et al. (2017) [11]. The details of crystallographic datasheets of monetite and β-tricalcium phosphate used in the refinements as well as the refinement data can be find in the supplementary material.

Scanning electron microscope (SEM)

SEM analyses were performed using a JEOL model JSM-6010 Scanning electron microscope, operating with an acceleration voltage of 10 kV and secondary electron detector. The semi-

quantitative EDS analysis was performed in the same equipment (JEOL, JSM-6010) detector for Ca, P, O, Co chemical elements using the same acceleration voltage (10 kV).

Biological analysis

Cell culture

MC3T3-E1 cell line (pre-osteoblast) cultures were maintained using Alpha-MEM containing antibiotics (100U/mL penicillin, 100 mg/mL streptomycin) and supplemented with 10% fetal bovine serum (FBS). The cultures were maintained in an incubator at 37°C, with 95% humidity and 5% CO_2. To test the materials, subconfluent cultures were challenged with a cell culture medium enriched with biomaterial (0.2g/mL), according to ISO 10993-12. Previously, the FBS-free medium was enriched for up to 24 hours with each CaP to prepare the conditioned medium. After that, FBS 10% was added and further used to challenge pre-osteoblasts.

Cytotoxicity evaluated by MTT assay

Pre-osteoblasts were seeded into 96-wells plates, and next, they were subjected to the CaP-enriched media for up to 24 hours. Therefore, the cell culture medium was removed, and MTT solution (1 mg mL^{-1}) was added in the cultures up to 3 hours when the MTT-containing medium was removed, and 1 mL of absolute ethanol was added to solubilize the blue dye formed by viable cells. The absorbance was then measured at 570 nm using a microplate reader (SYNERGY-HTX multi-mode reader, Biotek, USA).

Cell adhesion assay

Cell adhesion was evaluated by crystal violet method. The cells were conventionally maintained, trypsinized and seeded in 96-wells microplates at 100×10^3 cells/mL (100 μL/well) to evaluate the influence of CaP-enriched media on cell adhesion. For each group of materials, a control group was used, which was cultured with the conventional medium. After 24 h of challenge, cells were stained, and cell adhesion was estimated by incorporating the crystal violet, as detailed earlier elsewhere. Absorbance was measured at 540 nm using a microplate reader (SYNERGY-HTX multimode reader, Biotek, USA) to estimate the adherent cells.

RTqPCR

To evaluate the molecular mechanism related with the adaptation to each CaP's, the pre-osteoblasts were newly subjected to each CaP-conditioned medium up to 24h, when the cells were harvested and total RNA extracted using Ambion TriZOL Reagent (Life Sciences - Fisher Scientific Inc., Waltham, MA, USA) and treated with DNAse I (Invitrogen, Carls, CA, USA), as used and described earlier. According to the manufacturer's instructions, cDNA synthesis was performed with the High-Capacity cDNA Reverse Transcription Kit (Applied Biosystems, Foster City, CA, USA). Real-time PCR was performed on 10 μL containing PowerUpTM SYBR™ Green Master Mix 2x (5 μL) (Applied Biosystems, Foster City, CA, USA), 0.4 μmolL^{-1} of each primer,

50 ng of cDNA and nuclease-free H_2O. Results were expressed as relative amounts of transcripts using GAPDH and 18S as reference genes (housekeeping gene) using the cycle threshold (ct) method. Primers and race details are described in **Table 1**.

TABLE 1. Primers sequences and details of the cycle conditions.

Gene (ID)	Primer	5'-3' Sequence	Reaction condition
Runx2 (12393)	Forward	GGACGAGGCAAGAGTTTCA	95°C - 15s; 60°C - 30s; 72°C - 60s
	Reverse	TGGTGCAGAGTTCAGGGAG	
Osterix (170574)	Forward	CCCTTCCCTCACTCATTTCC	95°C - 15s; 60°C - 30s; 72°C - 60s
	Reverse	CAACCGCCTTGGGCTTAT	
Osteocalcin (12096)	Forward	AGACTCCGGCGCTACCTT	95°C - 15s; 60°C - 30s; 72°C - 60s
	Reverse	CTCGTCACAAGCAGGGTTAAG	
BSP (15891)	Forward	GTACCGGCCACGCTACTTTCT	95°C - 15s; 60°C - 30s; 72°C - 60s
	Reverse	GTTGACCGCCAGCTCGTTTT	
Integrin α1 (109700)	Forward	TATCCTCCTGAGCGCCTTT	95°C - 15s; 60°C - 30s; 72°C - 60s
	Reverse	TGGCCTTTTGAAGAATCCAA	
Integrin β1 (16412)	Forward	CTGATTGGCTGGAGGAATGT	95°C - 15s; 60°C - 30s; 72°C - 60s
	Reverse	TGAGCAATTGAAGGATAATCATAG	
Fak (14083)	Forward	TCCACCAAAGAAACCACCTC	95°C - 15s; 60°C - 30s; 72°C - 60s
	Reverse	ACGGCTTGACACCCTCATT	
Src (20779)	Forward	TCGTGAGGGAGAGTGAGAC	95°C - 15s; 60°C - 30s; 72°C - 60s
	Reverse	GCGGGAGGTGATGTAGAAAC	
Cofilin (12631)	Forward	CAGACAAGGACTGCCGCTAT	95°C - 15s; 60°C - 30s; 72°C - 60s
	Reverse	TTGCTCTTGAGGGGTGCATT	
Rank-L (21943)	Forward	CGCTCTGTTCCTGTACTTTCGAGC	95°C - 15s; 60°C - 30s; 72°C - 60s
	Reverse	TCGTGCTCCCTCCTTTCATCAGGTT	
HIF1α (15251)	Forward	CATAAAGTCTGCAACATGGAAGGT	95°C - 15s; 60°C - 30s; 72°C - 60s
	Reverse	ATTTGATGGGTGAGGAATGGGTT	
Gapdh (14433)	Forward	AGGCCGGTGCTGAGTATGTC	95°C - 15s; 60°C - 30s; 72°C - 60s
	Reverse	TGCCTGCTTC ACCACCTTCT	

Statistical analysis

Statistical analyzes were performed using GraphPad Prism 7 software (GraphPad Software, USA), by variance analysis (one-way ANOVA) and with Turkey's correction posttest or non-parametric analysis. The p value <0.05 was considered statistically significant.

RESULTS

Synthesis and characterization of Co-doped monetite

During the syntheses of cobalt doped apatite powders the pHs of solutions and suspensions fluctuated as shown in the **Table 2**.

Table 2. Variations of pH during the synthesis

	pH			
Material	Na_2HPO_4	$CaCl_2$	$CaCl_2$ + $CoCl_2$	CaP
CaP	8.86	5.80	5.80	6.00
CoCaP 2	8.86	-	7.18	6.46
CoCaP 5	8.9	-	7.67	6.46
CoCaP 10	8.89	-	7.47	6.26
CoCaP 20	8.87	-	7.57	5.80

The final pH is around 6, which explains why the stoichiometric precipitation did not occur. The results of the EDS semi-quantitative analysis corroborate this fact, as shown later.

The FTIR analysis depicts characteristic bands of apatite as it was described in previous study [11,28,29]. The spectra shown in **Figure 1**, exhibit characteristic P-O stretching peaks at 1125, 1048, and 998 cm^{-1} and the band observed at 559 cm^{-1} can be associated with the O-P-O(H) bending mode.

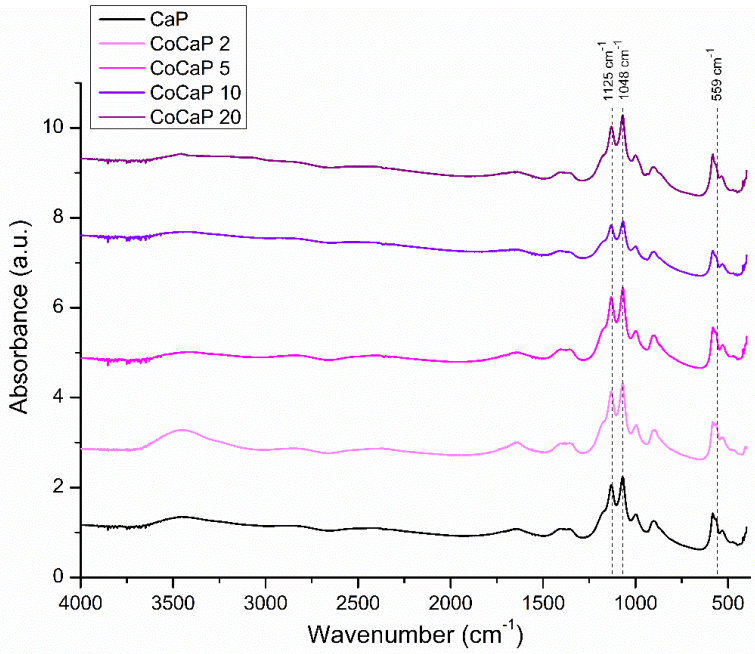

Figure 1:. FTIR spectra of cobalt-doped monetite, obtained by coprecipitation method.

The **Figure 2** exhibits the diffraction pattern of cobalt-doped apatite. Note that they are all predominantly single-phase consisting of monetite with unit formula of $Ca_xCo_{1-x}HPO_4$ with triclinic structure (space group P1), indexed as ICSD 10-503. The amount of substitutional element did not induce phase transformation after the synthesis by this route. This finding was confirmed by the Rietveld refinement, which indicated the presence of monetite (99.99%) compared to β-TCP (0.01). The structural parameters showed in **Figure 3** indicate that the cell parameters and crystallite size were directly affected by the amount of Co. The α and γ angles increased gradually with the amount of Co, while the β angle presented a step decay. The cell parameters (a, b, and c) reduced almost linearly with the Co doping, producing a shortening of the triclinic cell volume. The reduction in lattice parameters is expected since the ionic radius of Co^{2+} (0.65Å) is smaller than that of Ca^{2+} (1.00Å). In other words, if changes in the lattice parameter were observed this indicates that cobalt was incorporated to some extent, even though it may not be proportional to the amount of cobalt added. The incorporated amount cannot be estimated using Vegard's Law, as the variation of the lattice parameters may not be linear with the incorporated amount because the crystalline structure of monetite is complex (triclinic) and can affect parameters and angles in a non-linear way. However, it is possible to say that cobalt was incorporated to some extent by each addition. Lastly, the Co incorporation promoted an increasing of the crystallite size from around 30 nm to more than 70 nm in both curves (Scherrer and Williamson-Hall), and it corroborates with others [30,31]. Additional information about the XRD parameters can be found in the supplementary material.

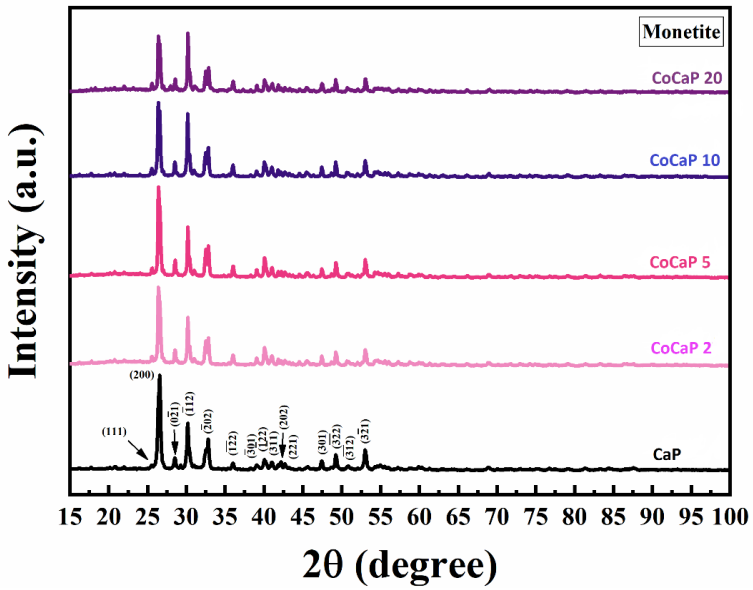

Figure 2. XRD patterns of cobalt-doped monetite, obtained by coprecipitation method.

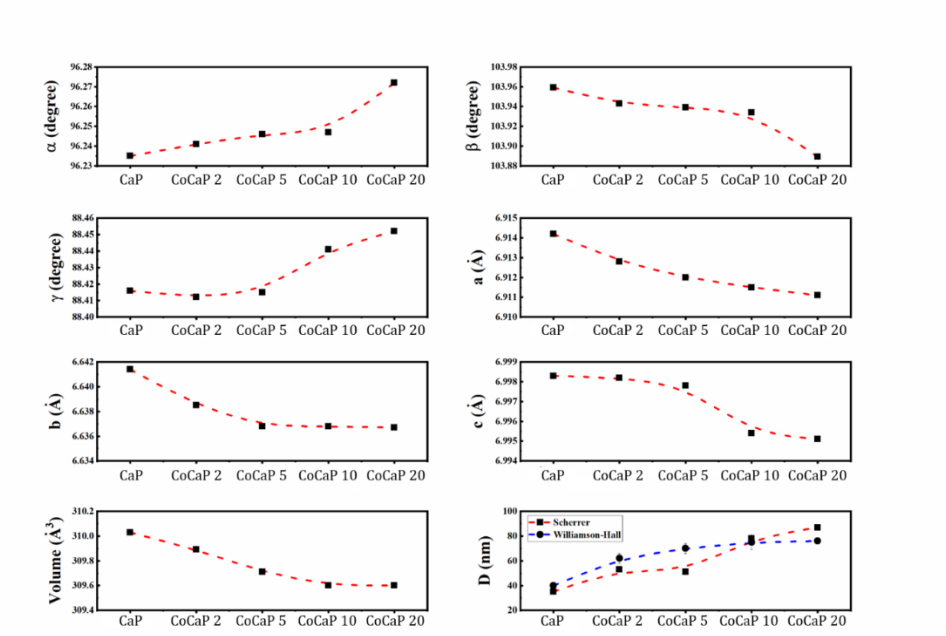

Figure 3 Cell parameters and crystallite size (D) of cobalt-doped apatite, determined by Rietveld refinement.

The SEM micrographs in **Figure 4** clearly illustrate the leaf-like morphology of the Monetite, being it already described by other authors [10–12,14]. The micrographs show that the morphology of the materials changes with cobalt addition, as the apparent size of the particles increases slightly. The mapping analysis showed that all the elements was found in a uniform distribution, not being concentrated at a specific region of the material. The quantification was performed by EDS and showed in the **Figure 5** and **Table 3**. The (Ca+Co)/P ratio of 1 was found, which characterizes the monetite. Note that the amount of cobalt incorporated was not proportional to the nominal substitutive amount of cobalt. The amount of cobalt incorporated when 20 mol% was added was greater than in the other increments.

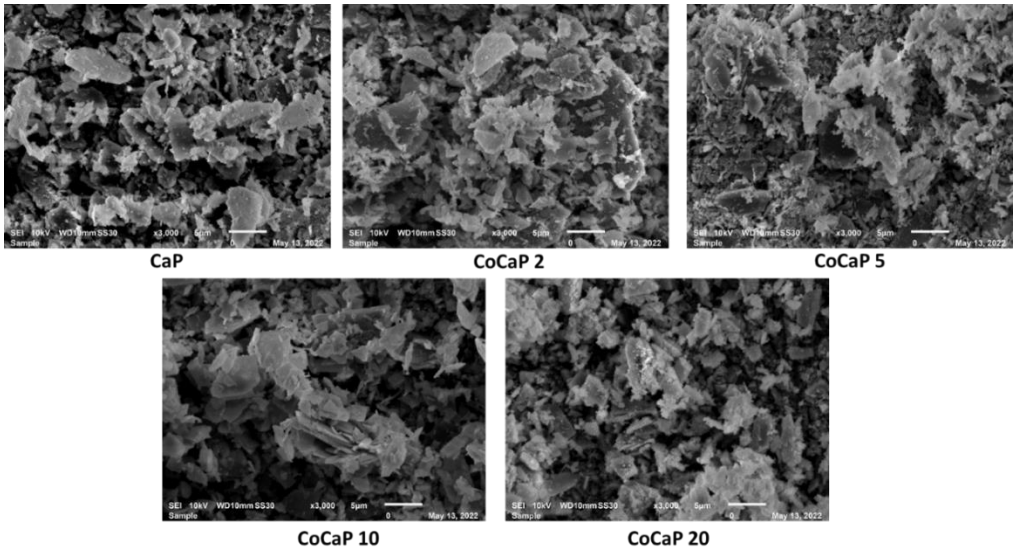

Figure 4. SEM micrographs of cobalt-doped apatite, obtained by coprecipitation method.

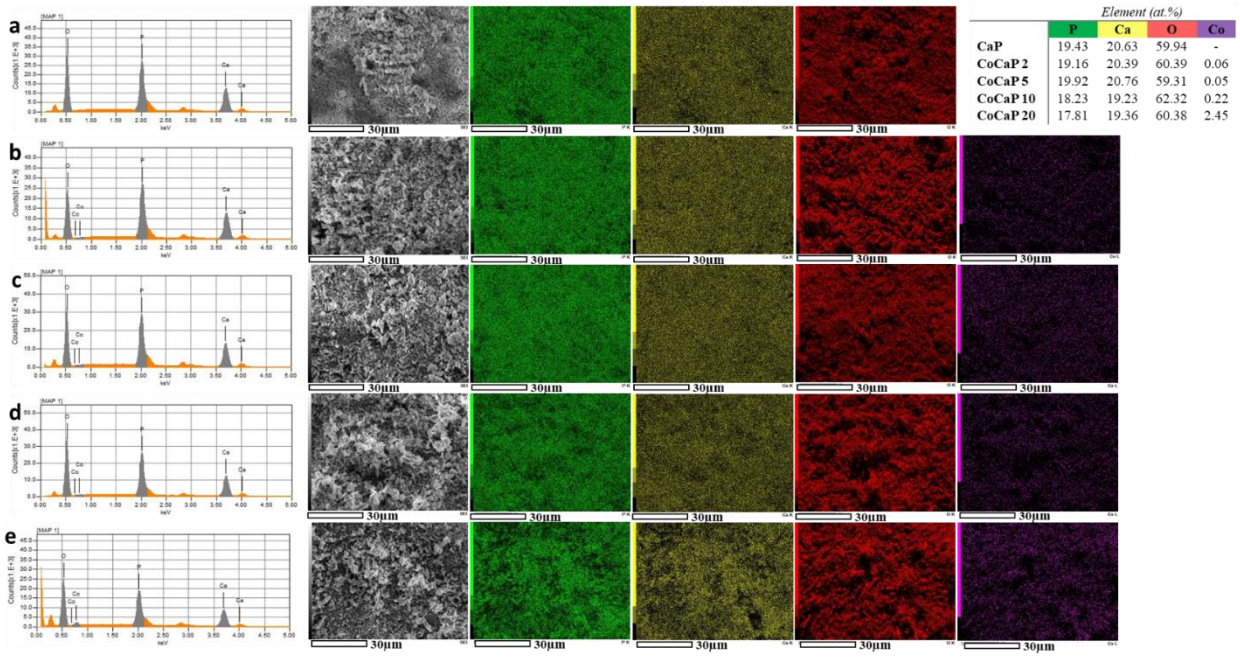

Figure 5. Semiquantitative analysis and elemental distribution of cobalt-doped apatite by EDS. a. CaP; b. CoCaP 2; c. CoCaP 5; d. CoCaP 10; e. CoCaP 20.

Table 3. EDS semiquantitative analysis of cobalt-doped monetite, obtained by coprecipitation method.

Material	Ca/(Ca+Co)	(Ca+Co)/P	(Ca)/P
CaP	1.00	1.062	1.062
CoCaP 2	0.0029	1.067 (1,064)	1.064
CoCaP 5	0.0024	1.045 (1,042)	1.042
CoCaP 10	0.0113	1.067 (1,055)	1.055
CoCaP 20	0.1123	1.225 (1,087)	1.087

Viability assays on pre-osteoblast cells suggest that the material is not cytotoxic

Using the medium conditioned by the materials according to the earlier described methodology, the cell viability assays (MTT and Cristal Violet) show there is no cytotoxicity effect in those cells. In the MTT assay (**Figure 6a**), the treatments do not show any reduction in cell viability when compared with the Ctrl group. The monetite group shows an increase in the concentration of the MTT dye when compared with the control group and also compared to the treated groups, with statistically significant differences (when compared with the groups: Ctrl $^{***}p$ =0.0002, CoCaP2 $^{**}p$ = 0.0044, CoCaP5 $^{***}p$ = 0.0002, CoCaP10 $^{****}p$ = 0.0001 and CoCaP20 $^{****}p$=0.0001).

The Crystal Violet assay depicted in the **Figure 6b** shows there is no significant changes when it was compared with the control group, in turn CoCaP10 and CoCaP20 groups show statistically significant increases when compared with the Ctrl $^{**}p$ = 0.0042 and Ctrl $^{**}p$ = 0.0028, when compared with CaP ^{+}p = 0.0218 and ^{+}p = 0.0131, when compared with CoCaP2 $^{¢¢}p$ = 0.0065 and $^{¢¢}p$ = 0.0043, and when compared with CoCaP5 $^{\&}p$ = 0.0166 and $^{\&}p$ = 0.0101.

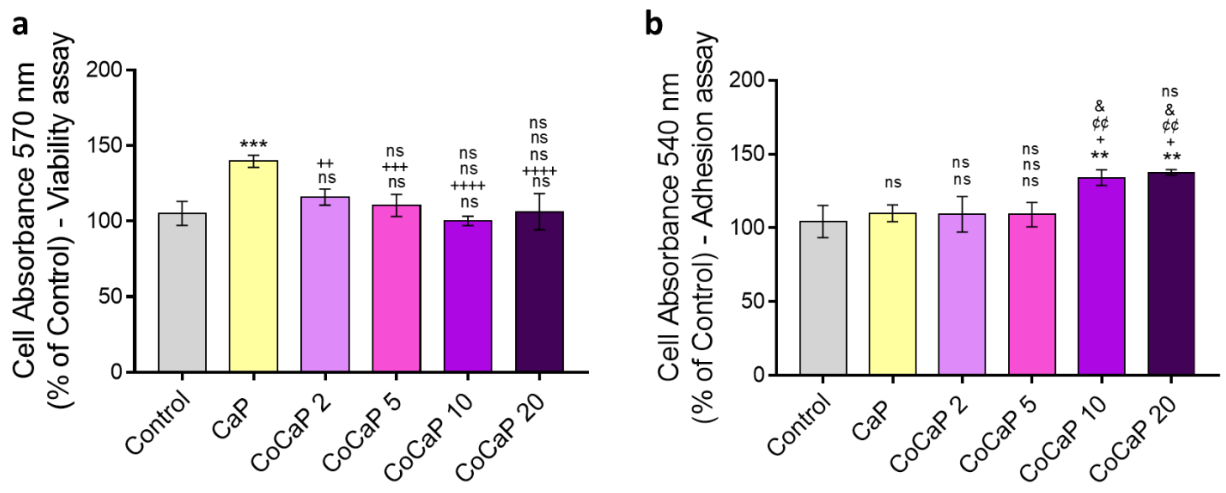

Figure 6. Cytotoxicity Assays. a. The cells showed there is no reduction in viability when compared to the control group. The CaP group showed a statistically significant increase when compared with the control group and the other treatments; **b.** All groups showed there is no reduction in staining by Crystal Violet. CoCaP10 and CoCaP20 showed a statistically significant increase when compared with the control group and the other treatments, but no differences when compared among themselves. All groups of samples n=6.

Evaluation of osteogenic differentiation gene markers in pre-osteoblast responding to synthesized monetites

RTqPCR technology was performed to assess whether treatments modulate pre-osteoblast phenotype in response to the materials evaluated in this study. In turn, the cultures were considered as follows: Control (Ctrl) – when the cells were subjected to the conventional cell culture medium and conditions, and separately the pre-osteoblasts were maintained in monetite-enriched medium distinguished by the concentration of doped cobalt, as follows: CaP, CoCaP2, CoCaP5, CoCaP10 and CoCaP20.

Firstly, we have evaluated the activity of genes related with osteoblastic phenotype such as Runx2, Osterix, Bsp and Osteocalcin (**Figure 7**), which presented differential profile of expression considering the response to the materials. Runx2 gene expression was higher in response to CaP and CoCaP2 groups when compared to the control cultures and among other treatments, while it was reduced in response to CoCaP5, CoCaP10, and CoCaP20, suggesting an effective concentration of cobalt to trigger osteogenic stimulus in pre-osteoblasts (**Figure 7a**). Additionally, Osterix gene was also investigated and it presents a very similar profile of Runx2 (**Figure 7b**).

BSP gene activity was higher in response to CaP and CoCaP2 groups, while this gene activity was lower responding to CoCaP20 group. Additionally, no statistical significances were observed in response to CoCaP5 and CoCaP10 groups (**Figure 7c**). Moreover, Osteocalcin gene was also investigated and our data shows this gene significantly higher in response to CoCaP2 group when compared among other groups. In response to CaP group any significance was shown, while other changes of cobalt-doped monetite seems reduce is expression (**Figure 7d**).

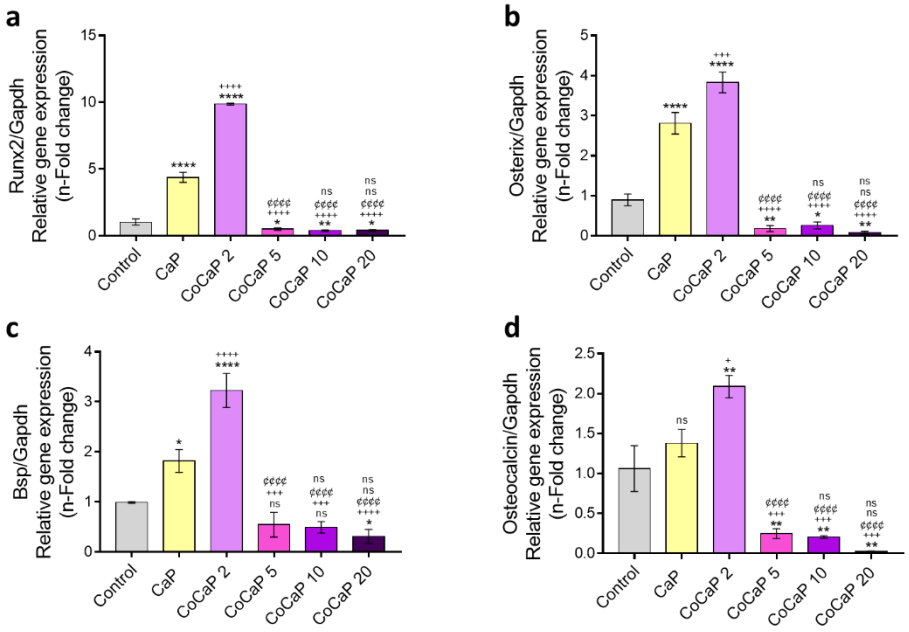

Figure 7. Osteogenic gene markers were modulated in response to Co-doped monetite. (a) Higher expression of RUNX2 gene: Ctrl ($^{****}p = 0.0001$ and $^{****}p = 0.0001$), CoCaP5 ($^{++++}p = 0.0001$, $^{¢¢¢¢}p = 0.0001$) CoCaP10 ($^{++++}p = 0.0001$, $^{¢¢¢¢}p = 0.0001$) and CoCaP20($^{++++}p = 0.0001$, $^{¢¢¢¢}p = 0.0001$); Lower expression: CoCaP5 ($^{*}p = 0.0292$), CoCaP10 ($^{**}p = 0.0082$) and CoCaP20 ($^{*}p = 0.0105$). There were also significant differences in expression between the CaP and CoCaP groups, with CoCaP showing a higher expression than CaP ($^{++++}p = 0.0001$). (**b**) Higher expression of Osterix gene: CaP and CoCaP2 groups, when compared with the groups: Ctrl ($^{****}p = 0.0001$ and $^{****}p = 0.0001$), CoCaP5 ($^{++++}p = 0.0001$, $^{¢¢¢¢}p = 0.0001$) CoCaP10 ($^{++++}p = 0.0001$, $^{¢¢¢¢}p = 0.0001$) and CoCaP20($^{++++}p = 0.0001$, $^{¢¢¢¢}p = 0.0001$); Lower expression: CoCaP5 ($^{**}p = 0.0062$), CoCaP10 ($^{*}p = 0.0137$) and CoCaP20 ($^{**}p = 0.0024$). There were also significant differences in expression between the CaP and CoCaP1 groups, with CoCaP showing an increase compared to CaP ($^{++++}p = 0.0001$). (**c**) The BSP gene expression was increased in the groups CaP ($^{*}p = 0.0147$) and CoCaP2 ($^{****}p = 0.0001$), and decreased in CoCaP20 ($^{*}p = 0.0499$) when compared to the control group. Higher expression: the expression was higher in the CaP and CoCaP groups compared to the other treatments, CoCaP5 ($^{+++}p = 0.0002$, $^{¢¢¢¢}p = 0.0001$) CoCaP10 ($^{+++}p = 0.0001$, $^{¢¢¢¢}p = 0.0001$) and CoCaP20($^{++++}p = 0.0001$, $^{¢¢¢¢}p = 0.0001$). Between the CaP and CoCaP groups, in the CoCaP2 ($^{++++}p = 0.0001$) group there is an increase in expression when compared to CaP. (**d**) Higher expression of Osteocalcin: CoCaP2 ($^{**}p = 0.0013$); Lower expression: CoCaP5 ($^{**}p = 0.0029$), CoCaP10 ($^{*}p = 0.0043$) and CoCaP20 ($^{**}p = 0.0012$). When comparing the treated groups, each other, the expression was higher in the CaP and CoCaP groups compared to the other treatments, CoCaP5 ($^{+++}p = 0.0007$, $^{¢¢¢¢}p = 0.0001$) CoCaP10 ($^{+++}p = 0.0010$, $^{¢¢¢¢}p = 0.0001$) and CoCaP20($^{+++}p = 0.0004$, $^{¢¢¢¢}p = 0.0001$). Between the CaP and CoCaP group, in the CoCaP2 group ($^{+}p = 0.0228$) there is an increase in expression when compared to CaP. All groups of samples n = 3.

Bone remodeling is governed by osteoblasts, osteoclasts and osteocytes. Besides investigating the activity of osteoblast-related genes, we have also studied the expression of RANKL gene, a marker related osteoclastogenesis (**Figure 8a**). Our data shows there is a higher expression in response to both CaP and CoCaP groups when compared to the control group, as well as considering CoCaP2, while the other materials showed no statistically significant differences when compared to the control. Lastly, as cobalt is related with experimental condition of hypoxia, we have also evaluated

the expression of HIF1α gene. HIF1α is an important and well-accepted biomarker of hypoxic condition. Our data shows an increase in HIF1α expression in response to CaP and CoCaP2 groups when compared to control and among other groups (**Figure 8b**).

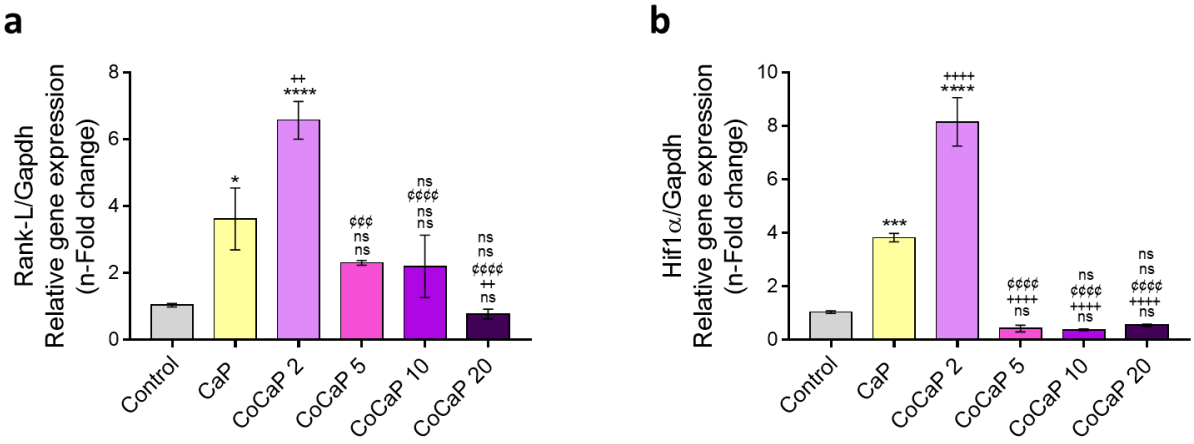

Figure 8. Osteoclastoegenesis-related gene (RANKL) and hypoxia biomarker were investigated in this study. (a) Higher expression of RANKL: CaP ($^{*}p = 0.0125$) and CoCaP2 ($^{****}p = 0.0001$) treatments there was an increase in its expression when compared with the control. When comparing the treated groups, the expression was higher in the CoCaP2 groups compared to the other treatments, CaP ($^{++}p = 0.0022$), CoCaP5 ($^{¢¢¢}p = 0.0003$) CoCaP10 ($^{¢¢¢¢}p = 0.0001$) and CoCaP20 ($^{¢¢¢¢}p = 0.0001$); (**b**) In order to analysis the effect of hypoxia in response to the treatments, the Hif1α gene was evaluated. The gene expression also revealed significant modulation in response to treatment in CaP ($^{***}p = 0.0005$) and CoCaP2 ($^{**}p = 0.0001$) when compared with the control and in the other treatments it was not statistically significant. When comparing the treated groups, the expression was higher in the CaP and CoCaP2 groups compared to the other treatments, CoCaP5 ($^{++++}p = 0.0001$, $^{¢¢¢¢}p = 0.0001$) CoCaP10 ($^{++++}p = 0.0001$, $^{¢¢¢¢}p = 0.0001$) and CoCaP20 ($^{++++}p = 0.0001$, $^{¢¢¢¢}p = 0.0001$). Between the CaP and CoCaP2 groups, in the CoCaP2 group ($^{++++}p = 0.0001$) there is an increase in expression when compared to CaP. All groups of samples n = 3.

Evaluation of genes involved with adhesion and cytoskeleton rearrangement

Cell adhesion is an important issue to be investigated in response to biomaterials, mainly during the development of novel biomimetic materials for bone regeneration. During the cell adhesion responding to biomaterials, we have shown there is a biological significance to integrin genes, as well as the cytoskeleton-related genes such as FAK, Src and Cofilin (**Figure 9**). Here, we have shown that integrin genes showed different responding to the proposed Co-doped monetites: α-integrin showed higher gene expression in response to CaP, CoCaP2, CoCaP10 and CoCaP20 groups than the control cultures (**Figure 9a**). In turn, ß-integrin gene expression was higher in response to CoCaP2 group when compared to the CaP group, but there was no significant difference when compared to the control, while CoCaP5, CoCaP10 and CoCaP20 groups showed a lower expression when compared to the control, CaP and CoCaP1 (**Figure 9b**).

Thereafter, we have also investigated FAK gene expression and its expression shows an increase in response to CoCaP2, CoCaP10 and CoCaP20 groups when compared to the control, while CoCaP20 group showed a higher expression among other groups. Upon integrin activation, FAK

and Src are activated downstream (**Figure 9c**). Thus, Src gene expression was also investigated. SRC gene was higher in response to CaP, CoCaP10 and CoCaP20 groups when compared to control, while both CoCaP2 and CoCaP5 seems requires Src without significance (**Figure 9d**). Lastly, cytoskeleton rearrangement is required when Cofilin modulated the polarization of actin fibers. We have also investigated Cofilin gene expression and our data shows significant expression in response to all groups, expect to CoCaP5 material, with more significance considering the response to CoCaP2 group (**Figure 9e**).

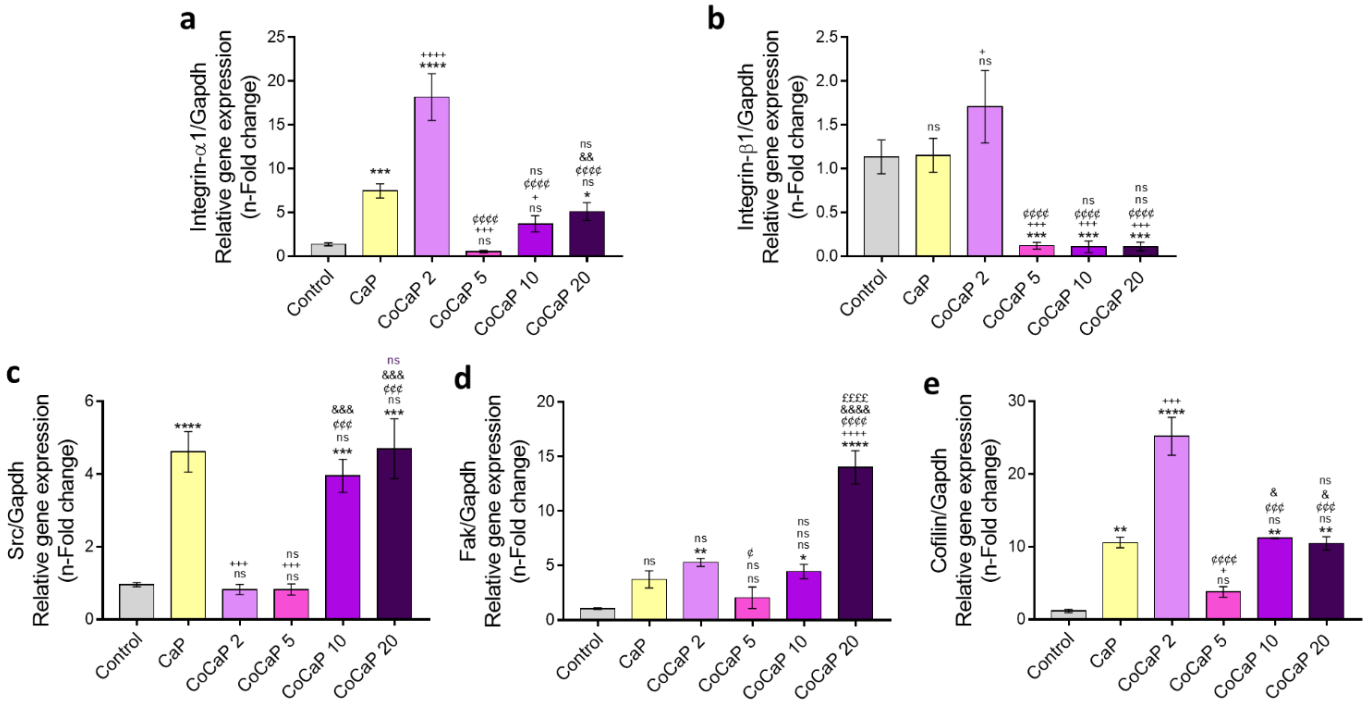

Figure 9. Molecular machinery related with cell adhesion and cytoskeleton rearrangement. (**a**) α1-integrin gene was higher in the groups: CaP ($^{***}p = 0.0009$), CoCaP2 ($^{****}p = 0.0001$), and CoCaP20 ($^{*}p = 0.0347$) when compared with control. Among the treatments, there were statistically significant differences, with a lower expression in the CoCaP2.5 group when compared with CaP ($^{++++}p = 0.0001$), CoCaP2 ($^{¢¢¢¢}p = 0.0001$), and CoCaP20 ($^{\&\&}p = 0,0091$). Among the groups, the expression was higher in the CaP and CoCaP2 groups compared to the other treatments, CoCaP5 ($^{+++}p = 0.0003$, $^{¢¢¢¢}p = 0.0001$) CoCaP10 ($^{+}p = 0.00326$, $^{¢¢¢¢}p = 0.0001$) and CoCaP20 ($^{¢¢¢¢}p = 0.0001$). Between the CaP and CoCaP2 groups, in the CoCaP2 group ($^{++++}p = 0.0001$) was higher in expression when compared to CaP; (**b**) β1-integrin expression was lower in response to CoCaP5 ($^{***}p = 0.0008$), CoCaP10 ($^{*}p = 0.0007$) and CoCaP20 ($^{***}p = 0.0007$). When comparing the treated groups, the expression was higher in the CaP and CoCaP2 groups compared to the other treatments, CoCaP5 ($^{+++}p = 0.0003$, $^{¢¢¢¢}p = 0.0001$) CoCaP10 ($^{+++}p = 0.0002$, $^{¢¢¢¢}p = 0.0001$) and CoCaP20($^{+++}p = 0.0003$, $^{¢¢¢¢}p = 0.0001$). Between the CaP and CoCaP2 genes, in the CoCaP2 group ($^{+}p = 0.0479$) there is an increase on expression when compared to CaP; (**c**) FAK gene expression was considered and it was higher in response to CoCaP2 ($^{**}p = 0.0069$), CoCaP10 ($^{*}p = 0.0154$) and CoCaP20 ($^{****}p = 0.0001$) when compared with the control, while CaP and CoCaP5 treatments it was not statistically significant. The other groups had statistically significant differences when compared among themselves, with increased expression in CoCaP2 and CoCaP20, the statistical differences were: CoCaP5 ($^{¢}p = 0.0210$, $^{+++}p = 0.0001$), CoCaP10 ($^{¢¢¢}p = 0.0010$) and CoCaP20 ($^{++++}p = 0.0001$, $^{¢¢¢¢}p = 0.0001$, $^{\&\&\&}p = 0.0002$, $^{£££¢}p = 0.0010$); (**d**) Src gene expression was higher in the groups: CaP ($^{****}p = 0.0001$), CoCaP10 ($^{***}p = 0.0007$) and CoCaP20 ($^{***}p = 0.0001$) when compared with control, between CoCaP2 and CoCaP5 treatments was

not statistically significant. The other groups showed statistically significant differences when compared among themselves, with higher expression in response to CaP, CoCaP10 and CoCaP20. The statistical differences were: CoCaP2 ($^{+++}p = 0.0001$), CoCaP5 ($^{+++}p = 0.0001$), CoCaP10 ($^{¢¢¢}p = 0.0010$, $^{\&\&\&}p = 0.0010$) and CoCaP20 ($^{¢¢¢}p = 0.0002$, $^{\&\&\&}p = 0.0002$); (**e**) Cofilin gene expression was higher in the groups as follows: CaP ($^{**}p = 0.0034$), CoCaP2 ($^{****}p = 0.0001$), CoCaP10 ($^{**}p = 0.0024$) and CoCaP20 ($^{**}p = 0.0037$) when compared with control, in the CoCaP5 it was not statistically significant. The other groups had statistically significant differences when compared among themselves, with higher expression in CaP, CoCaP2, CoCaP10 and CoCaP20, the statistical differences were: CoCaP2 ($^{+++}p = 0.0001$), CoCaP5 ($^{+}p = 0.0207$, $^{¢¢¢¢}p = 0.0001$), CoCaP10 ($^{¢¢¢}p = 0.0002$, $^{\&}p = 0.0134$) and CoCaP20 ($^{¢¢¢}p = 0.0001$, $^{\&}p = 0.0229$). All groups of samples n = 3.

DISCUSSION

Classical techniques to characterize the material were used in this study, such as XRD, FTIR, SEM, EDS. The combination of these techniques allowed us to confirm the effectiveness of the synthesis, as well as considering the modifications that the cobalt perform on the synthesis of the monetite. The FTIR technique showed the "fingerprint" bands of Monetite when compared to the literature [11,28,32]. It shows the phosphate bonds and the absence of the water band that would be characteristic of Brushite, which is also a member of the calcium phosphate family and also has its own characteristics [33,34]. Considering the XRD analysis, our data attests to the presence of a single monetite phase in the samples. As the EDS shows, the Co content remained below 2.5%, which was insufficient to produce phase decomposition to Ca-based compounds, such as other apatite, TCP, or $CaCO_3$. The great affinity of metallic ions to H and O atoms can deplete the monetite chemical composition and play a role in phase decomposition [35]. The cell parameters (α, β, γ, a, b, and c) changes can be related to the Co2+ ionic radius (0.79 Å), which is lower than the Ca2+ (0.99 Å).

Thus, the Co doping monetite crystal structure might produce significant modifications in the cell parameters. In addition, the distinct chemical characteristics of Co compared to Ca (e.g., electronegativity) might modify the surface chemistry of the particles, affecting the crystallite size, as observed. These aspects have also been found for metallic substitutional elements, such as Ag, Sr, Zn, Al, Ni, and Mn [11,36]. On the other hand, SEM imaging of the monetite did not exhibit apparent differences in size and morphology at the microscale range. Thereafter, to investigate whether the Co-doped monetites have some degree of cytotoxicity, the MTT and Crystal Violet assays were performed. Finally, the molecular mechanism was also investigated by evaluating specific genes related with osteoblast performance and activity. Important, cell viability was not affected considering the variation of Co-doped monetite. Specifically, MTT assay shows that CaP material was higher than other groups suggesting an increase in the number of viable cells when compared to the control and the other treatments. Important to mention that MTT is not appropriate

methodology to confirm number of cells and to confirm new experiments using novel methodologies are called for.

To evaluate the molecular involvement of genes in modulating the phenotype of osteoblasts, RTqPCR technology was performed as proposed earlier considering the analysis of other biomateriais [37–39]. Firstly, we have an important modulation of genes related with cell adhesion it being companied by cytoskeleton rearrangement (evaluated by the expression of Cofilin). Cofilin is related with cytoskeleton rearrangement by driving the (de)polymerization of actin fibers and also has been associated with cell morphological changes. Among genes involved in cell adhesion, integrin's are the largest family of receptors that mediate interactions between cells and extracellular matrix (ECM). The integrin family is composed of 22 heterodimers of two types of α- and β-subunits, which are correlated with signal transduction from extracellular to intracellular compartment, connecting the cells to the extracellular matrix. The adequate interaction of the cell to the ECM will drive biological processes including cell proliferation, migration, and later differentiation [40–42]. In general, integrin's are related to mediate the adhesion of various cell types to collagen and other extracellular matrix proteins [40,43].

With the differential expression of Integrin's, other genes such as Fak, Src and Cofilin were evaluated, since upon integrin's activation there is a multitude of downstream proteins related with this signaling cascade [43–45]. Fak receives the signal upon integrin activation and delivers to Src and LIM-kinase thereafter modulating the Cofilin activation in order to drive cytoskeleton rearrangement, which is related with cellular adaptation to different surface of biomaterials [37,43,46]. Thus, the activity of Cofilin was evaluated to better understand whether the involvement of cytoskeleton rearrangement during the adhesion of pre-osteoblasts was required. Our data supports this hypothesis once Cofilin was differentially modulated responding to Co-doped monetite and it might suggest a pre-requisite to osteoblast differentiation as it has been shown earlier that osteoblast differentiation requires significant cellular morphological changes.

In order to test this hypothesis, osteoblastic gene markers were investigated and we have shown there is a significant higher expression of all genes in response to Co-doped monetite (2%), suggesting this concentration of cobalt doping monetite displaying better performance in osteoblasts. This molecular analysis brings a range of genes involved with osteoblast differentiation, ranging from earlier involved genes, such as Runx2 and Osterix, to later involved genes, such as BSP and Osteocalcin [47–50]. Important to correlate this molecular machinery with the hypoxic microenvironment generated by Co-doped monetite, mainly found in response to CoCaP2 – as it was confirmed by osteoblasts expressing Hif1α – once cobalt is a known hypoxia-inducing agent, since it replaces the Fe^{2+} in this process by stimulating HIF1α expression [51,52]. Recent studies have shown that modulation of the HIF pathway in osteoblasts has revealed that

this pathway plays an important role in bone formation. Loss of HIF1α or HIF2α in mouse osteoblasts causes a considerable decrease in bone volume, while increased levels of these genes lead to their better performance [53,54]

Altogether, the combination of gene expressions may indicate an induction by cobalt doped monetite in stimulating osteoblastic phenotype and thus indicating be a biomimetic new material for bone regeneration application. Although they have similarities when comparing the characterization techniques, the amount of Cobalt was decisive in defining the ideal concentration for future applications. Thus, our data supports with decisive of cellular and molecular evidences on Co-doped monetite as potential new material for biomedical applications, opening new horizons in regenerative medicine.

Acknowledgements

The authors are grateful to Fundação de Amparo à Pesquisa do Estado de São Paulo - FAPESP (FAPESP: 2019/26854-2), Conselho Nacional de Desenvolvimento Científico e Tecnológico (CNPq – Bolsa Produtividade em Pesquisa, 314166/2021-1) and Coordenação de Aperfeiçoamento de Pessoal de Nível Superior (Capes), code 1.

REFERENCES

[1] Carreira ACO, Zambuzzi WF, Rossi MC, Filho RA, Sogayar MC, Granjeiro JM. Bone Morphogenetic Proteins: Promising Molecules for Bone Healing, Bioengineering, and Regenerative Medicine. Vitam. Horm., vol. 99, Academic Press Inc.; 2015, p. 293–322. https://doi.org/10.1016/bs.vh.2015.06.002.

[2] Pinto TS, Martins BR, Ferreira MR, Bezerra F, Zambuzzi WF. Nanohydroxyapatite-Blasted Bioactive Surface Drives Shear-Stressed Endothelial Cell Growth and Angiogenesis. Biomed Res Int 2022;2022:1–11. https://doi.org/10.1155/2022/1433221.

[3] Bertazzo S, Zambuzzi WF, Campos DDP, Ferreira C V., Bertran CA. A simple method for enhancing cell adhesion to hydroxyapatite surface. Clin Oral Implants Res 2010;21:1411–3. https://doi.org/10.1111/j.1600-0501.2010.01968.x.

[4] Bertazzo S, Zambuzzi WF, Campos DDP, Ogeda TL, Ferreira C V., Bertran CA. Hydroxyapatite surface solubility and effect on cell adhesion. Colloids Surfaces B Biointerfaces 2010;78:177–84. https://doi.org/10.1016/j.colsurfb.2010.02.027.

[5] Gemini-Piperni S, Milani R, Bertazzo S, Peppelenbosch M, Takamori ER, Granjeiro JM, et al. Kinome profiling of osteoblasts on hydroxyapatite opens new avenues on biomaterial cell signaling. vol. 111. John Wiley and Sons Inc.; 2014. https://doi.org/10.1002/bit.25246.

[6] Sartoretto SC, Calasans-Maia MD, Alves ATNN, Resende RFB, da Costa Fernandes CJ, de Magalhães Padilha P, et al. The role of apoptosis associated speck-like protein containing a caspase-1 recruitment domain (ASC) in response to bone substitutes. Mater Sci Eng C 2020;112:110965. https://doi.org/10.1016/J.MSEC.2020.110965.

[7] Koutsopoulos S, Kim JH, Kim SHC, Kim HK, Akaike T, Kim SHC. Synthesis and characterization of hydroxyapatite crystals: A review study on the analytical methods. J Biomed Mater Res 2002;62:600–12. https://doi.org/10.1002/jbm.10280.
[8] Aminzare M, Eskandari A, Baroonian MH, Berenov A, Razavi Hesabi Z, Taheri M, et al. Hydroxyapatite nanocomposites: Synthesis, sintering and mechanical properties. Ceram Int 2013;39:2197–206. https://doi.org/10.1016/j.ceramint.2012.09.023.
[9] Gao P, Zhang H, Liu Y, Fan B, Li X, Xiao X, et al. Beta-tricalcium phosphate granules improve osteogenesis in vitro and establish innovative osteo-regenerators for bone tissue engineering in vivo. Sci Rep 2016. https://doi.org/10.1038/srep23367.
[10] Motameni A, Alshemary AZ, Evis Z. A review of synthesis methods, properties and use of monetite cements as filler for bone defects. Ceram Int 2021;47:13245–56. https://doi.org/10.1016/j.ceramint.2021.01.240.
[11] Kaygili O, Tatar C, Keser S, Bulut N. Preparation and characterization of monetites co-doped with Ni/Al, Ni/Mn and Al/Mn. Mater Lett 2017;201:39–42. https://doi.org/10.1016/j.matlet.2017.05.015.
[12] Tamimi F, Torres J, Bassett D, Barralet J, Cabarcos EL. Resorption of monetite granules in alveolar bone defects in human patients. Biomaterials 2010;31:2762–9. https://doi.org/10.1016/J.BIOMATERIALS.2009.12.039.
[13] Tamimi F, Nihouannen D Le, Eimar H, Sheikh Z, Komarova S, Barralet J. The effect of autoclaving on the physical and biological properties of dicalcium phosphate dihydrate bioceramics: Brushite vs. monetite. Acta Biomater 2012;8:3161–9.
[14] Torres J, Tamimi I, Cabrejos-Azama J, Tresguerres I, Alkhraisat M, López-Cabarcos E, et al. Monetite granules versus particulate autologous bone in bone regeneration. Ann Anat - Anat Anzeiger 2015;200:126–33. https://doi.org/10.1016/j.aanat.2015.03.008.
[15] Lin WC, Chuang CC, Yao C, Tang CM. Effect of Cobalt Precursors on Cobalt-Hydroxyapatite Used in Bone Regeneration and MRI. J Dent Res 2020;99:277–84. https://doi.org/10.1177/0022034519897006.
[16] Anissian L, Stark A, Dahlstrand H, Granberg B, Good V, Bucht E. Cobalt ions influence proliferation and function of human osteoblast-like cells. Acta Orthop Scand 2002;73:369–74. https://doi.org/10.1080/000164702320155400.
[17] da Costa Fernandes CJ, de Almeida GS, Pinto TS, Teixeira SA, Bezerra FJ, Zambuzzi WF. Metabolic effects of CoCr-enriched medium on shear-stressed endothelial cell and osteoblasts: A possible mechanism involving a hypoxic condition on bone healing. Mater Sci Eng C 2021;128:112353. https://doi.org/10.1016/J.MSEC.2021.112353.
[18] Okamoto S, Eltis LD. The biological occurrence and trafficking of cobalt. Metallomics 2011;3:963–70. https://doi.org/10.1039/c1mt00056j.
[19] Machado MIP, Gomes AM, Rodrigues MF, Silva Pinto T, da Costa Fernandes CJ, Bezerra FJ, et al. Cobalt-chromium-enriched medium ameliorates shear-stressed endothelial cell performance. J Trace Elem Med Biol 2019;54:163–71. https://doi.org/10.1016/j.jtemb.2019.04.012.
[20] Ekren O, Ozkomur A, Ucar Y. Effect of layered manufacturing techniques, alloy powders, and layer thickness on metal-ceramic bond strength. J Prosthet Dent 2018;119:481–7. https://doi.org/10.1016/j.prosdent.2017.04.007.
[21] Hart AJ, Hester T, Sinclair K, Powell JJ, Goodship AE, Pele L, et al. The association between metal ions from hip resurfacing and reduced T-cell counts. J Bone Joint Surg Br 2006;88:449–54. https://doi.org/10.1302/0301-620X.88B4.17216.

[22] Keith B, Johnson RS, Simon MC. HIF1 α and HIF2 α: sibling rivalry in hypoxic tumour growth and progression. Nat Rev Cancer 2012;12:9–22. https://doi.org/10.1038/nrc3183.
[23] Wang Y, Wan C, Deng L, Liu X, Cao X, Gilbert SR, et al. The hypoxia-inducible factor α pathway couples angiogenesis to osteogenesis during skeletal development. J Clin Invest 2007;117:1616–26. https://doi.org/10.1172/JCI31581.
[24] Zagorac D, Muller H, Ruehl S, Zagorac J, Rehme S. Recent developments in the Inorganic Crystal Structure Database: Theoretical crystal structure data and related features. J Appl Crystallogr 2019;52:918–25. https://doi.org/10.1107/S160057671900997X.
[25] Allmann R, Hinek R. The introduction of structure types into the Inorganic Crystal Structure Database ICSD. Acta Crystallogr Sect A Found Crystallogr 2007;63:412–7. https://doi.org/10.1107/S0108767307038081.
[26] Hellenbrandt M. The inorganic crystal structure database (ICSD) - Present and future. Crystallogr. Rev., vol. 10, Taylor & Francis; 2004, p. 17–22. https://doi.org/10.1080/08893110410001664882.
[27] Belkly A, Helderman M, Karen VL, Ulkch P. New developments in the Inorganic Crystal Structure Database (ICSD): Accessibility in support of materials research and design. Acta Crystallogr Sect B Struct Sci 2002;58:364–9. https://doi.org/10.1107/S0108768102006948.
[28] Salimi E, Javadpour J. Synthesis and characterization of nanoporous monetite which can be applicable for drug carrier. J Nanomater 2012;2012. https://doi.org/10.1155/2012/931492.
[29] Zhou H, Yang L, Gbureck U, Bhaduri SB, Sikder P. Monetite, an important calcium phosphate compound–Its synthesis, properties and applications in orthopedics. Acta Biomater 2021;127:41–55. https://doi.org/10.1016/J.ACTBIO.2021.03.050.
[30] Rabiei M, Palevicius A, Monshi A, Nasiri S, Vilkauskas A, Janusas G. Comparing methods for calculating nano crystal size of natural hydroxyapatite using X-ray diffraction. Nanomaterials 2020;10:1–21. https://doi.org/10.3390/nano10091627.
[31] Chérif I, Dkhil YO, Smaoui S, Elhadef K, Ferhi M, Ammar S. X-Ray Diffraction Analysis by Modified Scherrer, Williamson–Hall and Size–Strain Plot Methods of ZnO Nanocrystals Synthesized by Oxalate Route: A Potential Antimicrobial Candidate Against Foodborne Pathogens. J Clust Sci 2022:1–16. https://doi.org/10.1007/s10876-022-02248-z.
[32] Cama G, Gharibi B, Sait MS, Knowles JC, Lagazzo A, Romeed S, et al. A novel method of forming micro- and macroporous monetite cements. J Mater Chem B 2013;1:958–69. https://doi.org/10.1039/C2TB00153E.
[33] Prado Da Silva MH, Lima JHC, Soares GA, Elias CN, De Andrade MC, Best SM, et al. Transformation of monetite to hydroxyapatite in bioactive coatings on titanium. Surf Coatings Technol 2001;137:270–6. https://doi.org/10.1016/S0257-8972(00)01125-7.
[34] Shah FA, Jolic M, Micheletti C, Omar O, Norlindh B, Emanuelsson L, et al. Bone without borders – Monetite-based calcium phosphate guides bone formation beyond the skeletal envelope. Bioact Mater 2023;19:103–14. https://doi.org/10.1016/j.bioactmat.2022.03.012.
[35] Duncan J, Macdonald JF, Hanna J V., Shirosaki Y, Hayakawa S, Osaka A, et al. The role of the chemical composition of monetite on the synthesis and properties of α-tricalcium phosphate. Mater Sci Eng C 2014;34:123–9. https://doi.org/10.1016/j.msec.2013.08.038.
[36] Adawy A, Diaz R. Probing the Structure, Cytocompatibility, and Antimicrobial Efficacy of Silver-, Strontium-, and Zinc-Doped Monetite. ACS Appl Bio Mater 2022;5:1648–57. https://doi.org/10.1021/acsabm.2c00047.
[37] Fernandes CJC, Bezerra F, Ferreira MR, Andrade AFC, Pinto TS, Zambuzzi WF. Nano hydroxyapatite-blasted titanium surface creates a biointerface able to govern Src-dependent

osteoblast metabolism as prerequisite to ECM remodeling. Colloids Surfaces B Biointerfaces 2018;163:321–8. https://doi.org/10.1016/j.colsurfb.2017.12.049.
[38] Albano CS, Moreira Gomes A, da Silva Feltran G, da Costa Fernandes CJ, Trino LD, Zambuzzi WF, et al. Biofunctionalization of titanium surfaces with alendronate and albumin modulates osteoblast performance. Heliyon 2020;6. https://doi.org/10.1016/j.heliyon.2020.e04455.
[39] Célio CJ, da Silva RA, Fretes Wood P, Teixeira SA, Bezerra F, Zambuzzi WF. The molecular pathway triggered by zirconia in endothelial cells involves epigenetic control. Tissue Cell 2021;73. https://doi.org/10.1016/j.tice.2021.101627.
[40] Da Silva RA, Da Silva Feltran G, Ferreira MR, Wood PF, Bezerra F, Zambuzzi WF. The Impact of Bioactive Surfaces in the Early Stages of Osseointegration: An in Vitro Comparative Study Evaluating the HAnano® and SLActive® Super Hydrophilic Surfaces. Biomed Res Int 2020;2020. https://doi.org/10.1155/2020/3026893.
[41] Daley WP, Peters SB, Larsen M. Extracellular matrix dynamics in development and regenerative medicine. J Cell Sci 2008;121:255–64. https://doi.org/10.1242/jcs.006064.
[42] Zambuzzi WF, Granjeiro JM, Parikh K, Yuvaraj S, Peppelenbosch MP, Ferreira C V. Modulation of Src activity by low molecular weight protein tyrosine phosphatase during osteoblast differentiation. Cell Physiol Biochem 2008;22:497–506. https://doi.org/10.1159/000185506.
[43] Zambuzzi WF, Coelho PG, Alves GG, Granjeiro JM. Intracellular signal transduction as a factor in the development of “Smart” biomaterials for bone tissue engineering. vol. 108. John Wiley & Sons, Ltd; 2011. https://doi.org/10.1002/bit.23117.
[44] da Costa Fernandes CJ, do Nascimento AS, da Silva RA, Zambuzzi WF. Fibroblast contributes for osteoblastic phenotype in a MAPK-ERK and sonic hedgehog signaling-independent manner. Mol Cell Biochem 2017;436:111–7. https://doi.org/10.1007/s11010-017-3083-0.
[45] van der Eerden BCJ, Teti A, Zambuzzi WF. Bone, a dynamic and integrating tissue. Arch Biochem Biophys 2014;561:1–2. https://doi.org/10.1016/j.abb.2014.08.012.
[46] Baroncelli M, Fuhler GM, van de Peppel J, Zambuzzi WF, van Leeuwen JP, van der Eerden BCJ, et al. Human mesenchymal stromal cells in adhesion to cell-derived extracellular matrix and titanium: Comparative kinome profile analysis. J Cell Physiol 2019;234:2984–96. https://doi.org/10.1002/jcp.27116.
[47] Komori T. Regulation of proliferation, differentiation and functions of osteoblasts by runx2. Int J Mol Sci 2019;20:1694. https://doi.org/10.3390/ijms20071694.
[48] Liu Q, Li M, Wang S, Xiao Z, Xiong Y, Wang G. Recent Advances of Osterix Transcription Factor in Osteoblast Differentiation and Bone Formation. Front Cell Dev Biol 2020;8:1575. https://doi.org/10.3389/fcell.2020.601224.
[49] Gordon JAR, Tye CE, Sampaio A V., Underhill TM, Hunter GK, Goldberg HA. Bone sialoprotein expression enhances osteoblast differentiation and matrix mineralization in vitro. Bone 2007;41:462–73. https://doi.org/10.1016/j.bone.2007.04.191.
[50] Tsao YT, Huang YJ, Wu HH, Liu YA, Liu YS, Lee OK. Osteocalcin mediates biomineralization during osteogenic maturation in human mesenchymal stromal cells. Int J Mol Sci 2017;18. https://doi.org/10.3390/ijms18010159.
[51] Osathanon T, Vivatbutsiri P, Sukarawan W, Sriarj W, Pavasant P, Sooampon S. Cobalt chloride supplementation induces stem-cell marker expression and inhibits osteoblastic differentiation in human periodontal ligament cells. Arch Oral Biol 2014;60:29–36. https://doi.org/10.1016/j.archoralbio.2014.08.018.

[52] Zhang Q, Riddle RC, Clemens TL. Bone and the regulation of global energy balance. J Intern Med 2015;277:681–9. https://doi.org/10.1111/joim.12348.
[53] Shomento SH, Wan C, Cao X, Faugere M-CC, Bouxsein ML, Clemens TL, et al. Hypoxia-inducible factors 1α and 2α exert both distinct and overlapping functions in long bone development. J Cell Biochem 2010;109:196–204. https://doi.org/10.1002/jcb.22396.
[54] Chen D, Tian W, Li Y, Tang W, Zhang C. Osteoblast-specific transcription factor Osterix (Osx) and HIF-1α cooperatively regulate gene expression of vascular endothelial growth factor (VEGF). Biochem Biophys Res Commun 2012;424:176–81. https://doi.org/10.1016/j.bbrc.2012.06.104.

Complementary assays

After the submission of the paper, other tests were performed to complement the results. Raman spectroscopy, Wound Healing assay, and bacteriological assay.

Methodology

Raman spectroscopy

Powdered samples were analyzed with Raman microscope (Renishaw Inc., Hoffman Estates, IL) equipped with a 514.5 nm laser line, 1800 lines/mm diffraction grating, 10 s acquisition time, laser power attenuated to 10%, and a 50× (NA = 0.75) dry objective (Leica Microsystems). This technique provides the Raman bands, which also allows to detect the molecular vibrations of the samples. Therefore, FTIR and Raman spectroscopy might be considered complementary techniques to evaluate the molecular structure of the compounds of the samples.

Bacteriological Assay

The disk-diffusion susceptibility test was performed according to Bauer et al. (1966) (BAUER et al., 1966). A suspension of *Staphylococcus aureus*, grown in BHI broth 35°C/6h with approximately $1.5x10^8$ CFU/ml (McFarland scale 0.5) was sown with a swab on the surface of the Müeller-Hinton Agar plate. After absorption of the inoculum by the culture medium, the disks of the materials were arranged on the surface of the plate, and incubated at 35°C/24h.

Wound healing assay

The cell migration and regeneration were estimated by using a scratch assay, as performed earlier (PINTO et al., 2022). The scratch assay estimates the cell migration and regeneration. Briefly, the cells were cultured in 12-well plates at $4×10^4$ cells/cm^2, and after 100% confluence, an introduced area was cleared using a pipet tip and then a monitoring of the healing and the migration of the cells up to 12 h and 16 h (PINTO et al., 2022). Thereafter, the cultures were subjected to fixation with 4% PFA and stained with Alizarin Red S. In the analysis of the healing in vitro, the wound healing area was measured in an inverted microscope with a coupled digital camera (Zeiss) and the acquired images analyzed using the ImageJ software (NIH, Bethesda, MD).

Results

In **Figure 1**, monetite can be easily distinguished from other CaP phases such as hydroxyapatite, TCP, and brushite by peaks detected by Raman spectroscopy due to its unique crystal structure (DESAI; BHADURI; TAS, 2008; WOPENKA; PASTERIS, 2005). Different

from HA, monetite has no hydroxyl ion, and as observed in brushite, monetite also has no H_2O in its crystal structure, i.e. no peak at about 3500 cm^{-1} originated by O-H vibrations are observed. A strong peak in the 988 cm^{-1} region of tetrahedral P-O bond vibration and a peak in the 900 cm^{-1} region due to P-O bonds that are in the P-O-H^+ configuration and can only be seen in monetite (DESAI; BHADURI; TAS, 2008; GHINA IMANIYYAH; SUNARSO; HERDA, 2022; ZHOU et al., 2020) can be observed.

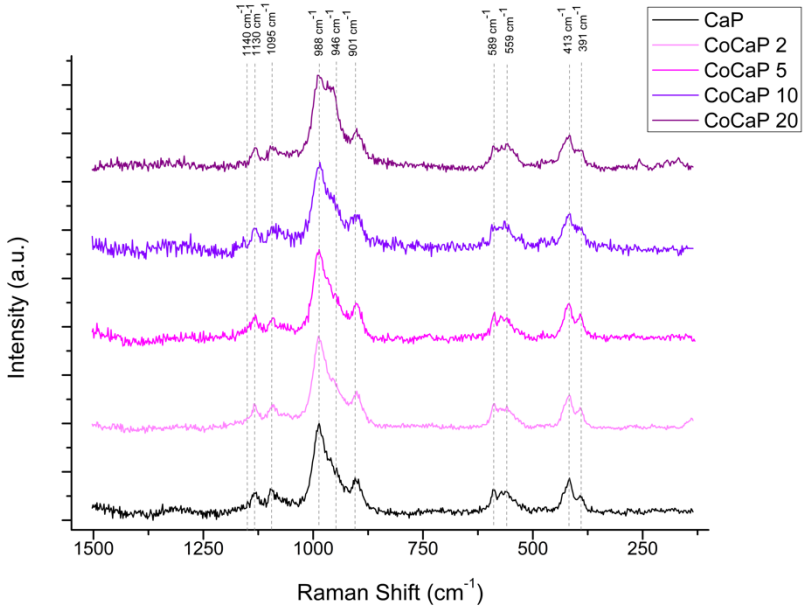

Figure 1. Raman spectra of monetite and cobalt-doped monetite, obtained by coprecipitation method.

The Wounding area assay in **Figure 2** cell proliferation after the cell was cut. In the treatment for 12 hours, the CaP group did not present statistically significant differences with the Ctrl group, since the regenerated area was equivalent, different from the other groups that regeneration was lower (CoCaP2, CoCaP5, CoCaP10, and CoCaP20 - $^{****}p = <0.0001$). When compared between treatment times 0 and 12 hours, the Ctrl ($^{****}p = <0.0001$), CaP ($^{++++}p = <0.0001$), CoCaP2 ($^{¢¢¢¢}p = <0.0001$), CoCaP5 ($^{\&\&\&\&}p = <0.0001$) and CoCaP20 ($^{\$\$\$\$}p = <0.0001$) groups showed statistically significant regeneration.

After 24-hours of treatment, the CaP and CoCaP2 groups showed no differences when compared to Ctrl, these groups had equivalent regenerated area. The CoCaP5, CoCaP10 and CoCaP20 groups ($^{****}p = <0.0001$) showed regeneration of the injured area but less when compared to the Control. When compared to their respective treatments at the other times, they showed an increase in the regenerated area CoCaP5 ($^{\&\&\&\&}p = <0.0001$), CoCaP10 ($^{££££}p = <0.0001$), and CoCaP20 ($^{\$\$\$\$}p = <0.0001$).

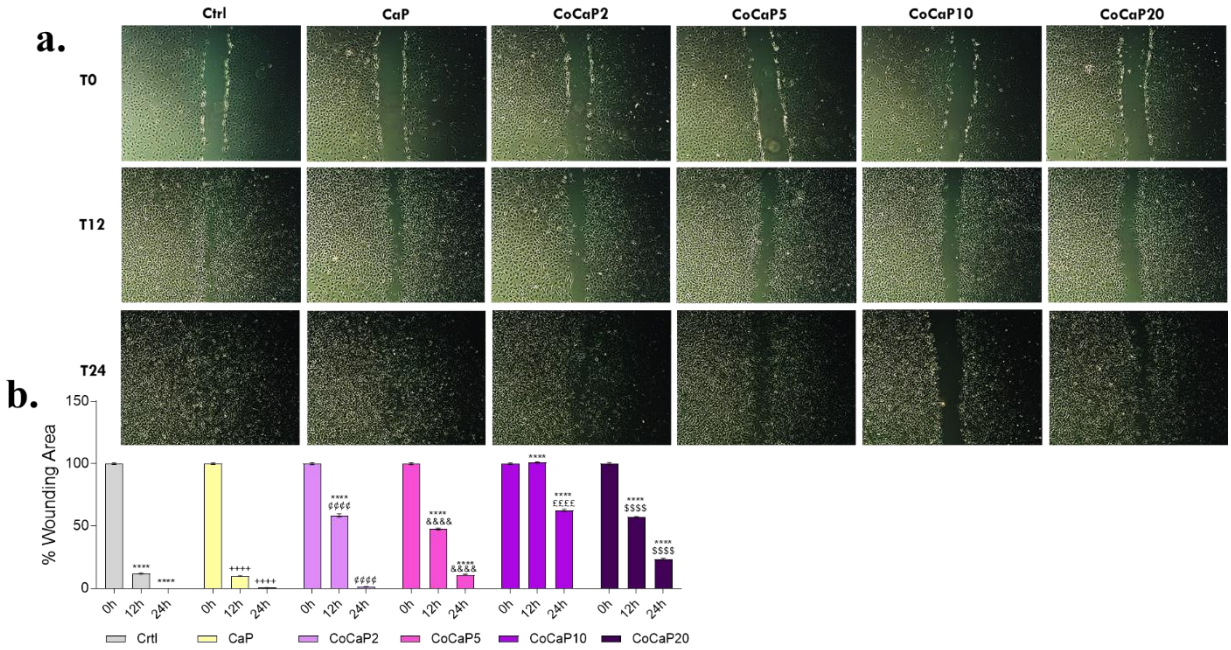

Figure 2. a. The cell regeneration effect of treatments with Ctrl (conventional medium), CaP, CoCaP2, CoCaP5, CoCaP10, and CoCaP20 was measured by a wound-healing assay. **b.** Quantification Wounding area. **b.** The wound area was estimated by calculating the cell-free area in captured images using the ImageJ software (NIH, Bethesda, MD)**.** The migration rate is expressed in percentage as the change in the wound area over time, the scratch area at time point 0 hours was set to 100%, and the other ones are represented as wound closure expressed as the remaining area uncovered by the cells in percentage. In the 12-hour treatment, only CaP showed comparable regeneration to Ctrl. At 24 hours' treatment, CaP and CoCaP were equivalent in regeneration when compared to Ctrl. The other groups showed regeneration, but lower than Ctrl.

The bacteriological test reports the inhibition effect of the materials in contact with the bacteria (**Figure 3**), it is possible to obtain the inhibition halo in the CoCaP20 material, a relationship can be made, that as the concentration of cobalt increases, there is an increase in the inhibition effect of bacteriological proliferation.

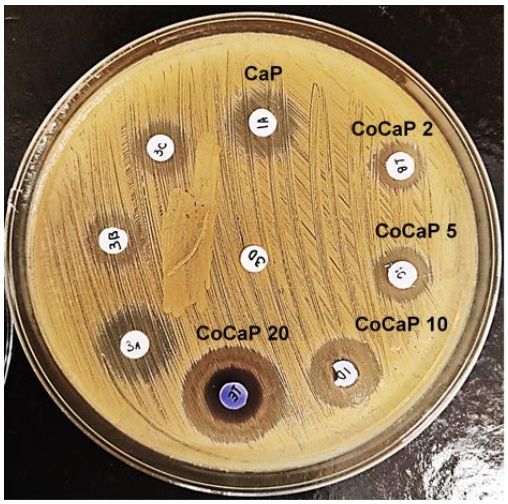

Figure 3. Discs of the materials in contact with the bacteria, inhibition halos are visible as the cobalt concentration increases.

Capitulo 5

Artigo 2: Cobalt-doped monetite induces biomimetic hypoxia and rapidly camouflages bone healing environment

Artigo submetido e em revisão

Cobalt-doped monetite induces biomimetic hypoxia and rapidly camouflages bone healing environment

Gerson Santos de Almeida[1], Thais Silva Pinto[1], Luísa Camilo Suter[1], Geórgia da Silva Feltran[1], Maria Gabriela Jacheto Carra[1], Paula Bertin de Morais[1], Diego Rafael Nespeque Corrêa[2], Margarida Juri Saeki[1], Paulo Noronha Lisboa Filho[3], Willian Fernando Zambuzzi[1].

[1]Laboratory of Bioassays and Cellular Dynamics, Department of Chemical & Biological Sciences, Institute of Biosciences, UNESP: São Paulo State University, Botucatu, São Paulo, 18618-970, Brazil.
[2]Laboratory of Anelasticity and Biomaterials, Department of Physics and Meteorology, School of Sciences, São Paulo State University - UNESP, Bauru, São Paulo, 17033-360, Brazil
[3]Department of Physics, School of Sciences, UNESP: São Paulo State University, Bauru, São Paulo, 17033-360, Brazil.

[#]Corresponding author:
Prof. Dr. Willian F Zambuzzi
UNESP - Campus de Botucatu - Instituto de Biociências
Rua Profª. Drª. Irina Delanova Gemtchujnicov, s/nº
18618-693 – Botucatu-SP - Brazil

e-mail: w.zambuzzi@unesp.br
Phone: +55-14 38800599
Fax: +55-14 3880 0573

Abstract

To address the need for a novel biomimetic material able to camouflage bone healing microenvironment, our proposed solution involves the synthesis of cobalt-doped monetite (CoCaP). The samples underwent a thorough structural analysis using various techniques, including X-ray diffraction, Fourier transform infrared spectroscopy, Raman spectroscopy, scanning electron microscopy, energy dispersive X-ray spectroscopy, X-ray photoelectron spectroscopy, and porosity and surface area analysis via BET. The outcome of these analyses effectively validated the synthesis's success and revealed distinct structural alterations resulting from cobalt doping. Crucially, our newly introduced material exhibited no cytotoxic effects on osteoblasts up to 7 days. Furthermore, our investigations demonstrated that CoCaP facilitates the expedited migration of osteoblasts, as observed in wound healing assays. This phenomenon may be linked to an upregulation of cyclin-dependent kinases (CDKs) in response to the material, suggesting a potential association with the dynamic involvement of adhesion-related machinery, including integrin’s, focal adhesion kinase (FAK), and Src. Regarding osteoblast differentiation mechanisms, our data unequivocally indicates a robust stimulus triggering intracellular signaling pathways, resulting in the overexpression of classical transcription factors Runx2 and Osterix in response to CoCaP. Concurrently, we observed extracellular matrix remodeling involving the activity of matrix metalloproteinase 9 (MMP9). In summary, our findings disclose, for the first time, the biological impact of Co-doped monetite on osteoblasts. Notably, cobalt-doped monetite induces biomimetic hypoxia, faithfully mimicking the bone healing environment and significantly enhancing the osteogenic performance of osteoblasts. Co-doped monetite emerges as a biomimetic and "smart" material, showcasing promising applications in the domain of bone development and positioning itself as a viable candidate for exploration in preclinical protocols.

Graphic Abstract

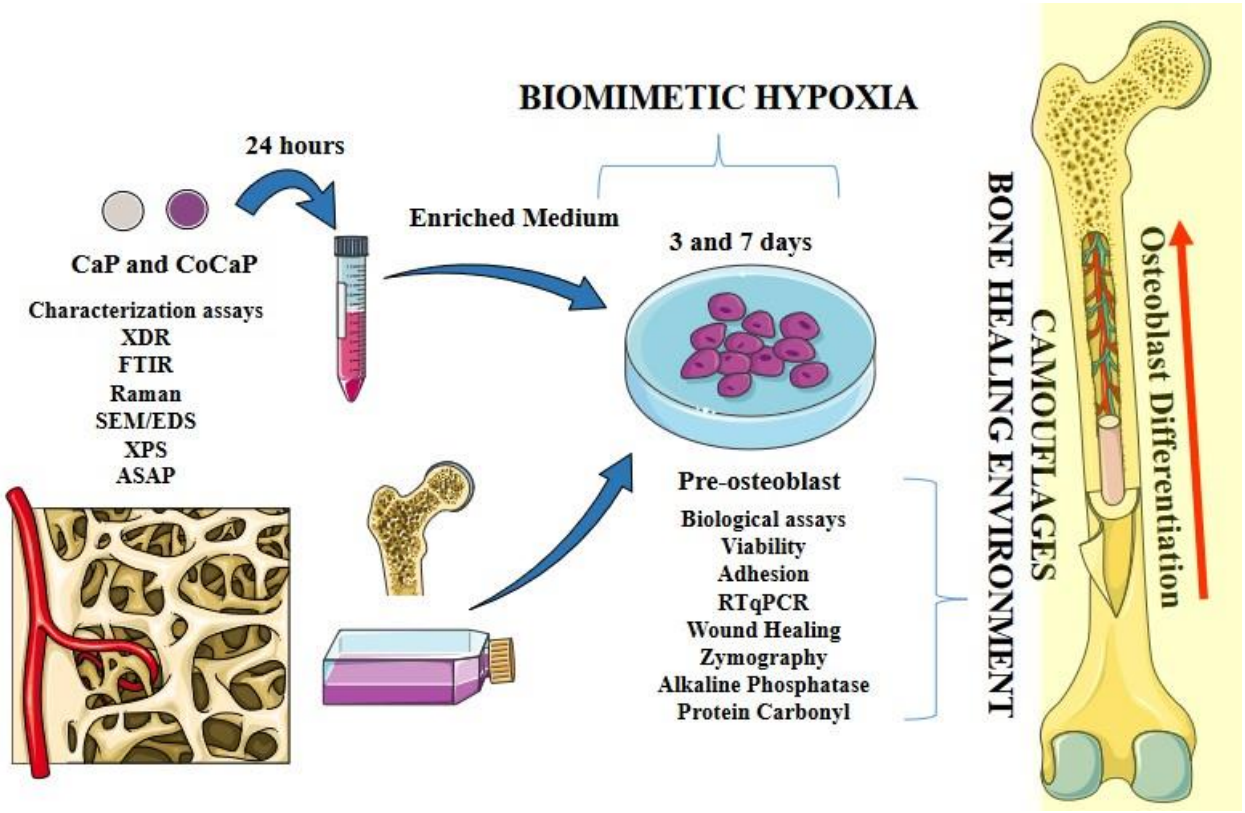

Introduction

Bone loss or damage can arise from various factors, including degenerative diseases, surgical procedures, and trauma, leading to a substantial impact on patients' quality of life (MARSELL; EINHORN, 2011; MARTINO et al., 2015). While bones possess intrinsic self-repair capabilities in non-critical defects, there are instances where complete regeneration is unattainable and requires external stimulation (VO; KASPER; MIKOS, 2012). Millions of individuals with bone defects necessitate bone grafts or substitutes, with the market estimated at over 2.3 billion US dollars in 2015, projected to exceed 3.6 billion US dollars between 2016 and 2024 (WANG; YEUNG, 2017). Autologous bone grafting is considered the gold standard and involves transferring host bone from one site to fill an injured site, but it has limitations such as the need for multiple surgeries, potential morbidity, and limited donor tissue availability (KIM et al., 2009; PAPE; EVANS; KOBBE, 2010; SEN; MICLAU, 2007). More importantly, autografts and allografts demonstrate no therapeutic efficacy in simulating a bone regenerative microenvironment. Innovative technologies in chemistry and biology have been suggested to achieve biomimetic scaffolding capable of mimicking the native site of regenerative microenvironment on various levels (HOLZWARTH; MA, 2011; MA, 2008; SHIN; JO; MIKOS, 2003) . To address these challenges, bone tissue engineering has emerged as a promising therapy, utilizing biomaterials to recreate the microenvironment and stimulate bone regeneration (DANG et al., 2018).

Among the biomaterials calcium phosphates are bioceramics applied in different areas of regenerative medicine (BOULER et al., 2017; CONSTANTZ et al., 1998; SHAH et al., 2023; WOPENKA; PASTERIS, 2005). They can fill bone lesions, coat metallic structures, and compose hydrogels and other scaffolds for bioprinting manufacturers. The most used calcium phosphates are hydroxyapatite and tricalcium phosphate, but these have some disadvantages, such as hydroxyapatite, which is not bioabsorbed by the body, and β-TCP which has poor mechanical properties. In addition, both of them require the use of sintering heat treatments to the structure under these phases (RH. OWEN; DARD; LARJAVA, 2018; SHEIKH et al., 2015c; WOPENKA; PASTERIS, 2005). The monetite or dibasic calcium phosphate anhydrate (DCPA) gained prominence in the last 20 years, which the main characteristics are the property of being bioabsorbed and its easy production by different synthesis routes such as coprecipitation, dehydration, heating, autoclaving, hydrothermal treatment, electrochemical electromagnetic, ultrasonication and others (DE ALMEIDA et al., 2023; TAMIMI; SHEIKH; BARRALET, 2012; ZHOU et al., 2020).

Different studies have been seeking to understand the properties of monetite for bone regeneration, among them, Tamimi et al (2010) have explored different experimental models (e.g.

cells, animals, and human) (SHEIKH et al., 2015c; TAMIMI et al., 2008, 2009, 2010; TAMIMI; SHEIKH; BARRALET, 2012) and they results are very promising once it is shown that monetite is bioabsorbed while inducing the formation of new bone in human patients and also in animal tests (TAMIMI et al., 2008, 2010, 2014; TORRES et al., 2015). Moreover, by comparing monetite to hydroxyapatite (gold standard), they showed that the new bone is formed by using monetite as primary materials for cells, and the formed bone is resistant enough to support the application of titanium implants, well supporting this, showing that it is an excellent material for future clinical practices (TAMIMI et al., 2010).

Although biomimetic bone scaffolds have been developed, their ability to robustly regenerate high-quality bone remains a challenge. In this way, we have over the last years been seeking to optimize the properties of the monetite looking for generating more biomimetic materials and its combination with cobalt during the syntheses seems optimize the capacity of monetite to camouflage the natural bone healing regeneration microenvironment. Bone defect healing is a complex process involving numerous cellular signaling pathways mediated by multiple factors, including hypoxia (HUNG et al., 2012; LI; WANG, 2014; YU et al., 2019). In this study, cobalt was chosen for its ability to induce hypoxia in cells and we have shown previously its capacity in stimulating bone cells (DE ALMEIDA et al., 2023). Therefore, based on these statements, we propose a route of synthesis of cobalt-doped monetite, which was extensively characterized and fully explored biological aspects by evaluating cell viability, adhesion, proliferation, and on the expression of osteogenic gene markers. Taken the data into account, the cobalt-doped monetite is a novel material able to improve the delivery of soluble signals to the bone defect sites and further camouflaging an active bone healing microenvironment with potential to facilitate bone regeneration.

METHODS

Route of monetite synthesis

The coprecipitation method followed that described by Almeida 2023 (DE ALMEIDA et al., 2023): Dibasic Sodium Phosphate (Na_2HPO_4, Sigma-Aldrich, 99%), Calcium Chloride ($CaCl_2$, Sigma-Aldrich, 97%) and Cobalt Chloride ($CoCl_2$, Sigma-Aldrich, 99%). Firstly, the Calcium Chloride and Cobalt Chloride were dissolved at 50 mmol/L under $Co^{2+}/(Co^{2+}+Ca^{2+})$ nominal ratio of 2 mol% in the water (18.2 mΩ cm) and added at a rate of 1 drop per second into the Dibasic Sodium Phosphate aqueous solution. The pH in the end of precipitation was $5.8 \leq pH \leq 6.5$. After dripping, the suspension was homogenized for 30 minutes in a magnetic stirrer and centrifuged for 15 minutes at 4000 rpm. The solid was suspended in water, then stirred on an orbital tube shaker

for one hour, centrifuged again and finally dried in an oven at 80ºC, obtaining the final product as powder. The samples were named CaP: Monetite and CoCaP: Co-doped Monetite.

Fourier transform infrared spectroscopy (FTIR)

The infrared spectroscopy technique was employed to identify the functional groups of the material using a Nicolet Nexus 670 (Thermo, USA) spectrometer. The samples were prepared as 200 mg KBr pellets containing 2% of the samples. The analysis was carried out in the transmittance mode with 4 cm^{-1} of resolutions and the spectra are averages of 200 scans.

Raman spectroscopy

Powdered samples were analyzed with Raman microscope (Renishaw Inc., Hoffman Estates, IL) equipped with a 514.5 nm laser line, 1800 lines/mm diffraction grating, 10 s acquisition time, laser power attenuated to 10%, and a 50× (NA = 0.75) dry objective (Leica Microsystems). This technique provides the Raman bands, which also allows to detect the molecular vibrations of the samples. Therefore, FTIR and Raman spectroscopy might be considered complementary techniques to evaluate the molecular structure of the compounds of the samples.

X-ray photoelectron spectroscopy (XPS)

The surface elemental composition of the materials was determined by XPS. The data were collected on a Thermo Fisher Scientific K-Alpha X-ray excited photoelectron spectrometer using AlKα radiation (1486.6 eV). With a beam of 300 µm diameter, three distinct regions were analyzed in each sample. In each region, Survey spectra were acquired - for semi-quantitative determination of the elements present in the sample, and high-resolution ones for the elements Calcium, Phosphorus, Cobalt, and Oxygen. The data were analyzed with Thermo Advantage V5.9925 software.

X-ray diffraction (XRD)

XRD patterns were collected using a Rigaku diffractometer (DMax 2100PC), employing Ni-filtered CuK_α radiation (λ = 1.5406 Å; 40 kV; 15 mA), in Bragg-Brentano configuration, under continuous scan mode, at $4^o min^{-1}$ and a step size of 0.04º. The peaks were indexed using Search-Match software (Malvern Panalytical) and PDF-2 database (ICSD, 2003) (ALLMANN; HINEK, 2007; BELKLY et al., 2002; HELLENBRANDT, 2004; ZAGORAC et al., 2019). Rietveld method (GSAS software) with the EXPGUI interface was used for the structural refinement to obtain cell parameters and crystalline information. The refinements were carried out with a standard Y_2O_3 sample for instrumental contribution, using the Pseudo-Voigt, Chebyshev, and March-Dollase

functions for profile, background, and preferred orientation adjustments, respectively. The crystallite size was calculated using Scherrer and Williamson-Hall equations from the FHWM (Full Width at Half Maximum) of the diffracted peaks, as detailed by Kaygili et al. (2017) (KAYGILI et al., 2017). The details of crystallographic datasheets of monetite and hydroxyapatite used in the refinements as well as the refinement data can be found in the supplementary material.

Porosity and surface area evaluation

The measurements for surface area and porosity of the powder samples were carried out by N_2 adsorption at 77 K (B.E.T Method) in Micromeritics equipment, model ASAP 2000. Before analysis, the materials were heat treated at 80ºC under vacuum until reaching a pressure <10mmHg and a change rate of less than 5μmHg/min over the material when the sample holder is isolated from the vacuum system. The isotherm was evaluated by measuring the volume of N_2 adsorbed at 77K on the solid under increasing relative pressures (P/P_0) until saturation ($P_0 \cong 1$). Once this condition is reached, the reverse process began in which the pressure gradually decreased. The adsorption isotherm profile registered at each increment of pressure until saturation and the hysteresis between that of the reverse path provide information about the texture of the solid. The data of the adsorbed N_2 volume in the relative pressure (P/P0) range between 0.03 and 0.20 (registered under increasing P/P_0) was used to calculate the surface area (S_{BET}) and the BJH method was used for the analysis of the pore size distribution (with data under decreasing P/P_0).

Scanning electron microscope (SEM)

SEM analyses were performed using a JEOL model JSM-6010 Scanning electron microscope, operating with an acceleration voltage of 10 kV and a secondary electron detector. The semi-quantitative EDS analysis was performed in the same equipment for Ca, P, O, and Co chemical elements using the same acceleration voltage (10 kV).

Osteoblast cultures

MC3T3-E1 cell line (pre-osteoblast, subclone 4) cultures were maintained using Alpha-MEM containing antibiotics (100U/mL penicillin, 100 mg/mL streptomycin) and supplemented with 10% fetal bovine serum (FBS). The cultures were maintained in an incubator at 37°C, with 95% humidity and 5% CO_2. To test the materials, sub confluent cultures were challenged with a cell culture medium enriched with biomaterial (0.2g/mL), according to ISO 10993-12:2016. Previously, the FBS-free medium was enriched for up to 24 hours with CaP and CoCaP to prepare the conditioned medium. After that, FBS 10% was added and further used to challenge pre-

osteoblasts. Osteoblasts were cultivated in different conditions: Control (Ctrl, Alpha-MEM medium); O.M. (Osteogenic Medium); CaP and CoCaP conditioned medium.

Osteogenic phenotype acquisition

To induce osteoblast differentiation, osteoblasts were cultured ($50x10^4$ cells/mL) up to 48 hours and in semiconfluence they were treated with ß-Glycerophosphate (10 mM) + Dexamethasone (0.03 g/mL) + Ascorbic Acid (50 μg/mL) (Sigma-Aldrich) culture with 10% FBS along the experimentation. This is important to mention that this treatment was used as a positive control.

Osteoblast toxicity was evaluated by MTT assay

Pre-osteoblasts were seeded into 96-well plates, and next, they were subjected to the CaP-enriched media for up to 24 and 72 hours. Therefore, the cell culture medium was removed, and MTT solution (1 mg mL^{-1}) was added to the cultures up to 3 hours when the MTT-containing medium was removed, and 1 mL of DMSO was added to solubilize the blue dye formed by viable cells. The absorbance was then measured at 570 nm using a microplate reader (SYNERGY-HTX multi-mode reader, Biotek, USA).

Osteoblast adhesion assay

Osteoblast adhesion was evaluated by the crystal violet assay. The cells were conventionally maintained in culture, trypsinized and seeded in 96-wells microplates at 100×10^3 cells/mL (100 μL/well) to evaluate the influence of CaP-enriched media on cell adhesion. For each group of materials, a control group was used, which was cultured with the conventional medium without any other treatment. After 24 and 72h of challenge with the materials, cells were properly stained, and the number of adherent cells was estimated by incorporating the crystal violet dye, as detailed earlier elsewhere (BEZERRA et al., 2017; DA COSTA FERNANDES et al., 2018a). Absorbance was measured at 540 nm using a microplate reader (SYNERGY-HTX multimode reader, Biotek, USA).

Wound healing assay

The cell migration was estimated by using a scratch assay, as performed earlier (PINTO et al., 2022). The scratch assay minimally estimates the cell migration and further tissue regeneration. Briefly, the cells were cultured in 12-well plates at 5×10^4 cells/cm^2, and after fully confluent cultures, an introduced area was cleared using a pipet tip and then a monitoring of the healing and the migration of the cells up to both 12 h and 16 h (PINTO et al., 2022). Thereafter, the cultures were subjected to fixation with 4% PFA and stained with hematoxylin-eosin. In the analysis of the wound healing *in vitro*, the healing area was measured in an inverted microscope with a coupled

digital camera (Zeiss) and the acquired images analyzed using the ImageJ software (NIH, Bethesda, MD).

RTqPCR

To evaluate the molecular mechanism related with the adaptation to each CaP's, the pre-osteoblasts were newly subjected to each CaP-conditioned medium up to 3 and 7 days, when the cells were harvested and total RNA extracted using Ambion TriZOL Reagent (Life Sciences - Fisher Scientific Inc., Waltham, MA, USA) and treated with DNAse I (Invitrogen, Carls, CA, USA), as used and described earlier. According to the manufacturer's instructions, cDNA synthesis was performed with the High-Capacity cDNA Reverse Transcription Kit (Applied Biosystems, Foster City, CA, USA). Real-time PCR was performed on 10 μL containing PowerUpTM SYBRTM Green Master Mix 2x (5 μL) (Applied Biosystems, Foster City, CA, USA), 0.4 μmolL-1 of each primer, 50 ng of cDNA and nuclease-free H_2O. Results were expressed as relative amounts of transcripts using GAPDH and 18S as reference genes (housekeeping gene) using the cycle threshold (ct) method. Primers and race details are described in **Table 1**.

Table 1. Primers sequences and details of the cycle conditions.

Gene (ID)	Primer	5'-3' Sequence	Reaction condition
Runx2 (12393)	Forward	GGACGAGGCAAGAGTTTCA	95°C - 15s; 60°C - 30s; 72°C - 60s
	Reverse	TGGTGCAGAGTTCAGGGAG	
Osterix (170574)	Forward	CCCTTCCCTCACTCATTTCC	95°C - 15s; 60°C - 30s; 72°C - 60s
	Reverse	CAACCGCCTTGGGCTTAT	
Osteocalcin (12096)	Forward	AGACTCCGGCGCTACCTT	95°C - 15s; 60°C - 30s; 72°C - 60s
	Reverse	CTCGTCACAAGCAGGGTTAAG	
BSP (15891)	Forward	GTACCGGCCACGCTACTTTCT	95°C - 15s; 60°C - 30s; 72°C - 60s
	Reverse	GTTGACCGCCAGCTCGTTTT	
Integrin α1 (109700)	Forward	TATCCTCCTGAGCGCCTTT	95°C - 15s; 60°C - 30s; 72°C - 60s
	Reverse	TGGCCTTTTGAAGAATCCAA	
Integrin β1 (16412)	Forward	CTGATTGGCTGGAGGAATGT	95°C - 15s; 60°C - 30s; 72°C - 60s
	Reverse	TGAGCAATTGAAGGATAATCATAG	
Fak (14083)	Forward	TCCACCAAAGAAACCACCTC	95°C - 15s; 60°C - 30s; 72°C - 60s
	Reverse	ACGGCTTGACACCCTCATT	
Src (20779)	Forward	TCGTGAGGGAGAGTGAGAC	95°C - 15s; 60°C - 30s; 72°C - 60s
	Reverse	GCGGGAGGTGATGTAGAAAC	
Cofilin (12631)	Forward	CAGACAAGGACTGCCGCTAT	95°C - 15s; 60°C - 30s; 72°C - 60s
	Reverse	TTGCTCTTGAGGGGTGCATT	
Rank-L (21943)	Forward	CGCTCTGTTCCTGTACTTTCGAGC	95°C - 15s; 60°C - 30s; 72°C - 60s
	Reverse	TCGTGCTCCCTCCTTTCATCAGGTT	
HIF1α (15251)	Forward	CATAAAGTCTGCAACATGGAAGGT	95°C - 15s; 60°C - 30s; 72°C - 60s
	Reverse	ATTTGATGGGTGAGGAATGGGTT	
VEGF (22339)	Forward	TGCAGATTATGCGGATCAAACC	

	Reverse	TGCATTCACATTTGTTGTGCTGTAG	95°C - 15s; 60°C - 30s; 72°C - 60s
Gapdh (14433)	Forward	AGGCCGGTGCTGAGTATGTC	95°C - 15s; 60°C - 30s; 72°C - 60s
	Reverse	TGCCTGCTTC ACCACCTTCT	
ALP (11647)	Forward	GAA GTC CGT GGG CAT CGT	95°C - 15s; 60°C - 30s; 72°C - 60s
	Reverse	CAG TGC GGT TCC AGA CAT AG	
Bmp2 (12156)	Forward	GGT CAC AGC TAA GGC CAT TGC	95°C - 15s; 60°C - 30s; 72°C - 60s
	Reverse	GCT TCC GCT GTT TGT GTT TG	
OPG (21943)	Forward	CAG AGA CTA ATA GAT CAA AGG CAG	95°C - 15s; 60°C - 30s; 72°C - 60s
	Reverse	ATG AAG TCT CAC CTG AGA AGA ACC	
eNOS (18127)	Forward	AAG CCG CAT ACG CAC CCA GAG	95°C - 15s; 60°C - 30s; 72°C - 60s
	Reverse	TGG GGT ACC GCT GCT GGG AGG	
MMP2 (17390)	Forward	AAC TTT GAG AAG GAT GGC AAG T	95°C - 15s; 60°C - 30s; 72°C - 60s
	Reverse	TGC CAC CCA TGG TAA ACA A	
MMP9 (17395)	Forward	TGT GCC CTG GAA CTC ACA CGA C	95°C - 15s; 60°C - 30s; 72°C - 60s
	Reverse	ACG TCG TCC ACC TGG TTC ACC T	
β-Actin (11461)	Forward	TCT TGG GTA TGG AAT CCT GTG	95°C - 15s; 60°C - 30s; 72°C - 60s
	Reverse	AGG TCT TTA CGG ATG TCA ACG	
18S (19791)	Forward	TAG TTG GAT CTT GGG AGC GG	95°C - 15s; 60°C - 30s; 72°C - 60s
	Reverse	TAG AAC CGC GGT CCT ATT CC	
CDK2 (12566)	Forward	TAC CCA GTA CTG CCA TCC GA	95°C - 15s; 60°C - 30s; 72°C - 60s
	Reverse	CGG GTC ACC ATT TCA GCA AA	
CDK4 (12567)	Forward	TCG ATA TGA ACC CGT GGC TG	95°C - 15s; 60°C - 30s; 72°C - 60s
	Reverse	TTC TCA CTC TGC GTC GCT TT	
CDK6 (12571)	Forward	CGC CGA TCA GCA GTA TGA GT	95°C - 15s; 60°C - 30s; 72°C - 60s
	Reverse	GCC GGG CTC TGG AAC TTT AT	

Zymography

During the experimental model applied in this study, aliquots of the medium conditioned by CaP's or osteoblasts were harvested to further estimate the activity of matrix metalloproteinases (MMP) using a widely explored gelatin proteolysis-based zymography. Briefly, the samples were centrifuged at 14,000 rpm for 15 min to avoid cell debris, when the protein concentration was determined by the Lowry method (HARTREE, 1972). The same amount of protein was resolved into a 12% polyacrylamide gel containing 4% gelatin. The gelatinolytic activity was evaluated in the bands, thereafter their renaturation using Triton X-100 aqueous solution (2% w/v), incubated for 18 hours in proteolysis buffer (Tris – $CaCl_2$) at 37ºC and then stained with Coomassie Blue R-250 dye solution 0.05% for 3 h, when the gels were washed in solution containing 30% methanol (v/v) and 10% glacial acetic acid solution (v/v). The opposite staining was obtained in the gels exactly where it was considered gelatinolytic activity (bands) of metalloproteinases 2 (MMP2, ~62 kDa) and 9 (MMP9, ~84 kDa), and then they were subjected to the densitometry analysis using software ImageJ (Bethesda, MD, USA), following a previous study (LEFEBVRE; PEETERS-JORIS; VAES, 1991).

Protein Carbonylation

Osteoblasts were grown in such as the other's biological tests and properly harvested for evaluating the protein's carbonylation as an indicator of oxidative stress using the alkaline method as described by Mesquita et al. (2014)(DA COSTA FERNANDES et al., 2021a; MESQUITA et al., 2014). The protein carbonyl concentrations were based on the average absorbance's and the micromolar extinction coefficient of 2,4-Dinitrophenylhydrazine (DNPH) reagent under alkaline conditions (0.022308 μmol cm^{-1} at 450 nm). Carbonylated proteins levels are expressed in nmol of DNPH/mg of protein.

Staining with Alkaline Phosphatase

The pre-osteoblasts were plated ($5x10^4$ cells/ml) in 24-well plates and were treated in semi-confluence with the medium's conditioned by CaP's for up to 3 and 7 days. The medium was changed every 3 days. Coloration with ALP was performed as recommended by the manufacturer (SIGMAFAST BCIP/NBT tablet). The wells were washed with PBS and the plate was photographed using an inverted microscope (Zeiss, Germany).

Statistical analysis

Statistical analyzes were performed using GraphPad Prism 7 software (GraphPad Software, USA), by variance analysis (two-way ANOVA) and with Turkey's correction posttest or non-parametric analysis. The p value <0.05 was considered statistically significant.

RESULTS

Synthesis and characterization of Co-doped monetite

During the synthesis of monetite and cobalt-doped monetite, the pHs of solutions and suspensions were modified as shown in **Table 2**. The final pH is around 6, which explains why the stoichiometric precipitation does not occur. The results of the XPS and EDS semi-quantitative analysis corroborate this fact, as shown later.

Table 2. Variations of pH during the synthesis

	pH			
Material	Na_2HPO_4	$CaCl_2$	$CaCl_2 + CoCl_2$	CaP
Monetite	8.86	5.80	5.80	6.00
Co-doped Monetite	8.86	-	7.18	6.46

The FTIR analysis depicts characteristic bands of apatite as it was described in previous study (KAYGILI et al., 2017; SALIMI; JAVADPOUR, 2012; ZHOU et al., 2021a). The spectra shown in **Fig.11a** exhibits P-O stretching peaks at 1125, 1048, and 998 cm^{-1}, and the band observed at 559 cm^{-1} can be associated with the O-P-O(H) bending mode. In **Fig.1b**, monetite can be easily distinguished from other CaP phases such as hydroxyapatite, TCP, and Brushite by peaks detected by Raman spectroscopy due to its unique crystal structure (DESAI; BHADURI; TAS, 2008; WOPENKA; PASTERIS, 2005). Different from HA, monetite has no hydroxyl ion, and as observed in Brushite, monetite also has no H_2O in its crystal structure, i.e. no peak at about 3,500 cm^{-1} originated by O-H vibrations are observed. A strong peak in the 988 cm^{-1} region of tetrahedral P-O bond vibration and a peak in the 900 cm^{-1} region due to P-O bonds that are in the P-O-H^+ configuration and can only be seen in monetite (DESAI; BHADURI; TAS, 2008; GHINA IMANIYYAH; SUNARSO; HERDA, 2022; ZHOU et al., 2020) can be observed.

The XPS survey was used to verify the surface's chemical composition through atomic content percentage. The XPS spectrum of the samples is shown in **Fig.1c**. The results demonstrated that the photoelectron peaks of calcium, phosphorus, and oxygen are evident in **Fi.1c (A)**, due to the monetite presence (LEBUGLE; SALLEK; TAI TAI, 1999). **Fig.1c. (B)** shows us, in addition to the presence of monetite, the cobalt in approximately 798 eV (SEMAN; AZAM; MOHAMED, 2016), which was added to the material. According to the XPS survey, the percentage of Co is around 0.65.

Figure 1d exhibits the diffraction pattern of cobalt-doped monetite. Note that they are all predominantly single-phase consisting of monetite with the unit formula of $Ca_xCo_{1-x}HPO4$ with triclinic structure (space group P1), indexed as ICSD 10-503. The amount of substitutional element does not induce phase transformation after the synthesis by this route. This finding was confirmed by the Rietveld refinement, which indicated the presence of monetite (100%) in CaP, and the presence of monetite (~ 95%) and hydroxyapatite (~ 5%) in the CoCaP. The structural parameters shown in **Figure 1,e** indicate that the structural parameters are crystallite sized and it affects the amount of Co. The α and γ angles increased with the amount of Co, while the β angle presented a step decay. The cell parameters (a, b, and c) reduced almost linearly with the Co doping, producing a shortening of the triclinic cell volume. The reduction in lattice parameters is expected since the

ionic radius of Co^{2+} (0.65 Å) is smaller than that of Ca^{2+} (1.00 Å). In other words, if changes in the lattice parameter were observed this indicates that cobalt was incorporated to some extent, even though it may not be proportional to the amount of cobalt added. The incorporated amount cannot be estimated using Vegard's law, as the variation of the lattice parameters may not be linear with the incorporated amount because the crystalline structure of monetite is complex (triclinic) and can affect parameters and angles in a non-linear way. However, it is possible to say that cobalt was incorporated to some extent by each addition.

Lastly, the Co incorporation promoted an increase of the crystallite size from around 30 nm to more than 70 nm in both curves (Scherrer and Williamson-Hall), and it corroborates with others (CHÉRIF et al., 2022; RABIEI et al., 2020). Additional information about the XRD parameters can be found in the supplementary material.

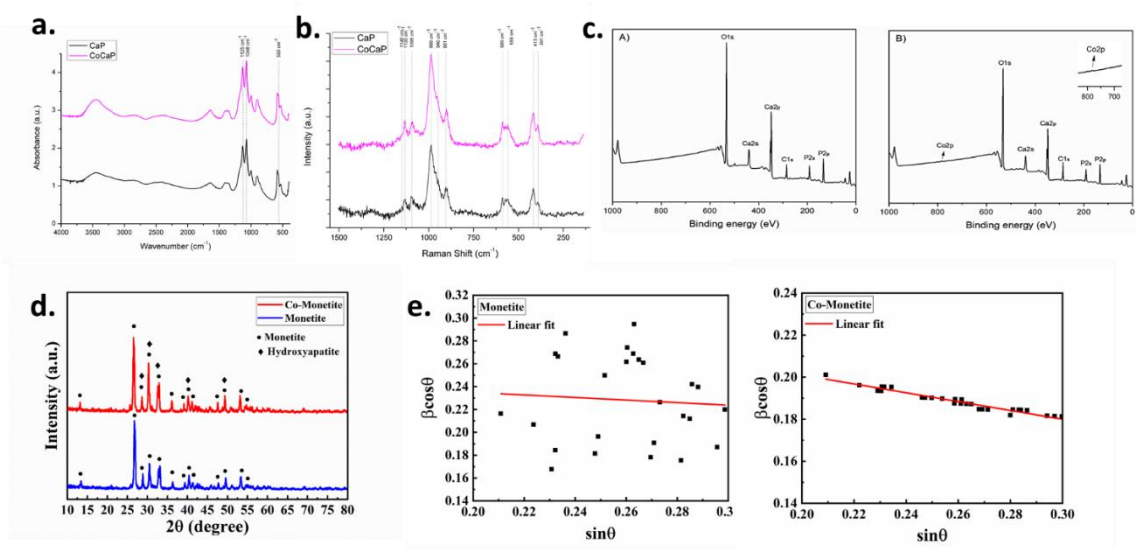

Fig.11. **a.** FTIR spectra and **b.** Raman spectra of monetite and cobalt-doped monetite, obtained by coprecipitation method. **c.** XPS survey spectra of the samples; **A.** Monetite; **B.** Co-doped Monetite. **d.** XRD patterns of cobalt-doped monetite, obtained by coprecipitation method. **e.** Cell parameters and crystallite size (D) of co-doped monetite, determined by Rietveld refinement.

Porosity (Pore Type and Distribution)

Fig.2a shows the N2 adsorption isotherms at 77 K on Monetite and Co-doped Monetite samples. Braunauer, Deming, and Teller (1982) proposed the classification of isotherm types, which associates the isotherm profile with the shape and pore sizes distribution in the solid (BARDESTANI; PATIENCE; KALIAGUINE, 2019; HAUL, 1982; WEBB; ORR, 2000). The obtained isotherms indicate that the samples can be classified like Type II, it being non-porous solids or solids with pores in the range of 2.5 to 100 nm (mesopores) or diameter greater than 50 nm (macro-pores).

The hysteresis observed in the samples Type H3, observed in materials with pores in wedge, cone, and/or parallel plate formats, which can be corroborated with the results obtained by

SEM, in which it was possible to visualize the plate format of the monetite. The analysis of the isotherm data by the BJH method allows one to obtain the average pore size distribution in the samples which can be appreciated in the plot of dV/dD values as a function of pore diameter (**Fig.2b)**.

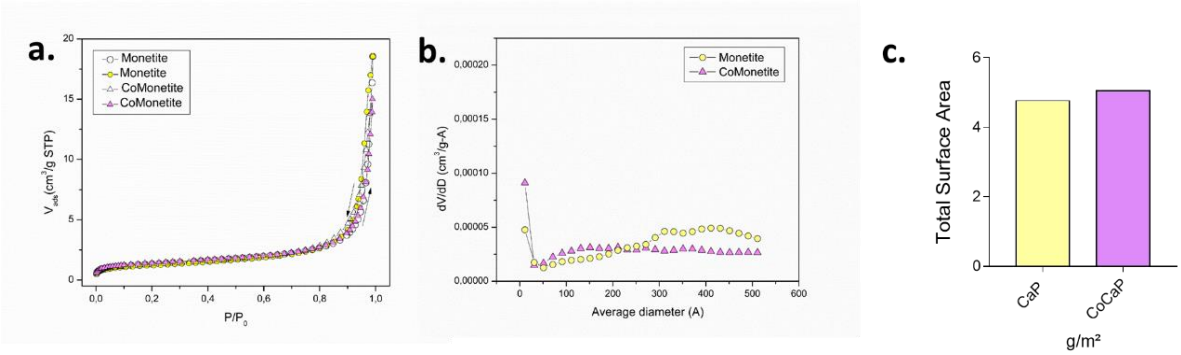

Fig.2 – **a**. N2 adsorption isotherms at 77K on Monetite and Co-doped Monetite (filled markers: adsorption branch and open markers: desorption branch). **b.** Pore distribution in the Monetite and Co-doped Monetite samples

Non-porous materials with a fairly wide distribution for monetite and Co-doped Monetite samples were produced. Despite the few pores they have, it can be noticed the presence of mesopores (2.5 to 100 nm) and macro-pores (diameter greater than 50 nm) and that Co seems to decrease porosity. Also, there is evidence of the presence of micropores (<50 A) in the samples analyzed. Important, the surfaces area was analyzed and the results are summarized in **Table 3**. The addition of Co does not affect the surface area.

Table 3 - SBET specific area (m^2/g) of Monetite and Co-doped Monetite.

Sample	**m_i (g)** (before treatment at 80ºC)	**m_f (g)** (after treatment at 80ºC)	**S_{BET} (m^2/g)**	**$V_{total\ pore}$ (CPPT) (cm^3/g) (d<683,9A)**	**$V_{total\ micropore}$ (CPPT) (cm^3/g)**	**Average Pore Diameter (A)**
Monetite	0.6913	0.6498	4.8±1.0	18.54	0.000020	125
Co doped Monetite	0.6877	0.6854	5.0±1.0	15.01	0.000021	112

The SEM micrographs and the quantification performed by EDS in **Fig.** clearly illustrate the leaf-like morphology of the Monetite, being it already described by other authors (KAYGILI et al., 2017; MOTAMENI; ALSHEMARY; EVIS, 2021; TAMIMI et al., 2010; TORRES et al., 2015). The micrographs show that the morphology of the material change with cobalt addition, as the apparent size of the particles increases slightly. The mapping analysis showed that all the elements were found in a uniform distribution, not concentrated at a specific region of the material.

The (Ca+Co)/P ratio of 1 was found (**Table 4**), which characterizes the monetite. Note that the amount of cobalt incorporated was not proportional to the nominal substitutive amount of cobalt.

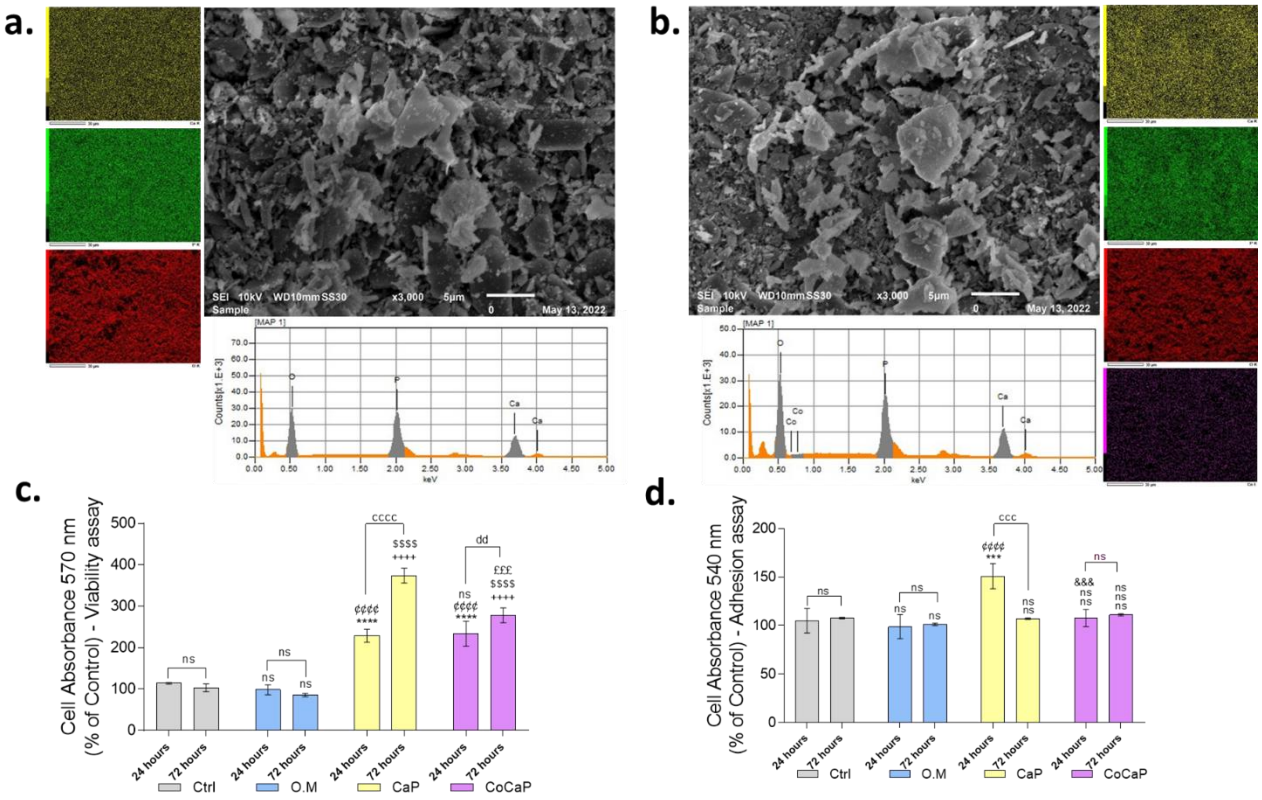

Fig.3. **SEM micrographs of cobalt-doped monetite, obtained by coprecipitation method and semiquantitative analysis and elemental distribution of cobalt-doped apatite by EDS**. **a.** Monetite; **b.** Co-doped Monetite. **c.** The cells showed no reduction in viability when compared to Ctrl. The CaP and CoCaP groups showed a statistically significant increase when compared to (****p <0.0001and $^{++++}$p < 0.0001) and O.M ($^{¢¢¢¢}$p <0.0001and ($^{\$\$\$\$}$p <0.0001) in both treatment times and the CoCaP ($^{£££}$p 0.0001) group showed a difference when compared to CaP. CaP (^{cccc}p <0.0001) and CoCaP (^{bb}p = 0.0042) also showed differences when compared to their respective treatments with time. **d.** All groups showed no reduction in Crystal Violet staining. CaP-3 days showed a statistically significant increase when compared to Ctrl (***p = 0.0001), O.M ($^{¢¢¢}$p <0.0001, and CoCaP ($^{\&\&\&}$p = 0.0003). When compared to the 7-day treatment, a significant difference was also found in CaP (^{cp} = 0.0003). Replicates: n = 6

Table 4. EDS semiquantitative analysis of cobalt-doped monetite, obtained by coprecipitation method.

Material	Ca/(Ca+Co)	(Ca+Co)/P	(Ca)/P
Monetite	1.00	1.062	1.062
Co-doped Monetite	0.0029	1.067 (1.064)	1.064

Biological characterization

Using the conditioned medium by the obtained materials, the cells showed no cytotoxicity (MTT assay – **Fig.3c**) when compared to the control group in both treatment times (24 or 72 hours). The OM group does not show significant differences when compared to the control. In the groups conditioned by the materials, CaP in the 24-hour treatment shows increased cell viability when compared to the Ctrl (****p <0.0001) and O.M (¢¢¢¢p <0.0001) groups, there was no significant difference with the CoCaP group. CoCaP shows a similar response profile in the 24-hour treatment, with increased viability when compared to Ctrl (****p <0.0001) and O.M ($^{¢¢¢¢}$p <0.0001). Considering a long-term treatment (72-hours) a similar response profile was followed: The CaP group showed an increase in viability when compared to the Ctrl ($^{++++}$p < 0.0001), O.M ($^{\$\$\$\$}$p <0.0001, and CoCaP ($^{£££}$p 0.0001) groups. CoCaP also showed an increase compared to Ctrl ($^{++++}$p <0.0001) and O.M ($^{\$\$\$\$}$p <0.0001). Considering the comparison among groups, there was no difference in the control and O.M. groups, but the CaP group shows differences (^{cccc}p<0.0001), increasing viability in 72 hours when compared to 24 hours. The CoCaP group also showed differences in viability (^{bb}p = 0.0042) when compared 72 hours with 24 hours treatments.

The crystal violet assay, here used to know about the cell adhesion, shows there is no changes (**Fig.3d)** in dye concentration when compared to the Ctrl group. The CaP group showed significant differences compared to the Ctrl (***p = 0.0001), O.M ($^{¢¢¢¢}$p <0.0001, and CoCaP ($^{\&\&\&}$p = 0.0003) groups in the 24 hours' treatment, and also shows differences when compared to the CaP treated for 72 hours (^{ccc}p = 0.0003).

Thereafter, considering the experiment to mimic the wound healing, the **Fig.4** brings evidences of cell proliferation and migration. The O.M group shows significant differences when compared to the control group, not decreasing the injured area when compared to the Ctrl (****p <0.0001) and other groups (CaP $^{¢¢¢¢}$p <0.0001, CoCaP $^{¢¢¢¢}$p <0.0001), and also when compared to the O.M group treated for 16 hours (^{b}p = 0.0182). The CaP group showed increased cell regeneration/proliferation when compared to the Ctrl (***p = 0.0001), O.M ($^{¢¢¢¢}$p <0.0001, and CoCaP ($^{\&\&\&\&}$p <0.0001) groups. The CoCaP group showed an increase in cell regeneration/proliferation when compared to the Ctrl (**p = 0.0017).

At 16 hours, the Ctrl group shows an increase in cell proliferation when compared to the Ctrl 12 hours group (^{aaaa}p <0.0001), showing that regeneration increases with time. The O.M.

group showed the same profile as the 12-hour treatment, showing a decrease in regeneration when compared to the Ctrl ($^{++++}$p <0.0001), maybe because the cells are under differentiation process. The CaP group does not present statistically significant differences when compared to the Ctrl group but presented a difference when compared to the O.M group ($^{\$\$\$\$}$p <0.0001) and the CaP 12 hours' group (^{cccc}p <0.0001), showing that regeneration continued. The CoCaP group presented differences when compared with all the Ctrl ($^{++++}$p <0.0001), O.M ($^{\$\$\$\$}$p <0.0001), and CaP ($^{££££}$p <0.0001) groups, and also with the 12-hour CoCaP group (^{dddd}p <0.0001).

CoCaP promotes osteoblast proliferation

The Cdk2, Cdk4, and Cdk6 genes were evaluated (**Fig.4)**. Firstly, the Cdk2 expression in the 3-day treatment there were no differences in expression between the groups and when compared to Ctrl and the others groups (**Fig.4c)**. At 7 days, Cdk2 expression was modulated only in the CoCaP group, being significantly increased when compared to the Ctrl ($^{++++}$p <0.0001), O.M ($^{\$\$\$\$}$p <0.0001) and CaP ($^{££££}$p <0.0001) groups, and when compared to the 3-day CoCaP (^{dddd}p = <0.0001). Considering Cdk4 expression (**Fig.4d**), in the 3 days' treatment there were differences in the expression in CaP (*p = 0.0115) and CoCaP (*p = 0.0326) groups when compared to the Ctrl group. In the 7-day treatment, there were no differences between the groups when compared to Ctrl, only a significant reduction in CaP ($^{£}$p = 0.0121) expression when compared to CoCaP. Comparing the groups in the two treatment times, the CaP group (^{cccc}p <0.0001) showed a reduction in its expression with time. Cdk6 CaP shows differences when compared to Ctrl (****p <0.0001) and O.M ($^{¢¢¢¢}$p <0.0001), and the CoCaP group showed differences when compared to O.M ($^{¢}$p = 0.0282) and CaP ($^{\&\&\&}$p = 0.0002) (**Fig.4e)**.

In the 7-day treatment, only the CoCaP group showed an increase in expression when compared to the Ctrl ($^{++++}$p <0.0001), O.M ($^{\$\$\$\$}$p <0.0001) and CaP ($^{££££}$p <0.0001) groups. Comparing the groups in both experimental times, the CaP group (^{cccc}p <0.0001) showed a reduction of its expression with time, and the CoCaP group (^{dddd}p <0.0001) showed an increase with time.

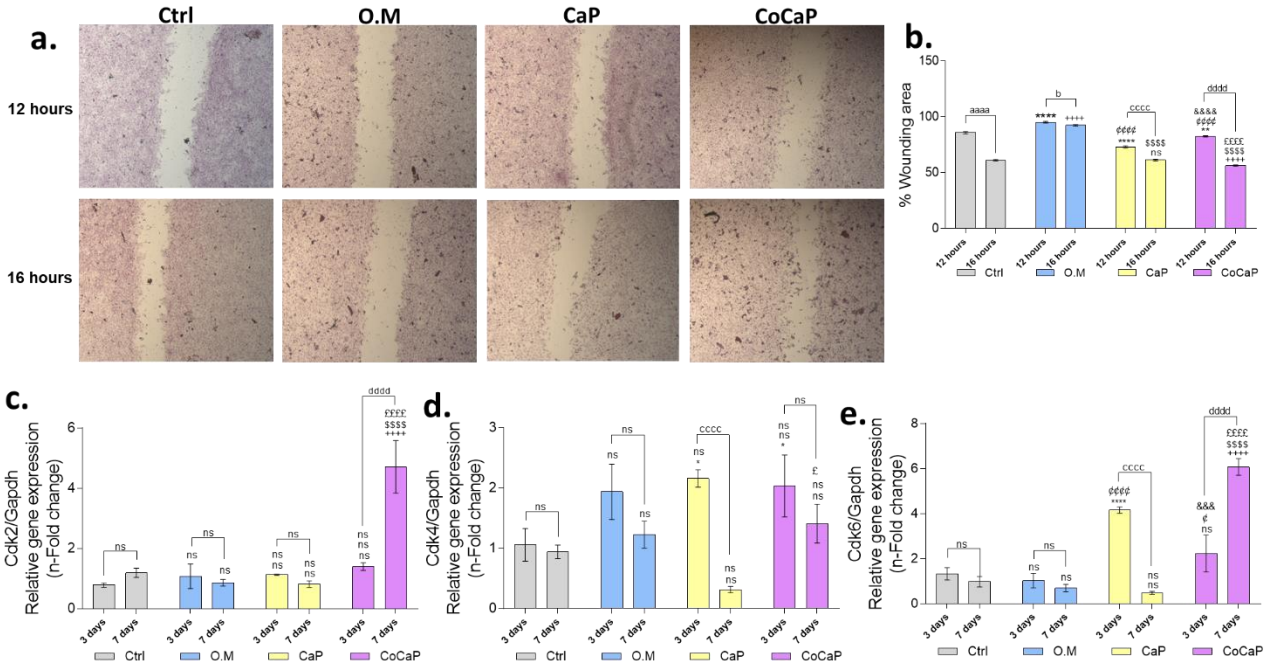

Fig.4. a. The wound healing is affected by the proliferative phenotype of osteoblasts responding to CoCaP. The cell regeneration effect of treatments with Ctrl (conventional medium), O.M (osteogenic-inducing medium), CaP (Monetite), and CoCaP (Co-doped Monetite) was measured by a wound-healing assay. **b.** Quantification of the wound healing area. The wound healing area was estimated by calculating the cell-free area in captured images using the ImageJ software (NIH, Bethesda, MD)**.** The migration rate is expressed in percentage as the change in the wound area over time, the scratch area at time point 0 hours was set to 100%, and the other ones are represented as wound closure expressed as the remaining area uncovered by the cells in percentage. At 12 hours' treatment: The CaP (***p = 0.0001) and CoCaP (**p = 0.0017) groups showed a reduction when compared to Ctrl, O.M. did not show the same profile. At 16 hours treatment: Only CoCaP ($^{++++}$p <0.0001) showed a statistically significant reduction when compared to Ctrl. **c.** there were no statistically significant differences in the 3-day treatment. In the 7-day treatment, the CoCaP group showed an increase in expression compared to Ctrl ($^{++++}$p <0.0001), O.M ($^{\$\$\$\$}$p <0.0001) and CaP ($^{££££}$p <0.0001). d**.** Cdk4, in the 3-day treatment there were differences in the expression in CaP (*p = 0.0115) and CoCaP (*p = 0.0326) groups when compared to the Ctrl group. In the 7-day treatment, no group showed statistically significant differences. e**.** Cdk6, 3-day treatment, only CaP (****p <0.0001) showed statistically significant differences when compared to Ctrl. At 7-day treatment, CoCaP showed increased expression when compared to Ctrl ($^{++++}$p <0.0001), O.M ($^{\$\$\$\$}$p <0.0001) and CaP ($^{££££}$p <0.0001. Replicates: n = 3. The Gapdh, β-actin, and 18S genes were used as housekeeping genes

Genes involved with osteoblast-mediated osteoclastogenesis.

The absorption of materials by osteoclast is expected for calcium phosphate as monetite. In this way, it was important to measure the capacity of osteoblast in governing osteoclastogenesis when challenged by CoCaP. Firstly, RANKL gene (**Fig.5a**) in the 3-day treatment showed an increase in its expression in the CaP (****p = <0.0001 and $^{¢¢¢}$p = 0.0007) and CoCaP (****p = <0.0001 and ($^{¢¢¢¢}$p = <0.0001) groups when compared to Ctrl and O.M, respectively. The CoCaP group ($^{\&\&\&}$p = 0.0001) showed an increase when compared to the CaP group. In the treatment for 7 days, the O.M ($^{++++}$p = <0.0001) and CoCaP ($^{++++}$p = <0.0001) show increases when compared to the Ctrl group. The O.M and CoCaP ($^{££££}$p = <0.0001) also show increases in expression when

compared to the CaP ($^{\$\$\$\$}$p = <0.0001). Comparing the influence of time on RANKL expression, it was shown that the O.M group (^{bbbb}p = <0.0001) presented an increase in its expression with time, and the CaP group (^{ccc}p = 0.0002) decrease.

Secondly, considering the activity of OPG gene (**Fig.5b**), in the 3-day treatment, only the CaP (*p = 0.0419 and $^{¢¢}$p = 0.0048) showed an increase when compared to the Ctrl and O.M. groups, respectively. In the 7-day treatment, the CoCaP group showed an increase in its expression when compared to the Ctrl ($^{++++}$p = <0.0001), O.M ($^{\$\$\$\$}$p = <0.0001), and CaP ($^{££££}$p = <0.0001). Considering the influence of time, the CaP group ($^{++}$p =<0.0029) showed a decrease with time, and the CoCaP group (^{dddd}p = <0.0001) a significant increase.

Thereafter, in order to effectively know about the capacity of osteoblast in influence on osteoclastogenesis, a ratio between RANKL and OPG was considered. RANKL/OPG ratio the following profiles were obtained: in the 3-day treatment the CaP (*p = 0.0351) and CoCaP (****p = <0.0001) showed higher than the Ctrl (**Fig.5c**). The CoCaP group also showed differences concerning the O.M ($^{¢¢¢¢}$p = <0.0001) and CaP ($^{¢¢¢¢}$p = <0.0001). In the 7-day treatment, only the O.M group showed an increase when compared to Ctrl ($^{+++}$p = 0.0001), CaP ($^{\$\$\$\$}$p = <0.0001) and CoCaP ($^{\$\$\$\$}$p = <0.0001). Between the treatment times, it was possible to observe an increase in the expression of RANKL in the O.M group (^{bbbb}p = <0.0001) and a decrease in the CoCaP group (^{dddd}p = <0.0001).

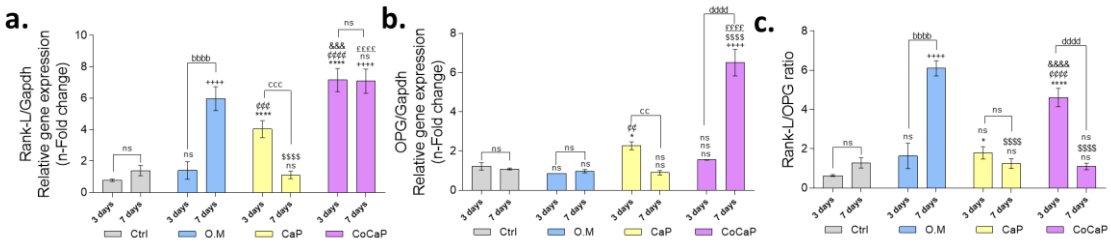

Fig.5. Cytokines were changes by CoCaP: **a.** RANKL, in the 3-day treatment showed an increase in its expression in the CaP (****p <0.0001 and $^{¢¢¢}$p = 0.0007) and CoCaP (****p <0.0001 and ($^{¢¢¢¢}$p <0.0001) groups when compared to Ctrl and O.M, respectively. The CoCaP group ($^{\&\&\&}$p = 0.0001) showed an increase when compared to the CaP group. In the treatment for 7 days, the O.M ($^{++++}$p <0.0001) and CoCaP ($^{++++}$p <0.0001) show increases when compared to the Ctrl group. The O.M and CoCaP ($^{££££}$p <0.0001) also show increases in expression when compared to the CaP ($^{\$\$\$\$}$p <0.0001). **b.** OPG, in the 3-day treatment, only the CaP (*p = 0.0419 and $^{¢¢}$p = 0.0048) showed an increase when compared to the Ctrl and O.M. groups. In the 7-day treatment, the CoCaP group showed an increase in its expression when compared to the Ctrl ($^{++++}$p <0.0001), O.M ($^{\$\$\$\$}$p <0.0001), and CaP ($^{££££}$p <0.0001). **c.** RANKL/OPG, in the 3-day treatment the CaP (*p = 0.0351) and CoCaP (****p <0.0001) was higher than the Ctrl. The CoCaP group also showed differences concerning the O.M ($^{¢¢¢¢}$p <0.0001) and CaP ($^{¢¢¢¢}$p <0.0001). In the 7-day treatment, only the O.M group ($^{+++}$p = 0.0001) showed an increase compared to Ctrl, CaP ($^{\$\$\$\$}$p <0.0001), and CoCaP ($^{\$\$\$\$}$p <0.0001). All sample groups n = 3. The Gapdh, β-actin, and 18S genes were used as housekeeping genes.

Genes related with osteoblast adhesion were changed by CoCaP

The expression of Integrin's subunits (α and β) were evaluated in this study. In the 3-day treatment, the O.M. group showed a reduction in the expression of α1integrin (**Fig.6a**) when compared to the Ctrl (*p = 0.0464). The CaP and CoCaP groups did not show statistically significant differences when compared with Ctrl and each other. The CoCaP group showed increased expression when compared to the O.M ($^{¢}$p = 0.0339). In the 7-day treatment, only the CoCaP group showed differences when compared to the Ctrl ($^{+}$p = 0.0242) and CaP ($^{££}$p = 0.0242). β1integrin evaluation, at 3 days, the O.M. group showed an increase in its expression when compared to the Ctrl (**p = 0.0019), while the CaP and CoCaP groups showed there are no differences (**Fig.6b**). Among the groups, the CaP group showed a reduction in its expression when compared to the O.M ($^{¢¢¢}$p = <0.0001), while CoCaP group does not show significant differences when compared to the O.M. group, but showed a significant increase when compared to CaP (&p = 0.0348). In the 7-day treatment, the O.M ($^{++}$p = 0.0065), CaP ($^{++++}$p = <0.0001) and CoCaP ($^{++++}$p = <0.0001) groups showed an increase in expression when compared to the Ctrl group. Among the groups, CaP shows an increase in expression when compared to the O.M ($^{$}$p = 0.0185). The CoCaP group shows an increase when compared to the O.M ($^{$$$$}$p = <0.0001) and CaP ($^{££££}$p = <0.0001) groups. Among the treatment times, differences in expression were observed, being increased at 7 days in the CaP (^{cccc}p = <0.0001) and CoCaP (^{dddd}p = <0.0001) groups.

Upon integrin activation both Src and FAK are required and therefore were evaluated here (ZAMBUZZI; MILANI; TETI, 2010). Src expression showed there were no statistically significant differences between the groups when compared to Ctrl and to each other at 3 days (**Fig.6c**). At 7 days, the O.M. group showed an increase when compared to the Ctrl ($^{++++}$p <0.0001). The CaP group showed there is no difference when compared to the Ctrl group, but differences when compared to the O.M ($^{$$$$}$p = <0.0001) were found. The CoCaP group showed a significant increase when compared to the Ctrl ($^{++++}$p <0.0001), O.M ($^{$$$$}$p <0.0001), and CaP ($^{££££}$p <0.0001) groups. Comparing the influence of the time on its expression, the O.M (^{bbbb}p <0.0001) and CoCaP (^{dddd}p <0.0001) groups showed an increase in its expression. Regarding the behavior of FAK expression, at the 3-day treatment, the O.M group showed there are no differences when compared to Ctrl. The CaP group showed an increase when compared to the Ctrl (**p = 0.0032). The CoCaP group showed an increase when compared to the Ctrl (***p = 0.0002) and O.M ($^{¢¢}$p = 0,0088) groups respectively. In the 7-day treatment, the O.M group showed an increase when compared to the Ctrl ($^{+++}$p = 0.0001) and CaP ($^{$$$$}$p <0.0001) (**Fig.6d**). The CoCaP group showed an increase in expression when compared to the Ctrl ($^{++++}$p <0.0001) and CaP ($^{££££}$p <0.0001). Considering the relevance of time on FAK expression, both O.M (^{bb}p = 0.0027) and CaP (^{cc}p = 0.0037) groups

showed differences, with the increase in the O.M group with time and the decrease in expression in CaP.

Finally, Cofilin is required during osteoblast adhesion (ZAMBUZZI et al., 2009b), mainly coordinating the cytoskeleton rearrangement necessary for morphological cell adaptation (ROSSI et al., 2017). Considering Cofilin expression, at the 3 days treatment, both O.M (****p <0.0001) and CaP (**p <0.0027) groups showed a significant increase in its expression when compared to the Ctrl and CoCaP ($^{¢¢¢¢}$p <0.0001 and $^{\&\&}$p = 0.0046, respectively). In the 7 day, only the O.M group showed an increase in its expression when compared to the Ctrl group ($^{++++}$p <0.0001), the CaP group ($^{\$}$p =0.0465) showed a statistically significant decrease when compared to the O.M group (**Fig.6e**). About the Cofilin behavior, it seems there is no significant changes up to 7 days.

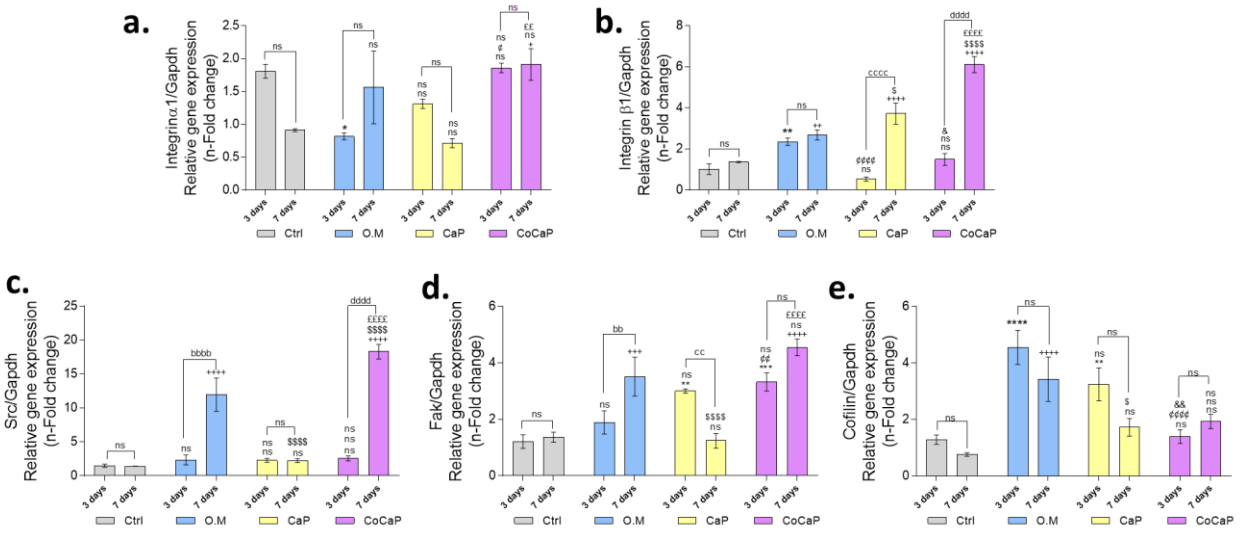

Fig.6. Osteoblast adhesion-related machinery is required by osteoblasts responding to monetite. a. α1Integrin - In the 3-day treatment, the O.M. showed a reduction in expression when compared to the Ctrl (*p = 0.0464). The CaP and CoCaP did not show statistically significant differences. In the 7-day treatment, only the CoCaP group showed differences when compared to the Ctrl ($^{+}$p = 0.0242) and CaP ($^{££}$p = 0.0242). **b.** β1Integrin, at 3 days, the O.M. showed an increase in its expression when compared to the Ctrl (**p = 0.0019), while the CaP and CoCaP groups showed no significances. In the 7-day treatment, the O.M ($^{++}$p = 0.0065), CaP ($^{++++}$p <0.0001), and CoCaP ($^{++++}$p <0.0001) groups showed an increase in expression when compared to the Ctrl. **c.** Src, at the 3-day time, showed there were no statistically significant differences between the groups when compared to Ctrl. At 7 days, the O.M. group showed an increase when compared to the Ctrl ($^{++++}$p <0.0001). The CoCaP group showed a significant increase when compared to the Ctrl ($^{++++}$p <0.0001), O.M ($^{\$\$\$\$}$p <0.0001), and CaP ($^{££££}$p <0.0001. **d.** FAK, at the 3-day treatment, the CaP group showed an increase when compared to the Ctrl (**p = 0.0032). The CoCaP group showed an increase when compared to the Ctrl (***p = 0.0002) and O.M ($^{¢¢}$p = 0,0088). In the 7-day treatment, the O.M and group showed an increase when compared to the Ctrl ($^{+++}$p = 0.0001) and CaP ($^{\$\$\$}$p <0.0001). The CoCaP group showed an increase in expression when compared to the Ctrl ($^{++++}$p <0.0001) and CaP ($^{££££}$p <0.0001). **e.** Cofilin, at the 3-day treatment the O.M (****p <0.0001) and CaP (**p <0.0027) groups showed a significant increase in its expression when compared to the Ctrl and CoCaP ($^{¢¢¢¢}$p <0.0001 and $^{\&\&}$p = 0.0046). In the 7-day treatment, only the O.M group showed an increase in its expression when compared

to the Ctrl group ($^{++++}$p <0.0001). Replicates: n = 3. The Gapdh, β-actin, and 18S genes were used as housekeeping genes.

Extracellular matrix remodeling

Over the last years, we have noticed that osteoblast maturation and matrix mineralization requires extracellular matrix remodeling as pre-requisite, mainly considering the response of osteoblasts to biomaterials. ECM remodeling is driven by matrix metalloproteinases (MMPs), and MMP-2 and MMP3 seems develop an important role in breaking down the extracellular matrix components (DA COSTA FERNANDES et al., 2018a, 2018b; FERNANDES et al., 2018). Here, we have better analyzed the involvement of both MMP-2 and MMP-9 in osteoblasts responding to monetite and its derivation by doping cobalt (CoCaP). Our data shows that, as follows:

1.Regarding MMP9, within 3 days of treatment, there were no differences between the investigated groups when compared to Ctrl and among themselves. However, up to 7 days, the O.M ($^{++++}$p <0.0001) and CoCaP ($^{++++}$p <0.0001 and $^{\text{£££}}$p <0.0001) showed significant increase when compared to Ctrl and CaP ($^{\$\$\$\$}$p <0.0001). Considering the difference between 3 and 7 days, the expression was increased with time in the O.M (^{bbbb}p = <0.0001) and CoCaP (^{dddd}p = <0.0001) groups (**Fig.7a**). Considering the activity of MMP9, it was assessed by zymography. Our data shows that MMP9 activity was evaluated in the 3 days' treatment, there was an increase in activity in response to CaP (****p <0.0001 and $^{¢¢¢¢}$p <0.0001) and CoCaP (****p <0.0001 and $^{¢¢¢¢}$p <0.0001) groups when compared to Ctrl and O.M, respectively. Considering the comparison between groups the activity was increased in CaP compared to CoCaP ($^{\&\&\&\&}$p = <0.0001) (**Fig.7e**). Up to 7 days, all groups showed an increase in their activity compared to Ctrl [O.M ($^{++++}$p <0.0001), CaP ($^{+}$p <0.0213), and CoCaP ($^{++++}$p <0.0001)]. Among the treatments, the activity was increased in O.M relative to CaP ($^{\$\$\$\$}$p <0.0001). The CoCaP group showed an increase in its activity relative to O.M ($^{\$\$\$\$}$p <0.0001) and CaP ($^{\text{£££}}$p <0.0001). Considering the data evaluation along the time, important to report that Ctrl (^{aaa}p = 0.0002), O.M (^{bbbb}p <0.0001), and CoCaP (^{dddd}p <0.0001) groups were significantly increased, and in the CaP group (^{cccc}p = <0.0001) it was significantly decreased.

2. Regarding the MMP-2 behavior, within 3 days of treatment, there was an increase in the activity of the O.M group (***p = 0.0001) when compared to the Ctrl, CaP ($^{¢¢¢¢}$p = <0.0001), and CoCaP ($^{¢¢}$p = 0.0015) (**Fig.7c**). The CoCaP group showed a significant increase in relation to the CaP group ($^{\&\&}$p = 0.0092). At 7 days, none of the treatments showed statistically significant differences with Ctrl or others among themselves. Between the treatment times, the expression was decreased in the O.M group (^{bbb}p = 0.0007); in the other groups, there was no statistically significant

difference. Considering the activity of MMP-2 (**Fig.7d**) and it was shown that at 3 days there was an increase in activity in the O.M (****p <0.0001) and CaP (****p <0.0001) groups when compared to the Ctrl. The CaP group showed an increase when compared to the O.M ($^{¢¢¢¢}$p <0.0001). Importantly, the CoCaP group showed a decrease when compared to the Ctrl (****p <0.0001), O.M ($^{¢¢¢¢}$p <0.0001), and CaP ($^{\&\&\&\&}$p <0.0001) groups. Considering the response of osteoblast responding to monetites up to 7 days, the CaP ($^{++++}$p <0.0001 and $^{\$\$\$\$}$p <0.0001) and CoCaP ($^{++++}$p <0.0001 and $^{\$\$\$}$p = 0.0004) showed increases in relation to Ctrl and O.M, respectively. Considering the analysis between CaP and CoCaP ($^{£££££}$p <0.0001), the statistics reported an increase in its activity in comparison. Considering the both tomes up to 7 days, the activity of MMP2 was decreased in Ctrl (^{aaaa}p<0.0001) and O.M (^{bbbb}p<0.0001), and in the CoCaP group (^{dddd}p<0.0001) the activity was increased considering the time.

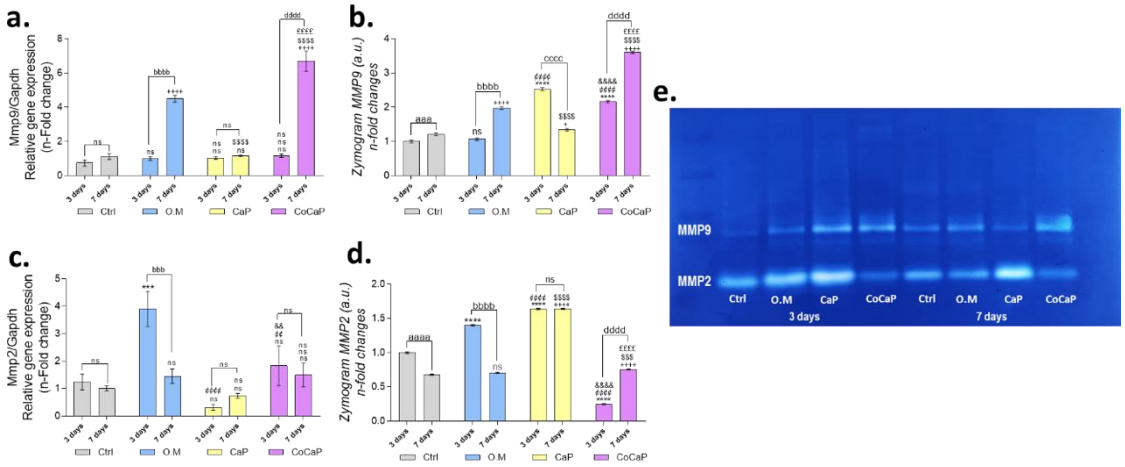

Fig.7. ECM remodeling by osteoblasts responding to monetites. a. MMP9, in the 3-day treatment, there were no differences between the groups when compared to Ctrl. In the 7-day treatment the O.M ($^{++++}$p<0.0001) and CoCaP ($^{++++}$p<0.0001; $^{£££££}$p<0.0001) showed increased expression when compared to Ctrl and CaP ($^{\$\$\$\$}$p<0.0001). **b.** MMP9 activity was evaluated by zymography and bands were quantified. In the 3 days' treatment, there was an increase in activity in CaP (****p<0.0001; $^{¢¢¢¢}$p<0.0001) and CoCaP (****p<0.0001; $^{¢¢¢¢}$p<0.0001) groups when compared to Ctrl and O.M, respectively. Between the monetites, the expression was increased in CaP compared to CoCaP ($^{\&\&\&\&}$p<0.0001). In the 7-day treatment, all groups showed an increase in their activity compared to Ctrl [O.M ($^{++++}$p<0.0001), CaP ($^{+}$p<0.0213), and CoCaP ($^{++++}$p<0.0001)]. The activity was increased in O.M relative to CaP ($^{\$\$\$\$}$p<0.0001). The CoCaP group showed an increase in its activity relative to O.M ($^{\$\$\$\$}$p<0.0001) and CaP ($^{£££££}$p<0.0001). **c.** MMP2 expression, in the 3-day treatment, there was an increase in the activity of the O.M group (***p = 0.0001) compared to the Ctrl, CaP ($^{¢¢¢¢}$p<0.0001), and CoCaP ($^{¢¢}$p = 0.0015). The CoCaP group showed an increase in relation to the CaP group ($^{\&\&}$p = 0.0092). Considering 7-day treatment, none of the treatments showed statistically significant differences with Ctrl. **d.** MMP2 activity was also evaluated by zymography and the bands were quantified, highlighting that, at 3 days of treatment, there was an increase in activity in the O.M. (****p<0.0001) and CaP (****p<0.0001) groups when compared to the Ctrl. The CaP group showed an increase when compared to the O.M ($^{¢¢¢¢}$p<0.0001). The CoCaP group showed a decrease when compared to the Ctrl (****p<0.0001), O.M ($^{¢¢¢¢}$p<0.0001), and CaP ($^{\&\&\&\&}$p<0.0001) groups. In the 7-day treatment, the CaP ($^{++++}$p<0.0001 and $^{\$\$\$\$}$p<0.0001) and CoCaP ($^{++++}$p<0.0001 and $^{\$\$\$}$p = 0.0004) showed increases in relation to Ctrl and O.M. Between CaP and CoCaP ($^{£££££}$p<0.0001), it was showed an increase

in the MMP-2 activity. **e.** Zymogram obtained by resolving the proteins content from the conditioned medium obtained by the osteoblasts responding to different cell culture conditions. The Gapdh, β-actin, and 18S genes were used as housekeeping genes.

Osteoblast differentiation was assessed by osteogenic gene markers

Osteoblast differentiation is a very complex event, where a myriad of genes guarantees the osteogenic phenotype. Among them, we have evaluated in this study the activities of Runx2, Osterix, Bsp, ALP, Bmp2, and Osteocalcin genes. Considering Runx2 gene, at the 3 days, the O.M (***p = 0.0002) and CoCaP (****p<0.0001) groups showed differences when compared to Ctrl. The O.M and CoCaP groups showed an increase when compared to the CaP group ($^{¢¢¢}$p = 0.0006 and $^{\&\&\&}$p = 0.0003); between them, no difference was presented (**Fig.8a**). At 7 days, only the CoCaP group showed an increase in expression when compared to the Ctrl ($^{++++}$p<0.0001), O.M ($^{\$\$\$\$}$p<0.0001) and CaP ($^{££££}$p<0.0001) groups. Considering the evaluation of the time line up to 7 days, O.M (^{bb}p = 0.0035) and CoCaP (^{dddd}p = <0.0001) groups showed differences between their expressions, it being decreased in the O.M group and increased in the CoCaP group along the time (**Fig.8a**).

For the Osterix gene, at 3-days, only the CoCaP group showed differences in its expression when compared to Ctrl (****p<0.0001), O.M ($^{¢¢¢¢}$p<0.0001) and CaP ($^{\&\&\&\&}$p<0.0001) (**Fig.8b**). At 7 days, the CaP group showed a reduction when compared to the O.M ($^{\$}$p<0.0408). The CoCaP group showed an increase in its expression when compared to the Ctrl ($^{++++}$p<0.0001), O.M ($^{\$\$\$\$}$p<0.0001), and CaP ($^{££££}$p<0.0001). Considering the evaluation of the time line up to 7 days, only the O.M group (^{b}p<0.0408) showed a statistically significant increase in its expression (**Fig.8b**).

The analysis of BSP gene, at 3 days, there was an increase in expression in the O.M (****p<0.0001) and CoCaP (**p = 0.0099) groups when compared to Ctrl (**Fig.8c**). The O.M group also showed an increase when compared to the CaP ($^{¢¢¢¢}$p<0.0001) and CoCaP ($^{¢¢¢}$p = 0.0008) (**Fig.8c**). At 7 days, only the O.M group showed statistically significant differences when compared to the Ctrl ($^{+}$p = 0.0383). Considering the evaluation of the time line up to 7 days, the O.M group (^{bb}p = 0.0016) showed a decrease in expression with time (**Fig.8c**).

Another important gene evaluated here was alkaline phosphatase (ALP). At 3 days responding to different conditions, the osteoblasts show an increased in response to the CaP group ($^{\&\&}$p = 0.0055) when compared to Ctrl (**Fig.8d**). Among the treatments, only the CaP group showed an increase when compared to the CoCaP group ($^{\&}$p = 0.0189) (**Fig.8d**). Considering the 7 days, O.M ($^{++++}$p<0.0001) and CoCaP ($^{++++}$p<0.0001) showed an increase when compared to Ctrl (**Fig.8d**). The expression of O.M was increased when compared to the CaP ($^{\$\$\$\$}$p<0.0001). The CoCaP group showed an increase in its expression when compared to the O.M ($^{\$\$\$\$}$p<0.0001)

and CaP ($^{\text{£££}}$p = <0.0001) treatments. Considering the evaluation of the time line up to 7 days, the O.M ($^{\text{bbbb}}$p<0.0001) and CoCaP ($^{\text{dddd}}$p<0.0001) groups showed an increase in expression up to 7 days (**Fig.8d**). The behavior of ALP gene corroborates with its distribution along the osteoblast cultures (**Fig.9**).

For BMP2 gene, within 3 day of treatments, only the CoCaP group showed an increase in its expression when compared to Ctrl (**p = 0.0060); there are no differences between treatments (**Fig.8e**). In the 7-day treatment, the O.M group showed an increase in its expression when compared to Ctrl ($^{+}$p = 0.0283) and CaP ($^{\$}$p = 0.0402). The CoCaP group showed an increase when compared to the Ctrl ($^{++++}$p<0.0001), O.M ($^{\$\$}$p = 0.0033), and CaP ($^{\text{£££}}$p<0.0001) groups. Considering the evaluation of the time line up to 7 days, only the CoCaP group ($^{\text{ddd}}$p = 0.0002) showed an increase in its expression (**Fig.8e**).

For the osteocalcin gene, at 3 days, the CaP (*p = 0.0413; $^{¢}$p = 0.0387) and CoCaP (****p<0.0001; $^{¢¢¢¢}$p<0.0001) showed increased expression when compared to the Ctrl and O.M, respectively (**Fig.8f**). At 7 days, no group showed differences when compared to Ctrl or other treatments. Considering the evaluation of the time line up to 7 days, CaP (^{cc}p = 0.0019) and CoCaP ($^{\text{dddd}}$p<0.0001) groups showed reductions in expression along the time (**Fig.8f**).

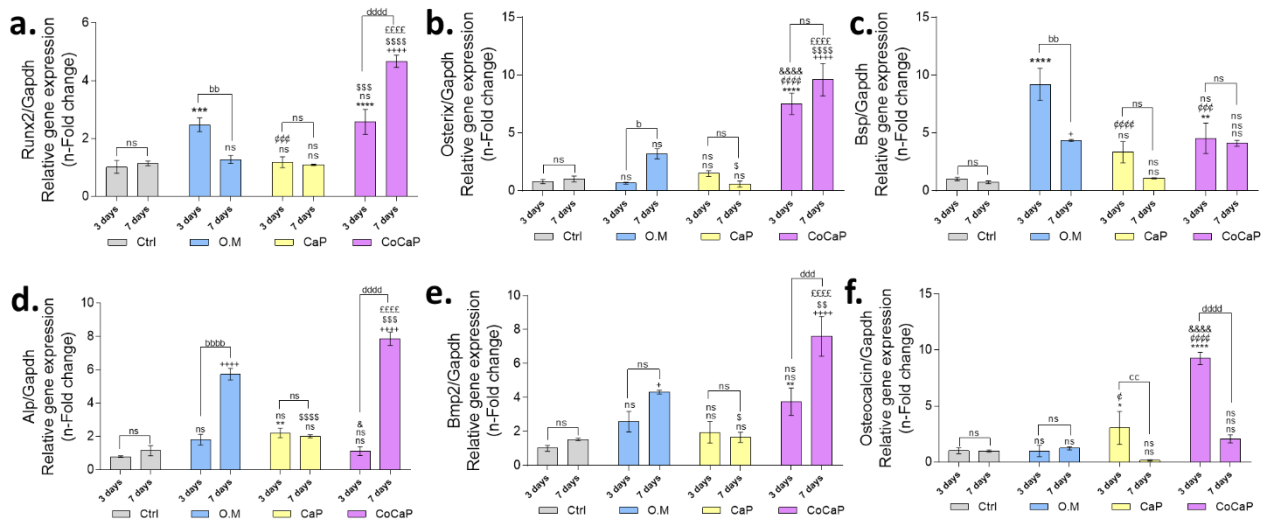

Fig.8. Osteogenic gene markers are reprogrammed in response to CoCaP. a. Runx2, at the 3-day treatment, the O.M (***p = 0.0002) and CoCaP (****p<0.0001) groups showed differences when compared to Ctrl. The O.M and CoCaP groups showed an increase when compared to the CaP group ($^{¢¢¢}$p = 0.0006; $^{\&\&\&}$p = 0.0003); At 7 days, only the CoCaP group showed an increase in expression when compared to the Ctrl ($^{++++}$p<0.0001), O.M ($^{\$\$\$\$}$p<0.0001) and CaP ($^{\text{££££}}$p<0.0001). **b.** Osterix, at the 3 days, only the CoCaP group showed differences in its expression when compared to Ctrl (****p<0.0001), O.M ($^{¢¢¢¢}$p<0.0001), and CaP ($^{\&\&\&\&}$p<0.0001). At 7 days, the CoCaP showed an increase in its expression when compared to the Ctrl ($^{++++}$p<0.0001), O.M ($^{\$\$\$\$}$p<0.0001), and CaP ($^{\text{££££}}$p<0.0001). **c.** BSP, at the 3 days, there was an increase in expression in the O.M (****p<0.0001) and CoCaP (**p = 0.0099) groups when compared to Ctrl. The O.M group also showed an increase when compared to the CaP ($^{¢¢¢¢}$p<0.0001) and CoCaP ($^{¢¢¢}$p = 0.0008). At 7 days, only the O.M group showed statistically significant differences when compared to the Ctrl ($^{+}$p = 0.0383). **d.** ALP, at 3 days, the ALP expression was increased in the CaP group

($^{\&\&}$p = 0.0055) when compared to Ctrl, and at 7 days, O.M ($^{++++}$p<0.0001) and CoCaP ($^{++++}$p<0.0001) showed an increase when compared to Ctrl. The expression of O.M. was increased when compared to the CaP ($^{\$\$\$\$}$p<0.0001). The CoCaP group showed an increase in its expression when compared to the O.M. ($^{\$\$\$\$}$p<0.0001) and CaP ($^{££££}$p<0.0001). **e.** Bmp2 gene, at 3 days, only the CoCaP group showed an increase in its expression when compared to Ctrl (**p = 0.0060), while at 7 days, the O.M. group showed an increase in its expression when compared to Ctrl ($^{+}$p = 0.0283) and CaP ($^{\$}$p = 0.0402). The CoCaP group showed an increase when compared to the Ctrl ($^{++++}$p<0.0001), O.M. ($^{\$\$}$p = 0.0033), and CaP ($^{££££}$p<0.0001). **f.** Osteocalcin gene, at 3 days, the CaP (*p = 0.0413; $^{¢}$p = 0.0387) and CoCaP (****p<0.0001; $^{¢¢¢¢}$p = <0.0001) showed increased expression when compared to the Ctrl and O.M. groups, respectively. At 7 days, there were no significances among the groups. Replicates: n=3. The Gapdh, β-actin, and 18S genes were used as housekeeping genes.

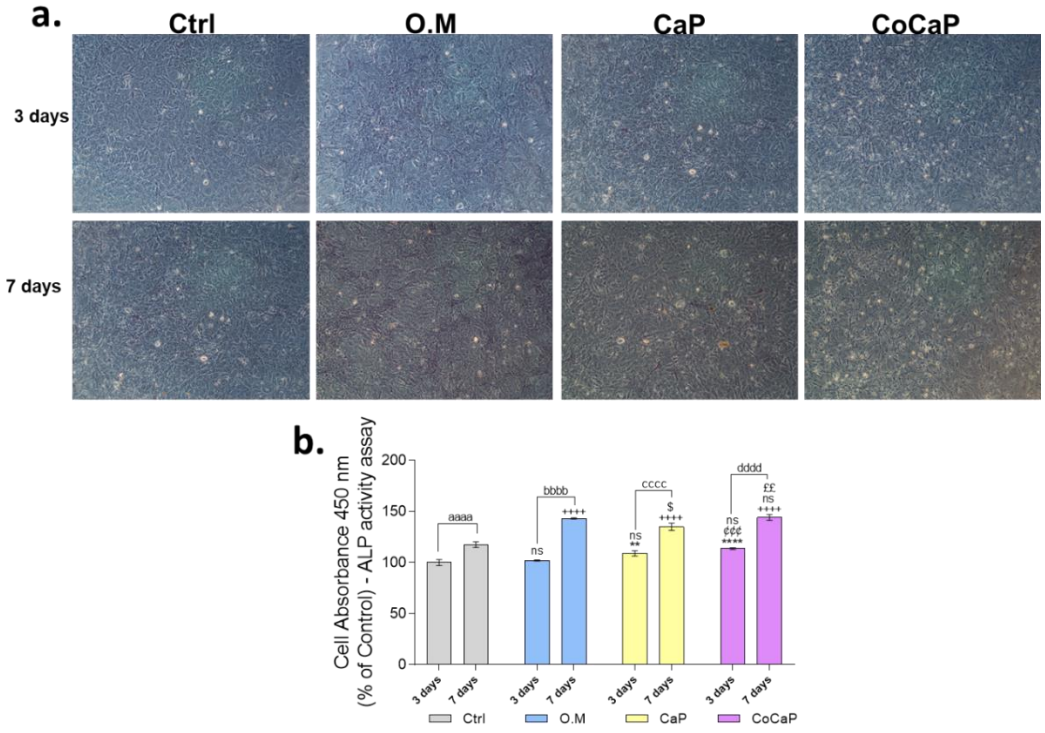

Fig.9. ALP activity and morphological distribution along the osteoblast cultures. a. Osteoblasts after treatment at their respective time-point on ALP staining (magnification 10x). **b**. At 3 days, the CaP group (**p = 0.0074) showed higher concentration when compared to the Ctrl group. The CoCaP group showed higher concentration when compared to the Ctrl (****p<0.0001) and O.M. ($^{¢¢¢}$p = 0.0005) groups. At the 7-day treatment, the O.M. group ($^{++++}$p<0.0001) showed higher concentration when compared to the Ctrl group. The CaP ($^{++++}$p<0.0001) showed an increased concentration compared to the Ctrl group, and a lower concentration compared to the O.M ($^{\$}$p = 0.0170). The CoCaP group showed the highest concentration compared to the Ctrl ($^{++++}$p<0.0001), and CaP ($^{££}$p = 0.0052). Replicates: n = 3.

Cobalt-doped monetite camuflages the necessary hypoxia required to mimic the bone regenerative microenvironment.

This is very accepted that the hypoxia is crucial for osteogenic differentiation of precursor cells (WANG et al., 2007a). On this hand, we have firstly investigated whether CoCaP was able to stimulate induced hypoxia and so stimulate osteoblast differentiation. In fact, our data brings that Hif1α gene was dynamically modulated by CoCaP; its expression, at 3 days, show that only

CoCaP group triggers an intracellular signaling able to increase in its expression compared to the Ctrl (****p<0.0001), O.M ($^{¢¢¢¢}$p<0.0001), and CaP ($^{\&\&\&\&}$p<0.0001) (**Fig.10a**), which also was replicated up to 7 days, where it was higher compared to the Crtl ($^{++++}$p<0.0001), O.M ($^{\$\$\$\$}$p<0.0001), and CaP ($^{\pounds\pounds\pounds\pounds}$p<0.0001) groups. Considering the time (up to 7 days), both O.M (^{bb}p = 0.0054) and CaP (^{cc}p = 0.0054) groups showed a statistically significant decrease.

For VEGF gene expression (**Fig.10b**), at 3 days, only the CaP group showed an increase in its expression compared to the Ctrl (***p = 0.0010) and also to the CoCaP group ($^{\&\&}$p = 0.0041). At 7 days, only the O.M. group showed an increase in its expression when it was compared to Ctrl ($^{+++}$p = 0.0002), CaP ($^{\$\$\$\$}$p<0.0001), and CoCaP ($^{\$\$}$p = 0.0050). Considering the relevance of time on its expression, it was shown that O.M, group showed an increase in its expression (^{bb}p = 0.0029), and the CaP group (^{cccc}p<0.0001) promoted a significant decrease.

Finally, considering eNOS as an important angiogenic stimulus factor responding to hypoxia, our data shows that eNOS gene expression, at 3-day treatment, was higher in osteoblasts responding to both O.M. (***p = 0.0002; $^{¢¢}$p =0.0074) and CoCaP (****p<0.0001 and $^{\&\&\&}$p = 0.0002) when compared to Ctrl and CaP, respectively (**Fig.10c**). Considering its expression at 7 days, both CaP ($^{++++}$p<0.0001; $^{\$\$\$}$p = 0.0003) and CoCaP ($^{++++}$p<0.0001; $^{\$\$\$\$}$p<0.0001) groups showed an increase in their expression when compared to Ctrl and O.M, respectively (**Fig.10c**).

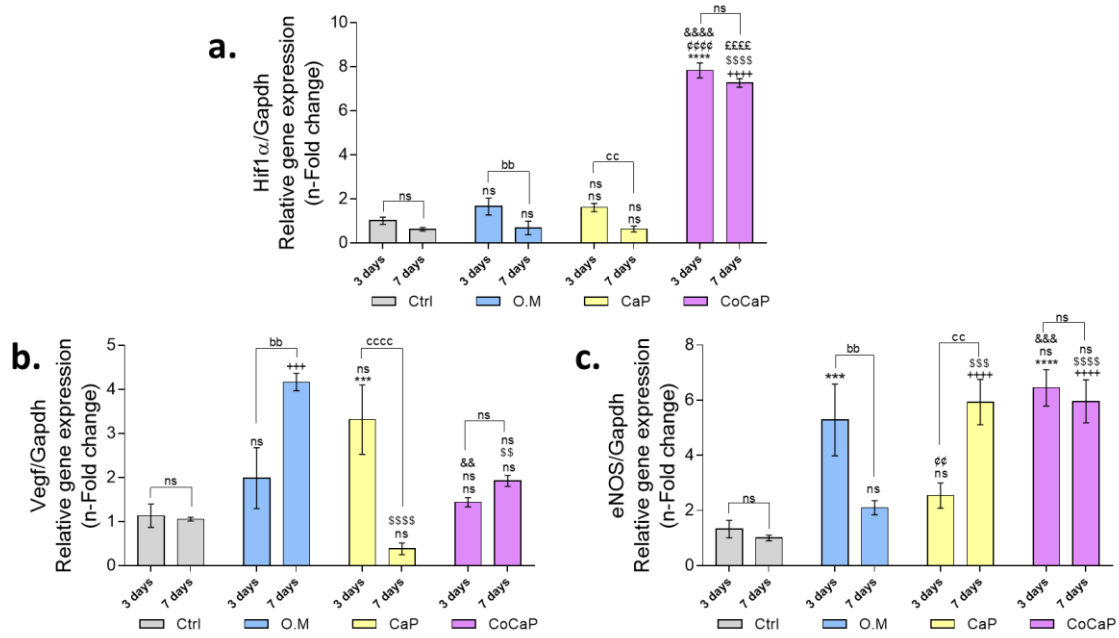

Fig.10. CoCaP promotes hypoxia and requires VEGF and eNOS. a. Hif1α, at 3 days, was higher only in osteoblasts responding to CoCaP group when compared to the Ctrl (****p<0.0001), O.M ($^{¢¢¢¢}$p<0.0001), and CaP ($^{\&\&\&\&}$p<0.0001). The same profile was observed in the 7 days' treatment, with a significant increase when compared to the Crtl ($^{++++}$p<0.0001), O.M ($^{\$\$\$\$}$p<0.0001), and CaP ($^{\pounds\pounds\pounds\pounds}$p<0.0001). **b.** VEGF, at 3 days, was higher only in osteoblast responding to CaP group when it was compared to the Ctrl (***p = 0.0010) and CoCaP group ($^{\&\&}$p = 0.0041). Considering the 7 day, only the O.M. group showed an increase in its expression in relation to Ctrl ($^{+++}$p = 0.0002), CaP ($^{\$\$\$\$}$p<0.0001), and CoCaP ($^{\$\$}$p = 0.0050). **c.** eNOS, at 3 days, was higher expressed in osteoblasts responding to O.M. (***p = 0.0002; $^{¢¢}$p =0.0074) and CoCaP

(****p = <0.0001; $^{\&\&\&}$p = 0.0002) when compared to Ctrl and CaP, respectively. At 7 days, both CaP ($^{++++}$p<0.0001; $^{\$\$\$}$p = 0.0003) and CoCaP ($^{++++}$p<0.0001; $^{\$\$\$\$}$p<0.0001) showed an increase in its expression when compared to Ctrl and O.M., respectively. Replicates: n = 3 and the Gapdh, β-actin, and 18S genes were used as housekeeping genes.

Oxidative stress was measured by protein carbonyl formation

All of mechanisms involved with cell growth requires a very balanced participation of protein phosphorylation, and most of them are regulated by phosphorylation at Y-residue (ZAMBUZZI; MILANI; TETI, 2010). As it is vastly discussed within literature, phosphatases modulate phosphorylation level of cells and they are regulated by reactive oxidative stress, which can be evaluated by protein carbonylation that was explored in this study (DE SOUZA MALASPINA et al., 2009; FERNANDES et al., 2014; ROSSI et al., 2017). Our data show that, at 3 days, the protein carbonylation was increased in osteoblasts responding to O.M group (***p = 0.0003) when it was compared to Ctrl (**Fig.11**), while CaP showed a decrease when compared to Ctrl (****p<0.0001), O.M ($^{¢¢¢¢}$p<0.0001), and CoCaP ($^{\&\&\&\&}$p<0.0001). CoCaP showed a significant decrease when compared to O.M ($^{¢}$p = 0.0104) (**Fig.11**). Considering 7 day, both O.M. (***p=0.0002) and CoCaP (****p<0.0001) groups showed a decrease when it was compared to Ctrl. The CaP group showed an increase compared to the both O.M ($^{\$\$\$}$p = 0.0005) and CoCaP ($^{££££}$p<0.0001) groups (**Fig.11**). Considering the evaluation of the time line up to 7 days, both Ctrl (^{a}p = 0.0104) and CaP (^{cccc}p<0.0001) groups showed an increase in carbonylation, while O.M. (^{bbbb}p<0.0001) and CoCaP (^{dd}p<0.0011) groups showed a decrease.

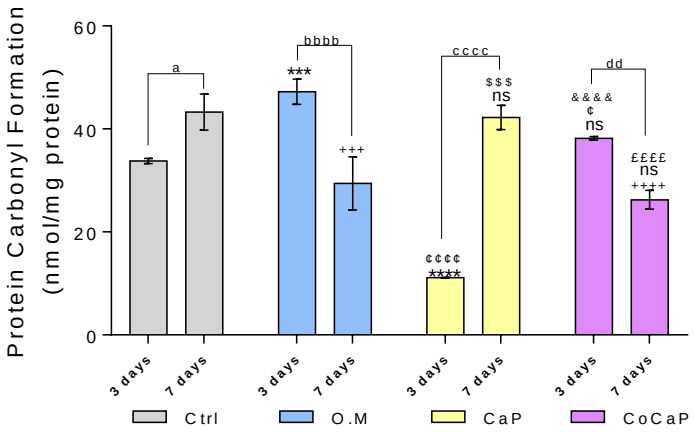

Fig.11. Protein Carbonylation was changed by monetites. At 3 days, osteoblast responding to O.M. group showed an increase compared to the Ctrl (***p = 0.0003). CaP showed a decrease when compared to Ctrl (****p<0.0001), O.M ($^{¢¢¢¢}$p<0.0001), and CoCaP ($^{\&\&\&\&}$p<0.0001). In turn, CoCaP showed a decrease when compared to O.M ($^{¢}$p = 0.0104). At 7 days, the both O.M (***p = 0.0002) and CoCaP (****p<0.0001) groups showed a decrease compared to Ctrl. The CaP group showed an increase compared to the both O.M ($^{\$\$\$}$p = 0.0005) and CoCaP ($^{££££}$p = <0.0001) groups. Replicates: n = 3.

DISCUSSION

In order to attend the necessity to propose a novel material preserving biomimetic characteristics to bone healing microenvironment, we proposed a calcium phosphate doped with cobalt. Firstly, calcium phosphate mimics the mineral phase of bone, as well as calcium favors the blood coagulation and arresting of platelets which contribute to bone growth, and cobalt promotes a chemically-induced hypoxia (BOYER; SHAINOFF; RATNOFF, 1972; MUÑOZ-SÁNCHEZ; CHÁNEZ-CÁRDENAS, 2019). Hypoxia brings at least 2 important outcomes to camouflages bone healing microenvironment, as follows: 1. It is commonly recognized that hypoxia plays a pivotal role in initiating the early stages of bone defect healing, therefore studies indicate that prolonged exposure to hypoxia can impede the osteogenic differentiation of precursor cells with association to activation of Notch1 signaling and the suppression of Runx2 although Notch1 signaling has been associated with osteogenesis responding to signals from endothelial cells (OSATHANON et al., 2014; RAMASAMY et al., 2014; XU et al., 2013; YANG et al., 2011); 2. In the initial phases of bone defect healing, hypoxia facilitates the migration of osteogenic and angiogenic precursor cells, promoting osteogenesis and angiogenesis (YU et al., 2019).

The induced formation of new vessels around the bone defect alleviates the hypoxic condition, allowing the healing process to progress. Hypoxia is essential for vascularization during embryo development and plays a vital role in endochondral ossification in fetal bone development. This hypoxia-mediated endochondral ossification is also implicated in the healing of large-sized bone defects, maybe recreating a biomimetic bone healing microenvironment where the crosstalk between osteoblasts and endothelial cells are required to promote osteogenesis and bone growth (ARALDI; SCHIPANI, 2010; DA COSTA FERNANDES et al., 2021a; RAMASAMY et al., 2016a, 2016b; RAMASAMY; KUSUMBE; ADAMS, 2015). Said that, important to report that the high level of HIF1α gene expression in response to CoCaP validates the capacity of this novel biomaterial in inducing biomimetic hypoxia and rapidly camouflages bone healing environment. By itself, hypoxia leads to the stimulation of osteoblast differentiation and consequently promotes release of signals to enhance angiogenesis, and osteoblast here seems develop an important role as source of angiogenic signals such as VEGF and eNOS. In turn, eNOS is known to activate signaling upstream to activate BMP2 gene as well as stimulate osteoblast differentiation.(AFZAL; POLAK; BUTTERY, 2004; YAN et al., 2021).

From the point of view of physicochemical characterization, important to mention that monetite and Co-doped monetite were synthesized and fully characterized by FTIR, Raman, XDR, XPS, SEM/EDS, and BET techniques, with attention on the modifications on Cobalt inducing in the monetite. The FTIR technique showed the characteristic bands of monetite, and that the addition of cobalt does not change them (CAMA et al., 2013; KAYGILI et al., 2017; SALIMI;

JAVADPOUR, 2012). Nonetheless, the FTIR does not show the bands referring to water bonds in the spectrum that is the main characteristic to differentiate the monetite from its hydrated brushite phase, being the first confirmation of the effectiveness of the synthesis (PRADO DA SILVA et al., 2001; SHAH et al., 2023). In turn, XRD data show the formation of a single monetite phase in the samples and, together with the XPS and EDS techniques, it is relevant to say that the cobalt concentration remained below 1% relative to the calcium concentration. However, this low concentration of cobalt is sufficient to produce a small phase decomposition of Ca-based compounds such as hydroxyapatite (5.4%), as obtained in the Rietveld refinement analysis and it seems presenting a biological advantage once the chemically-induced hypoxia is required only in the early stages of osteoblast differentiation, as discussed better upon earlier. Important, the affinity of metal ions for H and O atoms can induce a phase decomposition and change the monetite chemical composition (DUNCAN et al., 2014). The cell parameter changes (α, β, γ, a, b, and c) can be related to the substitution of Ca^{2+} (0.99 Å) by Co^{2+} with a smaller ionic radius (0.79 Å).

Thus, Co-doping can produce significant modifications in the monetite crystal structure in the form of changing in cell parameters. In addition, the distinct chemical characteristics of Co compared to Ca (e.g. electronegativity) can modify the surface chemistry of the particles, affecting the crystallite size, as observed. These effects were also found for metal replacement elements, such as Ag, Sr, Zn, Al, Ni, and Mn (ADAWY; DIAZ, 2022; KAYGILI et al., 2017). The SEM micrographs do not illustrate differences in the morphology of the monetites, but illustrate their sheet or plate shape, as described in the literature (MOTAMENI; ALSHEMARY; EVIS, 2021; TAMIMI; SHEIKH; BARRALET, 2012; ZHOU et al., 2021a). XPS analysis together with SEM, EDS, and XRD data confirm the effective synthesis and formation of monetite (GHINA IMANIYYAH; SUNARSO; HERDA, 2022; MOTAMENI; ALSHEMARY; EVIS, 2021; TAMIMI; SHEIKH; BARRALET, 2012; ZHOU et al., 2021a). The analyses of porosity, pore size, and surface area by BET, show the small influences of cobalt in the final monetites generated (BARDESTANI; PATIENCE; KALIAGUINE, 2019; WEBB; ORR, 2000).

From a biological perspective, soluble or insoluble cues have attracted significant attention due to their prospect of improving bone tissue formation by impacting on cellular responsiveness such as morphology, activity, and gene expression through the ECM–cell interactions and ultimately regulating cell migration, proliferation, and differentiation (GEMINI-PIPERNI et al., 2014b). All of these cellular aspects were better investigated here. Firstly, the proposed novel material is not cytotoxic in osteoblasts. Additionally, CoCaP accelerates osteoblast migration is suggested in wound healing assay and maybe this condition can be associated with the higher expression of CDKs responding to material and this phenotype seems being in association with the adhesion-related machinery once integrins, FAK and Src were also required.

In this regard, important to associate this molecular aspect to the expertise of osteoblast in balancing phospho-Y residue by modulating the activity of PTK and PTP, which are finely modulated by ROS content such as FAK and Src (ZAMBUZZI; MILANI; TETI, 2010). Src plays a pivotal role in osteoblasts participating in both adhesion by interacting with FAK and triggering survival signaling as well as contributing with osteoblast differentiation when its phosphorylation is modulated by protein tyrosine phosphatase (ZAMBUZZI et al., 2008, 2011). Importantly, ROS seems being modulated in osteoblasts responding to CoCaP once the carbonylation of proteins was decreased up to 7 days and it be very similar to osteoblasts responding to osteogenic medium.

Regarding the osteoblast differentiation mechanism, our data clearly shows there is an enough stimulus to activate intracellular signaling pathways able to require the over expression of both classical transcription factor Runx2 and Osterix in response to CoCaP. Important to report that both genes activities were more than 2-fold changes higher in osteoblasts under osteogenic conditions (osteogenic medium). The higher expression of these genes reflected on alkaline phosphatase (ALP) involvement, as well as bone sialoprotein (BSP) and osteocalcin (CASTRO-SILVA et al., 2012). Surprisingly, BMP2 was also up-expressed in response to CoCaP and it means the activation of an autocrine loop to maintain the osteogenic stimulus which can modulate late responses (or its maintenance) during bone healing. We have shown previously elsewhere that osteoblast differentiation and mineralization require extracellular matrix remodeling as prerequisite (ZAMBUZZI et al., 2009a). In fact, our data shows that the process of osteoblast differentiation is associated to ECM remodeling dependent to MMP9 involvement and it can being responsible for the regularity of angiogenesis stimulus delivering angiogenic signals such as vascular endothelial growth factor (VEGF) and eNOS (PRIDEAUX et al., 2012; SARAN; GEMINI PIPERNI; CHATTERJEE, 2014). During this mechanism, the resorption of CoCaP needs to be driven also by osteoblasts, although the inflammatory cells deserve attention on this matter. Our data show that osteoblast responding to CoCaP modulates the expression of RANKL and OPG and these findings suggest this event being finely regulated, once the balance of RANKL and OPG drives the osteoclastogenesis (TAKAYANAGI, 2021a).

In conclusion, considering our findings, this study unveils, for the first time, the biological impact of a novel Co-doped monetite on osteoblasts. It highlights that cobalt-doped monetite induces biomimetic hypoxia and swiftly mimics the bone healing environment, enhancing the osteogenic performance of osteoblasts. Co-doped monetite emerges as a biomimetic and “smart” material with promising applications in the field of bone development making it an eligible candidate for exploration in preclinical protocols.

Acknowledgments

The authors are grateful to Fundação de Amparo à Pesquisa do Estado de São Paulo - FAPESP (FAPESP: 2019/26854-2, 2022/15157-1), Conselho Nacional de Desenvolvimento Científico e Tecnológico (CNPq – Bolsa Produtividade em Pesquisa, 314166/2021-1) and Coordenação de Aperfeiçoamento de Pessoal de Nível Superior (Capes), code 1. The authors would like to thank the LNNano/CNPEM for the use of XPS (Proposal XPS-20220156).

References

ADAWY, A.; DIAZ, R. Probing the Structure, Cytocompatibility, and Antimicrobial Efficacy of Silver, Strontium-, and Zinc-Doped Monetite. **ACS Applied Bio Materials**, v. 5, n. 4, p. 1648–1657, 18 abr. 2022.

AFZAL, F.; POLAK, J.; BUTTERY, L. Endothelial nitric oxide synthase in the control of osteoblastic mineralizing activity and bone integrity. **Journal of Pathology**, v. 202, n. 4, p. 503–510, abr. 2004.

ALLMANN, R.; HINEK, R. The introduction of structure types into the Inorganic Crystal Structure Database ICSD. **Acta Crystallographica Section A: Foundations of Crystallography**, v. 63, n. 5, p. 412–417, 17 ago. 2007.

ARALDI, E.; SCHIPANI, E. Hypoxia, HIFs and bone development. **Bone**, 2010. Disponível em: <https://pubmed.ncbi.nlm.nih.gov/20444436/>

BARDESTANI, R.; PATIENCE, G. S.; KALIAGUINE, S. Experimental methods in chemical engineering: specific surface area and pore size distribution measurements—BET, BJH, and DFT. **Canadian Journal of Chemical Engineering**Wiley-Liss Inc., 1 nov. 2019.

BELKLY, A. et al. New developments in the Inorganic Crystal Structure Database (ICSD): Accessibility in support of materials research and design. **Acta Crystallographica Section B: Structural Science**, v. 58, n. 3 PART 1, p. 364–369, 29 jun. 2002.

BEZERRA, F. et al. Nano hydroxyapatite-blasted titanium surface affects pre-osteoblast morphology by modulating critical intracellular pathways. **Biotechnology and Bioengineering**, v. 114, n. 8, p. 1888–1898, 1 ago. 2017.

BOULER, J. M. et al. Biphasic calcium phosphate ceramics for bone reconstruction: A review of biological response. **Acta Biomaterialia**, v. 53, p. 1–12, 2017.

BOYER, M. H.; SHAINOFF, J. R.; RATNOFF, O. D. Acceleration of fibrin polymerization by calcium ions. **Blood**, 1972. Disponível em: <https://pubmed.ncbi.nlm.nih.gov/5059648/>

CAMA, G. et al. A novel method of forming micro- and macroporous monetite cements. **Journal of Materials Chemistry B**, v. 1, n. 7, p. 958–969, 23 jan. 2013.

CASTRO-SILVA, I. I. et al. Periosteal-derived cells for bone bioengineering: A promising candidate. Disponível em: <https://pubmed.ncbi.nlm.nih.gov/22221259/>. Acesso em: 3 mar. 2023.

CHÉRIF, I. et al. X-Ray Diffraction Analysis by Modified Scherrer, Williamson–Hall and Size–Strain Plot Methods of ZnO Nanocrystals Synthesized by Oxalate Route: A Potential Antimicrobial Candidate Against Foodborne Pathogens. **Journal of Cluster Science**, p. 1–16, 6 mar. 2022.

CONSTANTZ, B. R. et al. Histological, chemical, and crystallographic analysis of four calcium phosphate cements in different rabbit osseous sites. **Journal of Biomedical Materials Research**, v. 43, n. 4, p. 451–461, 1998.

DA COSTA FERNANDES, C. J. et al. Zirconia stimulates ECM-remodeling as a prerequisite to pre-osteoblast adhesion/proliferation by possible interference with cellular anchorage. **Journal of Materials Science: Materials in Medicine**, v. 29, n. 4, 1 abr. 2018a.

DA COSTA FERNANDES, C. J. et al. Titanium-enriched medium drives low profile of ECM remodeling as a pre-requisite to pre-osteoblast viability and proliferative phenotype. **Journal of Trace Elements in Medicine and Biology**, v. 50, n. February, p. 339–346, 1 dez. 2018b.

DA COSTA FERNANDES, C. J. et al. Metabolic effects of CoCr-enriched medium on shear-stressed endothelial cell and osteoblasts: A possible mechanism involving a hypoxic condition on bone healing. **Materials Science and Engineering C**, v. 128, p. 112353, 1 set. 2021.

DANG, M. et al. Biomimetic delivery of signals for bone tissue engineering. **Bone** ResearchSichuan University, , 2018.

DE ALMEIDA, G. S. et al. Development of cobalt (Co)-doped monetites for bone regeneration. **Journal of Biomedical Materials Research - Part B Applied Biomaterials**, v. 3, n. August, p. 1–12, 2023.

DE SOUZA MALASPINA, T. S. et al. A possible mechanism of low molecular weight protein tyrosine phosphatase (LMW-PTP) activity modulation by glutathione action during human osteoblast differentiation. **Archives of Oral Biology**, v. 54, n. 7, p. 642–650, 1 jul. 2009.

DESAI, T. R.; BHADURI, S. B.; TAS, A. C. A Self-Setting, Monetite (CaHPO4) Cement for Skeletal Repair. In: [s.l.] **John Wiley & Sons**, Ltd, 2008. p. 61–69.

DUNCAN, J. et al. The role of the chemical composition of monetite on the synthesis and properties of α-tricalcium phosphate. Disponível em: <https://www.sciencedirect.com/science/article/pii/S0928493113005018?via%3Dihub>. Acesso em: 13 jan. 2023.

FERNANDES, C. J. C. et al. Nano hydroxyapatite-blasted titanium surface creates a biointerface able to govern Src-dependent osteoblast metabolism as prerequisite to ECM remodeling. **Colloids and Surfaces B: Biointerfaces**, v. 163, p. 321–328, 1 mar. 2018.

FERNANDES, G. V. O. et al. Osteoblast adhesion dynamics: A possible role for ROS and LMW-PTP. **Journal of Cellular Biochemistry**, v. 115, n. 6, p. 1063–1069, 2014.

GEMINI-PIPERNI, S. et al. Cellular behavior as a dynamic field for exploring bone bioengineering: A closer look at cell-biomaterial interface. **Archives of Biochemistry and Biophysics**, v. 561, p. 88–98, 1 nov. 2014.

GHINA IMANIYYAH, A.; SUNARSO; HERDA, E. Monetite as a potential ideal bone substitute: A short review on fabrication and properties. **Materials Today**: **Proceedings**, v. 66, p. 2762–2766, 1 jan. 2022.

HARTREE, E. F. Determination of protein: A modification of the lowry method that gives a linear photometric response. **Analytical Biochemistry**, v. 48, n. 2, p. 422–427, 1972.

HAUL, R. S. J. Gregg, K. S. W. Sing: Adsorption, Surface Area and Porosity. 2. Auflage, **Academic Press, London** 1982. 303 Seiten. Berichte der Bunsengesellschaft für physikalische Chemie, v. 86, n. 10, p. 957–957, 1 out. 1982.

HELLENBRANDT, M. The inorganic crystal structure database (ICSD) - **Present and future. Crystallography Reviews**. Anais...Taylor & Francis, jan. 2004.

HOLZWARTH, J. M.; MA, P. X. Biomimetic nanofibrous scaffolds for bone tissue engineering. **Biomaterials**, 2011.

HUNG, S. P. et al. Hypoxia promotes proliferation and osteogenic differentiation potentials of human mesenchymal stem cells. **Journal of orthopaedic research** : official publication of the Orthopaedic Research Society, v. 30, n. 2, p. 260–266, fev. 2012.

KAYGILI, O. et al. Preparation and characterization of monetites co-doped with Ni/Al, Ni/Mn and Al/Mn. **Materials Letters**, v. 201, p. 39–42, 15 ago. 2017.

KIM, D. H. et al. Prospective study of iliac crest bone graft harvest site pain and morbidity. **Spine Journal**, v. 9, n. 11, p. 886–892, 2009.

LEBUGLE, A.; SALLEK, B.; TAI TAI, A. Surface modification of monetite in water at 37 °C: Characterisation by XPS. **Journal of Materials Chemistry**, v. 9, n. 10, p. 2511–2515, 1 jan. 1999.

LEFEBVRE, V.; PEETERS-JORIS, C.; VAES, G. Production of gelatin-degrading matrix metalloproteinases ('type IV collagenases') and inhibitors by articular chondrocytes during their dedifferentiation by serial subcultures and under stimulation by interleukin-1 and tumor necrosis factor alpha. **Biochimica et biophysica acta**, v. 1094, n. 1, p. 8–18, ago. 1991.

LI, J.; WANG, H.-M. M. Effects of cobalt chloride on phenotypes of normal human saphenous vein smooth muscle cells. Disponível em: <https://www.ncbi.nlm.nih.gov/pmc/articles/PMC4307437/>. Acesso em: 13 nov. 2019.

MA, P. X. Biomimetic materials for tissue engineering. **Advanced Drug Delivery Reviews**, 2008.

MARSELL, R.; EINHORN, T. A. The biology of fracture healing. Injury, v. 42, n. 6, p. 551–555, 2011.

MARTINO, M. M. et al. Extracellular matrix-inspired growth factor delivery systems for bone regeneration. **Advanced Drug Delivery Reviews**, 2015. Disponível em: <https://www.sciencedirect.com/science/article/abs/pii/S0169409X15000630>

MESQUITA, C. S. et al. Simplified 2,4-dinitrophenylhydrazine spectrophotometric assay for quantification of carbonyls in oxidized proteins. **Analytical Biochemistry**, v. 458, p. 69–71, 1 ago. 2014.

MOTAMENI, A.; ALSHEMARY, A. Z.; EVIS, Z. A review of synthesis methods, properties and use of monetite cements as filler for bone defects. **Ceramics International**, v. 47, n. 10, p. 13245–13256, 15 maio 2021.

MUÑOZ-SÁNCHEZ, J.; CHÁNEZ-CÁRDENAS, M. E. The use of cobalt chloride as a chemical hypoxia model. **Journal of Applied Toxicology**, v. 39, n. 4, p. 556–570, 1 abr. 2019.

OSATHANON, T. et al. Cobalt chloride supplementation induces stem-cell marker expression and inhibits osteoblastic differentiation in human periodontal ligament cells. **Archives of Oral Biology**, v. 60, n. 1, p. 29–36, 1 jan. 2014.

PAPE, H. C.; EVANS, A.; KOBBE, P. Autologous bone graft: Properties and techniques. **Journal of Orthopaedic Trauma**, 2010.

PINTO, T. S. et al. Nanohydroxyapatite-Blasted Bioactive Surface Drives Shear-Stressed Endothelial Cell Growth and Angiogenesis. **BioMed Research International**, v. 2022, 2022.

PRADO DA SILVA, M. H. et al. Transformation of monetite to hydroxyapatite in bioactive coatings on titanium. **Surface and Coatings Technology**, v. 137, n. 2–3, p. 270–276, 15 mar. 2001.

PRIDEAUX, M. et al. Extracellular matrix mineralization promotes E11/gp38 glycoprotein expression and drives osteocytic differentiation. **PLoS ONE**, v. 7, n. 5, 7 maio 2012.

RABIEI, M. et al. Comparing methods for calculating nano crystal size of natural hydroxyapatite using X-ray diffraction. **Nanomaterials**, v. 10, n. 9, p. 1–21, 1 set. 2020.

RAMASAMY, S. K. et al. Endothelial Notch activity promotes angiogenesis and osteogenesis in bone. **Nature**, v. 507, n. 7492, p. 376–380, 12 mar. 2014.

RAMASAMY, S. K. et al. Regulation of Hematopoiesis and Osteogenesis by Blood Vessel – **Derived Signals**. 2016a.

RAMASAMY, S. K. et al. Blood flow controls bone vascular function and osteogenesis. **Nature Communications**, v. 7, 6 dez. 2016b.

RAMASAMY, S. K.; KUSUMBE, A. P.; ADAMS, R. H. Regulation of tissue morphogenesis by endothelial cell-derived signals. 1 mar. 2015, p. 148–157.

RH. OWEN, G.; DARD, M.; LARJAVA, H. Hydoxyapatite/beta-tricalcium phosphate biphasic ceramics as regenerative material for the repair of complex bone defects. **Journal of Biomedical Materials Research - Part B Applied Biomaterials** John Wiley and Sons Inc., 1 ago. 2018.

ROSSI, M. C. et al. Titanium-released from dental implant enhances pre-osteoblast adhesion by ROS modulating crucial intracellular pathways. **Journal of Biomedical Materials Research - Part A**, v. 105, n. 11, p. 2968–2976, 1 nov. 2017.

SALIMI, E.; JAVADPOUR, J. Synthesis and characterization of nanoporous monetite which can be applicable for drug carrier. **Journal of Nanomaterials**, v. 2012, 2012.

SARAN, U.; GEMINI PIPERNI, S.; CHATTERJEE, S. Role of angiogenesis in bone repair. . 1 nov. 2014, p. 109–117.

SEMAN, R. N. A. R.; AZAM, M. A.; MOHAMED, M. A. Highly efficient growth of vertically aligned carbon nanotubes on Fe-Ni based metal alloy foils for supercapacitors. **Advances in Natural Sciences: Nanoscience and Nanotechnology,** v. 7, n. 4, 1 dez. 2016.

SEN, M. K.; MICLAU, T. Autologous iliac crest bone graft: Should it still be the gold standard for treating nonunions? **Injury,** v. 38, n. SUPPL. 1, p. S75–S80, 2007.
SHAH, F. A. et al. Bone without borders – Monetite-based calcium phosphate guides bone formation beyond the skeletal envelope. **Bioactive Materials**, v. 19, p. 103–114, 1 jan. 2023.
SHEIKH, Z. et al. In vitro degradation and in vivo resorption of dicalcium phosphate cement based grafts. Acta Biomaterialia, v. 26, p. 338–346, 15 out. 2015.
SHIN, H.; JO, S.; MIKOS, A. G. Biomimetic materials for tissue engineering. **Biomaterials** Elsevier BV, 2003.
TAKAYANAGI, H. RANKL as the master regulator of osteoclast differentiation. Disponível em: <https://pubmed.ncbi.nlm.nih.gov/33385253/>. Acesso em: 5 fev. 2023.
TAMIMI, F. et al. Bone regeneration in rabbit calvaria with novel monetite granules. **Journal of Biomedical Materials Research - Part A**, v. 87, n. 4, p. 980–985, 15 dez. 2008.
TAMIMI, F. et al. Craniofacial vertical bone augmentation: A comparison between 3D printed monolithic monetite blocks and autologous onlay grafts in the rabbit. **Biomaterials**, v. 30, n. 31, p. 6318–6326, 1 out. 2009.
TAMIMI, F. et al. Resorption of monetite granules in alveolar bone defects in human patients. **Biomaterials**, v. 31, n. 10, p. 2762–2769, 1 abr. 2010.
TAMIMI, F. et al. Osseointegration of dental implants in 3D-printed synthetic onlay grafts customized according to bone metabolic activity in recipient site. **Biomaterials**, v. 35, n. 21, p. 5436–5445, 1 jul. 2014.
TAMIMI, F.; SHEIKH, Z.; BARRALET, J. Dicalcium phosphate cements: Brushite and monetite. Acta **Biomaterialia** Elsevier Ltd, , 1 fev. 2012.
TORRES, J. et al. Monetite granules versus particulate autologous bone in bone regeneration. **Annals of Anatomy**, v. 200, p. 126–133, 1 jul. 2015.
VO, T. N.; KASPER, F. K.; MIKOS, A. G. Strategies for controlled delivery of growth factors and cells for bone regeneration. **Advanced Drug Delivery Reviews**, 2012.
WANG, W.; YEUNG, K. W. K. Bone grafts and biomaterials substitutes for bone defect repair: A review. **Bioactive Materials** KeAi Communications Co., 2017.
WANG, Y. et al. The hypoxia-inducible factor alpha pathway couples angiogenesis to osteogenesis during skeletal development. **J Clin Invest**, v. 117, 2007.
WEBB, P. A.; ORR, C. Modern Methods of Particle Characterization. 2000.
WOPENKA, B.; PASTERIS, J. D. A mineralogical perspective on the apatite in bone. **Materials Science and Engineering C**. Anais...Elsevier, 28 abr. 2005.
XU, N. et al. Hypoxia inhibits the differentiation of mesenchymal stem cells into osteoblasts by activation of Notch signaling. **Experimental and Molecular Pathology**, v. 94, n. 1, p. 33–39, 2013.
YAN, T. et al. Role of nitric oxide in orthodontic tooth movement (Review). **International Journal of Molecular Medicine** Spandidos Publications, , 1 set. 2021.
YANG, D. C. et al. Hypoxia inhibits osteogenesis in human mesenchymal stem cells through direct regulation of RUNX2 by TWIST**. PLoS ONE**, v. 6, n. 9, 2011.
YU, X. et al. Cellular hypoxia promotes osteogenic differentiation of mesenchymal stem cells and bone defect healing via STAT3 signaling. **Cellular and Molecular Biology Letters**, 2019. Disponível em: <https://www.ncbi.nlm.nih.gov/pmc/articles/PMC6889321/>
ZAGORAC, D. et al. Recent developments in the Inorganic Crystal Structure Database: Theoretical crystal structure data and related features. **Journal of Applied Crystallography**, v. 52, n. 5, p. 918–925, 23 set. 2019.
ZAMBUZZI, W. F. et al. Modulation of Src activity by low molecular weight protein tyrosine phosphatase during osteoblast differentiation. **Cellular Physiology and Biochemistry**, v. 22, n. 5–6, p. 497–506, 2008.
ZAMBUZZI, W. F. et al. Ascorbate-induced osteoblast differentiation recruits distinct MMP-inhibitors: RECK and TIMP-2. Disponível em: <https://pubmed.ncbi.nlm.nih.gov/18989628/>. Acesso em: 8 fev. 2023a.

ZAMBUZZI, W. F. et al. On the road to understanding of the osteoblast adhesion: Cytoskeleton organization is rearranged by distinct signaling pathways. **Journal of Cellular Biochemistry**, v. 108, n. 1, p. 134–144, 1 set. 2009b.
ZAMBUZZI, W. F. et al. Intracellular signal transduction as a factor in the development of "Smart" biomaterials for bone tissue engineering. 1 jun. 2011, p. 1246–1250.
ZAMBUZZI, W. F.; MILANI, R.; TETI, A. Expanding the role of Src and protein-tyrosine phosphatases balance in modulating osteoblast metabolism: Lessons from mice. 1 abr. 2010, p. 327–332.
ZHOU, H. et al. Monetite, an important calcium phosphate compound–Its synthesis, properties and applications in orthopedics. **Acta Biomaterialia**, v. 127, p. 41–55, 1 jun. 2021.

Capitulo 6

Artigo 3: The biological properties of Co-doped monetite are influenced by thermal treatment

Submetido

The biological properties of Co-doped monetite are influenced by thermal treatment

Gerson Santos de Almeida[1#], Luisa Camilo Suter[1], Thais Silva Pinto[1], Géorgia da Silva Feltran[1], Maria Gabriela Jacheto Carra[2], Diego Rafael Nespeque Corrêa[3], Margarida Juri Saeki[2], Paulo Noronha Lisboa-Filho[4], Willian Fernando Zambuzzi[1]

[1]Laboratory of Bioassays and Cellular Dynamics, Department of Chemical & Biological Sciences, Institute of Biosciences, UNESP: São Paulo State University, Botucatu, São Paulo, 18618-970, Brazil.
[2]Lab. of Materials and Electrochemistry, Department of Chemical & Biological Sciences, Institute of Biosciences, UNESP: São Paulo State University, Botucatu, São Paulo, 18618-970, Brazil.
[3]Laboratory of Anelasticity and Biomaterials, Department of Physics and Meteorology, School of Sciences, São Paulo State University - UNESP, Bauru, São Paulo, 17033-360, Brazil
[4]Department of Physics, School of Sciences, UNESP: São Paulo State University, Bauru, São Paulo, 17033-360, Brazil.

[#]Corresponding author:
Dr. Gerson Santos de Almeida
UNESP - Campus de Botucatu - Instituto de Biociências
Rua Profª. Drª. Irina Delanova Gemtchujnicov, s/nº
18618-693 – Botucatu-SP - Brazil

e-mail: gs.almeida@unesp.br
Phone: +55-14 38800599
Fax: +55-14 3880 0573

Abstract

In the realm of biomaterials for bone applications, calcium phosphates, exemplified by monetite, have gained considerable attention due to their unique ability to be readily absorbed by bone cells, inducing osteogenesis. To enhance these properties, various studies have explored the strategy of doping with additional elements, with cobalt being particularly noteworthy for its ability to induce hypoxia in cells, thereby promoting bone cell differentiation. Heat treatments are crucial in synthesizing certain calcium phosphates, resulting in purer and more crystalline phases, varied particle sizes, and optimized cellular responses. This study subjected both monetite and cobalt-doped monetite to heat treatments at temperatures of 700, 900, and 1050ºC. Comprehensive physicochemical characterization using XRD, FTIR, Raman, SEM/EDS, and ASAP revealed notable modifications in the phases of both materials, leading to the formation of pyrophosphate phases. When these materials were employed to condition a culture medium challenging MC3T3-E1 cells, they exhibited non-cytotoxic behavior and elicited distinct responses in genes related to the osteoblastic phenotype, angiogenesis, adhesion, and extracellular matrix remodeling. This research contributes valuable insights into the fabrication of calcium phosphates, specifically monetite and its cobalt-doped variant, showcasing their potential for future advancements in tissue regeneration and biomaterial design within the field of regenerative medicine.

Introduction

The integrity and functionality of bones, mainly serving as the mechanical and support for vertebrates, have garnered increased attention in the context of rising life expectancy and urbanization. Actually, diverse factors have contributed to an escalating demand for bone regeneration strategies such as traumas and tumor resection (BIGHAM-SADEGH; ORYAN, 2015; MACEDO et al., 2017; VAN DER EERDEN; TETI; ZAMBUZZI, 2014). Important to be coherent with the regeneration concept where it is expected to build up a new tissue preserving the original morpho-functional properties (VAN DER EERDEN; TETI; ZAMBUZZI, 2014), and bones exhibit intrinsic regenerative capabilities owing to a repertoire of bioactive molecules and cells to regenerate itself (IAQUINTA et al., 2019; RUNYAN; GABRICK, 2017). However, critical-sized injuries may surpass its inherent healing capacity, requiring clinical interventions, often involving the use of biomaterials as scaffold (DUKLE et al., 2022; HOU et al., 2022; ZAMBUZZI et al., 2011); once there is a limited therapeutic efficacy observed in autografts and allografts underscores the pressing need for alternative approaches in simulating a conducive bone regenerative microenvironment. Recognizing this lack, innovative technologies at the intersection of chemistry and biology have been proposed to develop biomimetic scaffolding capable of faithfully replicating the native regenerative microenvironment on multiple levels (BABIKER, 2013; HOU et al., 2022; LING et al., 2015; TODROS; TODESCO; BAGNO, 2021). In response to these challenges, bone tissue engineering has surfaced as a promising therapeutic avenue, leveraging the strategic use of biomaterials to recreate the intricate microenvironment and facilitate the stimulation of bone regeneration (BABIKER, 2013). This paradigm shift holds significant promise in addressing the shortcomings of traditional grafting techniques, offering a novel and potentially transformative solution for advancing bone regenerative therapies. Thus, tissue engineering, specifically the application of biomaterials, emerges as a pivotal strategy to enhance the efficiency of bone injury recovery, expediting the return of individuals to society quickly (BABIKER, 2013; CARDOSO et al., 2022; DA S. FELTRAN et al., 2019; HOU et al., 2022; LING et al., 2015; TODROS; TODESCO; BAGNO, 2021; TORRENTO et al., 2022).

Addressing the need for biomaterials that seamlessly integrate with bone tissue, our research aims to develop a biomaterial preserving bone mimetic characteristics, exemplified by Monetite (CaP). Additionally, we incorporate the functional predictability of hypoxia in tissue regeneration mechanisms (DA COSTA FERNANDES et al., 2021a; DE ALMEIDA et al., 2023). Hypoxia, known to stimulate angiogenesis, is intricately linked to osteogenesis mechanisms (DE ALMEIDA et al., 2023; STEGEN; VAN GASTEL; CARMELIET, 2015; ZELZER et al., 2001). To predict and harness this function, our proposed biomaterial introduces cobalt doping to Monetite (CoCaP), leveraging cobalt's role in inducing hypoxia. Cobalt, a transition metal essential

as a trace element in plants and animals, is capable of influencing cells by releasing metal ions into the extracellular environment (JANG et al., 2018; TAKAICHI et al., 2020). Previous applications of cobalt in metal alloys, such as Cobalt-Chromium (CoCr), in bone implants, prostheses, and stents underscore its familiarity, although limited attention has been directed towards its integration into ceramic biomaterials like calcium phosphates (DA COSTA FERNANDES et al., 2021a; DE ALMEIDA et al., 2023; JONITZ-HEINCKE et al., 2019; MADL et al., 2015).

Calcium phosphates, widely chosen as biomaterials due to their mineral similarity to bone and teeth, offer versatility in designing implantable biomaterials over time (STEVENS et al., 2005; WANG et al., 2009). Heat treatments, a common practice for obtaining crystalline phases, crystal sizes, and altering properties, are applied to calcium phosphates like Hydroxyapatite (HAp) and tricalcium phosphate (TCP) (BOHNER et al., 2008; RABIEI et al., 2020; SHEIKH et al., 2017; SINUSAITE et al., 2019). Monetite (CaP), a potential material for orthopedic and dental applications, is utilized in various forms, including coatings for metal prostheses, self-fixing injectable bone cement, and bone grafts (IDOWU et al., 2014; KO et al., 2015). In vitro studies demonstrate Monetite's ability to promote cell proliferation and elevate osteogenic gene expression (TAMIMI et al., 2012; TORRES et al., 2015), positioning it as a promising material for bone regeneration.

However, the structural changes observed in Monetite upon heating, influencing phases and cellular responses, prompt a need for a comprehensive understanding of its behavior under different temperature conditions (GALEA et al., 2008; SHEIKH et al., 2017). In this study, we subjected Monetite and Co-doped Monetite to heat treatments at 700, 900, and 1050°C, examining phase changes, crystallite size, porosity, and the subsequent biological effects. Characterization involved XRD, FTIR, Raman, and SEM/EDS assays, followed by the utilization of the materials in conditioning culture medium and challenging MC3T3-E1 cells. Assessment methods included MTT, CV, RTqPCR, and wound healing assays, providing insights into the impact of temperature variations on the material's properties and biological responses.

Methods

Synthesis of materials

The coprecipitation method was used for the syntheses starting from the following Almeida 2023 (DE ALMEIDA et al., 2023):Dibasic Sodium Phosphate (Na_2HPO_4, Sigma-Aldrich, 99%), Calcium Chloride ($CaCl_2$, Sigma-Aldrich, 97%), and Cobalt Chloride ($CoCl_2$, Sigma-Aldrich, 99%) were used in this study. Initially, Calcium Chloride and Cobalt Chloride were dissolved at a concentration of 50 mmol/L, maintaining a $Co^{2+}/(Co^{2+}+Ca^{2+})$ nominal ratio of 2 mol%, in water (18.2 mΩ cm). The solution was then added drop by drop into the Dibasic Sodium Phosphate

aqueous solution at a rate of 1 drop per second. The pH at the end of the precipitation process ranged between 5.8 and 6.5. After the dripping stage, the suspension was homogenized for 30 minutes using a magnetic stirrer and subsequently centrifuged for 15 minutes at 4000 rpm. The resulting solid was suspended in water, stirred on an orbital tube shaker for one hour, centrifuged once again, and finally dried in an oven at 80ºC. The end product was obtained in the form of powders. Following drying, the CaP's and CoCaPs were subjected to calcination at temperatures of 700, 900, and 1050ºC in a Muffle brand EDG oven (model F3000) for 2 hours with a ramp of 15ºC per minute. The resulting samples were named CaP, CoCaP, CaP700, CoCaP700, CaP900, CoCaP900, CaP1050, and CoCaP1050.

Thermogravimetry analyses (TGA)

Thermogravimetric analysis (TGA) and differential thermal analysis (DTA) were conducted employing a simultaneous thermal analyzer (STA 449 F3 Jupiter, Netzsch). Each sample, approximately 9.69 mg, was carefully placed in a 50 ml alumina crucible. TGA-DTA curves were generated with the following parameters: a temperature range of 30 to 1100°C, a heating rate of 10°C min^{-1}, and a flow rate of 50 mL min^{-1} under a dry air atmosphere.

Fourier transform infrared spectroscopy (FTIR)

Infrared spectroscopy was utilized to identify the functional groups of the material, employing a Nicolet Nexus 670 spectrometer (Thermo, USA). Sample preparation involved 200 mg KBr pellets, each containing 2% of the material. The analysis was conducted in transmittance mode with a resolution of 4 cm^{-1}, and the spectra represent averages of 200 scans.

Raman spectroscopy

The analysis of powdered samples was conducted using a Raman microscope (Renishaw Inc., Hoffman Estates, IL) equipped with a 514.5 nm laser line, 1800 lines/mm diffraction grating, 10 s acquisition time, laser power attenuated to 10%, and a 50× (NA = 0.75) dry objective (Leica Microsystems). This technique provides Raman bands, facilitating the detection of molecular vibrations in the samples. Consequently, FTIR and Raman spectroscopy may be considered complementary techniques for evaluating the molecular structure of the compounds within the samples.

X-ray diffraction (XRD)

XRD patterns were collected using a Rigaku diffractometer (DMax 2100PC), employing Ni-filtered CuK_{α} radiation (λ = 1.5406 Å; 40 kV; 15 mA), in Bragg-Brentano configuration,

continuous scan mode, at 4º for min^{-1} and a step size of 0.04º. The peaks were indexed using Search-Match software (Malvern Panalytical) and PDF-2 database (ICSD, 2003) (ALLMANN; HINEK, 2007; BELKLY et al., 2002; HELLENBRANDT, 2004; ZAGORAC et al., 2019). Rietveld method (GSAS software) with the EXPGUI interface was used for the structural refinement to obtain cell parameters and crystalline information. The refinements were carried out with a standard Y_2O_3 sample for instrumental contribution, using the Pseudo-Voigt, Chebyshev, and March-Dollase functions for profile, background, and preferred orientation adjustments, respectively. The crystallite size was calculated using Scherrer and Williamson-Hall equations from the FHWM (Full Width at Half Maximum) of the diffracted peaks, as detailed by Kaygili et al. (2017) (KAYGILI et al., 2017). The details of crystallographic datasheets of monetite and hydroxyapatite used in the refinements as well as the refinement data can be found in the supplementary material.

Scanning electron microscope (SEM)

SEM analyses were conducted using a JEOL model JSM-6010 Scanning Electron Microscope, operating with an acceleration voltage of 10 kV and a secondary electron detector. The semi-quantitative Energy-Dispersive X-ray Spectroscopy (EDS) analysis for Ca, P, O, and Co chemical elements was also performed using the same equipment detector and acceleration voltage (10 kV).

Porosity and surface area

Prior to analysis, the materials underwent heat treatment at 80ºC under vacuum conditions for a sufficient duration to achieve a pressure of <10 mmHg and a change rate of less than 5 μmHg/min. The sample carrier, containing the material, was isolated from the vacuum system during this time interval. Following mass determination, the isotherm assessment involved measuring the volume of N2 adsorbed at 77K on the solid (corrected to standard pressure-temperature conditions - CPTP). This was carried out under increasing relative pressures (adsorption isotherm, adsorption branch) until reaching saturation pressure, $P0 \approx 1$. The reverse path, starting from $P0 \approx 1$, was then performed to obtain the desorption branch of the adsorption isotherm. The profile of the adsorption isotherm and hysteresis offer insights into the texture of the solid. The measurement of the volume of N2 adsorbed in the relative pressure (P/P0) range between 0.03 and 0.20 (from the adsorption isotherm, adsorption branch) was employed to calculate the surface area (SBET). Additionally, the Barrett-Joyner-Halenda (BJH) method was utilized for the analysis of the pore size distribution, incorporating data from the isotherm's desorption branch.

Cell culture

The MC3T3-E1 cell line (pre-osteoblast) cultures were maintained in Alpha-MEM supplemented with antibiotics (100 U/mL penicillin, 100 mg/mL streptomycin) and 10% fetal bovine serum (FBS). Cultures were incubated at 37°C with 95% humidity and 5% CO2. For material testing, subconfluent cultures were exposed to a cell culture medium enriched with biomaterial (0.2g/mL), following ISO 10993-12 guidelines. To prepare the conditioned medium, the FBS-free medium was enriched for up to 24 hours with CaPs and CoCaPs. Subsequently, 10% FBS was added, and the resulting conditioned medium was used to challenge pre-osteoblasts. MC3T3 cells were cultivated under different conditions: Control (Ctrl, Alpha-MEM medium), Osteogenic Medium (O.M.), and conditioned medium derived from CaPs and CoCaPs, including CaP, CoCaP, CaP700, CoCaP700, CaP900, CoCaP900, CaP1050, and CoCaP1050.

Osteoblast differentiation

To induce differentiation, we treated pre-osteoblasts (MC3T3-E1, subclone 4) with ß-Glycerophosphate (10 mM), Dexamethasone (0.03 g/mL), and Ascorbic Acid (50 µg/mL) obtained from Sigma-Aldrich. The culture medium contained 10% FBS.

Cytotoxicity evaluated by MTT assay

Pre-osteoblasts were seeded into 96-well plates, and next, they were subjected to the CaP's and CoCaP 's-enriched media for up to 24 and 72 hours. Therefore, the cell culture medium was removed, and MTT solution (1 mg/mL^{-1}) was added to the cultures for up to 3 hours when the MTT-containing medium was removed, and 1 mL of absolute ethanol was added to solubilize the blue dye formed by viable cells. The absorbance was then measured at 570 nm using a microplate reader (SYNERGY-HTX multi-mode reader, Biotek, USA).

Cell adhesion assay

Cell adhesion was assessed using the crystal violet method. Cells were cultured conventionally, trypsinized, and seeded in 96-well microplates at a density of 100×10^3 cells/mL (100 µL/well) to investigate the impact of CaPs and CoCaPs-enriched media on cell adhesion. A control group, cultured with conventional medium, was included for each material group. Following 24 and 72 hours of exposure, cells were stained, and cell adhesion was evaluated by incorporating crystal violet, following previously described procedures. The absorbance was measured at 540 nm using a microplate reader (SYNERGY-HTX multimode reader, Biotek, USA) to estimate the number of adherent cells.

Wound healing assay

The cell migration and regeneration were estimated by using a scratch assay, as performed earlier (PINTO et al., 2022). The scratch assay estimates cell migration and regeneration. Briefly, the cells were cultured in 12-well plates at 4×10^4 cells/cm^2, and after 100% confluence, an introduced area was cleared using a pipet tip, and then monitoring of the healing and the migration of the cells up to 12h and 16h (PINTO et al., 2022). Thereafter, the cultures were subjected to fixation with 4% PFA and stained with Alizarin Red S. In the healing in vitro analysis, the wound healing area was measured in an inverted microscope with a coupled digital camera (Zeiss), and the acquired images were analyzed using the ImageJ software (NIH, Bethesda, MD).

RTqPCR

To investigate the molecular mechanisms associated with adaptation to each CaP, pre-osteoblasts were exposed to conditioned medium from each CaP and CoCaP for 3 and 7 days. Subsequently, cells were harvested, and total RNA was extracted using Ambion TriZOL Reagent (Life Sciences - Fisher Scientific Inc., Waltham, MA, USA). The RNA samples were treated with DNAse I (Invitrogen, Carls, CA, USA), following established protocols. Following the manufacturer's instructions, cDNA synthesis was carried out using the High-Capacity cDNA Reverse Transcription Kit (Applied Biosystems, Foster City, CA, USA). Real-time PCR was performed in 10 μL reactions containing PowerUpTM SYBRTM Green Master Mix 2x (5 μL) (Applied Biosystems, Foster City, CA, USA), 0.4 μmol/L of each primer, 50 ng of cDNA, and nuclease-free H_2O. The results were expressed as relative amounts of transcripts using GAPDH and 18S as reference genes (housekeeping genes) employing the cycle threshold (ct) method. Primers and reaction details are provided in **Table 1**.

Table 1. Primer sequences and details of the cycle conditions.

Gene (ID)	Primer	5'-3' Sequence	Reaction condition
Runx2 (12393)	Forward	GGACGAGGCAAGAGTTTCA	95°C - 15s; 60°C - 30s; 72°C - 60s
	Reverse	TGGTGCAGAGTTCAGGGAG	
Osterix (170574)	Forward	CCCTTCCCTCACTCATTTCC	95°C - 15s; 60°C - 30s; 72°C - 60s
	Reverse	CAACCGCCTTGGGCTTAT	
Osteocalcin (12096)	Forward	AGACTCCGGCGCTACCTT	95°C - 15s; 60°C - 30s; 72°C - 60s
	Reverse	CTCGTCACAAGCAGGGTTAAG	
BSP (15891)	Forward	GTACCGGCCACGCTACTTTCT	95°C - 15s; 60°C - 30s; 72°C - 60s
	Reverse	GTTGACCGCCAGCTCGTTTT	
Integrin α1 (109700)	Forward	TATCCTCCTGAGCGCCTTT	95°C - 15s; 60°C - 30s; 72°C - 60s
	Reverse	TGGCCTTTTGAAGAATCCAA	
Integrin β1 (16412)	Forward	CTGATTGGCTGGAGGAATGT	95°C - 15s; 60°C - 30s; 72°C - 60s
	Reverse	TGAGCAATTGAAGGATAATCATAG	

Fak (14083)	Forward	TCCACCAAAGAAACCACCTC	95°C - 15s; 60°C - 30s; 72°C - 60s
	Reverse	ACGGCTTGACACCCTCATT	
Src (20779)	Forward	TCGTGAGGGAGAGTGAGAC	95°C - 15s; 60°C - 30s; 72°C - 60s
	Reverse	GCGGGAGGTGATGTAGAAAC	
Cofilin (12631)	Forward	CAGACAAGGACTGCCGCTAT	95°C - 15s; 60°C - 30s; 72°C - 60s
	Reverse	TTGCTCTTGAGGGGTGCATT	
Rank-L (21943)	Forward	CGCTCTGTTCCTGTACTTTCGAGC	95°C - 15s; 60°C - 30s; 72°C - 60s
	Reverse	TCGTGCTCCCTCCTTTCATCAGGTT	
HIF1α (15251)	Forward	CATAAAGTCTGCAACATGGAAGGT	95°C - 15s; 60°C - 30s; 72°C - 60s
	Reverse	ATTTGATGGGTGAGGAATGGGTT	
VEGF (22339)	Forward	TGCAGATTATGCGGATCAAACC	95°C - 15s; 60°C - 30s; 72°C - 60s
	Reverse	TGCATTCACATTTGTTGTGCTGTAG	
Gapdh (14433)	Forward	AGGCCGGTGCTGAGTATGTC	95°C - 15s; 60°C - 30s; 72°C - 60s
	Reverse	TGCCTGCTTC ACCACCTTCT	
Il1β (16176)	Forward	GAC CTT CCA GGA TGA GGA CA	95°C - 15s; 60°C - 30s; 72°C - 60s
	Reverse	AGC TCA TAT GGG TCC GAC AG	
Il10 (16153)	Forward	CCA AGC CTT ATC GGA AAT GA	95°C - 15s; 60°C - 30s; 72°C - 60s
	Reverse	TTT TCA CAG GGG AGA AAT CG	
Il18 (16173)	Forward	ACT TTG GCC GAC TTC ACT GT	95°C - 15s; 60°C - 30s; 72°C - 60s
	Reverse	GGG TTC ACT GGC ACT TTG AT	
ALP (11647)	Forward	GAA GTC CGT GGG CAT CGT	95°C - 15s; 60°C - 30s; 72°C - 60s
	Reverse	CAG TGC GGT TCC AGA CAT AG	
Bmp2 (12156)	Forward	GGT CAC AGC TAA GGC CAT TGC	95°C - 15s; 60°C - 30s; 72°C - 60s
	Reverse	GCT TCC GCT GTT TGT GTT TG	
OPG (21943)	Forward	CAG AGA CTA ATA GAT CAA AGG CAG	95°C - 15s; 60°C - 30s; 72°C - 60s
	Reverse	ATG AAG TCT CAC CTG AGA AGA ACC	
eNOS (18127)	Forward	AAG CCG CAT ACG CAC CCA GAG	95°C - 15s; 60°C - 30s; 72°C - 60s
	Reverse	TGG GGT ACC GCT GCT GGG AGG	
MMP2 (17390)	Forward	AAC TTT GAG AAG GAT GGC AAG T	95°C - 15s; 60°C - 30s; 72°C - 60s
	Reverse	TGC CAC CCA TGG TAA ACA A	
MMP9 (17395)	Forward	TGT GCC CTG GAA CTC ACA CGA C	95°C - 15s; 60°C - 30s; 72°C - 60s
	Reverse	ACG TCG TCC ACC TGG TTC ACC T	
β-Actin (11461)	Forward	TCT TGG GTA TGG AAT CCT GTG	95°C - 15s; 60°C - 30s; 72°C - 60s
	Reverse	AGG TCT TTA CGG ATG TCA ACG	
18S (19791)	Forward	TAG TTG GAT CTT GGG AGC GG	95°C - 15s; 60°C - 30s; 72°C - 60s
	Reverse	TAG AAC CGC GGT CCT ATT CC	

Protein Carbonylation

MC3T3-E1 was grown in such as the other's biological testes and properly harvested for evaluating the protein's carbonylation as an indicator of oxidative stress using the alkaline method as described by Mesquita et al. (2014)(DA COSTA FERNANDES et al., 2021a; MESQUITA et al., 2014). The protein carbonyl concentrations were based on the average absorbance and the micromolar extinction coefficient of 2,4-Dinitrophenylhydrazine (DNPH) reagent under alkaline conditions (0.022308 μmol cm^{-1} at 450 nm). Carbonylated protein levels are expressed in nmol of DNPH/mg of protein.

Staining with Alkaline Phosphatase

Pre-osteoblasts were seeded at a concentration of 5 × 10^4 cells/mL in 24-well plates and treated when reaching semi-confluence with the medium conditioned by CaPs and CoCaPs for 3 and 7 days. The medium was refreshed every 2 days. Alkaline phosphatase (ALP) staining was conducted following the manufacturer's instructions using the SIGMAFAST BCIP/NBT tablet. Subsequently, the wells were washed with PBS, and the plate was photographed using an inverted microscope (Zeiss, Germany)

Statistical analysis

Statistical analyses were conducted using GraphPad Prism 7 software (GraphPad Software, USA). Variance analysis was performed through a two-way ANOVA, and post hoc analysis was carried out using Tukey's correction or non-parametric analysis. A p-value < 0.05 was considered statistically significant.

Results

After synthesis and thermal treatments, characterization tests revealed details about the phase and structural changes in Monetite and Co-doped Monetite. The thermogravimetric analysis depicted in **Fig. 1** reveals a similar event in both materials. The initial event, occurring around 190ºC, is possibly associated with the dehydration of water molecules bound within the structure or adsorbed from the environment. The second event, with mass losses of 5.69% and 7.43% between 400 and 480ºC, is attributed to the transformation of monetite into calcium pyrophosphate through the condensation of the HPO_4^{-2} group, according to the equation: $2CaHPO_4 \rightarrow \gamma Ca_2P_2O_7 + H_2O$, comparative studies is related to thermal conversion to calcium pyrophosphate by solid-state reaction..

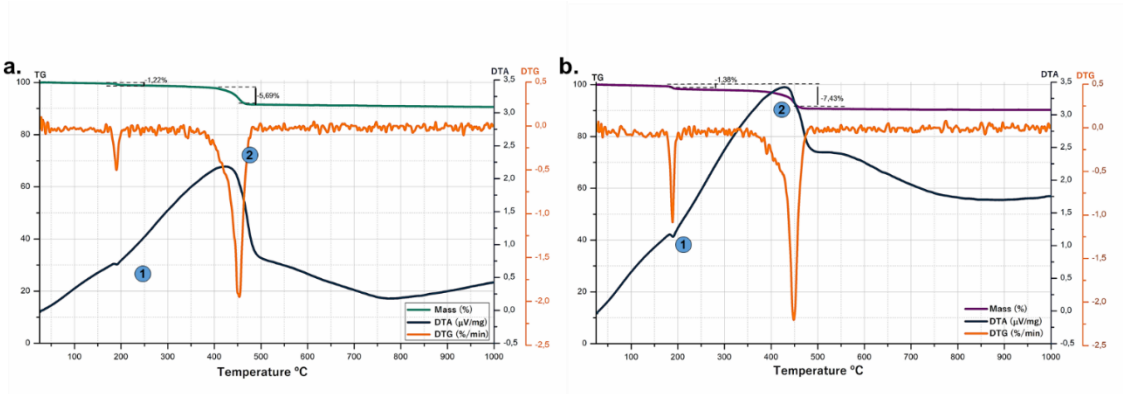

Fig. 1: Thermogravimetric analysis of (a) CaP and (b) CoCaP, illustrating one endothermic event linked to dehydration and two events associated with thermal decomposition.

The XRD tests and using ICSD showed in **Fig.2** and **Fig.3** the diffraction patterns of the materials when subjected to the thermal treatments, showing the differences in the peaks, and through refinement it was possible to understand the phase changes and crystal size.

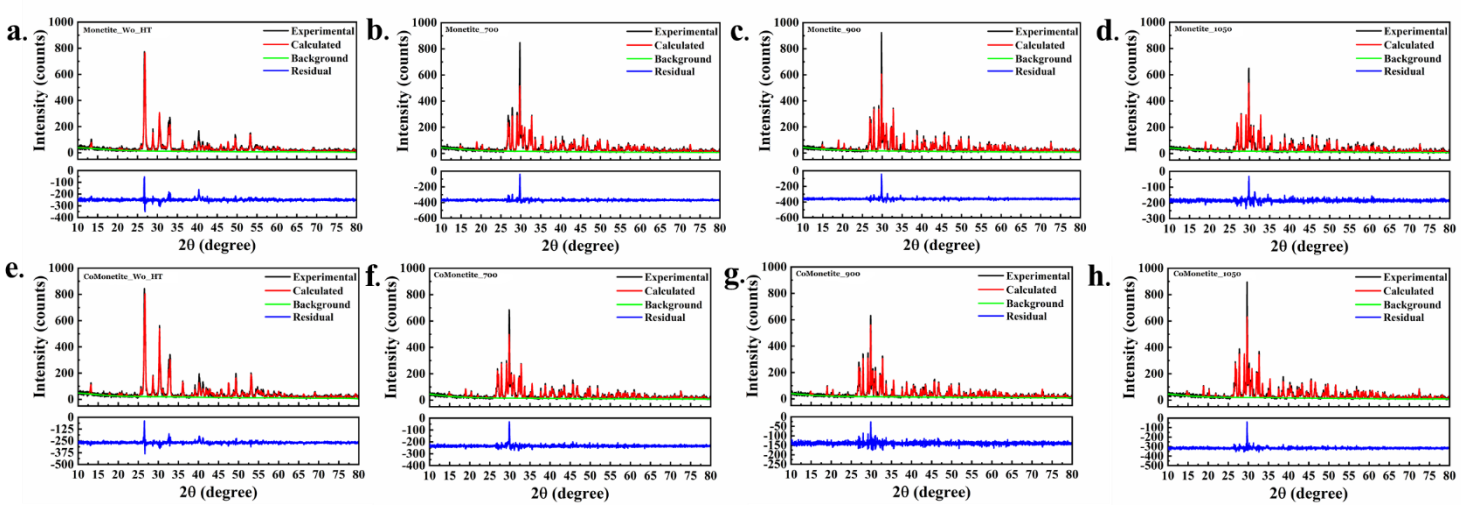

Fig. 2 - Visual plot of Rietveld refinements. **a.** Monetite_Wo_HT, **b.** Monetite_700, **c.** Monetite_900, **d.** Monetite_1050, **e.** Co-doped Monetite_Wo_HT, **f.** Co-doped Monetite_700, **g.** Co-doped Monetite_900, and **h.** Co-doped Monetite_1050.

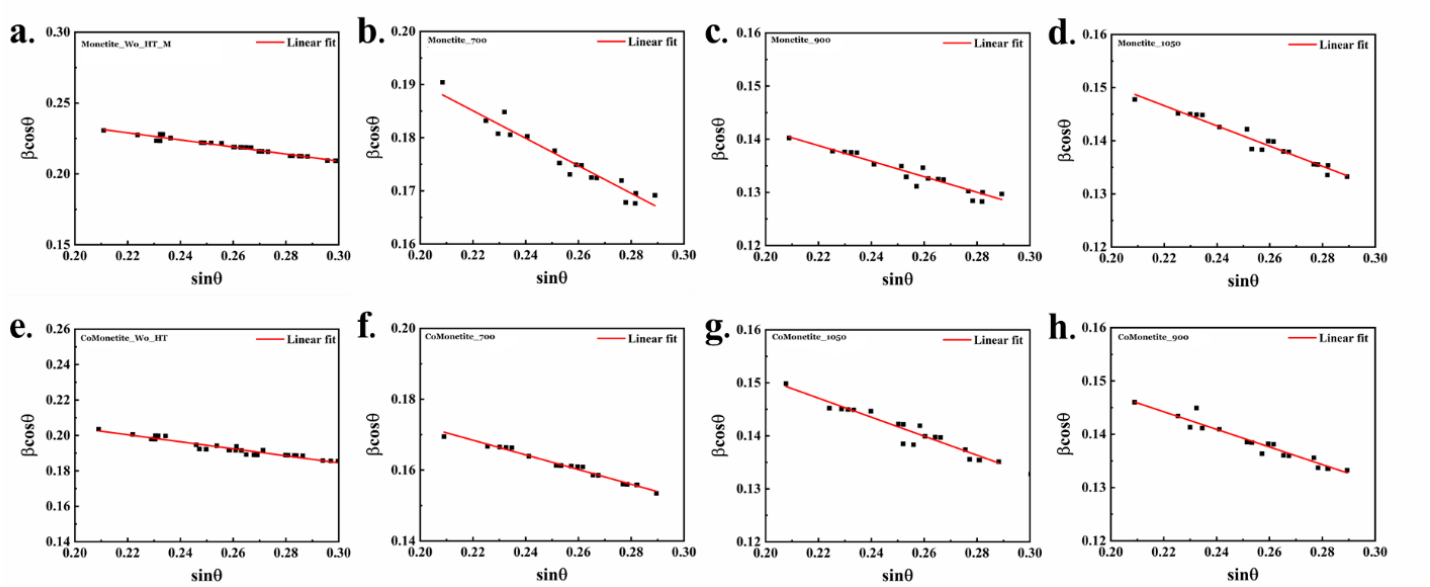

Fig. 3 - Visual plot of Williamson – Hall equation. **a.** Monetite_Wo_HT, **b.** Monetite_700, **c.** Monetite_900, **d.** Monetite_1050, **e.** Co-doped Monetite_Wo_HT, **f.** Co-doped Monetite_700, **g.** Co-doped Monetite_900, and **h.** Co-doped Monetite_1050. The results obtained by the refinement are Supplementary data.

The ASAP assay, as shown in **Table 2**, illustrates the impact of temperature on the pores and surface area of the materials, revealing a reduction in both area and the quantity and size of pores

Table 2 - SBET-specific area (m^2/g) of Monetite and Co-doped Monetite.

Samples	**m (g)**	**S_{BET} (m^2/g)**	**$V_{total\ pore}$ (CPPT) (cm^3/g) (d<683,9A)**	**$V_{total\ micropore}$ (CPPT) (cm^3/g)**	**Average Pore Diameter (A)**
Monetite	0,6498	4,8±1,0	18,54	0,000020	125
CoMonetite	0,6854	5,0±1,0	15,01	0,000021	112
CoMonetite 700	1,2035	2,5±1,0	5,74	0,000071	69
CoMonetite 900	2,2423	<1,0	1,65	0,000001	78
CoMonetite 1050	2,1532	<1,0	0,85	0,000004	-

The **Fig. 4** depicts the N2 adsorption isotherms at 77K for the Monetite, CoMonetite, CoMonetite 700, CoMonetite 900, and CoMonetite 1050 samples.

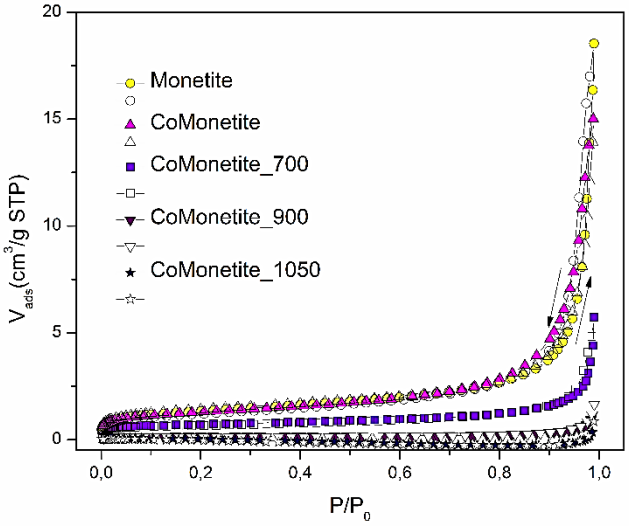

Fig. 4: N2 adsorption isotherms at 77K on Monetite and Co-doped Monetites treated at different temperatures (filled markers: adsorption branch and open markers: desorption branch).

Braunauer, Deming, Deming, and Teller proposed a classification associating the shape of isotherms with the characteristics and pore dimensions of the solid. The obtained isotherms for the samples indicate Type II behavior, suggesting non-porous solids or solids with pores in the range of mesopores (2.5 to 100 nm) or macropores (diameter greater than 50 nm). The distribution is broad for both CoMonetite and Monetite samples, with the presence of mesopores and macropores. There is also evidence of the presence of micropores (<50 Å) in most of the samples analyzed.

FTIR (**Fig. 5**) combined with Raman Spectroscopy (**Fig. 6**) highlights differences in the spectra of the materials, enabling the visualization of the formation of different phosphate phases. Monetite bands include a broad band (3600-3200 cm^{-1}) corresponding to hydroxyl vibrations, a peak around 1640 cm^{-1} indicative of water vibrations, a range between 1100-1000 cm^{-1} related to phosphate group vibrations, and a band around 600-500 cm^{-1} attributed to the stretching vibrations of the P-O-P group. Transformations into calcium pyrophosphates show changes, such as the disappearance or reduction of the hydroxyl band and shifts in peaks related to phosphate groups.

In Raman spectroscopy, characteristic peaks of monetite and pyrophosphates are identified. Monetite exhibits phosphate (PO_4) peaks in the 900 to 1100 cm^{-1} range, while pyrophosphates display P-O-P peaks in the 600 to 800 cm^{-1} range. Peaks related to P-OH bonds in some pyrophosphates are also observed. These peaks provide essential information for identifying and analyzing the molecular structures of monetite and pyrophosphates using Raman spectroscopy. The exact peak positions may vary based on sample purity and other experimental factors. Braunauer et al. proposed the classification, which associates the shape of the isotherm with the characteristics and pore dimensions of the solid. The isotherms obtained for the samples indicated that they are Type II, i.e. non-porous solids or with pores in the range of mesopores (2.5 to 100nm) or macropores (diameter greater than 50nm). The distribution is quite wide for CoMonetite and Monetite samples, with the presence of mesopores (2.5 to 100nm) and macropores (diameter greater than 50nm). There is evidence of the presence of micropores (<50 A) for most of the samples analyzed.

The FTIR (**Fig. 5**) combined with Raman Spectroscopy (**Fig. 6**), showed the differences in the spectra of the materials, making it possible to visualize the formation of different phases of the phosphate bands. The bands found in monetite can be summarized as follows: a broad band between 3600-3200 cm-1, corresponding to the vibrations of the hydroxyls (OH) present in the structure, a peak around 1640 cm^{-1}, indicative of the vibrations of the adsorbed water, a peak between 1100-1000 cm^{-1}, related to the vibrations of the phosphate groups (PO_4^{3-}), and a band around 600-500 cm^{-1}, this band is attributed to the stretching vibrations of the P-O-P group, which is also related to the presence of the phosphate group in the structure.

The peaks in the materials transformed into calcium pyrophosphates, showed the following changes: The disappearance or reduction of the broad hydroxyl band around 3500-3200 cm^{-1}, since pyrophosphates do not contain hydroxyls, 1128 cm^{-1}: ϒ6 PO_{3-} stretch in HPO_4^{2-}, 1100, 1093, 1047: ϒ3 asymmetric stretching of PO_4^{3-} or ϒ6 PO_3 stretching in HPO_4^{2-} , 965: ϒ1 symmetrical stretch of PO_4^{3-}, 918: ϒ3 P-OH stretch in HPO_4^{2-}, 650: OH vibrations of hydroxyl 616, 581: ϒ4 O-P-O strain in PO_4^{3-} or ϒ4 OP-O strain in HPO_4^{2-}, and 535: ϒ7 P-OH stretch in HPO_4^{2-}.

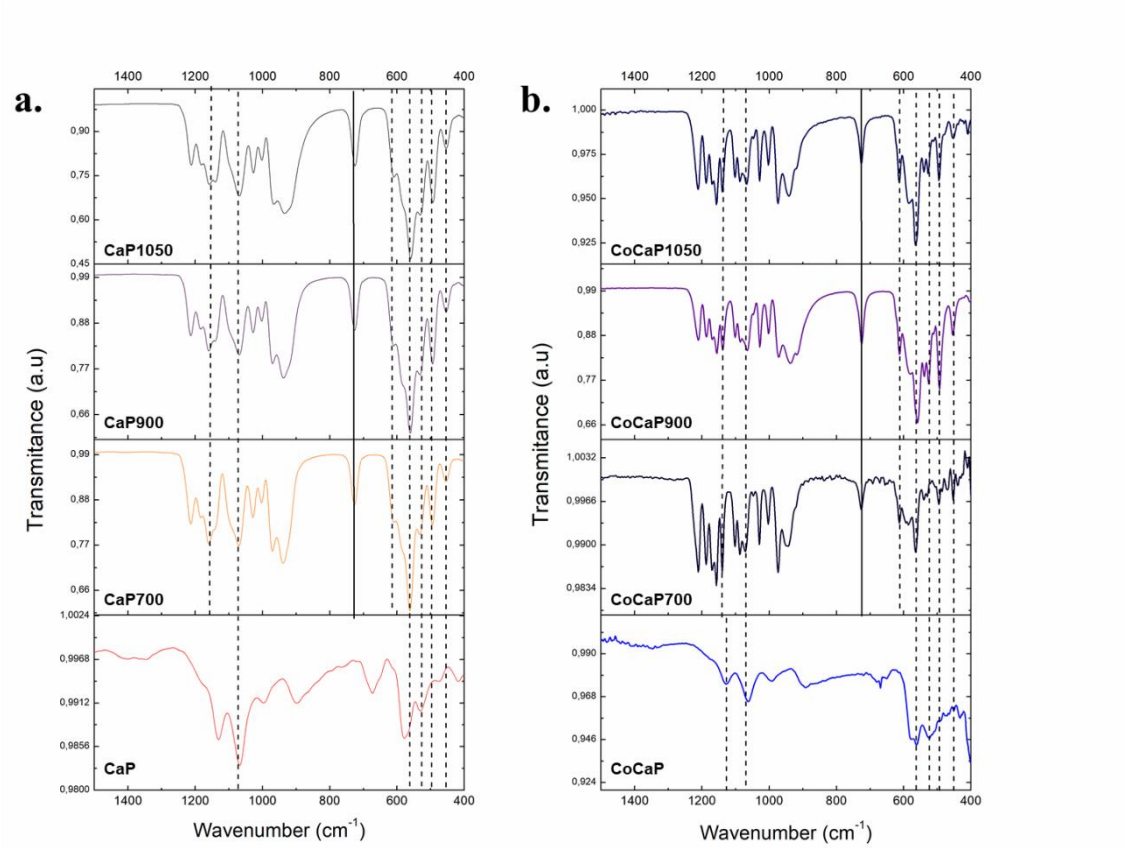

Fig. 5 - a. Monetite FTIR spectra, and **b.** Co-doped Monetite FTIR spectra.

In Raman spectroscopy, the characteristic peaks of monetite and pyrophosphates can be identified in different regions of the spectrum, and they provide valuable information about the molecular structure of these compounds. In monetite, it was possible to visualize the phosphate (PO_4) peak, in the region of approximately 900 to 1100 cm^{-1}, referring to angular deformation peaks and stretching vibration of the phosphate group (PO_4) present in the monetite structure. Phosphate (PO_4) and calcium (Ca) peaks: Around 500 cm^{-1}, it was possible to find two peaks related to the vibration modes of the phosphate group and calcium. In pyrophosphates, P-O-P peaks were identified: In the 600 to 800 cm^{-1} range, pyrophosphates exhibit characteristic peaks related to the vibrations of the P-O-P group, which are typical of this class of compounds. P-OH peaks: In some pyrophosphates, deformation and vibration peaks of the P-OH bonds can be found if there are hydroxyls attached to the phosphate group. These characteristic peaks are essential for identifying and analyzing the molecular structures of monetite and pyrophosphates samples and other experimental factors.

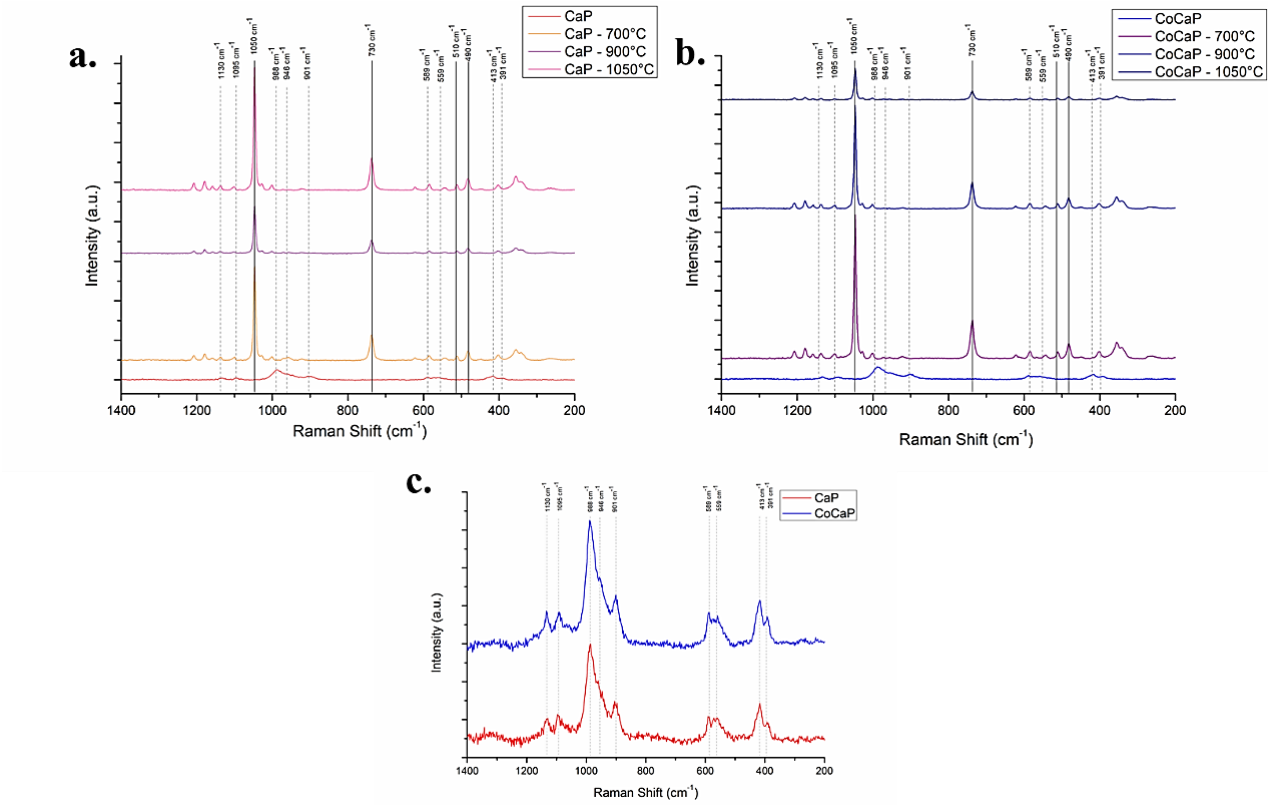

Fig. 6. Raman Spectroscopy: **a.** CaP's, **b.** CoCaP's, and **c.** CaP and CoCaP without heat treatment. Characteristic peaks of monetite are symbolized in the dashed lines and peaks of calcium pyrophosphates and other phases in the solid lines.

The SEM analysis in **Fig. 7** reveals variations in powder morphology. In the untreated materials, a sheet/plate-like profile is observed. At 700ºC, the sheets/plates exhibit a reduced size, and at 900 and 1050ºC, the material takes on a granular profile with particle aggregation, consistent with ASAP test results.

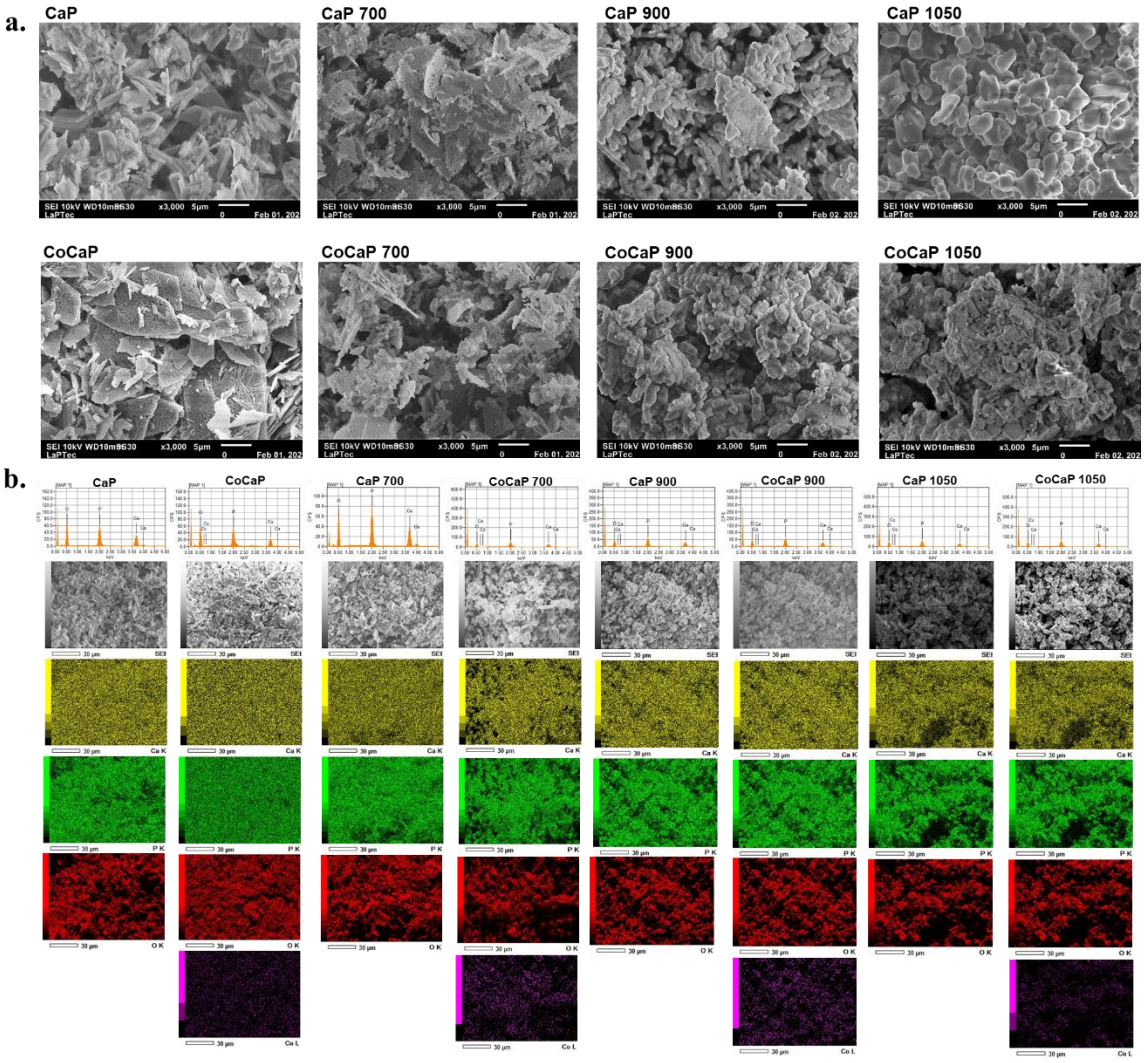

Fig. 7 - a. SEM micrographs. **b.** Semiquantitative analysis by EDS

The Wound Healing assay (**Fig. 8a**) demonstrated cell regeneration after cutting the cell mat. After 12 hours, cell regeneration was visible, with the CaP900 group showing regeneration similar to the Control group, and other treatments exhibiting superior regeneration compared to the Control. Among groups treated under the same thermal conditions, cobalt-doped groups showed greater regeneration than non-doped groups (**Fig. 8b**) (CaP vs CoCaP $^{aaaa}p < 0.0001$, CaP700 vs CoCaP700 $^{bbbb}p < 0.0001$, CaP900 vs CoCaP900 $^{cccc}p < 0.0001$, and CaP1050 vs CoCaP1050 $^{dddd}p < 0.0001$). In the 16-hour treatment (**Fig. 8c**), the CaP, CoCaP, CoCaP700, CoCaP900, and CoCaP1050 groups showed superior or similar regeneration compared to the Control group. The O.M., CaP700, CaP900, and CaP1050 groups exhibited inferior regeneration compared to the Control and their respective heat treatments with added cobalt. Among groups treated under the same thermal conditions, the CaP and CoCaP groups did not show statistically significant differences in regeneration. However, among thermally treated groups, differences were observed (CaP700 vs CoCaP700 $^{bbbb}p < 0.0001$, CaP900 vs CoCaP900 $^{cccc}p < 0.0001$, and CaP1050 vs CoCaP1050 $^{dddd}p < 0.0001$).

The MTT and Crystal Violet assays indicated that the materials exhibit no cytotoxicity and appear to induce increased cell proliferation. In the 24-hour MTT assay (**Fig. 8d**), only the O.M and CaP1050 groups did not show statistically significant differences compared to the control group, and neither exhibited cytotoxicity. In the 72-hour assay (**Fig. 8f**), only the CaP900 and CaP1050 groups did not show statistically significant differences from the control group, while the other groups showed an increase in dye concentration, potentially related to increased cell proliferation.

In the 24-hour Crystal Violet assay (**Fig. 8e**), only the CaP and CoCaP700 groups exhibited statistically significant differences; none of the other groups showed cytotoxicity. In the 72-hour assay (**Fig. 8g**), all groups showed no differences from the control group.

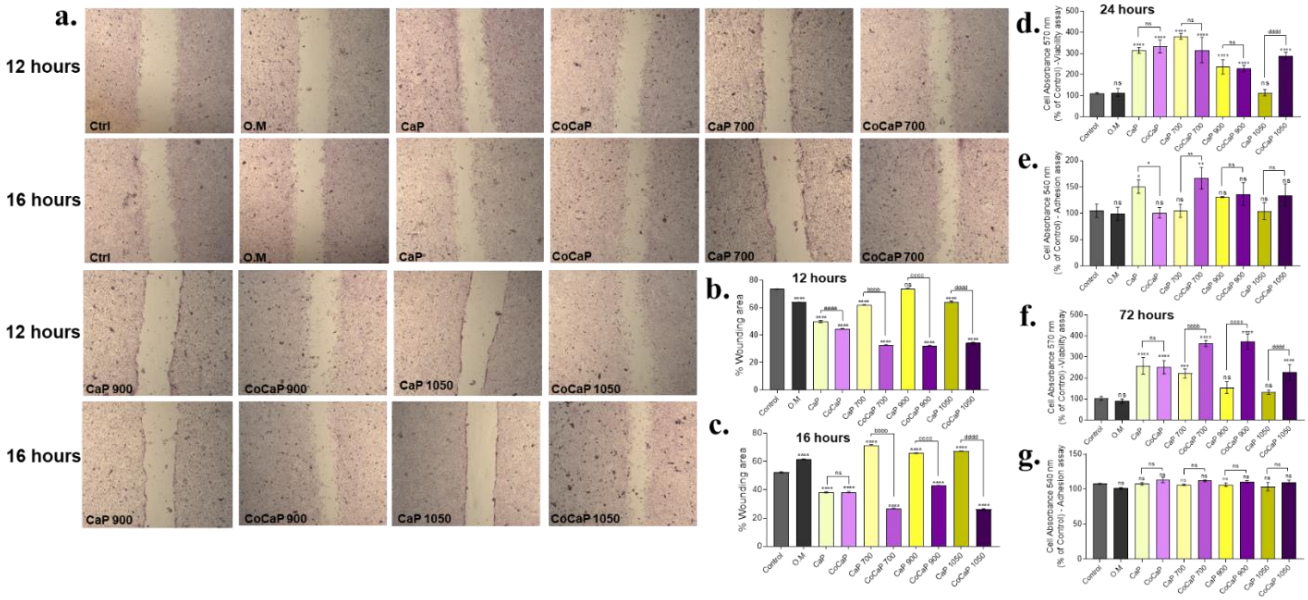

Fig. 8: a. Regeneration of cells after 12 and 16 hours. **b.** Quantification of the regenerated area in 12 hours, **c.** Quantification of the regenerated area in 16 hours, **d.** MTT 24 hours; **e.** CV 72 hours, **f.** MTT 72 hours, and **g.** CV 72 hours.

Gene expressions were evaluated at two treatment times, 3 and 7 days. For comparison, all groups were compared to the Control group and their respective heat treatments. The inflammatory phenotype was assessed by the expression of IL1β, IL10, and IL18 genes (**Fig. 9**). At the 3-day treatment time, in the IL1β gene (**Fig. 9a**), the CaP (****$p < 0.0001$), CoCaP (**$p = 0.0049$), CoCaP700 (***$p = 0.0001$), and CoCaP900 (****$p < 0.0001$) groups showed statistically significant differences compared to the Control group. CaP expression was increased compared to CoCaP ($^{a}p = 0.0424$), CoCaP700 had increased expression compared to CaP700 ($^{bbb}p = 0.0002$), and CoCaP900 showed increased expression compared to CaP900 ($^{cccc}p < 0.0001$). At the 7-day treatment time (**Fig. 9d**), the CoCaP (****$p < 0.0001$), CoCaP700 (**$p = 0.0050$), CoCaP900 (**$p = 0.019$), and CoCaP1050 (****$p < 0.0001$) groups showed increased expression compared to the

Control. Significant differences in expressions were observed among groups in the same conditions (CaP vs CoCaP $^{aaaaa}p < 0.0001$, CaP700 vs CoCaP700 $^{bb}p = 0.0015$, CaP900 vs CoCaP900 $^{c}p = 0.0187$, and CaP1050 vs CoCaP1050 $^{d}p = 0.0114$).

In the IL10 gene, at the 3-day treatment (**Fig. 9b**), the O.M. (**p = 0.0012), CaP700 (*p = 0.0185), CoCaP900 (****p < 0.0001), and CoCaP1050 (***p = 0.0004) groups showed a statistically significant increase compared to the Control group. Differences between treatments were found, with CoCaP 900 showing increased expression compared to CaP900 ($^{cccc}p < 0.0001$), and CoCaP1050 exhibiting an increase compared to CaP1050 ($^{dddd}p < 0.0001$). In the 7-day treatment (**Fig. 9e**), significant increases were found in the CaP (*p = 0.0488), CoCaP (**p = 0.0011), CaP700 (**p = 0.0023), CoCaP900 (****p < 0.0001), CaP1050 (****p < 0.0001), and CoCaP1050 (****p < 0.0001) groups compared to the Control. Between treatments, differences were found in the groups treated at 700 and 900°C, with an increase in expression in the CaP700 group ($^{bb}p = 0.0012$) compared to CoCaP700, and increased expression in CoCaP900 ($^{cccc}p < 0.0001$) compared to CaP900.

IL18 expression (**Fig. 9c**) increased in the O.M. (***p = 0.0001), CaP (****p < 0.0001), CaP700 (**p = 0.0092), and CaP900 (****p < 0.0001) groups and decreased in CoCaP700 (*p = 0.0290) and CoCaP900 (**p = 0.0067) compared to Control. Statistically significant differences were found between the groups, with non-doped groups showing increased expressions compared to cobalt-doped ones (CaP vs CoCaP $^{aaaaa}p < 0.0001$, CaP700 vs CoCaP700 $^{bbbb}p < 0.0001$, and CaP900 vs CoCaP900 $^{cccc}p < 0.0001$). In the 7-day treatment (**Fig. 9f**), expression increased in the CaP900 (**p = 0.0042) and CaP1050 (****p < 0.0001) groups compared to the Control. Among the treatments, the CaP700, CaP900, and CaP1050 groups (CaP700 vs CoCaP700 $^{bb}p = 0.0019$, CaP900 vs CoCaP900 $^{cccc}p < 0.0001$, and CaP1050 vs CoCaP1050 $^{dddd}p < 0.0001$) showed increases compared to their respective cobalt groups.

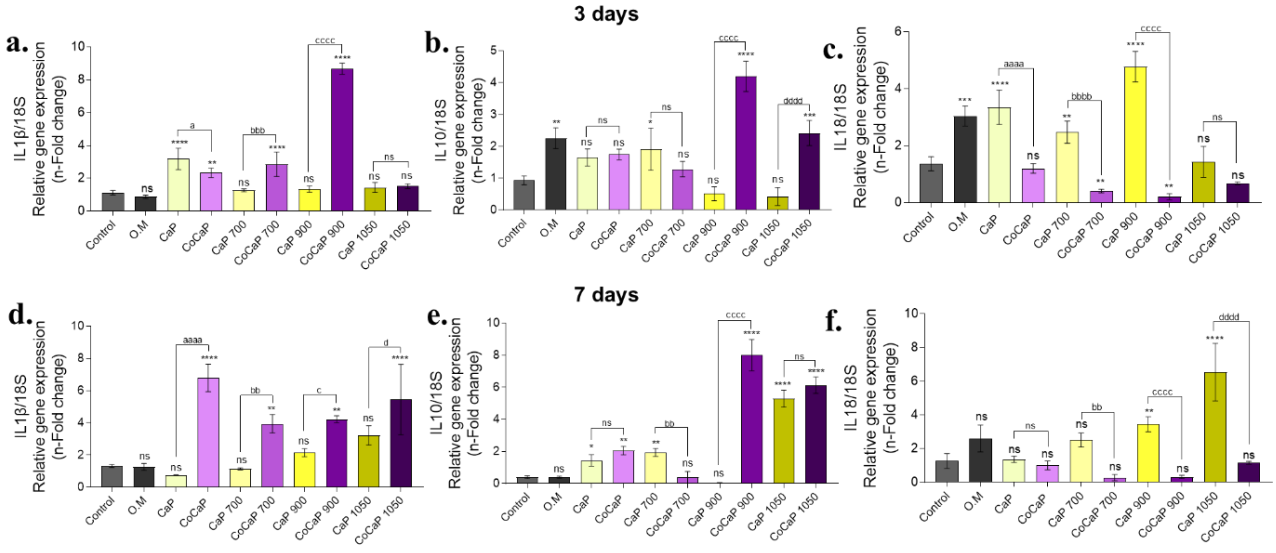

Fig. 9. The inflammatory phenotype: 3-day treatments. **a.** IL1β, **b.** IL10, **c.** IL18, 7-days treatments. **d.** IL1β, **e.** IL10, and **f.** IL18.

Genes involved in adhesion and ECM remodeling processes were assessed (**Fig. 10**), including Integrin-α1, Integrin-β1, Fak, Src, and Cofilin. In the 3-day treatment, Integrin-α1 expression (**Fig. 10a)** significantly increased in Control in the CoCaP700 (****$p < 0.0001$) and CoCaP900 (****$p < 0.0001$) groups. Differences in expression were found between the cobalt-doped and non-doped groups (CaP700 vs CoCaP700 $^{bbbb}p < 0.0001$, and CaP900 vs CoCaP900 $^{cccc}p < 0.0001$). In the 7-day treatment (**Fig. 10f**), the CoCaP900 (****$p < 0.0001$) and CoCaP1050 (****$p < 0.0001$) groups showed statistically significant increases. Differences in expression were found between groups treated under the same conditions, with materials containing cobalt showing increased expression compared to those without (CaP vs CoCaP $^{a}p = 0.0211$, CaP900 vs CoCaP900 $^{cccc}p < 0.0001$, and CaP1050 vs CoCaP1050 $^{dddd}p < 0.0001$).

In the analysis of the Integrin-β1 gene (**Fig. 10b**), in the 3-day treatment, statistically significant differences were found in the O.M. (****$p < 0.0001$) and CaP1050 (****$p < 0.0001$) groups. Differences in expression were observed in groups treated at 1050ºC, with CaP1050 showing increased expression compared to CoCaP1050 ($^{dddd}p < 0.0001$). In the 7-day treatment (**Fig. 10g**), the O.M. (*$p = 0.0010$), CaP (**$p = 0.0018$), CoCaP (**$p = 0.0010$), CaP900 (*$p = 0.0102$), CoCaP900 (****$p < 0.0001$), and CaP1050 (****$p < 0.0001$) groups showed a statistically significant increase. Differences were found between treatments under the same thermal conditions, with the CaP700 and CoCaP700 groups showing increased expression ($^{b}p = 0.0138$), and CaP1050 vs. CoCaP1050 ($^{dddd}p < 0.0001$), with increases in non-cobalt groups compared to cobalt groups.

In Src expression, in the 3-day treatment (**Fig. 10c**), statistically significant increases were found in the O.M (*$p = 0.0344$), CoCaP700 (****$p < 0.0001$), and CoCaP1050 (*$p = 0.0399$)

groups compared to Control. The CoCaP700 group showed an increase in expression compared to CaP 700 ($^{bbbb}p < 0.0001$). In the 7-day treatment (**Fig. 10h**), expression increased in the O.M. (**p = 0.0097), CoCaP (****p < 0.0001), CoCaP700 (****p < 0.0001), CoCaP900 (****p < 0.0001), and CoCaP1050 (****p < 0.0001) groups. Differences in expression were observed between CaP and CoCaP groups (CaP vs CoCaP $^{aaaaa}p < 0.0001$, CaP700 vs CoCaP700 $^{bbbb}p < 0.0001$, CaP900 vs CoCaP900 $^{cccc}p < 0.0001$, and CaP1050 vs CoCaP1050 $^{dddd}p < 0.0001$).

In the expression of Fak, in the 3-day treatment (**Fig. 10d**), increases were found in expressions compared to Control in the CaP (****p < 0.0001), CoCaP (****p < 0.0001), CaP700 (****p < 0.0001), CoCaP900 (****p < 0.0001), and CaP1050 (****p < 0.0001) groups. Differences in expression were observed between the cobalt and non-cobalt groups (CaP vs CoCaP $^{aaaaa}p < 0.0001$, and CaP900 vs CoCaP900 $^{cccc}p < 0.0001$), with increased expression in cobalt groups compared to those without. At 7-day treatment (**Fig. 10i**), expression increased in the O.M. (***p = 0.0004), CaP1050 (****p < 0.0001), and CoCaP1050 (****p < 0.0001) groups compared to Control. Between treatments, CaP and CoCaP groups showed a small increase in expression in CoCaP ($^{aa}p = 0.0029$), and the CaP1050 group showed an increase compared to CoCaP1050 ($^{dd}p = 0.0030$).

In Cofilin expression (**Fig. 10e**), the O.M. (****p < 0.0001), CaP (****p < 0.0001), and CoCaP900 (**p = 0.0015) groups showed an increase in expression compared to Control. The CoCaP900 (**p = 0.0015) and CoCaP1050 (*p = 0.0185) groups showed a decrease. Between treatments under the same thermal conditions, expression increased in the CaP group compared to CoCaP ($^{aaaaa}p < 0.0001$) and increased in CoCaP900 compared to CaP900 ($^{ccc}p = 0.0008$). In the 7-day treatment (**Fig.** 10j), expressions increased in O.M. (***p = 0.0009), and CoCaP1050 (****p < 0.0001) compared to Control. Among the treatments, only the CoCaP1050 group ($^{dddd}p < 0.0001$) showed an increase in expression compared to CaP1050.

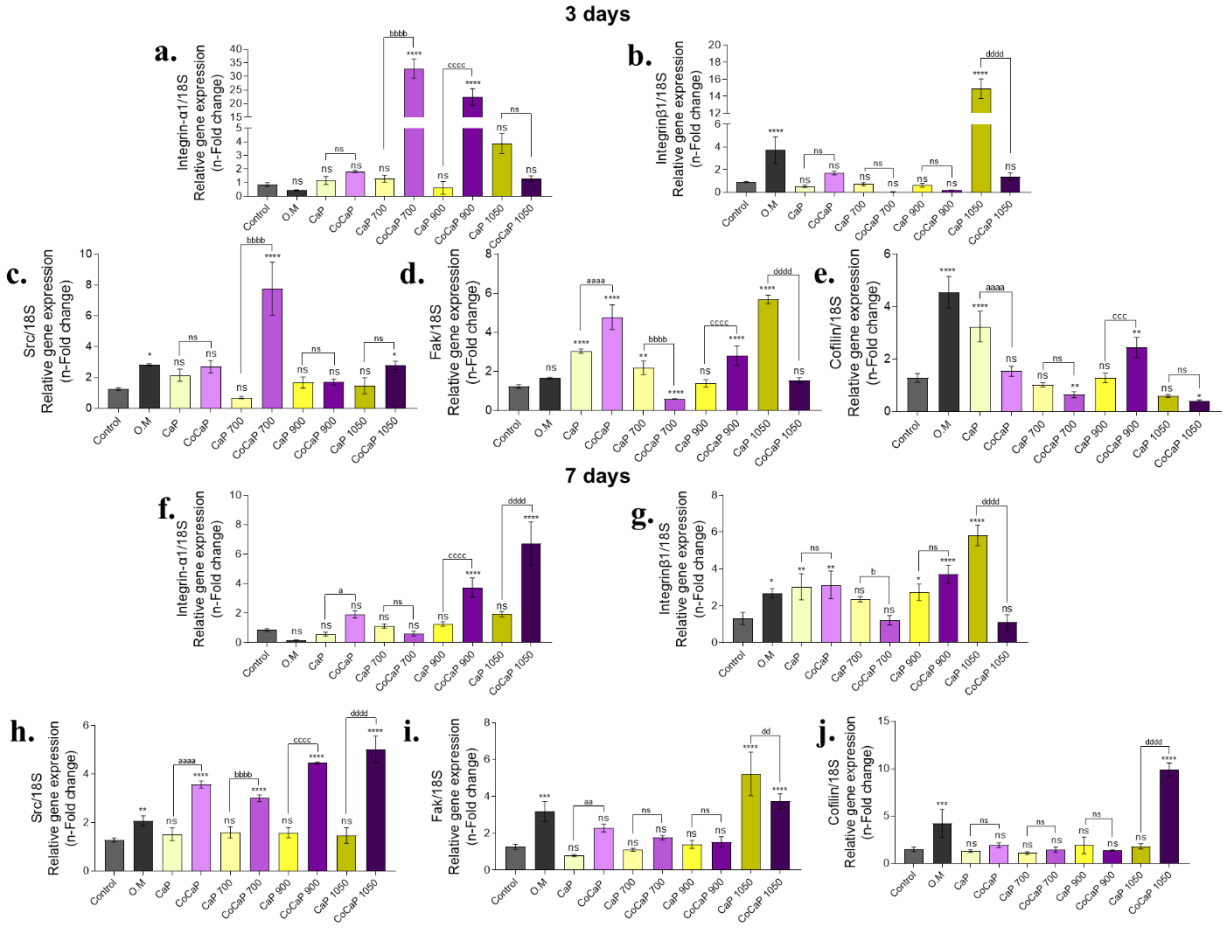

Fig. 10. Genes involved in adhesion and ECM remodeling: 3-day treatment: **a.** Integrin-α1, **b.** Integrin-β1 **c.** Src **d.** Fak **e.** Cofilin, 7-day treatment: **f.** Integrin-α1, **g.** Integrin-β1, **h.** Src, **i.** Fak, and **j.** Cofilin.

Genes involved in osteogenesis processes, such as Runx2, Bsp, Osterix, Osteocalcin, Alp, and Bmp2, were evaluated and illustrated in **Fig. 11**. In the 3-day treatment (**Fig. 11a**), the Runx2 gene showed a statistically significant increase in expression in the CoCaP (**p = <0.0024) and CaP1050 (****p = <0.0001) groups compared to Control. Among treatments under the same thermal conditions, the CoCaP (^{aa}p = 0.0026) and CoCaP700 (^{b}p = 0.0101) groups exhibited increased expression compared to CaP and CaP700, respectively. The CaP1050 group showed an increase compared to CoCaP1050 (^{dddd}p = <0.0001). In the 7-day treatment (**Fig. 11g**), the O.M. (****p = <0.0001), CoCaP (****p = <0.0001), CaP700 (***p = 0.0002), CoCaP900 (****p = <0.0001), CaP1050 (****p = <0.0001), and CoCaP1050 (****p = <0.0001) groups showed an increase in expression compared to Control. Among the treated groups, CaP700 and CaP1050 (^{bbbb}p = <0.0001 and ^{dddd}p = <0.0001) showed a significant increase compared to CoCaP700 and CoCaP1050, respectively. CoCaP and CoCaP900 showed an increase compared to CaP and CoCaP900 (^{aaaa}p = <0.0001 and ^{cccc}p = <0.0001).

In the Osterix gene, in the 3-day treatment (**Fig. 11b**), the CoCaP (*p = 0.0153), CaP700 (****p = <0.0001), and CoCaP1050 (*p = 0.0187) groups showed a statistically significant

increase compared to Ctrl. Between-group differences were observed, with the CoCaP1050 group showing an increase compared to CaP1050 (^{dd}p = 0.0014), and an increase in the CaP700 group compared to CoCaP700 (^{bb}p = 0.0010). In the 7-day treatment (**Fig. 11h**), the CoCaP (****p = <0.0001), CaP700 (***p = 0.0003), and CoCaP900 (****p = <0.0001) groups showed an increase in expression compared to Control. Among the treated groups, the CoCaP (^{aaaa}p = <0.0001) and CoCaP900 (^{cccc}p = <0.0001) showed an increase compared to CaP and CaP900, respectively. The CaP700 group (^{bbb}p = 0.0003) showed an increase compared to CoCaP700.

Bsp expression at 3 days of treatment (**Fig. 11c**) was increased in the O.M. (****p = <0.0001), CaP (*p = 0.0109), CoCaP (****p = <0.0001), and CaP1050 (****p = <0.0001) groups. Among the treatments, the CaP900 (^{c}p = 0.0193) and CaP1050 groups (^{dddd}p = <0.0001) showed an increase compared to their respective cobalt groups. In the 7-day treatment (**Fig.** 11i), BSP expression was increased in the O.M. (****p = <0.0001) and CaP900 (****p = <0.0001) groups, when compared to Control. Among the groups, CaP900 showed a significant increase compared to CoCaP900 (^{ccc}p = 0.0008).

The expression of Alp, upon treatment for 3 days (**Fig. 11d**), was increased in the CoCaP (****p = <0.0001) and CaP900 (**p = 0.0088) groups compared to Control. Among the groups, the CoCaP group showed a significant increase compared to CaP (^{aaaa}p = <0.0001), and the CaP900 group (^{cc}p = 0.0063) showed an increase compared to CoCaP900. In the 7-day treatment (**Fig. 11j**), the CoCaP (****p = <0.0001), CoCaP700 (**p = 0.0014), CoCaP900 (****p = <0.0001), CaP1050 (***p = 0.0003), and CoCaP1050 (****p = <0.0001) groups showed a significant increase compared to the Control. Among the groups, those doped with cobalt showed an increase compared to the non-doped groups (CaP vs CoCaP ^{aaaa}p = <0.0001, CaP700 vs CoCaP700 ^{bbb}p = 0.0010, CaP900 vs CoCaP900 ^{cccc}p = <0.0001, and CaP1050 vs CoCaP1050 ^{ddd}p = 0.0009).

In Bmp2, in the 3-day treatment (**Fig. 11e**), the O.M. (***p = 0.0008) and CoCaP (****p = <0.0001) groups showed a statistically significant increase, and the CaP700 (*p = 0.0108), CaP900 (*p = 0.0156), and CaP1050 (**p = 0.0073) groups showed a reduction compared to Control. Among the groups, CoCaP showed an increase compared to CaP (^{aaaa}p = <0.0001), and the CaP700 (^{b}p = 0.0214) and CaP900 (^{c}p = 0.0401) groups showed a reduction in expression compared to CoCaP700 and CoCaP900, respectively. In the 7-day treatment (**Fig. 11k**), CoCaP (****p = <0.0001) and CaP1050 (****p = <0.0001) groups showed a significant increase compared to Control. Between treatments, the CoCaP group showed an increase compared to CaP (^{aaaa}p = <0.0001), the CaP700 group showed a reduction in expression compared to CoCaP700 (^{bb}p = 0.0061), and the CaP1050 group showed an increase compared to CoCaP1050 (^{dddd}p = <0.0001).

Osteocalcin expression, in the treatment for 3 days (**Fig. 11f**), the CaP (****p = <0.0001), CaP700 (****p = <0.0001), and CaP1050 (****p = <0.0001) groups showed an increase in its

expression compared to Control. Among the treatments, the groups without Cobalt showed an increase compared to those doped with cobalt (CaP vs CoCaP ^{aaa}p = 0.0027, CaP700 vs CoCaP700 ^{bbb}p = 0.0007, and CaP1050 vs CoCaP1050 ^{dddd}p = <0.0001). At 7-day treatment (**Fig. 11l**), the O.M. (****p = <0.0001), CaP (****p = <0.0001), CoCaP (****p = <0.0001), CaP700 (****p = <0.0001), CoCaP700 (****p = <0. 0001), CaP900 (****p = <0.0001), and CoCaP900 (****p = <0.0001) showed a reduction compared to Control, and the CaP1050 group (****p = <0.0001) showed an increase. Among the groups, CaP1050 showed an increase compared to CoCaP1050 (^{dddd}p = <0.0001).

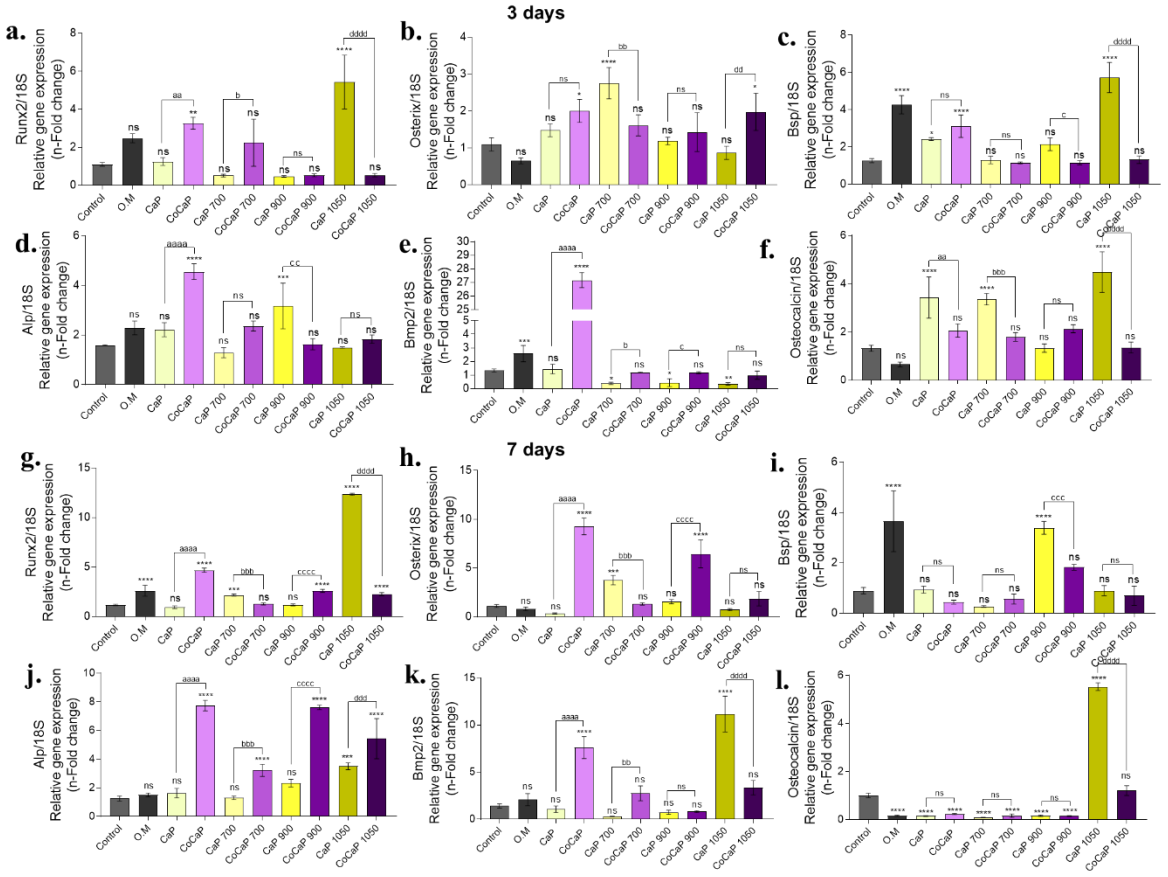

Fig. 11. Genes involved in osteogenesis processes: 3-day treatment: **a.** Runx2, **b.** Osterix, **c.** Bsp, **d.** Alp, **e.** Bmp2, and **f.** Osteocalcin. 7-days treatment: **g.** Runx2, **h.** Osterix, **i.** Bsp, **j.** Alp, **k.** Bmp2, and **l.** Osteocalcin

The OPG and RANKL genes, involved in bone resorption activity, were evaluated. In the 3-day treatment (**Fig. 12a**), Opg showed increased expression in the CaP (**p = 0.0049) and CoCaP (****p = <0.0001) groups compared to the Control; in the others, no statistically significant differences were found. Among the groups, CoCaP had its expression increased compared to CaP (^{aaaa}p = <0.0001). In the 7-day treatment (**Fig. 12f**), expression was increased in CoCaP (****p = <0.0001), CoCaP700 (****p = <0.0001), CoCaP900 (****p = <0.0001), CaP1050 (****p = <0.0001), and CoCaP1050 (**p = 0.0050) compared to the Control. Among the groups, those with

Cobalt had their expressions increased compared to those without doping (CaP vs CoCaP ^{aaaaa}p = <0.0001, CaP700 vs CoCaP700 ^{bbbb}p = <0.0001, and CaP900 vs CoCaP900 ^{cccc}p = <0.0001).

The expression of Rank-L in the treatment for 3 days (**Fig**. **12b**) showed an increase when compared to the Control in the CaP (****p = <0.0001), CoCaP (****p = <0.0001), CaP900 (***p = 0.0001), CoCaP900 (**p = 0.0075), and CoCaP1050 (****p = <0.0001) groups. Among the groups, CoCaP and CoCaP1050 showed increases in their expression relative to their respective groups without cobalt (CaP vs CoCaP (^{aaaaa}p = <0.0001), and CaP1050 vs CoCaP1050 (^{dddd}p = <0.0001)). In the 7-day treatment (**Fig**. **12g**), the expression of CoCaP (****p = <0.0001), CoCaP700 (****p = <0.0001), CaP900(**p = 0.0033), CoCaP900 (****p = <0.0001), CaP1050 (***p = 0.0005), and CoCaP1050 (**p = 0.0033) showed a statistically significant increase compared to the Control. Among the groups, significant increases were found in the CoCaP (^{aaaa}p = <0.0001) and CoCaP700 (^{bb}p = 0.0020) when compared with CaP and CaP700, respectively.

To evaluate the effects of Cobalt and heat treatment on angiogenesis and hypoxia, the expressions of VEGF, Hif1α, and eNOS were assessed. In the 3-day treatment (**Fig**. **12c**), VEGF expression was statistically increased in CaP (****p = <0.0001), CaP1050 (****p = <0.0001), and CoCaP1050 (****p = <0.0001) groups and decreased in CaP700 (**p = 0.0096), CaP900 (**p = 0.0027), and CoCaP900 (**p = 0.0016) when compared to the Control. Among the groups, CaP and CaP 1050 showed an increase in their expression compared to CoCaP (^{aaaa}p = <0.0001) and CoCaP1050 (^{dddd}p = <0.0001), respectively, and between CaP700 and CoCaP700 (^{bb}p = 0.0100), the group without cobalt showed a reduction in its expression when compared to the one with cobalt. In the treatment for 7 days (**Fig. 12h**), the expression in the O.M. (****p = <0.0001), CoCaP900 (****p = <0.0001), and CoCaP1050 (****p = <0.0001) groups showed an increase, and the CaP (****p = <0.0001), CaP700 (****p = <0.0001), CoCaP700 (****p = <0.0001), CaP900 (****p = <0.0001) groups showed a reduction in their expressions compared to the Control. Among the groups, CoCaP, CoCaP900, and CoCaP1050 showed an increase compared to their respective groups without cobalt doping (CaP vs CoCaP ^{aaaaa}p = <0.0001, CaP900 vs CoCaP900 ^{cccc}p = <0.0001, and CaP1050 vs CoCaP1050 ^{dddd}p = <0.0001).

In the expression of Hif1α, in the treatment for 3 days (**Fig. 12d**), the CaP (***p = 0.0010), CoCaP (****p = <0.0001), and CaP1050 (****p = <0.0001) groups showed an increase in its expression when compared to the Control. Among the groups, CaP1050 (^{dddd}p = <0.0001) showed a significant increase in its expression compared to CoCaP1050. In the treatment for 7 days (**Fig. 12i**), the expression was increased in CoCaP (****p = <0.0001), CoCaP700 (**p = 0.0010), and CoCaP900 (****p = <0.0001), in the other groups, there were no statistically significant differences. Among the groups, CoCaP, CoCaP700, and CoCaP900 showed an increase

in their expression compared to their respective groups without cobalt (CaP vs CoCaP $^{aaaaa}p$ = <0.0001, CaP700 vs CoCaP700 ^{bbb}p = 0.0004, and CaP900 vs CoCaP900 ^{cccc}p = <0.0001).

In the expression of eNOS, in the treatment for 3 days (Fig. 12e), the O.M. (****p = <0.0001), CaP (**p = 0.0015), CoCaP (****p = <0.0001), CaP700 (***p = 0.0008), CoCaP900 (****p = <0.0001), and CaP1050 (****p = <0.0001) groups showed an increase compared to the Control. Among the groups, CoCaP (^{aaaa}p = <0.0001) and CoCaP900 (^{cccc}p = <0.0001) showed increases relative to CaP and CaP900, and CaP 700 (^{b}p = 0.0447) and CaP1050 (^{dd}p = 0.0010) showed increases relative to CoCaP700 and CoCaP1050. In the 7-day treatment (**Fig. 12j**), O.M. (**p = 0.0011), CoCaP (****p = <0.0001), CaP700 (****p = <0.0001), CaP900 (**p = 0.0025), and CaP1050 (**p = 0.0048) showed statistically significant increases compared to the Control. Among the groups, CoCaP showed an increase in its expression relative to CaP (^{aaaa}p = <0.0001), and CaP700 (^{bb}p = 0.0043) and CaP900 (^{ccc}p = 0.0007) showed significant increases relative to CoCaP700 and CoCaP900.

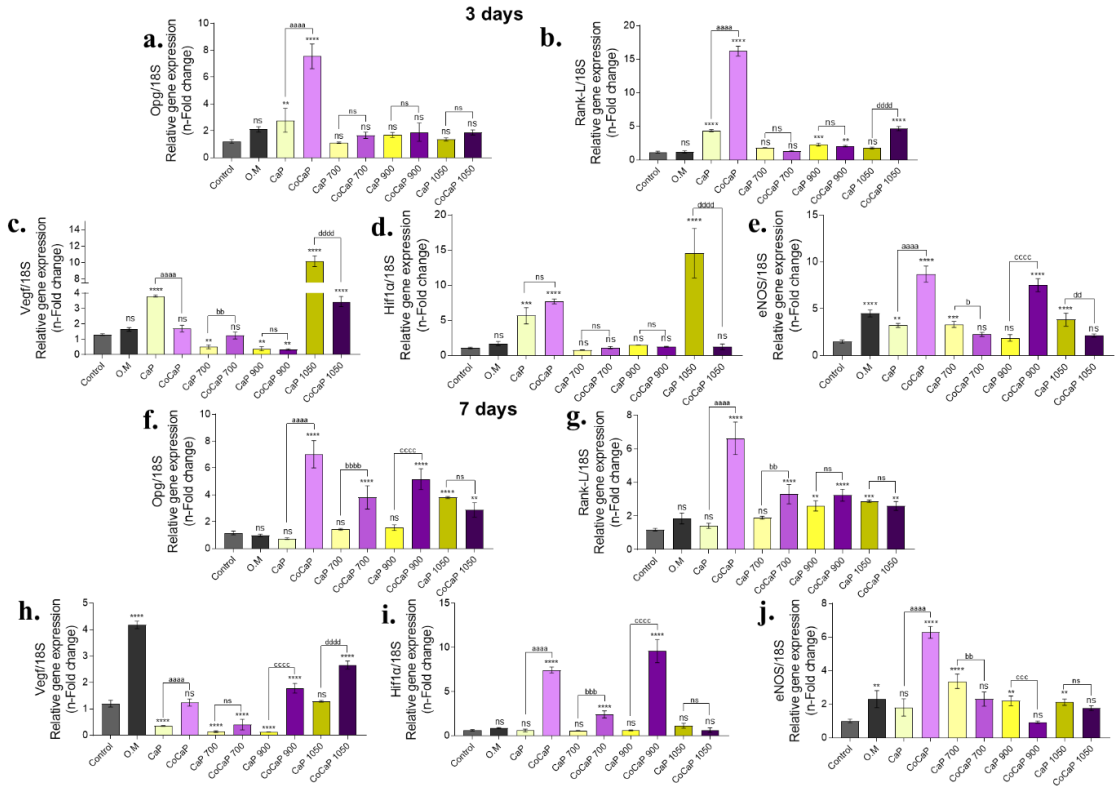

Fig. 12. Genes involved in Reabsorption and Angiogenesis processes: 3-day treatment: **a.** OPG, **b.** RANKL, **c.** VEGF, **d.** Hif1α, and **e.** eNOS. 7-days treatment: **f.** OPG, **g.** RANK-L, **h.** VEGF, i. Hif1α, and **j.** eNOS.

The expression of the metalloproteinases MMP2 and MMP9 was assessed. MMP2 expression (**Fig. 13a**) was increased in the O.M. (****p = <0.0001) and CaP1050 (****p = <0.0001) groups; in the other groups, no significant differences were observed. Among the groups, the expression of CoCaP (^{aaa}p = 0.0002) and CoCaP900 (^{cc}p = 0.0028) was increased compared to CaP and CaP900, and the expression in CaP1050 was increased compared to CoCaP1050 (^{dddd}p =

<0.0001). At 7-day treatment (**Fig. 13d**), expression was increased in O.M. (****p = <0.0001), and statistically reduced in CaP (****p = <0.0001), CoCaP (***p = 0.0002), CoCaP700 (****p = <0.0001), CaP900 (****p = <0.0001), CoCaP900 (***p = 0.0001), and CaP1050 (***p = 0.0002) compared to Control. Between groups, there were no statistically significant differences.

MMP9 expression, at 3 days of treatment (**Fig. 13b**), was increased in CaP (****p = <0.0001), CoCaP (****p = <0.0001), CoCaP900 (****p = <0.0001), and CoCaP1050 (****p = <0.0001), and reduced in the O.M. (***p = 0.0005), CaP700 (**p = 0.0042), CoCaP700 (*p = 0.0193), CaP900 (**p = 0.0011), and CoCaP1050 (****p = <0.0001) groups compared to Control. Among the groups, CoCaP, CoCaP900, and CoCaP1050 showed increases in their expression when compared to their respective groups without Cobalt (CaP vs CoCaP ^{aaaaa}p = <0.0001, CaP900 vs CoCaP900 ^{cccc}p = <0.0001, and CaP1050 vs CoCaP1050 ^{dddd}p = <0.0001). At 7-day treatment (**Fig.13e**), expression was increased relative to Control in the CoCaP (****p = <0.0001), CoCaP700 (****p = <0.0001), CoCaP900 (****p = <0.0001), CaP1050 (**p = 0.0034), and CoCaP1050 (****p = <0.0001) groups. Among the groups, those doped with cobalt showed an increase in their expression compared to their respective groups without cobalt (CaP vs CoCaP ^{aaaaa}p = <0.0001, CaP700 vs CoCaP700 ^{bbbb}p = <0.0001, CaP900 vs CoCaP900 ^{cccc}p = <0.0001, and CaP1050 vs CoCaP1050 ^{dddd}p = <0.0001), and increased in CaP900 when compared to CoCaP900 (^{c}p = 0.0291).

Using the indirect protein carbonylation method to assess ROS activity, at the 3-day treatment (**Fig. 13c**), activity was higher in the O.M. (****p = <0.0001) and CoCaP (**p = 0.0062), and reduced in CaP (****p = <0.0001), CaP700 (****p = <0.0001), CoCaP700 (****p = <0.0001), CaP900 (****p = <0.0001), CoCaP900 (****p = <0.0001), and CaP1050 (****p = <0.0001) compared to Control. Among groups, activity was increased in CoCaP, CoCaP700, and CoCaP1050 compared to their respective groups (CaP vs CoCaP ^{aaaaa}p = <0.0001, CaP700 vs CoCaP700 ^{bbbb}p = <0.0001, and CaP1050 vs CoCaP1050 ^{dddd}p = <0.0001), and increased in CaP900 when compared to CoCaP900 (^{c}p = 0.0291). At 7-day treatment (**Fig. 13f**), the O.M. (****p = <0.0001), CoCaP (****p = <0.0001), CaP700 (****p = <0.0001), CoCaP700 (****p = <0.0001), CaP900 (****p = <0.0001), CoCaP900 (****p = <0.0001), CaP1050 (****p = <0.0001), and CoCaP1050 (****p = <0.0001) showed a reduction in their activity when compared to Control. Among the groups, CoCaP had its activity reduced when compared to CaP (^{aaaa}p = <0.0001), and CaP900 had its activity reduced when compared to CoCaP900 (^{cccc}p = <0.0001).

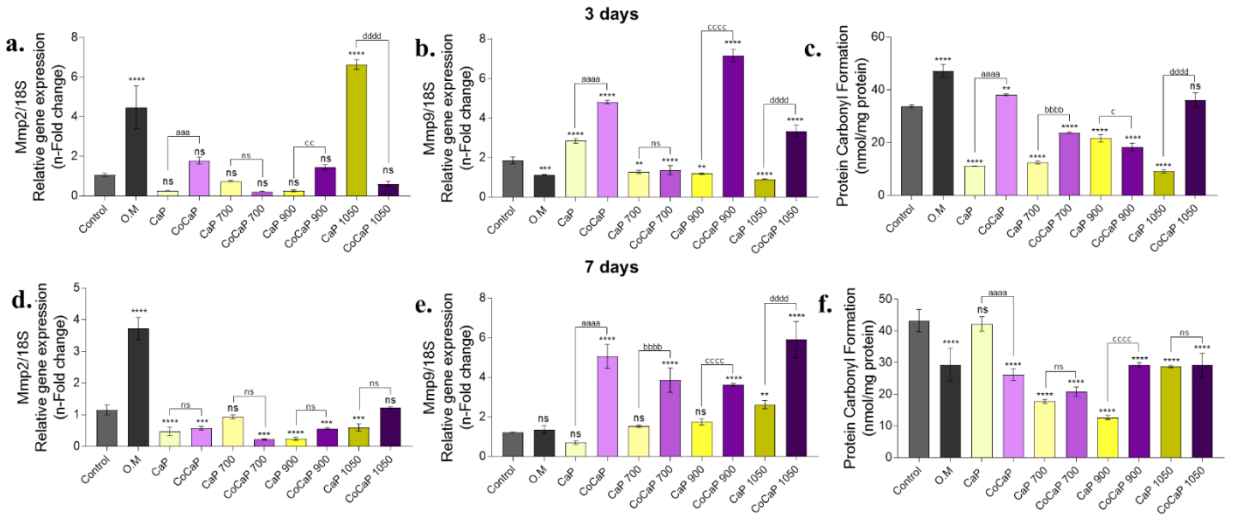

Fig. 13. Genes involved in MMP's expression and Carbonyl Protein analyses: 3-day treatment: **a.** MMP2, **b.** MMP9, and **c.** Protein Carbonyl Formation, 7-day treatment: **d.** MMP2, **e.** MMP9, and **f.** Protein Carbonyl Formation.

The Alkaline Phosphatase staining technique was employed to assess the mineralization of the cells (**Fig. 14**). The technique is based on the principle that a higher uptake of the dye indicates increased mineralization. Following the previously described methodology, cells were stained and analyzed. The images demonstrate a progressive increase in dye uptake over time, illustrating that the mineralization process is influenced by cell treatment. Greater dye uptake is evident in the treated groups compared to the Ctrl group, confirming the effects of conditioned media and O.M. in inducing cell mineralization. Notably, white dots, indicative of mineralization, are visible in the images, particularly in the CoCaP and CoCaP1050 groups. This observation further supports the notion that these treatments have a pronounced impact on cell mineralization.

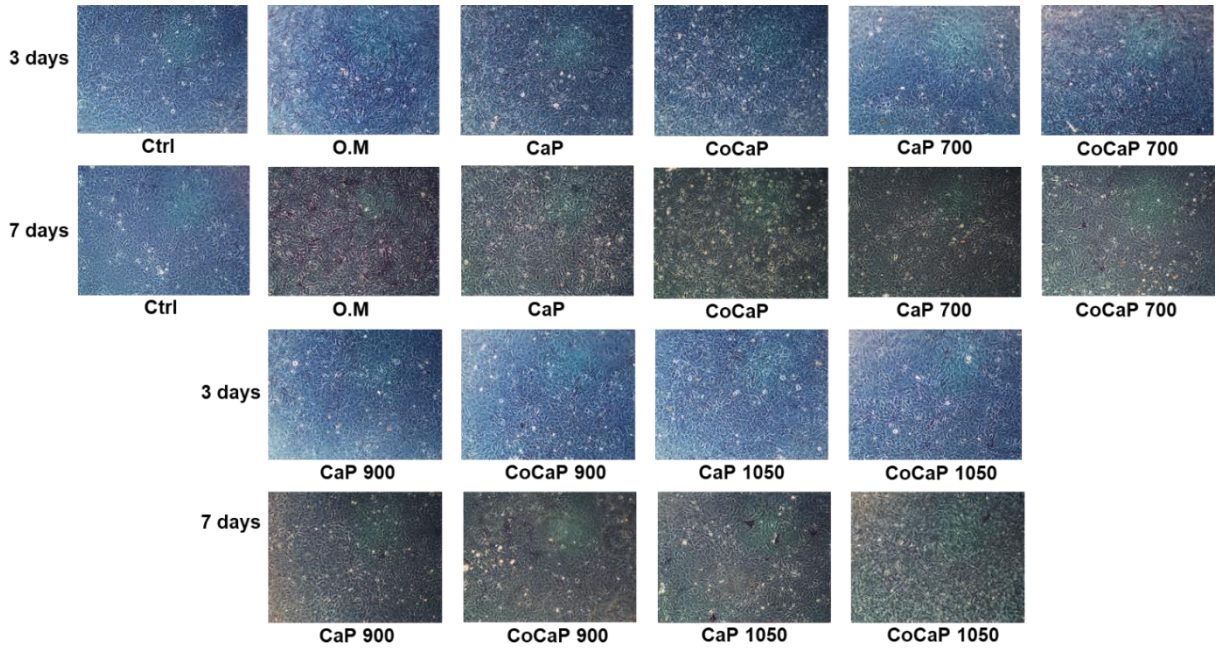

Fig. 14: ALP analyses

Discussion

The thermal decomposition of monetite and its subsequent transformation into calcium pyrophosphate have garnered significant attention for applications in the dental and biomedical materials industry. Specifically, the material is utilized in cement formulations and bone implants due to its bioactive properties, controlled release of calcium and phosphate ions, and potential for influencing cellular responses (GROSSARDT et al., 2010; HLEL; KAMOUN; GUIDARA, 2006; SHEIKH et al., 2017).

Our study, building on previous findings, provides valuable insights into the heat-induced transformations of monetite, particularly when doped with cobalt. The addition of cobalt enhances the material's mechanical strength, chemical stability, and its ability to release ions in a controlled manner (DA COSTA FERNANDES et al., 2021a; DE ALMEIDA et al., 2023). This is evidenced by the observed optimization of gene expressions related to the osteoblastic phenotype (DA COSTA FERNANDES et al., 2021a; DE ALMEIDA et al., 2023).

A pivotal aspect of our investigation involves the transformation of monetite into pyrophosphates, a phenomenon with profound implications for material characterization. X-ray diffraction analysis revealed distinct patterns before and after the transformation, illustrating the evolution from an amorphous structure to an ordered crystalline arrangement. The presence of cobalt subtly influenced these transformations at different temperatures (GUO et al., 2020; LOUATI et al., 2005; WIKHOLM; BEEBE; KITTELBERGER, 1975).

Complementary tests such as FTIR and Raman spectroscopy provided additional perspectives on phase changes. FTIR analysis highlighted significant alterations in chemical bonds and atomic arrangements during the transformation, enhancing our understanding of the material's structural modifications.

Morphological changes in monetite under heat, as elucidated by SEM combined with ASAP, showcased alterations in plate/leaf shape, porosity, and particle size. These changes further contribute to the comprehensive characterization of the material.

Moving beyond material characterization, our study delved into the biological responses to cobalt-doped monetite. Viability tests demonstrated the absence of cytotoxicity and an increase in cell proliferation compared to control groups. Wound healing assays indicated variations in the regeneration of injured areas, with cobalt-containing groups showing enhanced regeneration.

Investigating the conditioned media's effects on genes involved in inflammatory responses, ECM remodeling, and cell differentiation unveiled intriguing findings (GARLANDA; DINARELLO; MANTOVANI, 2013; HAMLET et al., 2012; KIM et al., 2019; LIANG et al., 2007). The expressions of IL-1β, IL-10, and IL-18 indicated the material's potential influence on inflammation, osteoblastic differentiation, and bone metabolism. The evaluation of genes related

to ECM adhesion and remodeling, as well as those fundamental to bone regeneration processes, further underscored the complex cellular responses to the material (BERTAZZO et al., 2010; DA COSTA FERNANDES et al., 2018b; FERNANDES et al., 2018; GARCÍA; KESELOWSKY, 2002; ZAMBUZZI et al., 2008).

The genes involved in angiogenesis and hypoxia, including VEGF, eNOS, and Hif1α, exhibited increased expressions, suggesting potential effects on osteogenesis (DA COSTA FERNANDES et al., 2021b; DE ALMEIDA et al., 2023; HANKENSON et al., 2011; JONITZ-HEINCKE et al., 2019; MACHADO et al., 2019). The eNOS gene, with its role in nitric oxide production, emerged as a regulator influencing bone formation and the cellular response to oxidative stress and inflammation (KANAZAWA et al., 2008; PINTO et al., 2022; VAN'T HOF; RALSTON, 2001; ZAMAN et al., 1999; ZHONG et al., 2011).

Crucial genes related to bone homeostasis, such as RANKL and OPG, displayed balanced expressions, indicating the material's activation of their expression and potential effects on osteoclast differentiation and bone resorption (KOBAYASHI; UDAGAWA; TAKAHASHI, 2009; TAKAYANAGI, 2021b).

In conclusion, our study highlights the multifaceted nature of cobalt-doped monetite as a biomaterial. The material's heat-induced transformations, coupled with its influence on cellular responses and gene expressions, offer a nuanced understanding of its potential applications in bone-related fields. Further research is warranted to comprehensively assess its performance and safety in clinical contexts, with a focus on translating these findings into practical applications such as bone lesions, implants, prosthesis coatings, and tissue engineering.

Acknowledgments

The authors express their gratitude to Fundação de Amparo à Pesquisa do Estado de São Paulo - FAPESP (FAPESP: 2019/26854-2, and 2022/15157-1), Conselho Nacional de Desenvolvimento Científico e Tecnológico (CNPq – Bolsa Produtividade em Pesquisa, 314166/2021-1), and Coordenação de Aperfeiçoamento de Pessoal de Nível Superior (Capes), code 1 for their valuable support.

References

1. van der Eerden BCJ, Teti A, Zambuzzi WF. Bone, a dynamic and integrating tissue. Arch Biochem Biophys. United States; 2014.
2. Bigham-Sadegh A, Oryan A. Basic concepts regarding fracture healing and the current options and future directions in managing bone fractures. Int Wound J [Internet]. Blackwell Publishing Ltd; 2015 [cited 2023 Jan 4];12:238–47. Available from: https://onlinelibrary.wiley.com/doi/10.1111/iwj.12231
3. Macedo F, Ladeira K, Pinho F, Saraiva N, Bonito N, Pinto L, Gonçalves F. Bone metastases: an overview. Oncol Rev [Internet]. 2017 [cited 2019 Jan 30];11. Available from:

http://www.oncologyreviews.org/index.php/or/article/view/321
4. Iaquinta MR, Mazzoni E, Manfrini M, D'Agostino A, Trevisiol L, Nocini R, Trombelli L, Barbanti-Brodano G, Martini F, Tognon M. Innovative biomaterials for bone regrowth. Int J Mol Sci. 2019;20:1–17.
5. Runyan CM, Gabrick KS. Biology of bone formation, fracture healing, and distraction osteogenesis. J Craniofac Surg. Lippincott Williams and Wilkins; 2017;28:1380–9.
6. Dukle A, Murugan D, Nathanael AJ, Rangasamy L, Oh TH. Can 3D-Printed Bioactive Glasses Be the Future of Bone Tissue Engineering? Polymers (Basel) [Internet]. MDPI; 2022 [cited 2023 Jan 7];14. Available from: http://www.ncbi.nlm.nih.gov/pubmed/35458377
7. Zambuzzi WF, Coelho PG, Alves GG, Granjeiro JM, Marque A, Caxias D De, Janeiro R De, Janeiro R De, Federal F. Intracellular signal transduction as a factor in the development of "Smart" biomaterials for bone tissue engineering [Internet]. Biotechnol Bioeng John Wiley & Sons, Ltd; 2011 [cited 2019 Apr 17]. Available from: https://pubmed.ncbi.nlm.nih.gov/21351075/
8. Hou X, Zhang L, Zhou Z, Luo X, Wang T, Zhao X, Lu B, Chen F, Zheng L. Calcium Phosphate-Based Biomaterials for Bone Repair. J Funct Biomater [Internet]. MDPI AG; 2022 [cited 2023 Jan 7];13:187. Available from: http://www.ncbi.nlm.nih.gov/pubmed/36278657
9. Todros S, Todesco M, Bagno A. Biomaterials and their biomedical applications: From replacement to regeneration. Processes. MDPI; 2021.
10. Ling LE, Feng L, Liu HC, Wang DS, Shi ZP, Wang JC, Luo W, Lv Y. The effect of calcium phosphate composite scaffolds on the osteogenic differentiation of rabbit dental pulp stem cells. J Biomed Mater Res - Part A. John Wiley and Sons Inc.; 2015;103:1732–45.
11. Babiker H. Bone graft materials in fixation of orthopaedic implants in sheep. Dan Med J. 2013;60:B4680.
12. da S. Feltran G, Bezerra F, da Costa Fernandes CJ, Ferreira MR, Zambuzzi WF. Differential inflammatory landscape stimulus during titanium surfaces obtained osteogenic phenotype. J Biomed Mater Res - Part A [Internet]. John Wiley and Sons Inc.; 2019 [cited 2021 Jul 10];107:1597–604. Available from: https://onlinelibrary.wiley.com/doi/full/10.1002/jbm.a.36673
13. Torrento JE, Sousa TDSP De, Cristino Da Cruz N, Santos De Almeida G, Zambuzzi WF, Grandini CR, Nespeque Correa DR. Development of non-equiatomic Bio-HEAs based on TiZrNbTa-(Mo and Mn). APL Mater [Internet]. American Institute of Physics Inc.; 2022 [cited 2023 Feb 21];10:081113. Available from: https://aip.scitation.org/doi/10.1063/5.0100465
14. Cardoso GC, de Almeida GS, Corrêa DOG, Zambuzzi WF, Buzalaf MAR, Correa DRN, Grandini CR. Preparation and characterization of novel as-cast Ti-Mo-Nb alloys for biomedical applications. Sci Rep [Internet]. Nature Research; 2022 [cited 2022 Jul 23];12:11874–11874. Available from: https://www.nature.com/articles/s41598-022-14820-8
15. de Almeida GS, Ferreira MR, da Costa Fernandes CJ, Suter LC, Carra MGJ, Correa DRN, Rangel EC, Saeki MJ, Zambuzzi WF. Development of cobalt (Co)-doped monetites for bone regeneration. J Biomed Mater Res - Part B Appl Biomater. 2023;3:1–12.
16. da Costa Fernandes CJ, de Almeida GS, Pinto TS, Teixeira SA, Bezerra FJ, Zambuzzi WF. Metabolic effects of CoCr-enriched medium on shear-stressed endothelial cell and osteoblasts: A possible mechanism involving a hypoxic condition on bone healing. Mater Sci Eng C [Internet]. Elsevier Ltd; 2021 [cited 2021 Aug 3];128:112353. Available from: https://linkinghub.elsevier.com/retrieve/pii/S0928493121004938
17. Zelzer E, Glotzer DJ, Hartmann C, Thomas D, Fukai N, Soker S, Olsen BR. Tissue specific regulation of VEGF expression during bone development requires Cbfa1/Runx2. Mech Dev. Elsevier Ireland Ltd; 2001;106:97–106.
18. Stegen S, van Gastel N, Carmeliet G. Bringing new life to damaged bone: The importance of angiogenesis in bone repair and regeneration. Bone. Elsevier Inc.; 2015;70:19–27.
19. Jang HJ, Park S Bin, Bedair TM, Oh MK, Ahn DJ, Park W, Joung YK, Han DK. Effect of various shaped magnesium hydroxide particles on mechanical and biological properties of poly(lactic-co-glycolic acid) composites. J Ind Eng Chem [Internet]. The Korean Society of Industrial and Engineering Chemistry; 2018;59:266–76. Available from: http://dx.doi.org/10.1016/j.jiec.2017.10.032
20. Takaichi A, Kajima Y, Kittikundecha N, Htat HL, Wai Cho HH, Hanawa T, Yoneyama T, Wakabayashi N. Effect of heat treatment on the anisotropic microstructural and mechanical properties of Co–Cr–Mo alloys produced by selective laser melting. J Mech Behav Biomed Mater. Elsevier Ltd; 2020;102.

21. Jonitz-Heincke, Sellin, Seyfarth, Peters, Mueller-Hilke, Fiedler, Bader, Klinder. Analysis of Cellular Activity Short-Term Exposure to Cobalt and Chromium Ions in Mature Human Osteoblasts. Materials (Basel) [Internet]. 2019 [cited 2019 Nov 14];12:2771. Available from: https://www.mdpi.com/1996-1944/12/17/2771
22. Madl AK, Liong M, Kovochich M, Finley BL, Paustenbach DJ, Oberdörster G. Toxicology of wear particles of cobalt-chromium alloy metal-on-metal hip implants Part I: Physicochemical properties in patient and simulator studies. Nanomedicine Nanotechnology, Biol Med. Elsevier Inc.; 2015.
23. Stevens MM, Marini RP, Schaefer D, Aronson J, Langer R, Shastri VP. In vivo engineering of organs: The bone bioreactor. Proc Natl Acad Sci. 2005;102:11450–5.
24. Wang Y, Ni M, Tang P-F, Li G. Novel application of HA-TCP biomaterials in distraction osteogenesis shortened the lengthening time and promoted bone consolidation. J Orthop Res [Internet]. 2009 [cited 2019 Aug 1];27:477–82. Available from: http://www.ncbi.nlm.nih.gov/pubmed/18973240
25. Sheikh Z, Zhang YL, Tamimi F, Barralet J. Effect of processing conditions of dicalcium phosphate cements on graft resorption and bone formation. Acta Biomater. Acta Materialia Inc; 2017;53:526–35.
26. Sinusaite L, Grigoraviciute-Puroniene I, Popov A, Ishikawa K, Kareiva A, Zarkov A. Controllable synthesis of tricalcium phosphate (TCP) polymorphs by wet precipitation: Effect of washing procedure. Ceram Int. Elsevier Ltd; 2019;45:12423–8.
27. Bohner M, Brunner TJ, Doebelin N, Tang R, Stark WJ. Effect of thermal treatments on the reactivity of nanosized tricalcium phosphate powders. J Mater Chem. 2008;18:4460–7.
28. Rabiei M, Palevicius A, Monshi A, Nasiri S, Vilkauskas A, Janusas G. Comparing methods for calculating nano crystal size of natural hydroxyapatite using X-ray diffraction. Nanomaterials. MDPI AG; 2020;10:1–21.
29. Idowu B, Cama G, Deb S, Di Silvio L. In vitro osteoinductive potential of porous monetite for bone tissue engineering. J Tissue Eng [Internet]. SAGE Publications Ltd; 2014 [cited 2022 Oct 12];5. Available from: https://journals.sagepub.com/doi/full/10.1177/2041731414536572
30. Ko C-L, Chen J-C, Tien Y-C, Hung C-C, Wang J-C, Chen W-C. Osteoregenerative capacities of dicalcium phosphate-rich calcium phosphate bone cement. J Biomed Mater Res Part A. John Wiley & Sons, Ltd; 2015;103:203–10.
31. Tamimi F, Nihouannen D Le, Eimar H, Sheikh Z, Komarova S, Barralet J. The effect of autoclaving on the physical and biological properties of dicalcium phosphate dihydrate bioceramics: Brushite vs. monetite. Acta Biomater. Elsevier Ltd; 2012;8:3161–9.
32. Torres J, Tamimi I, Cabrejos-Azama J, Tresguerres I, Alkhraisat M, López-Cabarcos E, Hernández G, Tamimi F. Monetite granules versus particulate autologous bone in bone regeneration. Ann Anat [Internet]. Elsevier GmbH; 2015 [cited 2022 Oct 12];200:126–33. Available from: https://linkinghub.elsevier.com/retrieve/pii/S0940960215000552
33. Galea LG, Bohner M, Lemaître J, Kohler T, Müller R. Bone substitute: Transforming β-tricalcium phosphate porous scaffolds into monetite. Biomaterials. Elsevier; 2008;29:3400–7.
34. Zagorac D, Muller H, Ruehl S, Zagorac J, Rehme S. Recent developments in the Inorganic Crystal Structure Database: Theoretical crystal structure data and related features. J Appl Crystallogr. International Union of Crystallography; 2019;52:918–25.
35. Allmann R, Hinek R. The introduction of structure types into the Inorganic Crystal Structure Database ICSD. Acta Crystallogr Sect A Found Crystallogr. International Union of Crystallography; 2007;63:412–7.
36. Hellenbrandt M. The inorganic crystal structure database (ICSD) - Present and future. Crystallogr Rev. Taylor & Francis; 2004.
37. Belkly A, Helderman M, Karen VL, Ulkch P. New developments in the Inorganic Crystal Structure Database (ICSD): Accessibility in support of materials research and design. Acta Crystallogr Sect B Struct Sci. International Union of Crystallography; 2002;58:364–9.
38. Kaygili O, Tatar C, Keser S, Bulut N. Preparation and characterization of monetites co-doped with Ni/Al, Ni/Mn and Al/Mn. Mater Lett [Internet]. Elsevier B.V.; 2017 [cited 2022 May 7];201:39–42. Available from: http://dx.doi.org/10.1016/j.matlet.2017.05.015
39. Pinto TS, Martins BR, Ferreira MR, Bezerra F, Zambuzzi WF. Nanohydroxyapatite-Blasted Bioactive Surface Drives Shear-Stressed Endothelial Cell Growth and Angiogenesis. Biomed Res Int. Hindawi Limited; 2022;2022.
40. Mesquita CS, Oliveira R, Bento F, Geraldo D, Rodrigues J V., Marcos JC. Simplified 2,4-

dinitrophenylhydrazine spectrophotometric assay for quantification of carbonyls in oxidized proteins. Anal Biochem [Internet]. Anal Biochem; 2014 [cited 2021 Jul 10];458:69–71. Available from: https://pubmed.ncbi.nlm.nih.gov/24814294/

41. Großardt C, Ewald A, Grover LM, Barralet JE, Gbureck U. Passive and active in vitro resorption of calcium and magnesium phosphate cements by osteoclastic cells. Tissue Eng - Part A. Mary Ann Liebert Inc.; 2010;16:3687–95.
42. Hlel F, Kamoun S, Guidara K. Investigation of Phosphorus Site Condensation in CaHPO4 by Analysis of 31P MAS-NMR Tensor and X-Ray Powder Patterns. Zeitschrift fur Naturforsch - Sect A J Phys Sci. De Gruyter; 2006;61:375–82.
43. Louati B, Hlel F, Guidara K, Gargouri M. Analysis of the effects of thermal treatments on CaHPO4 by 31P NMR spectroscopy. J Alloys Compd. Elsevier; 2005;394:13–8.
44. Wikholm NW, Beebe RA, Kittelberger JS. Kinetics of the conversion of monetite to calcium pyrophosphate. J Phys Chem. American Chemical Society; 1975;79:853–6.
45. Guo H, Pujari-Palmer M, Yu Y, Stevensson B, Engqvist H, Edén M. Quantitative phase analyses of biomedical pyrophosphate-bearing monetite and brushite cements by solid-state NMR and powder XRD. Ceram Int. Elsevier Ltd; 2020;46:11000–12.
46. Hamlet S, Alfarsi M, George R, Ivanovski S. The effect of hydrophilic titanium surface modification on macrophage inflammatory cytokine gene expression. Clin Oral Implants Res. 2012;23:584–90.
47. Liang KC, Lee CW, Lin WN, Lin CC, Wu C Bin, Luo SF, Yang CM. Interleukin-1β induces MMP-9 expression via p42/p44 MAPK, p38 MAPK, JNK, and nuclear factor-κB signaling pathways in human tracheal smooth muscle cells. J Cell Physiol. 2007;211:759–70.
48. Garlanda C, Dinarello CA, Mantovani A. The Interleukin-1 Family: Back to the Future. Immunity. 2013.
49. Kim SE, Choi S, Hong J-Y, Shim K-S, Kim T-H, Park K, Lee S-H. Accelerated Osteogenic Differentiation of MC3T3-E1 Cells by Lactoferrin-Conjugated Nanodiamonds through Enhanced Anti-Oxidant and Anti-Inflammatory Effects. Nanomaterials [Internet]. MDPI AG; 2019 [cited 2023 Aug 29];10:50. Available from: https://www.mdpi.com/2079-4991/10/1/50
50. Bertazzo S, Zambuzzi WF, Campos DDP, Ferreira C V., Bertran CA. A simple method for enhancing cell adhesion to hydroxyapatite surface. Clin Oral Implants Res [Internet]. John Wiley & Sons, Ltd; 2010 [cited 2021 Jun 20];21:1411–3. Available from: https://www.onlinelibrary.wiley.com/doi/full/10.1111/j.1600-0501.2010.01968.x
51. da Costa Fernandes CJ, Bezerra FJB, de Campos Souza B, Campos MA, Zambuzzi WF. Titanium-enriched medium drives low profile of ECM remodeling as a pre-requisite to pre-osteoblast viability and proliferative phenotype. J Trace Elem Med Biol [Internet]. Elsevier GmbH; 2018 [cited 2019 Mar 8];50:339–46. Available from: https://www.sciencedirect.com/science/article/pii/S0946672X18301433?via%3Dihub
52. Fernandes CJC, Bezerra F, Ferreira MR, Andrade AFC, Pinto TS, Zambuzzi WF. Nano hydroxyapatite-blasted titanium surface creates a biointerface able to govern Src-dependent osteoblast metabolism as prerequisite to ECM remodeling. Colloids Surfaces B Biointerfaces [Internet]. Elsevier B.V.; 2018 [cited 2019 Mar 8];163:321–8. Available from: https://pubmed.ncbi.nlm.nih.gov/29329077/
53. García AJ, Keselowsky BG. Biomimetic surfaces for control of cell adhesion to facilitate bone formation. Crit Rev Eukaryot Gene Expr. 2002.
54. Zambuzzi WF, Granjeiro JM, Parikh K, Yuvaraj S, Peppelenbosch MP, Ferreira C V. Modulation of Src activity by low molecular weight protein tyrosine phosphatase during osteoblast differentiation. Cell Physiol Biochem. Cell Physiol Biochem Press; 2008;22:497–506.
55. da Costa Fernandes CJ, de Almeida GS, Pinto TS, Teixeira SA, Bezerra FJ, Zambuzzi WF. Metabolic effects of CoCr-enriched medium on shear-stressed endothelial cell and osteoblasts: A possible mechanism involving a hypoxic condition on bone healing. Mater Sci Eng C. Elsevier Ltd; 2021;128:112353.
56. Hankenson KD, Dishowitz M, Gray C, Schenker M. Angiogenesis in bone regeneration. Injury. Elsevier Ltd; 2011;42:556–61.
57. Machado MIP, Gomes AM, Rodrigues MF, Silva Pinto T, da Costa Fernandes CJ, Bezerra FJ, Zambuzzi WF. Cobalt-chromium-enriched medium ameliorates shear-stressed endothelial cell performance. J Trace Elem Med Biol [Internet]. Elsevier; 2019 [cited 2019 Nov 10];54:163–71. Available from: https://doi.org/10.1016/j.jtemb.2019.04.012
58. Van't Hof RJ, Ralston SH. Nitric oxide and bone. Immunology. Wiley-Blackwell; 2001.

59. Zaman G, Pitsillides AA, Rawlinson SCF, Suswillo RFL, Mosley JR, Cheng MZ, Platts LAM, Hukkanen M, Polak JM, Lanyon LE. Mechanical strain stimulates nitric oxide production by rapid activation of endothelial nitric oxide synthase in osteocytes. J Bone Miner Res. 1999;14:1123–31.
60. Zhong X, Xiu LL, Wei GH, Liu YY, Su L, Cao XP, Li YB, Xiao HP. Bezafibrate enhances proliferation and differentiation of osteoblastic MC3T3-E1 cells via AMPK and eNOS activation. Acta Pharmacol Sin. 2011;32:591–600.
61. Kanazawa I, Yamaguchi T, Yano S, Yamauchi M, Sugimoto T. Metformin enhances the differentiation and mineralization of osteoblastic MC3T3-E1 cells via AMP kinase activation as well as eNOS and BMP-2 expression. Biochem Biophys Res Commun [Internet]. Academic Press; 2008 [cited 2023 Feb 14];375:414–9. Available from: https://www.sciencedirect.com/science/article/abs/pii/S0006291X08015465
62. Kobayashi Y, Udagawa N, Takahashi N. Action of RANKL and OPG for osteoclastogenesis. Crit Rev Eukaryot Gene Expr. Begell House Inc.; 2009.
63. Takayanagi H. RANKL as the master regulator of osteoclast differentiation. J Bone Miner Metab. Springer Japan; 2021.

SUPPLEMENTARY DATA:

Table 1 – Structural details of the crystallographic datasheets.

Phase	Monetite	β dicalcium phosphate	β tricalcium phosphate	Co-based calcium phosphate	Hydroxyapatite
Nomenclature	M	D	T	Co	HA
Chemical composition	$CaHPO_4$	$Ca_2P_2O_7$	$Ca_3(PO_4)_2$	$Ca_{9.5}Co(PO_4)_7$	$Ca_{10}(PO_4)_6(OH)_2$
CIF number	ICSD #10503	ICSD #14313	ICSD #6191	ICSD #86808	ICSD #26204
Crystal structure	Triclinic	Tetragonal	Hexagonal	Hexagonal	Hexagonal
Spatial group	$P\bar{1}$	P41	R3cH	R3cH	P63/m
Cell parameters	α = 96.18° β = 103.82° γ = 88.34° a = 6.916 Å b = 6.919 Å c = 6.946 Å	α = 90° β = 90° γ = 90° a = 6.684 Å b = 6.684 Å c = 24.144 Å	α = 90° β = 90° γ = 120° a = 10.439 Å b = 10.439 Å c = 37.375 Å	α = 90° β = 90° γ = 120° a = 10.3501 Å b = 10.3501 Å c = 37.1790 Å	α = 90° β = 90° γ = 120° a = 9.424 Å b = 9.424 Å c = 6.879 Å

Table 2 - Merit parameters.

Sample	Go	RF^2 (%)	Rwp (%)	Rp (%)
Monetite	1.723	12.46	22.11	17.39
Monetite_700	1.653	10.97	20.43	15.77
Monetite_900	1.682	13.93	21.26	16.09
Monetite_1050	1.553	12.78	20.88	15.48
CoMonetite	1.686	11.79	19.50	15.26
CoMonetite_700	1.359	10.14	19.28	14.84
CoMonetite_900	1.263	10.21	18.72	14.18
CoMonetite_1050	1.368	10.50	18.15	13.81

Table 3 - Cell parameters. XRD crystallography data of monetite and β-$Ca_2P_2O_7$ lattice parameters.

Sample	Phase* (%)	α (°)	β (°)	γ (°)	a (Å)	b (Å)	c (Å)	V ($Å^3$)
Monetite	M = 92 (2) HA = 8 (2)	96.23 (1) 90	103.94 (1) 90	88.41 (1) 120	6.9147 (4) 9.64 (1)	6.6369 (6) 9.64 (1)	6.9971 (6) 6.90 (1)	309.83 (3) 556 (2)
Monetite_700	D = 100%	90	90	90	6.6895 (4)	6.6895 (4)	24.159 (2)	1081.1 (2)
Monetite_900	D = 100%	90	90	90	6.6899 (2)	6.6899 (2)	24.161 (1)	1081.3 (1)
Monetite_1050	D = 100%	90	90	90	6.6903 (3)	6.6903 (3)	24.162 (1)	1081.5 (1)
CoMonetite	M = 100%	96.24 (1)	103.96 (1)	88.42 (1)	6.9089 (5)	6.6349 (5)	6.9942 (6)	309.30 (5)
CoMonetite_700	D = 100%	90	90	90	6.6897 (3)	6.6897 (3)	24.160 (1)	1081.2 (1)
CoMonetite_900	D = 100%	90	90	90	6.6906 (2)	6.6906 (2)	24.162 (1)	1081.6 (1)
CoMonetite_1050	D = 100%	90	90	90	6.6900 (2)	6.6900 (2)	24.157 (1)	1081.1 (1)

Table 4 - Crystallite and microstrain of Monetite phase.

Sample	Phase	Ds (nm)	Dwh (nm)	ε (%)
Monetite	M	78.0	48.9	- 0.6
	HA	69.0	35.4	- 0.3
Monetite_700	D	100.0	57.4	- 0.7
Monetite_900	D	133.0	81.2	- 0.4
Monetite_1050	D	127.0	73.8	- 0.5
CoMonetite	M	89.0	54.4	- 0.5
CoMonetite_700	D	130.0	64.9	- 0.5
CoMonetite_900	D	128.0	76.9	- 0.4
CoMonetite_1050	D	126.0	74.0	- 0.5

Capitulo 7

Artigo 4: Optimizing titanium osseointegration using thermally modified Co-doped monetite coatings

Submetido e em revisão

Optimizing titanium osseointegration using thermally modified Co-doped monetite coatings

Gerson Santos de Almeida[1*#], Maria Gabriela Jacheto Carra[2*], Luisa Camilo Suter[1], Julia Bucci[2], Diego Rafael Nespeque Correa[3], Margarida Juri Saeki[2], Willian Fernando Zambuzzi[1].

*These both authors contributed equally

[1]Lab. of Bioassays and Cell Dynamics, Department of Chemical and Biological Sciences, Institute of Biosciences, UNESP - Universidade Estadual Paulista, Botucatu, São Paulo 18618-970, Brazil
[2]Lab. of Materials and Electrochemistry, Department of Chemical and Biological Sciences, Institute of Biosciences, UNESP - Universidade Estadual Paulista, Botucatu, São Paulo 18618-970, Brazil
[3]Laboratory of Anelasticity and Biomaterials, Department of Physics and Meteorology, School of Sciences, São Paulo State University - UNESP, Bauru, São Paulo, 17033-360, Brazil

[#]Corresponding author:
Dr. Gerson Santos de Almeida
UNESP - Campus de Botucatu - Instituto de Biociências
Rua Profª. Drª. Irina Delanova Gemtchujnicov, s/nº
18618-693 – Botucatu-SP - Brazil

e-mail: gs.almeida@unesp.br
Phone: +55-14 38800599
Fax: +55-14 3880 0573

ABSTRACT

This study advances the application of monetite and cobalt-doped monetite coatings on commercially pure titanium (c.p.-Ti), demonstrating their potential to significantly improve the osseointegration of dental implants and bone fixators. Employing hydrothermal methods, we achieved coatings with pronounced surface roughness and inherent hydrophilicity, as evidenced by SEM imaging and dynamic contact angle analysis. Notably, peaks and valleys of up to 35 µm and 37 µm, respectively, were identified on the coatings, which directly influenced cell morphology. Our cytotoxicity evaluations, following ISO 10993 standards, revealed no adverse effects on pre-osteoblast cells, with MTT and Crystal Violet assays confirming the coatings' biocompatibility. SEM observations further substantiated positive cell-material interactions, indicating that the coated surfaces facilitate cellular processes essential for bone regeneration. These results highlight the coatings' capacity to modulate surface properties conducive to cell function, marking a significant stride towards their application in biomedical devices.

INTRODUCTION

Titanium's illustrious history in regenerative medicine commenced with Branemark's pioneering work in the 1960s, establishing it as a quintessential biomaterial for bone implants due to its commendable biocompatibility, mechanical strength, and resistance to corrosion (ALBREKTSSON et al., 1981). Its status as the 'gold standard' has been reaffirmed through extensive clinical usage and academic endorsements (BAUER et al., 2013; THARANI KUMAR et al., 2020). Despite the advancements and the evolutionary trajectory of titanium implants over the decades, challenges such as postoperative inflammation and implant rejection persist, underscoring an imperative need for surface optimization (ALBREKTSSON; WENNERBERG, 2019; DOHAN EHRENFEST et al., 2010; PINTO et al., 2022).

Surface modification strategies, particularly the application of bioactive coatings, have emerged as a formidable approach to mitigate these issues (BEZERRA et al., 2017; DA SILVA et al., 2020; FERNANDES et al., 2018; FERREIRA et al., 2020; GOMES et al., 2023). In this realm, calcium phosphates stand out due to their osteoconductive properties and compositional similarity to bone mineral, making them an attractive choice for enhancing implant integration (JEONG et al., 2019; PRADO DA SILVA et al., 2001; SIKDER et al., 2018a, 2018b). Monetite, a calcium phosphate compound, has garnered research interest owing to its bioactivity and inherent capability to be bioabsorbed, thus supporting the natural remodeling process of bone (AATI, 2017; ALI et al., 2019).

Building upon this background, the current study introduces an innovative application of monetite and cobalt-doped monetite (Co-monetite) coatings on titanium substrates. The choice of cobalt as a dopant is informed by its known angiogenic properties and its role in stimulating bone growth by mimicking a hypoxia microenvironment (DE ALMEIDA et al., 2023; MACHADO; GOMES; ZAMBUZZI, 2024). Here, the coatings are synthesized using a hydrothermal method, selected for its efficacy in producing high-purity, crystalline coatings at relatively low temperatures, which is advantageous for preserving the structural integrity of both the coating and the underlying titanium.

Thus, this study aims to elucidate the impact of these novel coatings on the biological performance of titanium implants. By integrating the osteoinductive potential of monetite with the enhanced bioactivity afforded by cobalt doping, we hypothesize that Co-monetite coatings could significantly augment the osseointegration of titanium. The overarching goal is to optimize implant surfaces to such an extent that they not only prevent adverse reactions but actively facilitate the regenerative process, paving the way for a new generation of bone implants with superior clinical outcomes.

EXPERIMENTAL

The methodology employed was adapted from the protocol proposed by Zhou et al. (ZHOU et al., 2021b), utilizing hydrothermal treatment for the coatings. To coat with monetite, reagents were used at the following concentrations: 0.2M $CaCl_2$, 0.12M NaH_2PO_4, and 0.1M $Na_2EDTA\text{-}2H_2O$, dissolved in deionized water. The solution was adjusted to a final pH of 3.4-3.6 by carefully adding HCl or NH_4OH. For the Co-monetite coating, the concentrations of all reagents remained the same, except for calcium and cobalt, which were present at 0.18M and 0.02M, respectively. Commercially pure titanium (cp-Ti, ASTM F67 GR2) served as the substrate; it was abraded and then treated with a 10% hydrochloric acid solution. Subsequently, it was placed into a PTFE reactor containing the aforementioned solutions and subjected to hydrothermal conditions at 190°C for 8 hours. After the hydrothermal treatment concluded, the reactor was allowed to cool to room temperature. The titanium plates with the applied coating were then extracted, washed with deionized water, and subsequently subjected to a thermal treatment at 200°C for 2 hours to enhance the crystallinity of the monetite coating. After coating, the samples were characterized by XRD, SEM/EDX, profilometry, contact angle, and cytotoxicity tests (MTT and CV), and the morphology of the MC3T3-E1 cells was evaluated by SEM.

X-Ray Diffraction Analysis:

The applied coatings underwent crystalline structure analysis utilizing a RIGAKU X-ray diffractometer (DMAX-2100), employing Cu-Kα radiation at a wavelength of 1.5418Å. This was performed under a potential of 40 kV and a current of 20 mA, utilizing a grazing incidence angle of 2°. The diffractograms were recorded over a 2θ range from 10° to 80°, with a step size of 0.020° and a dwell time of 1 second per step. Phase identification was conducted through comparison with standard references from the Powder Diffraction File (PDF-2003) and the Inorganic Crystal Structures Database (ICSD, Version 2.2), using Crystallographica Search Match software for assistance. Structural parameters and the degree of crystallinity were refined using the Rietveld method through GSAS software and the EXPGUI graphical user interface. Instrumental broadening corrections were applied using a standard Y_2O_3 sample, and the profiles were adjusted using functions such as Pseudo-Voigt for peak shapes, Chebyshev for background subtraction, and March-Dollase for preferred orientation correction. Calculations of the crystallite size were based on the full-width at half-maximum (FWHM) of the peaks, applying both Scherrer and Williamson-Hall equations (CHÉRIF et al., 2022; KAYGILI et al., 2017; NATH; SINGH; DAS, 2020; RABIEI et al., 2020).

Scanning Electron Microscopy Evaluation:

Observations of the surface morphology and cellular interactions on the titanium coatings were conducted with a FEI Quanta 200 scanning electron microscope. For the coatings, a magnification of 2000x was used with an accelerating voltage of 12.5 kV. When examining cellular morphology, the magnification was increased to 5000x, under the same voltage, to capture finer details. The semi-quantitative EDS analysis was performed in the same equipment for Ca, P, O, and Co chemical elements using the same acceleration voltage (10 kV).

Contact Angle Determination:

Wettability assessments were performed using the VCA 2500 XE system to measure the static contact angle at ambient conditions. Droplets of 1 µL of ultrapure water were delicately placed on three separate areas of each specimen, with this process repeated across three individual samples to ensure reliability of the data.

Profilometry Measurements:

The topographical attributes, specifically the roughness of both uncoated and coated titanium samples, were quantified through profilometry. Employing a Bruker Dektak XT Profilometer, we scanned a surface area of 1 mm by 1 mm, utilizing a stylus with a tip radius of 12.5 µm and applying a force of 3 mg to trace the surface contours.

Osteoblasts cultures:

Pre-osteoblast MC3T3-E1 cells were propagated in MEMα enriched with a blend of antibiotics (penicillin at 100 units/mL and streptomycin at 100 mg/mL) and fortified with 10% fetal bovine serum (FBS). Incubation was carried out at 37°C, ensuring a humidified atmosphere with 95% relative humidity and a 5% CO_2 environment. The evaluation of the biomaterials' effects was initiated by introducing the cells to a medium that contained biomaterials at a concentration of 0.2g/mL, in alignment with ISO 10993-12 standards. This process began with the enrichment of an FBS-deprived medium with the alloys (Ticp, CaPTicp, and CoCaPTicp) for a full day to create a conditioned medium, which was then supplemented with 10% FBS before introducing it to the pre-osteoblasts. The MC3T3 cells were then cultivated under various conditions including a control setting (utilizing Alpha-MEM), and environments conditioned with Ticp, CaP, and CoCaP.

Assessment of Cytotoxicity by MTT Assay:

For cytotoxicity testing, pre-osteoblasts were plated in 96-well plates and incubated with biomaterial-enriched media for 24 hours at a standard cell culture temperature of 37°C, as specified

by ISO 10993, as we have widely explored earlier (BERTAZZO et al., 2010; DA COSTA FERNANDES et al., 2019). This biomaterial concentration was set at 0.2 g/mL. Post incubation, the medium was replaced with an MTT solution (concentration: 1 mg/mL), and cells were further incubated for three hours. Following this, the MTT solution was discarded and replaced with DMSO to solubilize the resultant formazan crystals. The optical density of the solution, indicative of cell viability, was quantified at 570 nm using a SYNERGY-HTX multi-mode microplate reader.

Cell Adhesion Evaluation:

The cell adhesion assay was conducted using the crystal violet staining technique (DA COSTA FERNANDES et al., 2018a). Cells, after routine cultivation and trypsinization, were dispensed into 96-well plates at a density of 1×10^5 cells/mL This assessment was performed to gauge the impact of biomaterial-conditioned media on cell adhesion properties. The cell groups included a control set maintained in standard culture medium and sets exposed to various biomaterials. After a 24-hour incubation period, the cells were stained using crystal violet. The degree of cell adhesion was quantitatively estimated by measuring the absorbance of the stained cells at 540 nm, utilizing the SYNERGY-HTX multimode microplate reader.

RESULTS

The sample denominations were as follows: c.p.-Ti + CaP for the titanium samples coated with monetite and c.p.-Ti + CoCaP for the titanium samples where monetite was augmented with cobalt. When examined structurally, both the coated and the original titanium materials displayed XRD spectra consistent with reference patterns from the standard database: entry 71-1760 for Monetite ($CaHPO_4$) associated with the coated samples, and entry 44-1294 corresponding to the unaltered titanium. These findings are depicted in **Fig.1**.

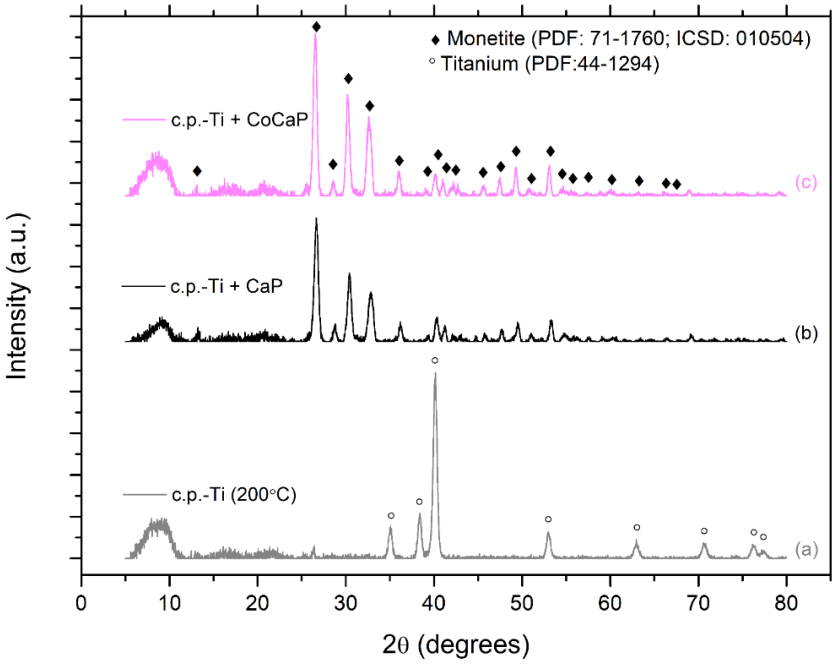

Fig.1. Depicts the X-ray diffraction patterns of the various samples, where (**a**) represents c.p.-Ti heated to 200°C, (**b**) illustrates c.p.-Ti with a CaP coating, and (**c**) showcases c.p.-Ti with a CoCaP coating. Detailed crystallographic information, including lattice and unit cell parameters, as well as data pertaining to the crystallite size and microstrain within the Monetite phase, are collated in Tables 1-3.

Table 1. Structural details of the crystallographic datasheets.

Phase	Monetite	α-Ti
Nomenclature	M	α
Chemical composition	$CaHPO_4$	Ti
CIF number	ICSD #10503	ICSD #43416
Crystal structure	Triclinic	Hexagonal
Spatial group	$P\bar{1}$	P63/mmc
Cell parameters	α = 96.18° β = 103.82° γ = 88.34° a = 6.916 Å b = 6.919 Å c = 6.946 Å	α = 90° β = 90° γ = 120° a = 2.951 Å b = 2.951 Å c = 4.684 Å

Table 2. Cell parameters.

Sample	Phase* (%)	α (°)	β (°)	γ (°)	a (Å)	b (Å)	c (Å)	V (Å ^{3})
cp-Ti	α - 100	90	90	120	2.953 (1)	2.953 (1)	4.687 (1)	35.39 (1)
Monetite	M – 99 α - 1	96.2 (1)	104.0 (1)	88.4 (1)	6.906 (1)	6.626 (1)	6.999 (1)	308.5 (1)
Co doped Monetite	M – 99 α - 1	96.2 (1)	104.0 (1)	88.4 (1)	6.868 (1)	6.599 (4)	6.959 (4)	304.2 (5)

Table 3. Crystallite and microstrain of Monetite phase.

Sample	Phase	Ds (nm)	Dwh (nm)	ε (%)
cp-Ti	α	12.8 (2)	27.7 (2)	- 0.04 (4)
Monetite	M	41.1 (9)	58.3 (4)	- 0.01 (1)
Co doped Monetite	M	41.4 (6)	54.2 (4)	- 0.75 (2)

Morphological characterization of the surfaces was performed through Scanning Electron Microscopy (SEM) and surface profilometry, as illustrated in **Fig.2**. Concurrently, **Fig.3** depicts the interaction between the cells and the surfaces through SEM micrographs, highlighting the details of cellular morphology. The morphological analyses of the surfaces were carried out using SEM and profilometry (**Fig.2**) and **Fig.3** brings micrographs of the cells interacting with the surfaces, highlighting the cell morphology changes.

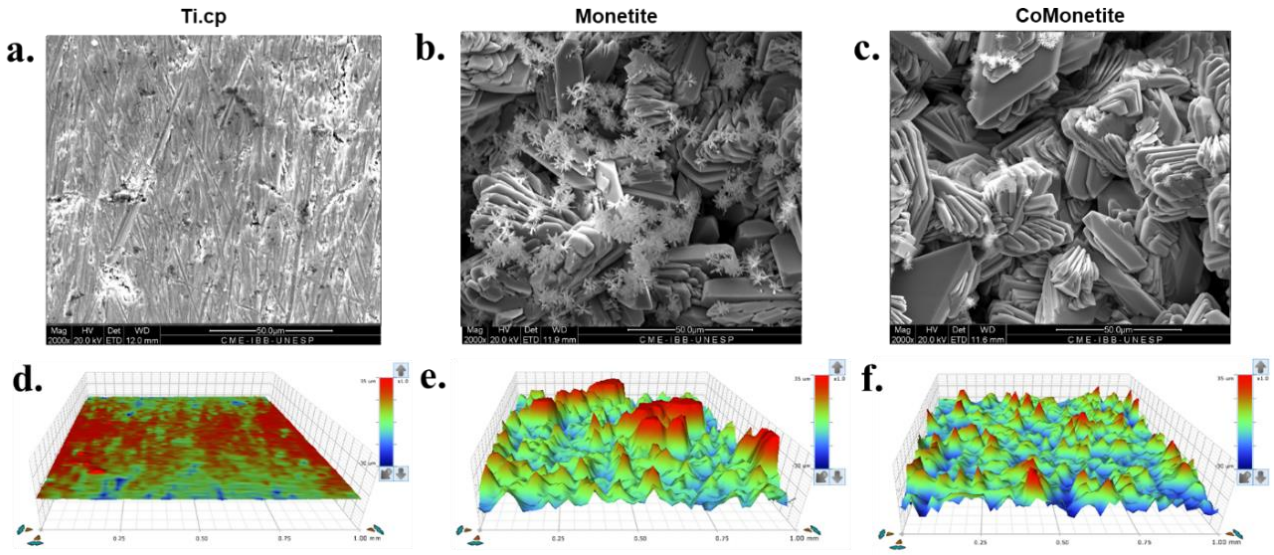

Fig.2. Surface characterization of titanium samples. Top row - Scanning Electron Microscopy (SEM) images showing the texture and morphology of (**a**) uncoated commercially pure titanium (cp-Ti), (**b**) cp-Ti with a Monetite coating, and (**c**) cp-Ti with a Cobalt-doped Monetite (Co-Monetite) coating. Bottom row - Profilometry scans depicting the surface topography of (**d**) uncoated cp-Ti, (**e**) Monetite-coated cp-Ti, and (**f**) Co-Monetite-coated cp-Ti, illustrating the variations in surface roughness and structure post-coating application.

Thereafter, the **Fig.3** presents the SEM micrographs depicting the cellular architecture as the cells proliferate in direct adherence with the various material surfaces. Notably, changes in cell morphology were observed, which can be correlated to the varying degrees of surface roughness provided by each type of evaluated coating.

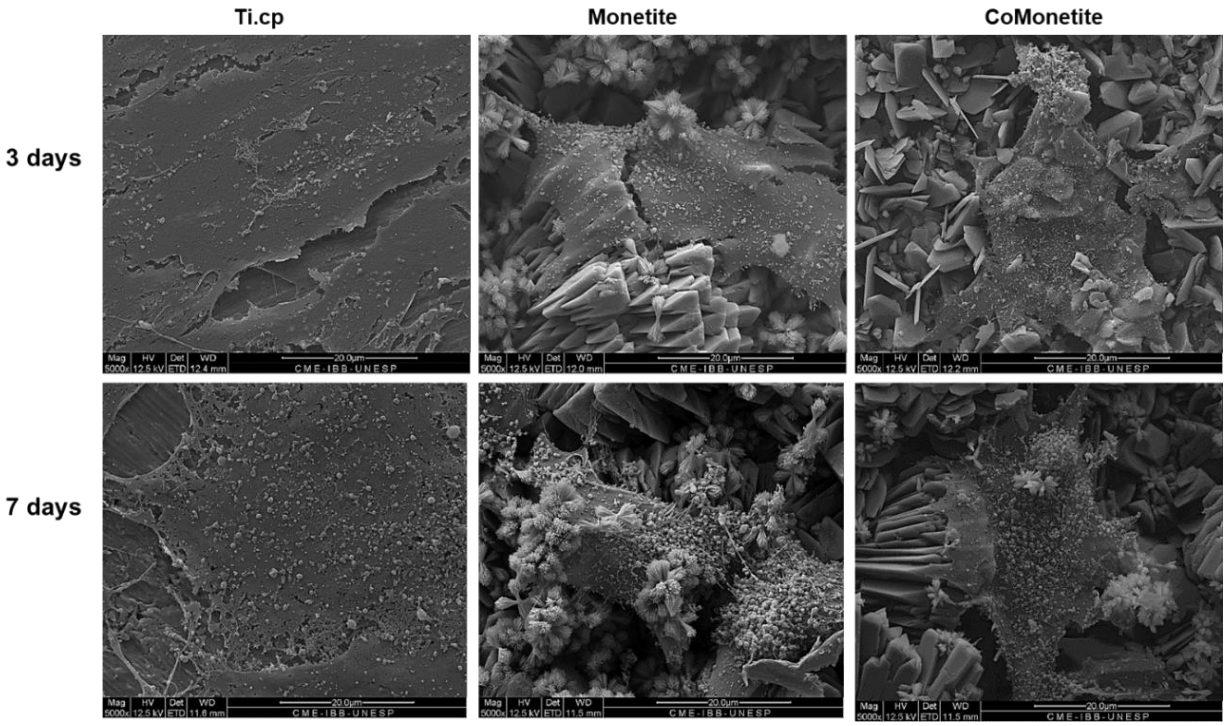

Fig.3. Osteoblast morphology on different titanium surfaces over time. This series of SEM micrographs captures the growth pattern of cells after 3 and 7 days of direct contact with (**a**) untreated commercially pure titanium (cp-Ti), (**b**) cp-Ti coated with Monetite, and (**c**) cp-Ti coated with Cobalt-doped Monetite (Co-Monetite). The images illustrate the influence of surface microtopography on cell morphology, with differences becoming more pronounced over the course of the observation period.

The EDS analyses showed the homogeneous distribution of cobalt in the sample (**Fig 4.**)

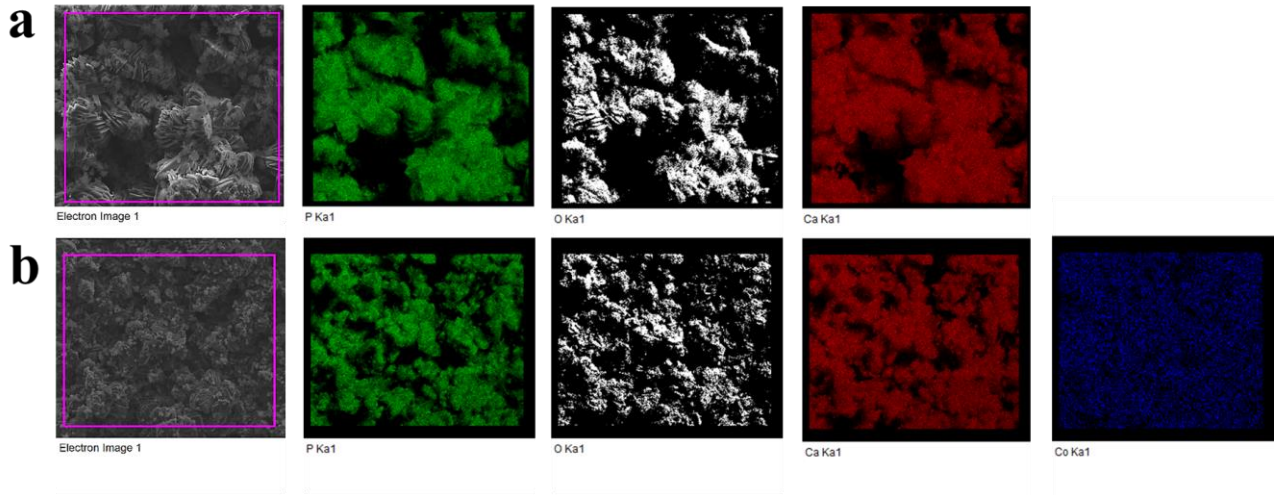

Fig.4. Semiquantitative analysis and elemental distribution of cobalt-doped by EDS. **a.** Monetite; **b.** Co-doped Monetite

The contact angle analysis revealed an enhancement in hydrophilicity across the various coatings, as delineated in **Fig.5**. The recorded contact angles of water droplets on the surfaces exhibit discernible differences, reflecting the impact of the coatings. Dynamic mode measurement

was employed to capture the interaction between the droplet and the surface in real-time, enabling the determination of the initial contact angle precisely upon droplet placement.

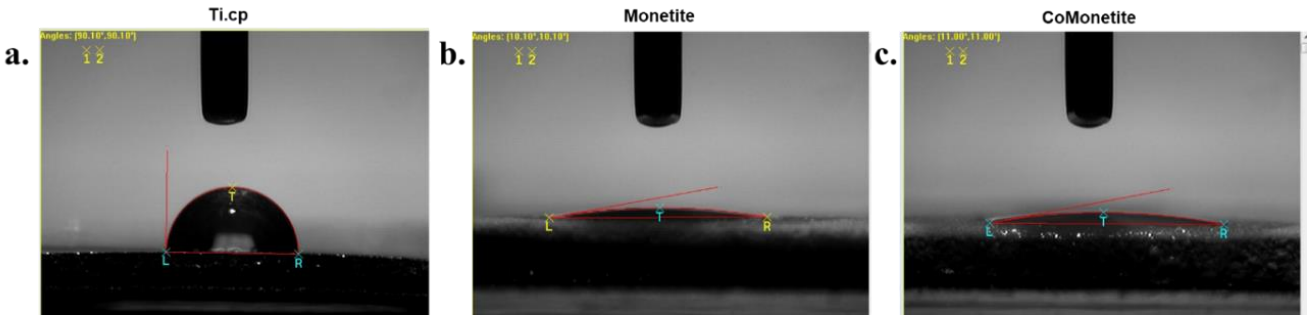

Fig.5. Evaluation of surface hydrophilicity through contact angle measurements. Panel (**a**) illustrates the contact angle on uncoated commercially pure titanium (cp-Ti), while panels (**b**) and (**c**) depict the contact angles on Monetite-coated cp-Ti and Cobalt-doped Monetite (Co-Monetite)-coated cp-Ti, respectively. The snapshots in panels (**b**) and (**c**) were captured approximately 0.099 seconds after the water droplet made contact with the coatings, highlighting the immediate wetting response due to the surface modifications.

DISCUSSION

This study delineates the physicochemical attributes of monetite and cobalt-doped monetite coatings on titanium surfaces and their subsequent impact on osteoblast activity. Our XRD analysis reveals distinct phase formations in consonance with established literature, demonstrating that the incorporation of cobalt does not disrupt the structural integrity of monetite, a factor crucial for biological efficacy. The formation of these phases is pivotal as previous studies have shown that the crystalline structure of surface coatings can modulate cellular responses.

The SEM observations illustrate a topography that not only emulates natural bone but also promotes osteoconductivity, affirming the findings of Zhou et. al (ZHOU et al., 2021b) and Alexander et al. (ZAVGORODNIY et al., 2012) who reported similar morphological influences on cell function. Regarding the plate-like and flower-like structures we observe parallel natural osseous formations, which have been shown to enhance osteoblast adhesion and proliferation (JINAWATH et al., 2001; ZHU et al., 2017).

EDS data add to the growing body of evidence that the homogeneity of elemental distribution is critical in biomedical coatings, with cobalt's role in angiogenesis and bone growth being particularly emphasized (DA COSTA FERNANDES et al., 2021a). Additionally, SEM analyses of cellular interactions align with recent investigations (ALI et al., 2019; KLAMMERT et al., 2010; NAVARRO DA ROCHA et al., 2019; ZAVGORODNIY et al., 2012; ZHOU et al., 2021b), who highlighted the role of the microenvironment in directing cell fate. The thriving osteoblasts on our coatings are not only evidence of viability but also functional activity,

suggesting that the Monetite and Co-doped Monetite surfaces act as more than passive substrates; they serve as active participants in the bone regeneration process.

Profilometry results further elaborate on the surface characteristics, suggesting an optimal roughness that aligns with the study of Zavgorodniy et al. (ZAVGORODNIY et al., 2011), who found that specific topographical scales could upregulate osteogenic differentiation markers. Our findings contribute to this discourse by demonstrating that such microscale roughness can be achieved with Monetite coatings, enhancing the material's bioactivity.

The increase in hydrophilicity observed in our coatings correlates with a growing consensus in the literature regarding the importance of surface wettability in osseointegration (HAMLET et al., 2019; MENZIES; JONES, 2010). Hydrophilic surfaces have been consistently linked with improved protein adsorption and initial cell interaction, a key for the successful integration of implants (BRODBECK et al., 2001; PARISI et al., 2020; WILSON et al., 2005). Our study's compliance with ISO10993 standards for biological assays reaffirms the coatings' biocompatibility and supports their potential for clinical application.

In conclusion, the physicochemical properties of Monetite and Co-Monetite coatings demonstrate relevance on osteoblast performance, with clear implications for the enhancement of orthopedic and dental implant integration. Our study not only aligns with but also builds upon existing previous studies, offering new insights into the design of implant coatings that can effectively mediate between the material and biological outcomes to better drive regenerative processes.

Acknowledgments

The authors are grateful to FAPESP: Fundação de Amparo à Pesquisa do Estado de São Paulo (grant number: 2022/15157-1), Coordenação de Aperfeiçoamento de Pessoal de Nível Superior - Brasil (CAPES) (code 0001), and CNPq for the financial support (PQ2).

REFERENCES

Aati SY. 2017. Monetite layer by layer coating for bone regeneration application.

Albrektsson T, Brånemark PI, Hansson HA, Lindström J. 1981. Osseointegrated titanium implants: Requirements for ensuring a long-lasting, direct bone-to-implant anchorage in man. *Acta Orthop*. 52:155–170.

Albrektsson T, Wennerberg A. 2019. On osseointegration in relation to implant surfaces. *Clin. Implant Dent. Relat. Res*. Blackwell Publishing Ltd.

Ali A, Iqbal F, Ahmad A, Ikram F, Nawaz A, Chaudhry AA, Siddiqi SA, Rehman I. 2019. Hydrothermal deposition of high strength calcium phosphate coatings on magnesium alloy for biomedical applications. *Surf. Coatings Technol*. 357:716–727.

de Almeida GS, Ferreira MR, da Costa Fernandes CJ, Suter LC, Carra MGJ, Correa DRN, Rangel EC, Saeki MJ, Zambuzzi WF. 2023. Development of cobalt (Co)-doped monetites for bone regeneration. *J. Biomed. Mater. Res. - Part B Appl. Biomater*. 3:1–12.

Bauer S, Schmuki P, von der Mark K, Park J. 2013. Engineering biocompatible implant surfaces: Part I: Materials and surfaces. *Prog. Mater. Sci*. Elsevier Ltd.

Bertazzo S, Zambuzzi WF, Campos DDP, Ferreira C V., Bertran CA. 2010. A simple method for enhancing cell adhesion to hydroxyapatite surface. *Clin. Oral Implants Res*. 21:1411–1413. https://www.onlinelibrary.wiley.com/doi/full/10.1111/j.1600-0501.2010.01968.x.

Bezerra F, Ferreira MR, Fontes GN, da Costa Fernandes CJ, Andia DC, Cruz NC, da Silva RA, Zambuzzi WF. 2017. Nano hydroxyapatite-blasted titanium surface affects pre-osteoblast morphology by modulating critical intracellular pathways. *Biotechnol. Bioeng*. 114:1888–1898. http://doi.wiley.com/10.1002/bit.26310.

Brodbeck WG, Shive MS, Colton E, Nakayama Y, Matsuda T, Anderson JM. 2001. Influence of biomaterial surface chemistry on the apoptosis of adherent cells. *J. Biomed. Mater. Res*. 55:661–668.

Chérif I, Dkhil YO, Smaoui S, Elhadef K, Ferhi M, Ammar S. 2022. X-Ray Diffraction Analysis by Modified Scherrer, Williamson–Hall and Size–Strain Plot Methods of ZnO Nanocrystals Synthesized by Oxalate Route: A Potential Antimicrobial Candidate Against Foodborne Pathogens. *J. Clust. Sci*.:1–16. https://link.springer.com/article/10.1007/s10876-022-02248-z.

da Costa Fernandes C, Pinto TS, Kang HR, de Magalhães Padilha P, Koh IHJ, Constantino VRL, Zambuzzi WF. 2019. Layered Double Hydroxides Are Promising Nanomaterials for Tissue Bioengineering Application. *Adv. Biosyst*. 3:1800238. https://onlinelibrary.wiley.com/doi/10.1002/adbi.201800238.

da Costa Fernandes CJ, Ferreira MR, Bezerra FJB, Zambuzzi WF. 2018. Zirconia stimulates ECM-remodeling as a prerequisite to pre-osteoblast adhesion/proliferation by possible interference with cellular anchorage. *J. Mater. Sci. Mater. Med.* 29. https://pubmed.ncbi.nlm.nih.gov/29582191/.

da Costa Fernandes CJ, de Almeida GS, Pinto TS, Teixeira SA, Bezerra FJ, Zambuzzi WF. 2021. Metabolic effects of CoCr-enriched medium on shear-stressed endothelial cell and osteoblasts: A possible mechanism involving a hypoxic condition on bone healing. *Mater. Sci. Eng. C* 128:112353. https://linkinghub.elsevier.com/retrieve/pii/S0928493121004938.

Dohan Ehrenfest DM, Coelho PG, Kang BS, Sul YT, Albrektsson T. 2010. Classification of osseointegrated implant surfaces: Materials, chemistry and topography. *Trends Biotechnol*. Elsevier Ltd. http://dx.doi.org/10.1016/j.tibtech.2009.12.003.

Fernandes CJC, Bezerra F, Ferreira MR, Andrade AFC, Pinto TS, Zambuzzi WF. 2018. Nano hydroxyapatite-blasted titanium surface creates a biointerface able to govern Src-dependent osteoblast metabolism as prerequisite to ECM remodeling. *Colloids Surfaces B Biointerfaces* 163:321–328. https://pubmed.ncbi.nlm.nih.gov/29329077/.

Ferreira MR, Milani R, Rangel EC, Peppelenbosch M, Zambuzzi W. 2020. OsteoBLAST: Computational Routine of Global Molecular Analysis Applied to Biomaterials Development. *Front. Bioeng. Biotechnol*. 8:565901. https://www.frontiersin.org/article/10.3389/fbioe.2020.565901/full.

Gomes AM, da Silva DF, Bezerra FJ, Zambuzzi WF. 2023. Nanohydroxyapatite-Coated Titanium Surface Increases Vascular Endothelial Cells Distinct Signaling Responding to High Glucose Concentration. *J. Funct. Biomater*. 14:188. https://www.mdpi.com/2079-4983/14/4/188.

Hamlet SM, Lee RSB, Moon HJ, Alfarsi MA, Ivanovski S. 2019. Hydrophilic titanium surface-induced macrophage modulation promotes pro-osteogenic signalling. *Clin. Oral Implants Res*. 30:1085–1096.

Jeong J, Kim JH, Shim JH, Hwang NS, Heo CY. 2019. Bioactive calcium phosphate materials and applications in bone regeneration. *Biomater. Res*. 23:4.

Jinawath S, Pongkao D, Suchanek W, Yoshimura M. 2001. Hydrothermal synthesis of monetite and hydroxyapatite from monocalcium phosphate monohydrate. *Int. J. Inorg. Mater*. 3:997–1001.

Kaygili O, Tatar C, Keser S, Bulut N. 2017. Preparation and characterization of monetites co-doped with Ni/Al, Ni/Mn and Al/Mn. *Mater. Lett*. 201:39–42. http://dx.doi.org/10.1016/j.matlet.2017.05.015.

Klammert U, Gbureck U, Vorndran E, Rödiger J, Meyer-Marcotty P, Kübler AC. 2010. 3D powder printed calcium phosphate implants for reconstruction of cranial and maxillofacial defects. *J. Cranio-Maxillofacial Surg*. 38:565–570.

Machado MIP, Gomes AM, Zambuzzi WF. 2024. Hypoxia modulates the phenotype of mechanically stressed endothelial cells responding to CoCr-enriched medium. *J. Trace Elem. Med. Biol*. 82:127341.

Menzies KL, Jones L. 2010. The Impact of Contact Angle on the Biocompatibility of Biomaterials. *Optom. Vis.* Sci. 87:387–399. https://journals.lww.com/00006324-201006000-00004.

Nath D, Singh F, Das R. 2020. X-ray diffraction analysis by Williamson-Hall, Halder-Wagner and size-strain plot methods of CdSe nanoparticles- a comparative study. *Mater. Chem. Phys*. 239:122021–122029.

Navarro da Rocha D, Cruz LR de O, de Campos JB, Santos JL dos, Marçal RLSB, Mijares DQ, Barbosa RM, Coelho PG, Prado da Silva MH. 2019. Bioactivity of strontium-monetite coatings for biomedical applications. *Ceram. Int*. 45:7568–7579.

Parisi L, Ghezzi B, Bianchi MG, Toffoli A, Rossi F, Bussolati O, Macaluso GM. 2020. Titanium dental implants hydrophilicity promotes preferential serum fibronectin over albumin competitive adsorption modulating early cell response. *Mater. Sci. Eng. C* 117:111307.

Pinto TS, Martins BR, Ferreira MR, Bezerra F, Zambuzzi WF. 2022. Nanohydroxyapatite-Blasted Bioactive Surface Drives Shear-Stressed Endothelial Cell Growth and Angiogenesis. *Biomed Res*. Int. 2022.

Prado Da Silva MH, Lima JHC, Soares GA, Elias CN, De Andrade MC, Best SM, Gibson IR. 2001. Transformation of monetite to hydroxyapatite in bioactive coatings on titanium. *Surf. Coatings Technol*. 137:270–276.

Rabiei M, Palevicius A, Monshi A, Nasiri S, Vilkauskas A, Janusas G. 2020. Comparing methods for calculating nano crystal size of natural hydroxyapatite using X-ray diffraction. *Nanomaterials* 10:1–21.

Sikder P, Grice CR, Lin B, Goel VK, Bhaduri SB. 2018a. Single-Phase, Antibacterial Trimagnesium Phosphate Hydrate Coatings on Polyetheretherketone (PEEK) Implants by Rapid Microwave Irradiation Technique. *ACS Biomater*. Sci. Eng. 4:2767–2783.

Sikder P, Koju N, Ren Y, Goel VK, Phares T, Lin B, Bhaduri SB. 2018b. Development of single-phase silver-doped antibacterial CDHA coatings on Ti6Al4V with sustained release. *Surf. Coatings Technol*. 342:105–116.

Da Silva RA, Da Silva Feltran G, Ferreira MR, Wood PF, Bezerra F, Zambuzzi WF. 2020. The Impact of Bioactive Surfaces in the Early Stages of Osseointegration: An in Vitro Comparative Study Evaluating the HAnano® and SLActive® Super Hydrophilic *Surfaces.* Biomed Res. Int. 2020.

Tharani Kumar S, Prasanna Devi S, Krithika C, Raghavan RN. 2020. Review of metallic biomaterials in dental applications. *J. Pharm. Bioallied Sci*. Wolters Kluwer Medknow Publications.

Wilson CJ, Clegg RE, Leavesley DI, Pearcy MJ. 2005. Mediation of biomaterial-cell interactions by adsorbed proteins: A review. *Tissue Eng*.

Zavgorodniy A V., Borrero-López O, Hoffman M, LeGeros RZ, Rohanizadeh R. 2011. Mechanical stability of two-step chemically deposited hydroxyapatite coating on Ti substrate: Effects of various surface pretreatments. *J. Biomed. Mater. Res. Part B Appl. Biomater.* 99B:58–69. https://onlinelibrary.wiley.com/doi/10.1002/jbm.b.31872.

Zavgorodniy A V., Mason RS, LeGeros RZ, Rohanizadeh R. 2012. Adhesion of a chemically deposited monetite coating to a Ti substrate. *Surf. Coatings Technol*. 206:4433–4438.

Zhou L, You J, Wang Z, Gu Y, Chen D, Lin B, Zhao X, Lin J, Lin J, Liu W. 2021. 3D printing monetite-coated Ti-6Al-4V surface with osteoimmunomodulatory function to enhance osteogenesis. *Mater. Sci. Eng. C*:112562. https://doi.org/10.1016/j.msec.2021.112562.

Zhu Y, Zhang K, Zhao R, Ye X, Chen X, Xiao Z, Yang X, Zhu X, Zhang K, Fan Y, Zhang X. 2017. Bone regeneration with micro/nano hybrid-structured biphasic calcium phosphate bioceramics at segmental bone defect and the induced immunoregulation of MSCs. *Biomaterials* 147:133–144.

Supplementary material

Figure 1: Coating titanium with monetite by hydrothermal technique: **a.** Solutions used for monetite (right) and co-monetite (left) coating; **b.** Ti.cp plates; **c.** hydrothermal reactor; **d.** titanium plates inside the reactor and adding the solution; **e.** closing the reactor; **f.** placing the reactor in the autoclave; **g.** closing the autoclave; **h.** samples after coating, with the monetite.

Capitulo 8

Constatações, Conclusão e Perspectivas

Constatações

- O processo de síntese de monetita dopada com cobalto mostrou-se efetivo e reprodutível;
- Os ensaios de caracterização realizados nos proporcionaram informações sobre os materiais, como a morfologia, porosidade, estrutura, parâmetros de rede e mudanças de fase;
- A proporção de cobalto adicionado na monetita não apresentou citotoxicidade, induziu diferentes expressões de genes envolvidos com a diferenciação de osteoblastos, processo de adesão e remodelamento da matriz, também foi constatado que com o aumento da concentração de cobalto o efeito antibacteriano é apresentado e a regeneração pelo ensaio de Wound Healing não é comprometida;
- Quando comparado o material sem dopagem com o de menor dopagem (2%), os ensaios de caracterização não apresentação mudanças significativas na maioria dos ensaios, porém com o refinamento Rietveld dos dados de difração de raios X, observou-se uma padronização do tamanho de cristais;
- Os ensaios moleculares mostraram que genes envolvidos com a diferenciação de osteoblastos, atividade de Hif1α e eNOS foram diferencialmente expressos pelo grupo dopado com cobalto, e a atividade das metalloproteinases também apresentou diferenças;
- Quando submetido a tratamentos térmicos, os materiais mostraram mudanças de fases, apresentado a fase de pirofosfatos de beta cálcio e formação de fosfato tricálcico. Os ensaios de caracterização físico-químicos nos trouxeram informações sobre essas mudanças, mostrando um comportamento similar do material sem dopagem com o dopado (2%);
- O material dopado apresentou melhor regeneração pelo ensaio de Wound Healing quando submetido aos tratamentos térmicos superior a sua contraparte não dopada, os materiais não apresentaram citotoxicidade e diferentes expressões de genes envolvidos com os processos de inflamação, adesão, remodelamento da MEC, diferenciação de osteoblastos, atividade de Hif1α e eNOS foram observados;
- Com a aplicação da monetita e monetita dopada com cobalto em revestimento de estruturas metálicas pela técnica hidrotermal, os ensaios de caracterização mostraram a efetividade da técnica, uma padronização do tamanho de cristais, morfologia similar e formação de whiskers/flores, a presença de cobalto demonstrou padronizar os picos/vales observados no ensaio de perfilômetria. Os materiais não apresentaram citotoxicidade pelos ensaios de MTT e Cristal Violeta e a morfologia das células foi visualidade pelo ensaio de MEV.

Conclusão

Em conclusão, considerando nossos achados, este estudo revela pela primeira vez o impacto biológico de uma nova monetita dopado com cobalto em osteoblastos. Destaca-se que a monetita dopada com cobalto induz uma hipoxia biomimética e imita rapidamente o ambiente de regeneração óssea, aprimorando o desempenho osteogênico das células. A monetita dopada com cobalto surge como um material biomimético e 'inteligente', com aplicações promissoras no campo do desenvolvimento ósseo.

Perspectivas Futuras

Nossos resultados abrem caminho promissor para o aprofundamento da sinergia entre biomimética e regeneração do tecido ósseo. Espera-se que os avanços futuros se orientem para a elaboração e refinamento de unidades biomiméticas que não apenas simulem, mas também potencializam os processos biológicos essenciais para a osteogênese e recuperação óssea. Essa abordagem inovadora tem o potencial de revolucionar as terapias para lesões ósseas, com a incorporação de técnicas de ponta como a bioimpressão 3D e a engenharia de tecidos. A expectativa é desenvolver *scaffolds* avançados que não só apoiem, mas também acelerem a regeneração óssea de maneira eficiente, dinâmica e alinhada com as exigências fisiológicas do esqueleto.

Além disso, prevê-se a exploração de novos biomateriais e aprimoramento dos já existentes, com o intuito de otimizar a osteointegração e funcionalidade em uma miríade de aplicações clínicas, tanto no campo humano como veterinário. Isso inclui a investigação de implantes e próteses que se integram de forma mais natural e eficaz ao tecido hospedeiro, minimizando o risco de rejeição e maximizando a eficácia terapêutica. A longo prazo, o objetivo é que tais avanços conduzam a uma melhora significativa na qualidade de vida dos pacientes, reduzindo os tempos de recuperação e aumentando a durabilidade e funcionalidade dos implantes. No futuro, ainda, a pesquisa poderá se expandir para a modulação controlada de ambientes hipóxicos para otimizar o acoplamento angiogênese-osteogênese, explorando as propriedades do cobalto e outros agentes para criar um ambiente propício à regeneração óssea.

Referencias

AATI, S. Y. Monetite layer by layer coating for bone regeneration application. n. January, 2017.

ADAWY, A.; DIAZ, R. Probing the Structure, Cytocompatibility, and Antimicrobial Efficacy of Silver-, Strontium-, and Zinc-Doped Monetite. **ACS Applied Bio Materials**, v. 5, n. 4, p. 1648–1657, 18 abr. 2022.

AERSSENS, J. et al. Variations in trabecular bone composition with anatomical site and age: Potential implications for bone quality assessment. **Journal of Endocrinology**, v. 155, n. 3, p. 411–421, 1997.

AERSSENS, J. et al. Interspecies differences in bone composition, density, and quality: Potential implications for in vivo bone research. **Endocrinology**, v. 139, n. 2, p. 663–670, 1998.

AFZAL, F.; POLAK, J.; BUTTERY, L. Endothelial nitric oxide synthase in the control of osteoblastic mineralizing activity and bone integrity. **Journal of Pathology**, v. 202, n. 4, p. 503–510, abr. 2004.

ALBREKTSSON, T. et al. Osseointegrated titanium implants: Requirements for ensuring a long-lasting, direct bone-to-implant anchorage in man. **Acta Orthopaedica**, v. 52, n. 2, p. 155–170, 1981.

ALBREKTSSON, T.; WENNERBERG, A. **On osseointegration in relation to implant surfaces**. **Clinical Implant Dentistry and Related Research**Blackwell Publishing Ltd, , 1 mar. 2019.

ALI, A. et al. Hydrothermal deposition of high strength calcium phosphate coatings on magnesium alloy for biomedical applications. **Surface and Coatings Technology**, v. 357, p. 716–727, 15 jan. 2019.

ALI, M. et al. Allograft bone banking experience in Pakistan. **Cell and Tissue Banking**, v. 23, n. 2, p. 367–373, 1 jun. 2022.

ALLMANN, R.; HINEK, R. The introduction of structure types into the Inorganic Crystal Structure Database ICSD. **Acta Crystallographica Section A: Foundations of Crystallography**, v. 63, n. 5, p. 412–417, 17 ago. 2007.

APELT, D. et al. In vivo behavior of three different injectable hydraulic calcium phosphate cements. **Biomaterials**, v. 25, n. 7–8, p. 1439–1451, 1 mar. 2004.

APONTE-TINAO, L. A. et al. Should Fractures in Massive Intercalary Bone Allografts of the Lower Limb Be Treated With ORIF or With a New Allograft? **Clinical Orthopaedics and Related Research**, v. 473, n. 3, p. 805–811, 1 mar. 2015.

ARALDI, E.; SCHIPANI, E. **Hypoxia, HIFs and bone development**. **Bone**, 2010. Disponível em: <https://pubmed.ncbi.nlm.nih.gov/20444436/>

ARO, H. T. et al. Internal remodeling of periosteal new bone during fracture healing. **Journal of Orthopaedic Research**, v. 8, n. 2, p. 238–246, 1990.

ASLANKOOHI, N. et al. **Bone repair and regenerative biomaterials: Towards recapitulating the microenvironment**. **Polymers**MDPI AG, , 2019.

BABIKER, H. Bone graft materials in fixation of orthopaedic implants in sheep. **Danish medical journal**, v. 60, n. 7, p. B4680, 1 jul. 2013.

BABILOTTE, J. et al. Development and characterization of a PLGA-HA composite material to fabricate 3D-printed scaffolds for bone tissue engineering. **Materials Science and Engineering C**, v. 118, p. 111334, 1 jan. 2021.

BAHNEY, C. S. et al. **Cellular biology of fracture healing**. **Journal of Orthopaedic Research**John Wiley and Sons Inc., , 1 jan. 2019.

BALDWIN, P. et al. Autograft, Allograft, and Bone Graft Substitutes: Clinical Evidence and Indications for Use in the Setting of Orthopaedic Trauma Surgery. **Journal of Orthopaedic Trauma**, v. 33, n. 4, p. 203–213, 1 abr. 2019.

BALOUL, S. S. Osteoclastogenesis and Osteogenesis during Tooth Movement. **Frontiers of Oral Biology**, v. 18, p. 75–79, 2015.

BANTAWAL, H.; SHENOY, U. S.; BHAT, D. K. Vanadium-Doped SrTiO3 Nanocubes: Insight into role of vanadium in improving the photocatalytic activity. **Applied Surface Science**, v. 513, 30 maio 2020.

BARDESTANI, R.; PATIENCE, G. S.; KALIAGUINE, S. **Experimental methods in chemical engineering: specific surface area and pore size distribution measurements—BET, BJH, and DFT**. **Canadian Journal of Chemical Engineering**Wiley-Liss Inc., , 1 nov. 2019.

BAROU, O. et al. Relationships between trabecular bone remodeling and bone vascularization: A quantitative study. **Bone**, v. 30, n. 4, p. 604–612, abr. 2002.

BAUER, A. W. et al. Antibiotic Susceptibility Testing by a Standardized Single Disk Method. **American Journal of Clinical Pathology**, v. 45, n. 4_ts, p. 493–496, 1 abr. 1966.

BAUER, S. et al. **Engineering biocompatible implant surfaces: Part I: Materials and surfaces**. **Progress in Materials Science**Elsevier Ltd, , 1 abr. 2013.

BECK, T. J. et al. Structural adaptation to changing skeletal load in the progression toward hip fragility: The study of osteoporotic fractures. **Journal of Bone and Mineral Research**, v. 16, n. 6, p. 1108–1119, 2 jun. 2001.

BELKLY, A. et al. New developments in the Inorganic Crystal Structure Database (ICSD): Accessibility in support of materials research and design. **Acta Crystallographica Section B: Structural Science**, v. 58, n. 3 PART 1, p. 364–369, 29 jun. 2002.

BERTAZZO, S. et al. A simple method for enhancing cell adhesion to hydroxyapatite surface.

Clinical Oral Implants Research, v. 21, n. 12, p. 1411–1413, 1 dez. 2010.
BEZERRA, F. et al. Nano hydroxyapatite-blasted titanium surface affects pre-osteoblast morphology by modulating critical intracellular pathways. **Biotechnology and Bioengineering**, v. 114, n. 8, p. 1888–1898, 1 ago. 2017.
BHATTACHARJEE, A. et al. Antibacterial and magnetic response of site-specific cobalt incorporated hydroxyapatite. **Ceramics International**, v. 46, n. 1, p. 513–522, 1 jan. 2020.
BIGHAM-SADEGH, A.; ORYAN, A. Basic concepts regarding fracture healing and the current options and future directions in managing bone fractures. **International Wound Journal**, v. 12, n. 3, p. 238–247, 1 jun. 2015.
BLUMENTHAL, N. M. et al. Defect-Determined Regenerative Options for Treating Periodontal Intrabony Defects in Baboons. **Journal of Periodontology**, v. 74, n. 1, p. 10–24, jan. 2003.
BOANINI, E. et al. Monetite vs. Brushite: Different Influences on Bone Cell Response Modulated by Strontium Functionalization. **Journal of Functional Biomaterials**, v. 13, n. 2, p. 65, 24 maio 2022.
BOHNER, M. et al. Compositional changes of a dicalcium phosphate dihydrate cement after implantation in sheep. **Biomaterials**, v. 24, n. 20, p. 3463–3474, 1 set. 2003.
BOHNER, M. et al. Effect of thermal treatments on the reactivity of nanosized tricalcium phosphate powders. **Journal of Materials Chemistry**, v. 18, n. 37, p. 4460–4467, 2008.
BOHNER, M. Bone substitute materials. In: **Encyclopedia of Biomedical Engineering**. [s.l.] Elsevier, 2019. v. 1–3p. 513–529.
BORD, S. et al. Production of collagenase by human osteoblasts and osteoclasts in vivo. **Bone**, v. 19, n. 1, p. 35–40, jul. 1996.
BOSE, S.; ROY, M.; BANDYOPADHYAY, A. Recent advances in bone tissue engineering scaffolds. **Trends in Biotechnology**, v. 30, n. 10, p. 546–554, 2012.
BOSKEY, A. L.; ROBEY, P. G. The composition of bone. . 3 out. 2018, p. 84–92.
BOULER, J. M. et al. Biphasic calcium phosphate ceramics for bone reconstruction: A review of biological response. **Acta Biomaterialia**, v. 53, p. 1–12, 2017.
BOYER, M. H.; SHAINOFF, J. R.; RATNOFF, O. D. **Acceleration of fibrin polymerization by calcium ions. Blood**, 1972. Disponível em: <https://pubmed.ncbi.nlm.nih.gov/5059648/>
BRANDI, M. L.; COLLIN-OSDOBY, P. Vascular biology and the skeleton. . 1 fev. 2006, p. 183–192.
BRODBECK, W. G. et al. Influence of biomaterial surface chemistry on the apoptosis of adherent cells. **Journal of Biomedical Materials Research**, v. 55, n. 4, p. 661–668, 15 jun. 2001.
BROWN, O. et al. Sintering of biphasic calcium phosphates. **Journal of Materials Science:**

Materials in Medicine, v. 21, n. 8, p. 2271–2279, 16 ago. 2010.
CAMA, G. et al. A novel method of forming micro- and macroporous monetite cements. **Journal of Materials Chemistry B**, v. 1, n. 7, p. 958–969, 23 jan. 2013.
CAMPANA, V. et al. Bone substitutes in orthopaedic surgery: from basic science to clinical practice. **Journal of Materials Science: Materials in Medicine**, v. 25, n. 10, p. 2445–2461, 20 set. 2014.
CAO, L. et al. Vascularization and bone regeneration in a critical sized defect using 2-N,6-O-sulfated chitosan nanoparticles incorporating BMP-2. **Biomaterials**, v. 35, n. 2, p. 684–698, jan. 2014.
CAPLAN, M. R.; SHAH, M. M. **Translating biomaterial properties to intracellular signaling**. **Cell Biochemistry and Biophysics**, jul. 2009.
CARDOSO, G. C. et al. Preparation and characterization of novel as-cast Ti-Mo-Nb alloys for biomedical applications. **Scientific Reports**, v. 12, n. 1, p. 11874–11874, 1 dez. 2022.
CARREIRA, A. C. et al. Bone morphogenetic proteins: Facts, challenges, and future perspectives. **Journal of Dental Research**, v. 93, n. 4, p. 335–345, 2014.
CARREIRA, A. C. O. et al. Bone Morphogenetic Proteins: Promising Molecules for Bone Healing, Bioengineering, and Regenerative Medicine. In: **Vitamins and Hormones**. [s.l.] Academic Press Inc., 2015. v. 99p. 293–322.
CARRODEGUAS, R. G.; DE AZA, S. **α-Tricalcium phosphate: Synthesis, properties and biomedical applications**. **Acta Biomaterialia**Elsevier Ltd, , out. 2011.
CASTRO-SILVA, I. I. et al. **Periosteal-derived cells for bone bioengineering: A promising candidate**. Disponível em: <https://pubmed.ncbi.nlm.nih.gov/22221259/>. Acesso em: 3 mar. 2023.
CATTI, M.; FERRARIS, G.; FILHOL, A. Hydrogen bonding in the crystalline state. CaHPO4 (monetite), P1 or P1? A novel neutron diffraction study. **Acta Crystallographica Section B Structural Crystallography and Crystal Chemistry**, v. 33, n. 4, p. 1223–1229, 15 abr. 1977.
CATTI, M.; FERRARIS, G.; MASON, S. A. Low-temperature ordering of hydrogen atoms in CaHPO 4 (monetite): X-ray and neutron diffraction study at 145 K . **Acta Crystallographica Section B Structural Crystallography and Crystal Chemistry**, v. 36, n. 2, p. 254–259, 1 fev. 1980.
CHAI, F. et al. Biomaterials as bone substitute: Classification and contribution. **Revue de Stomatologie et de Chirurgie Maxillo-Faciale**, v. 112, n. 4, p. 212–221, set. 2011.
CHANG, B.; LIU, X. **Osteon: Structure, Turnover, and Regeneration**. **Tissue Engineering - Part B: Reviews**Mary Ann Liebert Inc., , 1 abr. 2022.
CHEN, S. et al. Synthesis of Ag doped calcium phosphate particles and their antibacterial effect

as additives in dental glass ionomer cements. **Journal of Materials Science: Materials in Medicine**, v. 27, n. 11, 1 nov. 2016.

CHÉRIF, I. et al. X-Ray Diffraction Analysis by Modified Scherrer, Williamson–Hall and Size–Strain Plot Methods of ZnO Nanocrystals Synthesized by Oxalate Route: A Potential Antimicrobial Candidate Against Foodborne Pathogens. **Journal of Cluster Science**, p. 1–16, 6 mar. 2022.

CHIM, S. M. et al. Angiogenic factors in bone local environment. . jun. 2013, p. 297–310.

CHOI, I. H. et al. **Angiogenesis and mineralization during distraction osteogenesis. Journal of Korean medical science**, 2002.

CONSTANTZ, B. R. et al. Histological, chemical, and crystallographic analysis of four calcium phosphate cements in different rabbit osseous sites. **Journal of Biomedical Materials Research**, v. 43, n. 4, p. 451–461, 1998.

COWIN, S. C. **Bone poroelasticity**. **Journal of Biomechanics**J Biomech, , mar. 1999.

CRUBEZY, E. et al. **False teeth of the Roman world [3]**. **Nature**Nature Publishing Group, , 1 jan. 1998.

CUPERSCHMID, E. M.; CAMPOS, T. P. R. DE. Os curiosos xenoimplantes glandulares do doutor Voronoff. **História, Ciências, Saúde-Manguinhos**, v. 14, n. 3, p. 737–760, set. 2007.

CZITROM, A. A. et al. **Bone and cartilage allotransplantation: A review of 14 years of research and clinical studies**. **Clinical Orthopaedics and Related Research**, 1986.

DA COSTA FERNANDES, C. et al. Layered Double Hydroxides Are Promising Nanomaterials for Tissue Bioengineering Application. **Advanced Biosystems**, v. 3, n. 7, p. 1800238, 1 jul. 2019.

DA COSTA FERNANDES, C. J. et al. Zirconia stimulates ECM-remodeling as a prerequisite to pre-osteoblast adhesion/proliferation by possible interference with cellular anchorage. **Journal of Materials Science: Materials in Medicine**, v. 29, n. 4, 1 abr. 2018a.

DA COSTA FERNANDES, C. J. et al. Titanium-enriched medium drives low profile of ECM remodeling as a pre-requisite to pre-osteoblast viability and proliferative phenotype. **Journal of Trace Elements in Medicine and Biology**, v. 50, n. February, p. 339–346, 1 dez. 2018b.

DA COSTA FERNANDES, C. J. et al. Metabolic effects of CoCr-enriched medium on shear-stressed endothelial cell and osteoblasts: A possible mechanism involving a hypoxic condition on bone healing. **Materials Science and Engineering C**, v. 128, p. 112353, 1 set. 2021a.

DA COSTA FERNANDES, C. J. et al. Metabolic effects of CoCr-enriched medium on shear-stressed endothelial cell and osteoblasts: A possible mechanism involving a hypoxic condition on bone healing. **Materials Science and Engineering C**, v. 128, p. 112353, 1 set. 2021b.

DA S. FELTRAN, G. et al. Differential inflammatory landscape stimulus during titanium

surfaces obtained osteogenic phenotype. **Journal of Biomedical Materials Research - Part A**, v. 107, n. 8, p. 1597–1604, 1 ago. 2019.

DA SILVA, R. A. et al. The Impact of Bioactive Surfaces in the Early Stages of Osseointegration: An in Vitro Comparative Study Evaluating the HAnano® and SLActive® Super Hydrophilic Surfaces. **BioMed Research International**, v. 2020, 2020.

DANG, M. et al. **Biomimetic delivery of signals for bone tissue engineering**. **Bone Research**Sichuan University, , 2018.

DE ALMEIDA, G. S. et al. Development of cobalt (Co)-doped monetites for bone regeneration. **Journal of Biomedical Materials Research - Part B Applied Biomaterials**, v. 3, n. August, p. 1–12, 2023.

DE SOUZA MALASPINA, T. S. et al. A possible mechanism of low molecular weight protein tyrosine phosphatase (LMW-PTP) activity modulation by glutathione action during human osteoblast differentiation. **Archives of Oral Biology**, v. 54, n. 7, p. 642–650, 1 jul. 2009.

DENNE, W. A.; JONES, D. W. Neutron diffraction investigation of the hydrogen positions in the crystal structure of monetite, CaHPO4. **Journal of Crystal and Molecular Structure**, v. 1, n. 5, p. 347–354, out. 1971.

DESAI, T. R.; BHADURI, S. B.; TAS, A. C. A Self-Setting, Monetite (CaHPO4) Cement for Skeletal Repair. In: [s.l.] John Wiley & Sons, Ltd, 2008. p. 61–69.

DICKENS, B.; BOWEN, J. S.; BROWN, W. E. A refinement of the crystal structure of CaHPO4 (synthetic monetite). **Acta Crystallographica Section B Structural Crystallography and Crystal Chemistry**, v. 28, n. 3, p. 797–806, 15 mar. 1972.

DIRCKX, N.; VAN HUL, M.; MAES, C. Osteoblast recruitment to sites of bone formation in skeletal development, homeostasis, and regeneration. **Birth defects research. Part C, Embryo today : reviews**, v. 99, n. 3, p. 170–191, set. 2013.

DIVYA RANI, V. V. et al. Osteointegration of titanium implant is sensitive to specific nanostructure morphology. **Acta Biomaterialia**, v. 8, n. 5, p. 1976–1989, 2012.

DJOŠIĆ, M. S. et al. Electrochemical synthesis of nanosized monetite powder and its electrophoretic deposition on titanium. **Colloids and Surfaces A: Physicochemical and Engineering Aspects**, v. 341, n. 1–3, p. 110–117, 5 jun. 2009.

DOHAN EHRENFEST, D. M. et al. **Classification of osseointegrated implant surfaces: Materials, chemistry and topography**. Disponível em: <http://dx.doi.org/10.1016/j.tibtech.2009.12.003>. Acesso em: 8 fev. 2023.

DOROZHKIN, S. V. Bioceramics based on calcium orthophosphates (Review). **Glass and Ceramics (English translation of Steklo i Keramika)**, v. 64, n. 11–12, p. 442–447, 2007.

DOROZHKIN, S. V. Calcium orthophosphates: Occurrence, properties and major applications.

Apatite: Synthesis, Structural Characterization and Biomedical Applications, v. 4, n. 2, p. 1–47, 2014.

DUKLE, A. et al. Can 3D-Printed Bioactive Glasses Be the Future of Bone Tissue Engineering? **Polymers**, v. 14, n. 8, 18 abr. 2022.

DUNCAN, J. et al. **The role of the chemical composition of monetite on the synthesis and properties of α-tricalcium phosphate**. Disponível em: <https://www.sciencedirect.com/science/article/pii/S0928493113005018?via%3Dihub>. Acesso em: 13 jan. 2023.

DUNWOODIE, S. L. The role of hypoxia in development of the Mammalian embryo. **Developmental cell**, v. 17, n. 6, p. 755–773, dez. 2009.

EBRAHIMI, M.; BOTELHO, M. Biphasic calcium phosphates (BCP) of hydroxyapatite (HA) and tricalcium phosphate (TCP) as bone substitutes: Importance of physicochemical characterizations in biomaterials studies. **Data in Brief**, v. 10, p. 93–97, 2017.

ESHKAR-OREN, I. et al. The forming limb skeleton serves as a signaling center for limb vasculature patterning via regulation of Vegf. **Development (Cambridge, England)**, v. 136, n. 8, p. 1263–1272, abr. 2009.

FERNANDES, C. J. C. et al. Nano hydroxyapatite-blasted titanium surface creates a biointerface able to govern Src-dependent osteoblast metabolism as prerequisite to ECM remodeling. **Colloids and Surfaces B: Biointerfaces**, v. 163, p. 321–328, 1 mar. 2018.

FERNANDES, C. J. DA C. et al. Mechanosignaling-related angiocrine factors drive osteoblastic phenotype in response to zirconia. **Journal of Trace Elements in Medicine and Biology**, v. 81, p. 127337, 1 jan. 2023.

FERNANDES, G. V. O. et al. Osteoblast adhesion dynamics: A possible role for ROS and LMW-PTP. **Journal of Cellular Biochemistry**, v. 115, n. 6, p. 1063–1069, 2014.

FERREIRA, M. R. et al. OsteoBLAST: Computational Routine of Global Molecular Analysis Applied to Biomaterials Development. **Frontiers in Bioengineering and Biotechnology**, v. 8, p. 565901, 8 out. 2020.

FINE, N. et al. Differential response of human blood leukocytes to brushite, monetite, and calcium polyphosphate biomaterials. **Journal of Biomedical Materials Research Part B: Applied Biomaterials**, v. 108, n. 1, p. 253–262, 22 jan. 2020.

FISCHER, C. et al. FLT1 and its ligands VEGFB and PlGF: drug targets for anti-angiogenic therapy? **Nature reviews. Cancer**, v. 8, n. 12, p. 942–956, dez. 2008.

FLORENCIO-SILVA, R. et al. **Biology of Bone Tissue: Structure, Function, and Factors That Influence Bone Cells**. **BioMed Research International**Hindawi Publishing Corporation, , 2015.

GALEA, L. G. et al. Bone substitute: Transforming β-tricalcium phosphate porous scaffolds into monetite. **Biomaterials**, v. 29, n. 24–25, p. 3400–3407, 1 ago. 2008.
GAO, C. et al. Bone biomaterials and interactions with stem cells. **Bone Research**, v. 5, p. 17059, 21 dez. 2017.
GARCÍA-GARETA, E.; COATHUP, M. J.; BLUNN, G. W. **Osteoinduction of bone grafting materials for bone repair and regeneration**. Disponível em: <https://pubmed.ncbi.nlm.nih.gov/26163110/>. Acesso em: 7 jan. 2023.
GARCÍA, A. J.; KESELOWSKY, B. G. **Biomimetic surfaces for control of cell adhesion to facilitate bone formation**. **Critical Reviews in Eukaryotic Gene Expression**, 2002.
GARLANDA, C.; DINARELLO, C. A.; MANTOVANI, A. **The Interleukin-1 Family: Back to the Future**. **Immunity**, 12 dez. 2013.
GBURECK, U. et al. Resorbable Dicalcium Phosphate Bone Substitutes Prepared by 3D Powder Printing. **Advanced Functional Materials**, v. 17, n. 18, p. 3940–3945, 17 dez. 2007.
GEMINI-PIPERNI, S. et al. Cellular behavior as a dynamic field for exploring bone bioengineering: A closer look at cell-biomaterial interface. **Archives of Biochemistry and Biophysics**, v. 561, p. 88–98, 2014a.
GEMINI-PIPERNI, S. et al. Cellular behavior as a dynamic field for exploring bone bioengineering: A closer look at cell-biomaterial interface. **Archives of Biochemistry and Biophysics**, v. 561, p. 88–98, 1 nov. 2014b.
GERBER, H. P.; FERRARA, N. Angiogenesis and bone growth. **Trends in cardiovascular medicine**, v. 10, n. 5, p. 223–228, jul. 2000.
GERSTENFELD, L. C. et al. Fracture healing as a post-natal developmental process: Molecular, spatial, and temporal aspects of its regulation. **Journal of Cellular Biochemistry**, v. 88, n. 5, p. 873–884, 1 abr. 2003.
GHINA IMANIYYAH, A.; SUNARSO; HERDA, E. Monetite as a potential ideal bone substitute: A short review on fabrication and properties. **Materials Today: Proceedings**, v. 66, p. 2762–2766, 1 jan. 2022.
GIACCIA, A. J.; SIMON, M. C.; JOHNSON, R. The biology of hypoxia: The role of oxygen sensing in development, normal function, and disease. . 15 set. 2004, p. 2183–2194.
GINEBRA, M. P. et al. New processing approaches in calcium phosphate cements and their applications in regenerative medicine. **Acta Biomaterialia**, v. 6, n. 8, p. 2863–2873, 2010.
GIORI, N. J.; BEAUPRE, G. S. Femoral fracture after harvesting of autologous bone graft using a reamer/irrigator/aspirator. **Journal of Orthopaedic Trauma**, v. 25, n. 2, p. e12–e14, 2011.
GOLDBERG, V. M. **The biology of bone grafts**. Disponível em: <https://pubmed.ncbi.nlm.nih.gov/10148544/>. Acesso em: 7 jan. 2023.

GOLDBERG, V. M.; STEVENSON, S. Natural history of autografts and allografts. **Clinical Orthopaedics and Related Research**, v. 225, p. 7–16, 1987.

GOMES, A. M. et al. Nanohydroxyapatite-Coated Titanium Surface Increases Vascular Endothelial Cells Distinct Signaling Responding to High Glucose Concentration. **Journal of Functional Biomaterials**, v. 14, n. 4, p. 188, 2023.

GOMES, O. P. et al. A novel BSA immobilizing manner on modified titanium surface ameliorates osteoblast performance. **Colloids and Surfaces B: Biointerfaces**, v. 190, p. 110888, 1 fev. 2020.

GRIFFONI, C. et al. Ceramic bone graft substitute (Mg-HA) in spinal fusion: A prospective pilot study. **Frontiers in bioengineering and biotechnology**, v. 10, p. 1050495, 2022.

GROEN, N. et al. Exploring the Material-Induced Transcriptional Landscape of Osteoblasts on Bone Graft Materials. **Advanced Healthcare Materials**, v. 4, n. 11, p. 1691–1700, 1 ago. 2015.

GROSSARDT, C. et al. Passive and active in vitro resorption of calcium and magnesium phosphate cements by osteoclastic cells. **Tissue Engineering - Part A**, v. 16, n. 12, p. 3687–3695, 1 dez. 2010.

GUO, H. et al. Quantitative phase analyses of biomedical pyrophosphate-bearing monetite and brushite cements by solid-state NMR and powder XRD. **Ceramics International**, v. 46, n. 8, p. 11000–11012, 1 jun. 2020.

GUTFLEISCH, O. **Peg legs and bionic limbs: The development of lower extremity prosthetics**. **Interdisciplinary Science Reviews**Taylor & Francis, , jun. 2003.

HABIBOVIC, P. et al. Osteoconduction and osteoinduction of low-temperature 3D printed bioceramic implants. **Biomaterials**, v. 29, n. 7, p. 944–953, 1 mar. 2008.

HABIBOVIC, P.; DE GROOT, K. **Osteoinductive biomaterials - properties and relevance in bone repair**. **Journal of Tissue Engineering and Regenerative Medicine**John Wiley and Sons Ltd, , 2007.

HABRAKEN, W. et al. Calcium phosphates in biomedical applications: Materials for the future? **Materials Today**, v. 19, n. 2, p. 69–87, 1 mar. 2016.

HAIDER, A. et al. **Recent advances in the synthesis, functionalization and biomedical applications of hydroxyapatite: a review**. **RSC Advances**, 2017.

HAMADA, K. et al. Hydrothermal modification of titanium surface in calcium solutions. **Biomaterials**, v. 23, n. 10, p. 2265–2272, 2002.

HAMLET, S. et al. The effect of hydrophilic titanium surface modification on macrophage inflammatory cytokine gene expression. **Clinical Oral Implants Research**, v. 23, n. 5, p. 584–590, maio 2012.

HAMLET, S. M. et al. Hydrophilic titanium surface-induced macrophage modulation promotes

pro-osteogenic signalling. **Clinical Oral Implants Research**, v. 30, n. 11, p. 1085–1096, 1 nov. 2019.

HAN, K.; CHEN, X. THE ARCHAEOLOGICAL EVIDENCE OF TREPANATION IN EARLY CHINA. **Bulletin of the Indo-Pacific Prehistory Association**, v. 27, n. 0, p. 22–27, 5 set. 2007.

HANKENSON, K. D. et al. Angiogenesis in bone regeneration. **Injury**, v. 42, n. 6, p. 556–561, 2011.

HARADA, S. I.; RODAN, G. A. **Control of osteoblast function and regulation of bone mass**. **Nature**Nature, , 15 maio 2003.

HARTREE, E. F. Determination of protein: A modification of the lowry method that gives a linear photometric response. **Analytical Biochemistry**, v. 48, n. 2, p. 422–427, 1972.

HAUGE, E. M. et al. Cancellous bone remodeling occurs in specialized compartments lined by cells expressing osteoblastic markers. **Journal of bone and mineral research : the official journal of the American Society for Bone and Mineral Research**, v. 16, n. 9, p. 1575–1582, set. 2001.

HAUGEN, H. J. et al. Bone grafts: which is the ideal biomaterial? **Journal of Clinical Periodontology**, v. 46, n. S21, p. 92–102, 2019.

HAUL, R. S. J. Gregg, K. S. W. Sing: Adsorption, Surface Area and Porosity. 2. Auflage, Academic Press, London 1982. 303 Seiten. **Berichte der Bunsengesellschaft für physikalische Chemie**, v. 86, n. 10, p. 957–957, 1 out. 1982.

HAYASHI, K. Three-dimensional organization of the cartilage canal--a scanning electron-microscopic study by vascular cast of the rabbit's femoral head. **Nihon Seikeigeka Gakkai zasshi**, v. 66, n. 5, maio 1992.

HE, X. et al. BMP2 genetically engineered MSCs and EPCs promote vascularized bone regeneration in rat critical-sized calvarial bone defects. **PloS one**, v. 8, n. 4, p. e60473, 2013.

HELLENBRANDT, M. **The inorganic crystal structure database (ICSD) - Present and future**. Crystallography Reviews. **Anais**...Taylor & Francis, jan. 2004.

HENCH, L. L. Bioceramics: From Concept to Clinic. **Journal of the American Ceramic Society**, v. 74, n. 7, p. 1487–1510, 1991.

HENRIKSEN, K. et al. Local communication on and within bone controls bone remodeling. **Bone**, v. 44, n. 6, p. 1026–1033, jun. 2009.

HILDEBRAND, H. F. Biomaterials - a history of 7000 years. **BioNanoMaterials**, v. 14, n. 3–4, p. 119–133, 2013.

HLEL, F.; KAMOUN, S.; GUIDARA, K. Investigation of Phosphorus Site Condensation in CaHPO4 by Analysis of 31P MAS-NMR Tensor and X-Ray Powder Patterns. **Zeitschrift fur Naturforschung - Section A Journal of Physical Sciences**, v. 61, n. 7–8, p. 375–382, 1 ago.

2006.
HOLZWARTH, J. M.; MA, P. X. **Biomimetic nanofibrous scaffolds for bone tissue engineering**. **Biomaterials**, 2011.
HOU, X. et al. Calcium Phosphate-Based Biomaterials for Bone Repair. **Journal of Functional Biomaterials**, v. 13, n. 4, p. 187, 14 out. 2022.
HUEBSCH, N.; MOONEY, D. J. Inspiration and application in the evolution of biomaterials. . 26 nov. 2009, p. 426–432.
HUNG, S. P. et al. Hypoxia promotes proliferation and osteogenic differentiation potentials of human mesenchymal stem cells. **Journal of orthopaedic research : official publication of the Orthopaedic Research Society**, v. 30, n. 2, p. 260–266, fev. 2012.
HURLE, K. et al. Osteogenic lithium-doped brushite cements for bone regeneration. **Bioactive Materials**, 31 dez. 2021.
IAQUINTA, M. R. et al. Innovative biomaterials for bone regrowth. **International Journal of Molecular Sciences**, v. 20, n. 3, p. 1–17, 2019.
IDOWU, B. et al. In vitro osteoinductive potential of porous monetite for bone tissue engineering. **Journal of Tissue Engineering**, v. 5, 17 jan. 2014.
IMAI, K. et al. Selective transendothelial migration of hematopoietic progenitor cells: a role in homing of progenitor cells. **Blood**, v. 93, n. 1, p. 149–156, jan. 1999.
ITKIN, T. et al. Distinct bone marrow blood vessels differentially regulate haematopoiesis. **Nature**, v. 532, n. 7599, p. 323–328, 21 abr. 2016.
IVAN, M. et al. HIFalpha targeted for VHL-mediated destruction by proline hydroxylation: implications for O2 sensing. **Science (New York, N.Y.)**, v. 292, n. 5516, p. 464–468, abr. 2001.
JAAKKOLA, P. et al. Targeting of HIF-alpha to the von Hippel-Lindau ubiquitylation complex by O2-regulated prolyl hydroxylation. **Science (New York, N.Y.)**, v. 292, n. 5516, p. 468–472, abr. 2001.
JACOBSEN, K. A. et al. Bone formation during distraction osteogenesis is dependent on both VEGFR1 and VEGFR2 signaling. **Journal of bone and mineral research : the official journal of the American Society for Bone and Mineral Research**, v. 23, n. 5, p. 596–609, maio 2008.
JANG, H. J. et al. Effect of various shaped magnesium hydroxide particles on mechanical and biological properties of poly(lactic-co-glycolic acid) composites. **Journal of Industrial and Engineering Chemistry**, v. 59, p. 266–276, 2018.
JEONG, J. et al. Bioactive calcium phosphate materials and applications in bone regeneration. **Biomaterials Research**, v. 23, n. 1, p. 4, dez. 2019.
JINAWATH, S. et al. Hydrothermal synthesis of monetite and hydroxyapatite from monocalcium phosphate monohydrate. **International Journal of Inorganic Materials**, v. 3, n.

7, p. 997–1001, 1 nov. 2001.
JONES, D. W.; CRUICKSHANK, D. W. J. The crystal structures of two calcium orthophosphates: CaHPO 4 and Ca(H 2 PO 4) 2 · H 2 O . **Zeitschrift für Kristallographie - Crystalline Materials**, v. 116, n. 1–6, p. 101–125, 1 dez. 1961.
JONITZ-HEINCKE et al. Analysis of Cellular Activity Short-Term Exposure to Cobalt and Chromium Ions in Mature Human Osteoblasts. **Materials**, v. 12, n. 17, p. 2771, 28 ago. 2019.
KANAZAWA, I. et al. Metformin enhances the differentiation and mineralization of osteoblastic MC3T3-E1 cells via AMP kinase activation as well as eNOS and BMP-2 expression. **Biochemical and Biophysical Research Communications**, v. 375, n. 3, p. 414–419, 24 out. 2008.
KANCZLER, J. M.; OREFFO, R. O. C. Osteogenesis and angiogenesis: The potential for engineering bone. . maio 2008, p. 100–114.
KANG, H. R. et al. Mg–Al and Zn–Al Layered Double Hydroxides Promote Dynamic Expression of Marker Genes in Osteogenic Differentiation by Modulating Mitogen-Activated Protein Kinases. **Advanced Healthcare Materials**, v. 7, n. 4, p. 1–12, 21 fev. 2018.
KAO, S. T.; SCOTT, D. D. **A Review of Bone Substitutes**. **Oral and Maxillofacial Surgery Clinics of North America**, nov. 2007.
KARSENTY, G. How many factors are required to remodel bone? . set. 2000 a, p. 970–971.
KARSENTY, G. **How many factors are required to remodel bone? Nature medicine**United States, set. 2000b.
KARSENTY, G.; FERRON, M. The contribution of bone to whole-organism physiology. **Nature**, v. 481, n. 7381, p. 314–320, jan. 2012.
KARSENTY, G.; KRONENBERG, H. M.; SETTEMBRE, C. Genetic control of bone formation. **Annual review of cell and developmental biology**, v. 25, p. 629–648, 2009.
KAYGILI, O. et al. Preparation and characterization of monetites co-doped with Ni/Al, Ni/Mn and Al/Mn. **Materials Letters**, v. 201, p. 39–42, 15 ago. 2017.
KEITH, B.; JOHNSON, R. S.; SIMON, M. C. HIF1alpha and HIF2alpha: sibling rivalry in hypoxic tumour growth and progression. **Nature reviews. Cancer**, v. 12, n. 1, p. 9–22, dez. 2011.
KIM, D. H. et al. Prospective study of iliac crest bone graft harvest site pain and morbidity. **Spine Journal**, v. 9, n. 11, p. 886–892, 2009.
KIM, M. et al. PCL infiltration into a BCP Scaffold Strut to improve the mechanical strength while retaining other properties. **Korean Journal of Materials Research**, v. 20, n. 6, p. 331–337, 2010.
KIM, S. E. et al. Accelerated Osteogenic Differentiation of MC3T3-E1 Cells by Lactoferrin-

Conjugated Nanodiamonds through Enhanced Anti-Oxidant and Anti-Inflammatory Effects. **Nanomaterials**, v. 10, n. 1, p. 50, 24 dez. 2019.

KLAMMERT, U. et al. Cytocompatibility of brushite and monetite cell culture scaffolds made by three-dimensional powder printing. **Acta Biomaterialia**, v. 5, n. 2, p. 727–734, 1 fev. 2009.

KLAMMERT, U. et al. 3D powder printed calcium phosphate implants for reconstruction of cranial and maxillofacial defects. **Journal of Cranio-Maxillofacial Surgery**, v. 38, n. 8, p. 565–570, 1 dez. 2010.

KO, C.-L. et al. Osteoregenerative capacities of dicalcium phosphate-rich calcium phosphate bone cement. **Journal of Biomedical Materials Research Part A**, v. 103, n. 1, p. 203–210, 1 jan. 2015.

KOBAYASHI, Y.; UDAGAWA, N.; TAKAHASHI, N. **Action of RANKL and OPG for osteoclastogenesis**. **Critical Reviews in Eukaryotic Gene Expression**Begell House Inc., , 2009.

KOJU, N. et al. **Biomimetic coating technology for orthopedic implants**. **Current Opinion in Chemical Engineering**Elsevier Ltd, , 1 fev. 2017.

KOMORI, T. Regulation of proliferation, differentiation and functions of osteoblasts by runx2. **International Journal of Molecular Sciences**, v. 20, n. 7, p. 1694, 4 abr. 2019.

KOSTENUIK, P.; MIRZA, F. M. Fracture healing physiology and the quest for therapies for delayed healing and nonunion. **Journal of Orthopaedic Research**, v. 35, n. 2, p. 213–223, 1 fev. 2017.

KRAMER, E.; ITZKOWITZ, E.; WEI, M. Synthesis and characterization of cobalt-substituted hydroxyapatite powders. **Ceramics International**, v. 40, p. 13471–13480, 1 set. 2014.

KULANTHAIVEL, S. et al. Improving the osteogenic and angiogenic properties of synthetic hydroxyapatite by dual doping of bivalent cobalt and magnesium ion. **Ceramics International**, v. 41, n. 9, p. 11323–11333, 1 nov. 2015.

KURODA, K. et al. Preparation of Calcium Phosphate Coatings on Titanium Using the Thermal Substrate Method and Their <I>in vitro</I> Evaluation. **MATERIALS TRANSACTIONS**, v. 43, n. 12, p. 3015–3019, 2002.

KUSUMBE, A. P.; ADAMS, R. H. Osteoclast progenitors promote bone vascularization and osteogenesis. . 1 nov. 2014, p. 1238–1240.

KUSUMBE, A. P.; RAMASAMY, S. K.; ADAMS, R. H. Coupling of angiogenesis and osteogenesis by a specific vessel subtype in bone. **Nature**, v. 507, n. 7492, p. 323–328, 12 mar. 2014.

LAD, S. E.; MCGRAW, W. S.; DAEGLING, D. J. Haversian remodeling corresponds to load frequency but not strain magnitude in the macaque (Macaca fascicularis) skeleton. **Bone**, v. 127,

p. 571–576, 1 out. 2019.
LAROCHE, M. Intraosseous circulation from physiology to disease. **Joint, bone, spine : revue du rhumatisme**, v. 69, n. 3, maio 2002.
LE GUÉHENNEC, L. et al. Surface treatments of titanium dental implants for rapid osseointegration. **Dental Materials**, v. 23, n. 7, p. 844–854, jul. 2007.
LE NOBLE, F.; LE NOBLE, J. Bone biology: Vessels of rejuvenation. . mar. 2014, p. 313–314.
LEBUGLE, A.; SALLEK, B.; TAI TAI, A. Surface modification of monetite in water at 37 °C: Characterisation by XPS. **Journal of Materials Chemistry**, v. 9, n. 10, p. 2511–2515, 1 jan. 1999.
LEDFORD, C. K. et al. Bovine xenograft failures in pediatric foot reconstructive surgery. **Journal of Pediatric Orthopaedics**, v. 33, n. 4, p. 458–463, jun. 2013.
LEE, Y. C. et al. **Comparing the osteogenic potentials and bone regeneration capacities of bone marrow and dental pulp mesenchymal stem cells in a rabbit calvarial bone defect model**. Disponível em: <https://pubmed.ncbi.nlm.nih.gov/31658685/>. Acesso em: 7 jan. 2023.
LEFEBVRE, V.; PEETERS-JORIS, C.; VAES, G. Production of gelatin-degrading matrix metalloproteinases ('type IV collagenases') and inhibitors by articular chondrocytes during their dedifferentiation by serial subcultures and under stimulation by interleukin-1 and tumor necrosis factor alpha. **Biochimica et biophysica acta**, v. 1094, n. 1, p. 8–18, ago. 1991.
LEI, B. et al. **Hybrid polymer biomaterials for bone tissue regeneration**. **Frontiers of Medicine**Higher Education Press, , 1 abr. 2019.
LI, J.; WANG, H.-M. M. **Effects of cobalt chloride on phenotypes of normal human saphenous vein smooth muscle cells**. Disponível em: <https://www.ncbi.nlm.nih.gov/pmc/articles/PMC4307437/>. Acesso em: 13 nov. 2019.
LIANG, K. C. et al. Interleukin-1β induces MMP-9 expression via p42/p44 MAPK, p38 MAPK, JNK, and nuclear factor-κB signaling pathways in human tracheal smooth muscle cells. **Journal of Cellular Physiology**, v. 211, n. 3, p. 759–770, jun. 2007.
LIEBERMAN, J. R.; FRIEDLAENDER, G. E. **Bone regeneration and repair: Biology and clinical applications**. [s.l.] Humana Press, 2005.
LIN, W. C. et al. A comparative study on the direct and pulsed current electrodeposition of cobalt-substituted hydroxyapatite for magnetic resonance imaging application. **Materials**, v. 12, n. 1, p. 116, 31 dez. 2018.
LING, L. E. et al. The effect of calcium phosphate composite scaffolds on the osteogenic differentiation of rabbit dental pulp stem cells. **Journal of Biomedical Materials Research - Part A**, v. 103, n. 5, p. 1732–1745, 1 maio 2015.
LIU, W. C. et al. **Angiogenesis Assays for the Evaluation of Angiogenic Properties of**

Orthopaedic Biomaterials – A General Review. **Advanced Healthcare Materials**Wiley-VCH Verlag, , 8 mar. 2017. Disponível em: <https://pubmed.ncbi.nlm.nih.gov/28135051/>. Acesso em: 20 jun. 2021

LOUATI, B. et al. Analysis of the effects of thermal treatments on CaHPO4 by 31P NMR spectroscopy. **Journal of Alloys and Compounds**, v. 394, n. 1–2, p. 13–18, 17 maio 2005.

MA, P. X. **Biomimetic materials for tissue engineering**. **Advanced Drug Delivery Reviews**, 2008.

MACEDO, F. et al. Bone metastases: an overview. **Oncology Reviews**, v. 11, n. 1, 9 maio 2017.

MACHADO, M. I. P. et al. Cobalt-chromium-enriched medium ameliorates shear-stressed endothelial cell performance. **Journal of Trace Elements in Medicine and Biology**, v. 54, n. April, p. 163–171, 1 jul. 2019.

MACHADO, M. I. P.; GOMES, A. M.; ZAMBUZZI, W. F. Hypoxia modulates the phenotype of mechanically stressed endothelial cells responding to CoCr-enriched medium. **Journal of Trace Elements in Medicine and Biology**, v. 82, p. 127341, 1 mar. 2024.

MACLENNAN, G.; BEEVERS, C. A. The crystal structure of dicalcium phosphate, CaHPO 4 . **Acta Crystallographica**, v. 8, n. 9, p. 579–583, 1 set. 1955.

MADL, A. K. et al. **Toxicology of wear particles of cobalt-chromium alloy metal-on-metal hip implants Part I: Physicochemical properties in patient and simulator studies**. **Nanomedicine: Nanotechnology, Biology, and Medicine**Elsevier Inc., , 1 jul. 2015.

MAES, C. et al. Osteoblast precursors, but not mature osteoblasts, move into developing and fractured bones along with invading blood vessels. **Developmental cell**, v. 19, n. 2, p. 329–344, ago. 2010.

MAES, C. Role and regulation of vascularization processes in endochondral bones. **Calcified tissue international**, v. 92, n. 4, p. 307–323, abr. 2013.

MAES, C.; CARMELIET, G.; SCHIPANI, E. Hypoxia-driven pathways in bone development, regeneration and disease. **Nature reviews. Rheumatology**, v. 8, n. 6, p. 358–366, mar. 2012.

MAIA, F. R. et al. Recent approaches towards bone tissue engineering. **Bone**, v. 154, p. 116256, 1 jan. 2022.

MANOLAGAS, S. C. Birth and Death of Bone Cells: Basic Regulatory Mechanisms and Implications for the Pathogenesis and Treatment of Osteoporosis*. **Endocrine Reviews**, v. 21, n. 2, p. 115–137, 1 abr. 2000.

MARSELL, R.; EINHORN, T. A. The biology of fracture healing. **Injury**, v. 42, n. 6, p. 551–555, 2011.

MARTIN, T. J.; SEEMAN, E. Bone remodelling: its local regulation and the emergence of bone fragility. **Best practice & research. Clinical endocrinology & metabolism**, v. 22, n. 5, p. 701–

722, out. 2008.
MARTINO, M. M. et al. **Extracellular matrix-inspired growth factor delivery systems for bone regeneration**. **Advanced Drug Delivery Reviews**, 2015. Disponível em: <https://www.sciencedirect.com/science/article/abs/pii/S0169409X15000630>
MATTA, C. et al. Osteogenic differentiation of human bone marrow-derived mesenchymal stem cells is enhanced by an aragonite scaffold. **Differentiation**, v. 107, p. 24–34, 1 maio 2019.
MENZIES, K. L.; JONES, L. The Impact of Contact Angle on the Biocompatibility of Biomaterials. **Optometry and Vision Science**, v. 87, n. 6, p. 387–399, jun. 2010.
MESQUITA, C. S. et al. Simplified 2,4-dinitrophenylhydrazine spectrophotometric assay for quantification of carbonyls in oxidized proteins. **Analytical Biochemistry**, v. 458, p. 69–71, 1 ago. 2014.
MINE, Y. et al. Involvement of ERK and p38 MAPK pathways on interleukin-33-induced RANKL expression in osteoblastic cells. **Cell Biology International**, v. 38, n. 5, p. 655–662, maio 2014.
MINOZZI, S. et al. **A Gold Dental Prosthesis of Roman Imperial Age**. **American Journal of Medicine**Am J Med, , maio 2007.
MIRTCHI, A. A.; LEMAITRE, J.; TERAO, N. Calcium phosphate cements: study of the β-tricalcium phosphate - monocalcium phosphate system. **Biomaterials**, v. 10, n. 7, p. 475–480, 1989.
MOEINZADEH, S.; JABBARI, E. Morphogenic peptides in regeneration of load bearing tissues. In: **Advances in Experimental Medicine and Biology**. [s.l.] Springer New York LLC, 2015. v. 881p. 95–110.
MOIRANGTHEM, R. D. et al. Hypoxic niche-mediated regeneration of hematopoiesis in the engraftment window is dominantly affected by oxygen tension in the milieu. **Stem Cells and Development**, v. 24, n. 20, p. 2423–2436, 15 out. 2015.
MONTAZEROLGHAEM, M. et al. Resorption of monetite calcium phosphate cement by mouse bone marrow derived osteoclasts. **Materials Science and Engineering C**, v. 52, p. 212–218, 1 jul. 2015.
MOTAMENI, A.; ALSHEMARY, A. Z.; EVIS, Z. A review of synthesis methods, properties and use of monetite cements as filler for bone defects. **Ceramics International**, v. 47, n. 10, p. 13245–13256, 15 maio 2021.
MOUNTZIARIS, P. M.; MIKOS, A. G. Modulation of the inflammatory response for enhanced bone tissue regeneration. **Tissue engineering. Part B, Reviews**, v. 14, n. 2, p. 179–186, jun. 2008.
MUÑOZ-SÁNCHEZ, J.; CHÁNEZ-CÁRDENAS, M. E. The use of cobalt chloride as a

chemical hypoxia model. **Journal of Applied Toxicology**, v. 39, n. 4, p. 556–570, 1 abr. 2019.

NASCIMENTO, A. S. et al. Phosphoproteome profiling reveals critical role of JAK-STAT signaling in maintaining chemoresistance in breast cancer. **Oncotarget**, v. 8, n. 70, p. 114756–114768, 29 dez. 2017.

NATH, D.; SINGH, F.; DAS, R. X-ray diffraction analysis by Williamson-Hall, Halder-Wagner and size-strain plot methods of CdSe nanoparticles- a comparative study. **Materials Chemistry and Physics**, v. 239, p. 122021–122029, 1 jan. 2020.

NAVARRO DA ROCHA, D. et al. Bioactivity of strontium-monetite coatings for biomedical applications. **Ceramics International**, v. 45, n. 6, p. 7568–7579, 15 abr. 2019.

OSATHANON, T. et al. Cobalt chloride supplementation induces stem-cell marker expression and inhibits osteoblastic differentiation in human periodontal ligament cells. **Archives of Oral Biology**, v. 60, n. 1, p. 29–36, 1 jan. 2014.

PALUMBO, C.; FERRETTI, M.; DE POL, A. Apoptosis during intramembranous ossification. **Journal of Anatomy**, v. 203, n. 6, p. 589–598, dez. 2003.

PAPE, H. C.; EVANS, A.; KOBBE, P. **Autologous bone graft: Properties and techniques**. **Journal of Orthopaedic Trauma**, 2010.

PARISI, L. et al. Titanium dental implants hydrophilicity promotes preferential serum fibronectin over albumin competitive adsorption modulating early cell response. **Materials Science and Engineering C**, v. 117, p. 111307, 1 dez. 2020.

PASCHOS, N. K. et al. Advances in tissue engineering through stem cell-based co-culture. **Journal of Tissue Engineering and Regenerative Medicine**, v. 9, n. 5, p. 488–503, maio 2015.

PERCIVAL, C. J.; RICHTSMEIER, J. T. Angiogenesis and intramembranous osteogenesis. . 1 ago. 2013, p. 909–922.

PINTO, T. S. et al. Nanohydroxyapatite-Blasted Bioactive Surface Drives Shear-Stressed Endothelial Cell Growth and Angiogenesis. **BioMed Research International**, v. 2022, 2022.

POUYSSEGUR, J.; DAYAN, F.; MAZURE, N. M. Hypoxia signalling in cancer and approaches to enforce tumour regression. **Nature**, v. 441, n. 7092, p. 437–443, maio 2006.

PRADO DA SILVA, M. H. et al. Transformation of monetite to hydroxyapatite in bioactive coatings on titanium. **Surface and Coatings Technology**, v. 137, n. 2–3, p. 270–276, 15 mar. 2001.

PREETHI SOUNDARYA, S. et al. Bone tissue engineering: Scaffold preparation using chitosan and other biomaterials with different design and fabrication techniques. **International Journal of Biological Macromolecules**, v. 119, p. 1228–1239, 1 nov. 2018.

PRIDEAUX, M. et al. Extracellular matrix mineralization promotes E11/gp38 glycoprotein expression and drives osteocytic differentiation. **PLoS ONE**, v. 7, n. 5, 7 maio 2012.

RABIEI, M. et al. Comparing methods for calculating nano crystal size of natural hydroxyapatite using X-ray diffraction. **Nanomaterials**, v. 10, n. 9, p. 1–21, 1 set. 2020.

RAHMAN, M. A. **Understanding of doping sites and versatile applications of heteroatom modified BaTiO3 ceramic**. **Journal of Asian Ceramic Societies**Taylor and Francis Ltd., , 3 abr. 2023.

RAMASAMY, S. K. et al. Endothelial Notch activity promotes angiogenesis and osteogenesis in bone. **Nature**, v. 507, n. 7492, p. 376–380, 12 mar. 2014.

RAMASAMY, S. K. et al. Regulation of Hematopoiesis and Osteogenesis by Blood Vessel – Derived Signals. 2016a.

RAMASAMY, S. K. et al. Blood flow controls bone vascular function and osteogenesis. **Nature Communications**, v. 7, 6 dez. 2016b.

RAMASAMY, S. K.; KUSUMBE, A. P.; ADAMS, R. H. Regulation of tissue morphogenesis by endothelial cell-derived signals. . 1 mar. 2015, p. 148–157.

RATNER, B. D.; BRYANT, S. J. Biomaterials: Where we have been and where we are going. **Annual Review of Biomedical Engineering**, v. 6, n. 1, p. 41–75, 15 ago. 2004.

RATNER, B. D.; ZHANG, G. **A History of BiomaterialsBiomaterials Science: An Introduction to Materials in Medicine**. [s.l.] Elsevier, 1 jan. 2013. Disponível em: <http://www.tup.tsinghua.edu.cn/upload/books/yz/013996-01.pdf>. Acesso em: 15 abr. 2019.

RAU, J. V. et al. Sic Parvis Magna: Manganese-Substituted Tricalcium Phosphate and Its Biophysical Properties. **ACS Biomaterials Science and Engineering**, p. 6632–6644, 2019.

RAVINDRAN, S.; GEORGE, A. Multifunctional ECM proteins in bone and teeth. **Experimental cell research**, v. 325, n. 2, p. 148–154, jul. 2014.

REZZA, A.; SENNETT, R.; RENDL, M. Adult Stem Cell Niches. Cellular and Molecular Components. **Current Topics in Developmental Biology**, v. 107, p. 333–372, 2014.

RH. OWEN, G.; DARD, M.; LARJAVA, H. **Hydoxyapatite/beta-tricalcium phosphate biphasic ceramics as regenerative material for the repair of complex bone defects**. **Journal of Biomedical Materials Research - Part B Applied Biomaterials**John Wiley and Sons Inc., , 1 ago. 2018.

ROBINTON, D. A.; DALEY, G. Q. The promise of induced pluripotent stem cells in research and therapy. **Nature**, v. 481, n. 7381, p. 295–305, jan. 2012.

ROSSI, M. C. et al. Titanium-released from dental implant enhances pre-osteoblast adhesion by ROS modulating crucial intracellular pathways. **Journal of Biomedical Materials Research - Part A**, v. 105, n. 11, p. 2968–2976, 1 nov. 2017.

RUNYAN, C. M.; GABRICK, K. S. Biology of bone formation, fracture healing, and distraction osteogenesis. **Journal of Craniofacial Surgery**, v. 28, n. 5, p. 1380–1389, 1 jul. 2017.

RUTKOVSKIY, A.; STENSLØKKEN, K.-O.; VAAGE, I. J. Osteoblast Differentiation at a Glance. **Medical Science Monitor Basic Research**, v. 22, p. 95–106, 26 set. 2016.

RYU, H. S. et al. An improvement in sintering property of β-tricalcium phosphate by addition of calcium pyrophosphate. **Biomaterials**, v. 23, n. 3, p. 909–914, 1 fev. 2002.

SADOWSKA, J. M. et al. The effect of biomimetic calcium deficient hydroxyapatite and sintered β-tricalcium phosphate on osteoimmune reaction and osteogenesis. **Acta biomaterialia**, 30 jun. 2019.

SALGADO, A. J.; COUTINHO, O. P.; REIS, R. L. Bone tissue engineering: state of the art and future trends. **Macromolecular bioscience**, v. 4, n. 8, p. 743–765, ago. 2004.

SALIMI, E.; JAVADPOUR, J. Synthesis and characterization of nanoporous monetite which can be applicable for drug carrier. **Journal of Nanomaterials**, v. 2012, 2012.

SANDERS, R. **Bone graft substitutes: Separating fact from fiction**. **Journal of Bone and Joint Surgery**Journal of Bone and Joint Surgery Inc., , 2007.

SANTOS, M. I.; REIS, R. L. Vascularization in bone tissue engineering: Physiology, current strategies, major hurdles and future challenges. . 11 jan. 2010, p. 12–27.

SANTOS, P. L. et al. Bone substitutes for peri-implant defects of postextraction implants. **International journal of biomaterials**, v. 2013, p. 307136, 2013.

SARAN, U.; GEMINI PIPERNI, S.; CHATTERJEE, S. Role of angiogenesis in bone repair. . 1 nov. 2014, p. 109–117.

SCHATZ, P. **Bone Formation and Development, Anatomy and Physiology**. Disponível em: <https://opentextbc.ca/anatomyandphysiology/chapter/6-4-bone-formation-and-development/%0Ahttps://opentextbc.ca/anatomyandphysiology/chapter/6-4-bone-formation-and-development/%0Ahttp://philschatz.com/anatomy-book/contents/m46301.html>. Acesso em: 4 jan. 2023.

SCHIPANI, E. et al. Regulation of osteogenesis-angiogenesis coupling by HIFs and VEGF. . 1 ago. 2009, p. 1347–1353.

SCOTLANDI, K. et al. Murine model for skeletal metastases of Ewing's sarcoma. **Journal of Orthopaedic Research**, v. 18, n. 6, p. 959–966, nov. 2000.

SEMAN, R. N. A. R.; AZAM, M. A.; MOHAMED, M. A. Highly efficient growth of vertically aligned carbon nanotubes on Fe-Ni based metal alloy foils for supercapacitors. **Advances in Natural Sciences: Nanoscience and Nanotechnology**, v. 7, n. 4, 1 dez. 2016.

SEMENZA, G. L. Hypoxia-inducible factors in physiology and medicine. . 3 fev. 2012, p. 399–408.

SEN, M. K.; MICLAU, T. Autologous iliac crest bone graft: Should it still be the gold standard for treating nonunions? **Injury**, v. 38, n. SUPPL. 1, p. S75–S80, 2007.

SHADANBAZ, S. et al. Monetite and brushite coated magnesium: In vivo and in vitro models for degradation analysis. **Journal of Materials Science: Materials in Medicine**, v. 25, n. 1, p. 173–183, 1 jan. 2014.

SHAH, F. A. et al. Bone without borders – Monetite-based calcium phosphate guides bone formation beyond the skeletal envelope. **Bioactive Materials**, v. 19, p. 103–114, 1 jan. 2023.

SHEEN, J. R.; GARLA, V. V. **Fracture Healing Overview**. [s.l.] StatPearls Publishing, 2019.

SHEIKH, Z. et al. Biodegradable materials for bone repair and tissue engineering applications. **Materials**, v. 8, n. 9, p. 5744–5794, 2015a.

SHEIKH, Z. et al. Mechanisms of in vivo degradation and resorption of calcium phosphate based biomaterials. **Materials**, v. 8, n. 11, p. 7913–7925, 2015b.

SHEIKH, Z. et al. In vitro degradation and in vivo resorption of dicalcium phosphate cement based grafts. **Acta Biomaterialia**, v. 26, p. 338–346, 15 out. 2015c.

SHEIKH, Z. et al. Controlling Bone Graft Substitute Microstructure to Improve Bone Augmentation. **Advanced Healthcare Materials**, v. 5, n. 13, p. 1646–1655, 6 jul. 2016.

SHEIKH, Z. et al. Effect of processing conditions of dicalcium phosphate cements on graft resorption and bone formation. **Acta Biomaterialia**, v. 53, p. 526–535, 15 abr. 2017.

SHI, X. et al. Preparation of Dicalcium Phosphate Anhydrous (Monetite) Biological Coating on Titanium by Spray-Drying Method. **Advances in Materials Science and Engineering**, v. 2017, 2017.

SHIBUYA, N.; JUPITER, D. C. **Bone Graft Substitute: Allograft and Xenograft**. Disponível em: <https://pubmed.ncbi.nlm.nih.gov/25440415/>. Acesso em: 7 jan. 2023.

SHIH, Y.-R. V et al. Calcium phosphate-bearing matrices induce osteogenic differentiation of stem cells through adenosine signaling. **Proceedings of the National Academy of Sciences of the United States of America**, v. 111, n. 3, p. 990–995, jan. 2014.

SHIN, H.; JO, S.; MIKOS, A. G. **Biomimetic materials for tissue engineering**. **Biomaterials**Elsevier BV, , 2003.

SHIN, S. R. et al. Graphene-based materials for tissue engineering. **Advanced Drug Delivery Reviews**, v. 105, p. 255–274, 2016.

SHOMENTO, S. H. et al. Hypoxia-inducible factors 1alpha and 2alpha exert both distinct and overlapping functions in long bone development. **Journal of cellular biochemistry**, v. 109, n. 1, p. 196–204, jan. 2010.

SIKDER, P. et al. Development of single-phase silver-doped antibacterial CDHA coatings on Ti6Al4V with sustained release. **Surface and Coatings Technology**, v. 342, p. 105–116, 25 maio 2018a.

SIKDER, P. et al. Single-Phase, Antibacterial Trimagnesium Phosphate Hydrate Coatings on

Polyetheretherketone (PEEK) Implants by Rapid Microwave Irradiation Technique. **ACS Biomaterials Science and Engineering**, v. 4, n. 8, p. 2767–2783, 13 ago. 2018b.

SIMS, N. A.; GOOI, J. H. Bone remodeling: Multiple cellular interactions required for coupling of bone formation and resorption. . out. 2008, p. 444–451.

SINUSAITE, L. et al. Controllable synthesis of tricalcium phosphate (TCP) polymorphs by wet precipitation: Effect of washing procedure. **Ceramics International**, v. 45, n. 9, p. 12423–12428, 15 jun. 2019.

SIONKOWSKA, A.; KACZMAREK, B. Preparation and characterization of composites based on the blends of collagen, chitosan and hyaluronic acid with nano-hydroxyapatite. **International Journal of Biological Macromolecules**, v. 102, p. 658–666, 1 set. 2017.

SPANGENBERG, A. et al. Bone Mineral Density and Body Composition are Associated with Circulating Angiogenic Factors in Post-menopausal Women. **Calcified Tissue International**, v. 99, n. 6, p. 608–615, 1 dez. 2016.

STEGEN, S.; VAN GASTEL, N.; CARMELIET, G. Bringing new life to damaged bone: The importance of angiogenesis in bone repair and regeneration. **Bone**, v. 70, p. 19–27, 1 jan. 2015.

STEVENS, M. M. et al. In vivo engineering of organs: The bone bioreactor. **Proceedings of the National Academy of Sciences**, v. 102, n. 32, p. 11450–11455, 2005.

STREET, J. et al. Vascular endothelial growth factor stimulates bone repair by promoting angiogenesis and bone turnover. **Proceedings of the National Academy of Sciences of the United States of America**, v. 99, n. 15, p. 9656–9661, 23 jul. 2002.

SUNTERS, A. et al. Mechano-transduction in osteoblastic cells involves strain-regulated estrogen receptor α-mediated control of insulin-like growth factor (IGF) I receptor sensitivity to ambient IGF, leading to phosphatidylinositol 3-kinase/AKT-dependent Wnt/LRP5 receptor-i. **Journal of Biological Chemistry**, v. 285, n. 12, p. 8743–8758, 19 mar. 2010.

TAKAICHI, A. et al. Effect of heat treatment on the anisotropic microstructural and mechanical properties of Co–Cr–Mo alloys produced by selective laser melting. **Journal of the Mechanical Behavior of Biomedical Materials**, v. 102, 1 fev. 2020.

TAKAYANAGI, H. **RANKL as the master regulator of osteoclast differentiation**. Disponível em: <https://pubmed.ncbi.nlm.nih.gov/33385253/>. Acesso em: 5 fev. 2023a.

TAKAYANAGI, H. **RANKL as the master regulator of osteoclast differentiation**. **Journal of Bone and Mineral Metabolism**Springer Japan, , 1 jan. 2021b.

TAKUBO, K. et al. Regulation of the HIF-1alpha level is essential for hematopoietic stem cells. **Cell stem cell**, v. 7, n. 3, p. 391–402, set. 2010.

TAMIMI, F. et al. Bone regeneration in rabbit calvaria with novel monetite granules. **Journal of Biomedical Materials Research - Part A**, v. 87, n. 4, p. 980–985, 15 dez. 2008.

TAMIMI, F. et al. Craniofacial vertical bone augmentation: A comparison between 3D printed monolithic monetite blocks and autologous onlay grafts in the rabbit. **Biomaterials**, v. 30, n. 31, p. 6318–6326, 1 out. 2009.

TAMIMI, F. et al. Resorption of monetite granules in alveolar bone defects in human patients. **Biomaterials**, v. 31, n. 10, p. 2762–2769, 1 abr. 2010.

TAMIMI, F. et al. The effect of autoclaving on the physical and biological properties of dicalcium phosphate dihydrate bioceramics: Brushite vs. monetite. **Acta Biomaterialia**, v. 8, n. 8, p. 3161–3169, 1 ago. 2012.

TAMIMI, F. et al. Osseointegration of dental implants in 3D-printed synthetic onlay grafts customized according to bone metabolic activity in recipient site. **Biomaterials**, v. 35, n. 21, p. 5436–5445, 1 jul. 2014.

TAMIMI, F.; SHEIKH, Z.; BARRALET, J. **Dicalcium phosphate cements: Brushite and monetite**. **Acta Biomaterialia**Elsevier Ltd, , 1 fev. 2012.

TARASOVA, N.; BEDARKOVA, A. Advanced Proton-Conducting Ceramics Based on Layered Perovskite BaLaInO4 for Energy Conversion Technologies and Devices. **Materials**, v. 15, n. 19, 1 out. 2022.

THARANI KUMAR, S. et al. **Review of metallic biomaterials in dental applications**. **Journal of Pharmacy and Bioallied Sciences**Wolters Kluwer Medknow Publications, , 1 ago. 2020.

THEISS, F. et al. Biocompatibility and resorption of a brushite calcium phosphate cement. **Biomaterials**, v. 26, n. 21, p. 4383–4394, 1 jul. 2005.

THURSTON, A. J. **Paré and prosthetics: The early history of artificial limbs**. ANZ Journal of Surgery. **Anais**...ANZ J Surg, dez. 2007.

TODROS, S.; TODESCO, M.; BAGNO, A. **Biomaterials and their biomedical applications: From replacement to regeneration**. **Processes**MDPI, , 1 nov. 2021.

TORRENTO, J. E. et al. Development of non-equiatomic Bio-HEAs based on TiZrNbTa-(Mo and Mn). **APL Materials**, v. 10, n. 8, p. 081113, 1 ago. 2022.

TORRES, J. et al. Monetite granules versus particulate autologous bone in bone regeneration. **Annals of Anatomy**, v. 200, p. 126–133, 1 jul. 2015.

TUYEN, D. VAN; LEE, B. T. Formation and characterization of porous spherical biphasic calcium phosphate (BCP) granules using PCL. **Ceramics International**, v. 37, n. 6, p. 2043–2049, 2011.

VALENCIA-LLANO, C. H. et al. Comparison of Two Bovine Commercial Xenografts in the Regeneration of Critical Cranial Defects. **Molecules**, v. 27, n. 18, 1 set. 2022.

VAN'T HOF, R. J.; RALSTON, S. H. **Nitric oxide and bone**. **Immunology**Wiley-Blackwell, , 2001.

VAN DER EERDEN, B. C. J.; TETI, A.; ZAMBUZZI, W. F. **Bone, a dynamic and integrating tissue. Archives of biochemistry and biophysics**United States, nov. 2014.

VINING, N. C.; WARME, W. J.; MOSCA, V. S. Comparison of structural bone autografts and allografts in pediatric foot surgery. **Journal of Pediatric Orthopaedics**, v. 32, n. 7, p. 719–723, out. 2012.

VO, T. N.; KASPER, F. K.; MIKOS, A. G. **Strategies for controlled delivery of growth factors and cells for bone regeneration**. **Advanced Drug Delivery Reviews**, 2012.

WANG, G. L.; SEMENZA, G. L. Desferrioxamine induces erythropoietin gene expression and hypoxia-inducible factor 1 DNA-binding activity: implications for models of hypoxia signal transduction. **Blood**, v. 82, n. 12, p. 3610–3615, dez. 1993.

WANG, M. et al. Association of parameters of mineral bone disorder with mortality in patients on hemodialysis according to level of residual kidney function. **Clinical Journal of the American Society of Nephrology**, v. 12, n. 7, p. 1118–1127, maio 2017.

WANG, W.; YEUNG, K. W. K. **Bone grafts and biomaterials substitutes for bone defect repair: A review**. **Bioactive Materials**KeAi Communications Co., , 2017.

WANG, Y. et al. The hypoxia-inducible factor alpha pathway couples angiogenesis to osteogenesis during skeletal development. **J Clin Invest**, v. 117, 2007a.

WANG, Y. et al. The hypoxia-inducible factor α pathway couples angiogenesis to osteogenesis during skeletal development. **Journal of Clinical Investigation**, v. 117, n. 6, p. 1616–1626, 1 jun. 2007b.

WANG, Y. et al. Novel application of HA-TCP biomaterials in distraction osteogenesis shortened the lengthening time and promoted bone consolidation. **Journal of orthopaedic research : official publication of the Orthopaedic Research Society**, v. 27, n. 4, p. 477–82, abr. 2009.

WARDEN, S. J. et al. Bone adaptation to a mechanical loading program significantly increases skeletal fatigue resistance. **Journal of Bone and Mineral Research**, v. 20, n. 5, p. 809–816, maio 2005.

WEBB, P. A.; ORR, C. Modern Methods of Particle Characterization. 2000.

WIKHOLM, N. W.; BEEBE, R. A.; KITTELBERGER, J. S. Kinetics of the conversion of monetite to calcium pyrophosphate. **Journal of Physical Chemistry**, v. 79, n. 8, p. 853–856, 1975.

WILLIAMS, D. F. The Language of Biomaterials-Based Technologies. **Regenerative Engineering and Translational Medicine**, v. 5, n. 1, p. 53–60, 15 mar. 2019.

WILSON, A.; TRUMPP, A. Bone-marrow haematopoietic-stem-cell niches. . fev. 2006, p. 93–106.

WILSON, C. J. et al. **Mediation of biomaterial-cell interactions by adsorbed proteins: A review**. **Tissue Engineering**, jan. 2005.

WOOD, P. F. et al. The Action of Angiocrine Molecules Sourced from Mechanotransduction-Related Endothelial Cell Partially Explain the Successful of Titanium in Osseointegration. **Journal of functional biomaterials**, v. 14, n. 8, p. 415, 8 ago. 2023.

WOPENKA, B.; PASTERIS, J. D. **A mineralogical perspective on the apatite in bone**. Materials Science and Engineering C. **Anais**...Elsevier, 28 abr. 2005.

XIONG, J. et al. Matrix-embedded cells control osteoclast formation. **Nature medicine**, v. 17, n. 10, p. 1235–1241, set. 2011.

XIONG, X. et al. Effect of substrate temperature on CaHPO4 coating on HT-C/C composites prepared by ultrasonic induction heating method. **Xiyou Jinshu Cailiao Yu Gongcheng/Rare Metal Materials and Engineering**, v. 43, n. 7, p. 1594–1599, 1 jul. 2014.

XIONG, X. BO et al. A study of monetite precipitation on HT-C/C composites by induction heating method at different substrate temperatures. **Surface and Coatings Technology**, v. 223, p. 6–10, 25 maio 2013.

XU, N. et al. Hypoxia inhibits the differentiation of mesenchymal stem cells into osteoblasts by activation of Notch signaling. **Experimental and Molecular Pathology**, v. 94, n. 1, p. 33–39, 2013.

XUE, W. et al. **Synthesis and characterization of tricalcium phosphate with Zn and Mg based dopants**. Journal of Materials Science: Materials in Medicine. **Anais**...jul. 2008.

YAN, T. et al. **Role of nitric oxide in orthodontic tooth movement (Review)**. **International Journal of Molecular Medicine**Spandidos Publications, , 1 set. 2021.

YANG, D. C. et al. Hypoxia inhibits osteogenesis in human mesenchymal stem cells through direct regulation of RUNX2 by TWIST. **PLoS ONE**, v. 6, n. 9, 2011.

YANG, Y. Q. et al. **The role of vascular endothelial growth factor in ossification**. **International Journal of Oral Science**, jun. 2012.

YASHIMA, M. et al. Crystal structure analysis of b-tricalcium phosphate Ca 3 (PO 4) 2 by neutron powder diffraction. **Journal of Solid State Chemistry**, v. 175, p. 272–277, 2003.

YASUDA, H. et al. Osteoclast differentiation factor is a ligand for osteoprotegerin/osteoclastogenesis-inhibitory factor and is identical to TRANCE/RANKL. **Proceedings of the National Academy of Sciences of the United States of America**, v. 95, n. 7, p. 3597–3602, mar. 1998.

YE, X. et al. Ectopic bone regeneration by human bone marrow mononucleated cells, undifferentiated and osteogenically differentiated bone marrow mesenchymal stem cells in beta-tricalcium phosphate scaffolds. **Tissue Engineering - Part C: Methods**, v. 18, n. 7, p. 545–556,

jul. 2012.
YILDIRIM, M. et al. Maxillary sinus augmentation using xenogenic bone substitute material Bio-Oss® in combination with venous blood. A histologic and histomorphometric study in humans. **Clinical Oral Implants Research**, v. 11, n. 3, p. 217–229, 2000.
YOSHIDA, K. et al. Effect of substitutional monovalent and divalent metal ions on mechanical properties of β-tricalcium phosphate. **Journal of the American Ceramic Society**, v. 88, n. 8, p. 2315–2318, ago. 2005.
YU, X. et al. **Cellular hypoxia promotes osteogenic differentiation of mesenchymal stem cells and bone defect healing via STAT3 signaling**. **Cellular and Molecular Biology Letters**, 2019. Disponível em: <https://www.ncbi.nlm.nih.gov/pmc/articles/PMC6889321/>
ZAGORAC, D. et al. Recent developments in the Inorganic Crystal Structure Database: Theoretical crystal structure data and related features. **Journal of Applied Crystallography**, v. 52, n. 5, p. 918–925, 23 set. 2019.
ZAMAN, G. et al. Mechanical strain stimulates nitric oxide production by rapid activation of endothelial nitric oxide synthase in osteocytes. **Journal of Bone and Mineral Research**, v. 14, n. 7, p. 1123–1131, 1999.
ZAMBUZZI, W. F. Mecanismos de transdução de sinal envolvidos com a diferenciação de osteoblastos e osteocitos. 2008.
ZAMBUZZI, W. F. et al. Modulation of Src activity by low molecular weight protein tyrosine phosphatase during osteoblast differentiation. **Cellular Physiology and Biochemistry**, v. 22, n. 5–6, p. 497–506, 2008.
ZAMBUZZI, W. F. et al. **Ascorbate-induced osteoblast differentiation recruits distinct MMP-inhibitors: RECK and TIMP-2**. Disponível em: <https://pubmed.ncbi.nlm.nih.gov/18989628/>. Acesso em: 8 fev. 2023a.
ZAMBUZZI, W. F. et al. On the road to understanding of the osteoblast adhesion: Cytoskeleton organization is rearranged by distinct signaling pathways. **Journal of Cellular Biochemistry**, v. 108, n. 1, p. 134–144, 1 set. 2009b.
ZAMBUZZI, W. F. et al. Intracellular signal transduction as a factor in the development of “Smart” biomaterials for bone tissue engineering. . 1 jun. 2011, p. 1246–1250.
ZAMBUZZI, W. F. et al. Nanometer scale titanium surface texturing are detected by signaling pathways involving transient FAK and Src activations. **PLoS ONE**, v. 9, n. 7, p. e95662, 7 jul. 2014.
ZAMBUZZI, W. F.; MILANI, R.; TETI, A. Expanding the role of Src and protein-tyrosine phosphatases balance in modulating osteoblast metabolism: Lessons from mice. . 1 abr. 2010, p. 327–332.

ZAVGORODNIY, A. V. et al. Mechanical stability of two-step chemically deposited hydroxyapatite coating on Ti substrate: Effects of various surface pretreatments. **Journal of Biomedical Materials Research Part B: Applied Biomaterials**, v. 99B, n. 1, p. 58–69, 28 out. 2011.

ZAVGORODNIY, A. V. et al. Adhesion of a chemically deposited monetite coating to a Ti substrate. **Surface and Coatings Technology**, v. 206, n. 21, p. 4433–4438, 15 jun. 2012.

ZDOROVETS, M. V.; PRMANTAYEVA, B. A.; KOZLOVSKIY, A. L. Synthesis and Properties of SrTiO3 Ceramic Doped with Sm2O3. **Materials**, v. 14, n. 24, p. 7549, 9 dez. 2021.

ZELZER, E. et al. Tissue specific regulation of VEGF expression during bone development requires Cbfa1/Runx2. **Mechanisms of Development**, v. 106, n. 1–2, p. 97–106, 2001.

ZHANG, K. et al. Application of hydroxyapatite nanoparticles in tumor-associated bone segmental defect. **Science Advances**, v. 5, n. 8, 2 ago. 2019.

ZHANG, X.; WILLIAMS, D. F. **Definitions of biomaterials for the Twenty-First Century: Proceedings of a Consensus Conference held in Chengdu, People's Republic of China, June 11th and 12th 2018, organized under the auspices of the International Union of Societies for Biomaterials Sci**. [s.l: s.n.].

ZHONG, X. et al. Bezafibrate enhances proliferation and differentiation of osteoblastic MC3T3-E1 cells via AMPK and eNOS activation. **Acta Pharmacologica Sinica**, v. 32, n. 5, p. 591–600, maio 2011.

ZHOU, H. et al. **Injectable biomaterials for translational medicine**. **Materials Today**Elsevier B.V., , 1 set. 2019.

ZHOU, H. et al. Monetite (Dcpa), an Important Calcium Phosphate Compound - its Structure, Processing, and Applications. **SSRN Electronic Journal**, 22 out. 2020.

ZHOU, H. et al. Monetite, an important calcium phosphate compound–Its synthesis, properties and applications in orthopedics. **Acta Biomaterialia**, v. 127, p. 41–55, 1 jun. 2021a.

ZHOU, L. et al. 3D printing monetite-coated Ti-6Al-4V surface with osteoimmunomodulatory function to enhance osteogenesis. **Materials Science and Engineering C**, n. November, p. 112562, 2021b.

ZHOU, Y. et al. Protonic Conduction in the BaNdInO4Structure Achieved by Acceptor Doping. **Chemistry of Materials**, v. 33, n. 6, p. 2139–2146, 23 mar. 2021c.

ZHU, Y. et al. Bone regeneration with micro/nano hybrid-structured biphasic calcium phosphate bioceramics at segmental bone defect and the induced immunoregulation of MSCs. **Biomaterials**, v. 147, p. 133–144, 1 dez. 2017.

ZUNINO, J. H. et al. Immunologic and osteogeneic properties of xenogeneic and allogeneic demineralized bone transplants. **Cell and Tissue Banking**, v. 5, n. 3, p. 141–148, 2004.

Anexo I: Atividades Desenvolvidas no Período

Disciplinas Cursadas no Doutorado

. Dinâmica Molecular de Tecidos Mineralizados
. DOHaD: Do conceito à prática clínica
. Fundamentos sobre Ética e Prática na Experimentação Animal
. Isótopos Estáveis Ambientais – Aplicação Biotecnológica
. Metodologias avançadas e aplicadas em tecidos mineralizados
. O cientista e o professor universitário
. Tópicos Especiais em Biologia Geral e Aplicada
. Tópicos Especiais em Biologia Geral e Aplicada: "Seminários de Pesquisa – Avaliação de projetos de pesquisa"

Disciplinas Aproveitadas do Mestrado

. Prática Pedagógica no Ensino Superior (II): Recursos de Ensino-Aprendizagem;
. Química Metabólica da Célula: Carboidratos;
. Sinalização Celular;
. Tópicos em Biossegurança e Organismos Geneticamente Modificados (OGMs e AnGMs);
. Tópicos Especiais em Biologia Geral e Aplicada: 3D-printing: medical applications.

Atividades de Docência

1. **Aprimoramento Didático nos Cursos de Graduação da Unesp –** Estágio na disciplina Física Radiológica do Departamento de Biofísica e Farmacologia, sob supervisão do Prof. Assoc. Vladimir Eliodoro Costa – 2020
2. **Programa institucional de Aperfeiçoamento e Apoio à Docência no Ensino Superior**- PAADES - Realizado na disciplina Física Radiológica do Departamento de Biofísica e Farmacologia, sob supervisão do Prof. Assoc. Vladimir Eliodoro Costa – 2021

Cursos

1. IV Escola de Inverno em Física Aplicada à Medicina e Biologia - Departamento de Física da Faculdade de Filosofia, Ciências e Letras de Ribeirão Preto da Universidade de São Paulo – 2020;
2. Citometria de fluxo, princípios e aplicações – 2020;
3. Toxicologia aplicada na área da saúde - realizado pelo Ceatox - Centro de Assistência Toxicológica do Instituto de Biociências – UNESP – 2020;
4. Introduction to the Biology of Cancer - Johns Hopkins University – 2020;

5. Treinamento Preparo de Soluções Químicas, realizado pelo Ceatox - Centro de Assistência Toxicológica do Instituto de Biociências – UNESP – 2020;
6. Comunicação e escrita cientifica – 2020;
7. Biologia Estrutural Aplicada à Biotecnologia – 2020;
8. Docência no ensino superior: fundamentos e práticas pedagógicas - Instituto de Educação e Pesquisa em Práticas Pedagógicas - IEP³; – 2021;
9. Implant Dentistry - The University of Hong Kong, – 2021;
10. Anatomy: Musculoskeletal and Integumentary Systems – University of Michigan – 2021;
11. Técnicas Aplicadas al Estudio de Materiales Porosos – Micrometics – 2021;
12. Análise de Dados em Linguagem R – Enap – 2021;
13. Advanced Functional Ceramics – Yonsei University – 2021;
14. VIII Curso de Oncologia Integrada – Hospital Sírio Libanês – 2021;
15. Plágio e Turnitin - Divisão Técnica de Biblioteca e Documentação-Unesp-Campus de Botucatu-Rubião Jr – 2021;
16. Boas Práticas de Laboratório e Biossegurança – Instituto de Biociências de Botucatu – UNESP – 2021;
17. Vigésimo Curso de Radioterapia de Última Geração e Controle de Qualidade – Hospital Sírio-Libanês – 2021;
18. Teranóstico em Medicina Nuclear – Faculdade de Medicina de Botucatu – UNESP – 2021;
19. Workshop: PCR em Tempo Real Sem Segredos – Universo da Biologia Molecular – 2022;
20. Gestão de Projetos e Aplicativos de Impacto – Recode – 2022;
21. Technical Support Fundamentals – Coursera – Google – 2022;
22. Toxinologia básica & Aplicada: Biotecnologias de Toxinas Úteis à Saúde – 2022 – FIOCRUZ;
23. XXI Curso de Radioterapia de Última Geração e Controle da Qualidade – Hospital Sírio Libanês – 2022;
24. Radiação na saúde: aplicações em medicina nuclear – Faculdade de Medicina de Botucatu – UNESP – 2023;
25. Mini-Curso de Braquiterapia - Braquiterapia de baixa taxa de dose de próstata - Hospital Sírio Libanês – 2023;
26. Comunicação e Escrita Científica" – American Chemical Society – 2023;

Eventos

1. Unesp Conecta 2020 - "Reflexões sobre Inovação, Empoderamento e Empreendedorismo" – 2020

2. I Fórum On-line de Tecnologias da Luz na Saúde – 2020
3. XI Congresso Internacional de Uro-Oncologia – 2020
4. IV Simpósio de Fotobiofísica: UV e Vírus – 2020
5. II Congresso Brasil–Germânico de Oncologia – 2020
6. Congresso de Biociências – 2020
7. VI simpósio internacional de câncer de mama oncologia D'OR – 2020
8. V simpósio internacional de câncer de pulmão oncologia D'OR – 2020
9. XIX Semana da Física Médica – 2020
10. I Simpósio Digital de Genética e Biotecnologia da UFJF – 2020
11. III Semana de Biotecnologia USP – 2020
12. 1º Encontro Internacional de Metrologia e Examinologia em Química – 2020
13. V Congresso de Urologia da USP – 2020
14. IV Simpósio Internacional GU-REVIEW 2020
15. VIII Simpósio Internacional de Melanoma e VI Simpósio Internacional de Imuno-oncologia – 2020
16. Global Fórum – Fronteiras da Saúde – 2020
17. XXII Congresso da Sociedade Brasileira de Radioterapia – 2020
18. IX Simpósio Internacional Multidisciplinar de Câncer de Mama – 2020
19. III Simpósio "Bases da Carcinogênese: da célula às repercussões clínicas" – 2020
20. IV Simpósio Câncer de Pulmão – 2020
21. I Congresso {Virtual} Brasileiro de Engenharia de Tecidos – 2020
22. XX Congress of the Brazilian Society for Cell Biology (SBBC) – 2021
23. IV Simpósio Internacional de Onco-Hematologia – 2021
24. 9º Simpósio Internacional do Câncer de Pulmão – 2021
25. Conferência Brasileira de Câncer de Mama - LACOG-GBECAM – 2021
26. 5º Congresso Brasileiro de Qualidade em Laboratórios – 2021
27. III Simpósio de Atualização no Tratamento dos Tumores Ginecológicos – 2021
28. VI Simpósio de Biotecnologia do IFRJ – 2021
29. II Congresso Digital de Nanobiotecnologia e Bioengenharia (II CDNB) – 2021
30. SNMMI 2021 Virtual Annual Meeting – 2021
31. 3rd Industrial Biotechnology and Synthetic Biology Workshop (IBSB) – 2021
32. Virtual Educational Symposium – Oncoclínicas e Dana-Farber Cancer Institute – 2021
33. XII Congresso Internacional de Uro Oncologia – 2021
34. II ASCO em contexto – 2021
35. III Workshop de Física da Unesp Bauru – 2021

36. XII Board Review in Medical Oncology: Atualização, Discussão e Inovação – 2021
37. 6º Simpósio Internacional de Tumores Gastrointestinais – 2021
38. V Workshop de Biotecnologia – 2021
39. XIX Brazilian MRS Meeting – 2021
40. Genomic Summit – 2021
41. IX Simpósio Internacional de Melanoma e VII Simpósio Internacional de Imuno-oncologia – 2021
42. I Simpósio Internacional de Oncologia de Precisão – 2021
43. XAYNAN Workshop - International Sirius Workshop on X-ray Nanospectroscopy, Nanodiffraction and Nanoimaging – 2021;
44. X Proteomics Workshop – 2021;
45. 31st LNLS Annual Users´ Meeting (RAU) – 2021;
46. IV Semana de Biotecnologia da USP – 2021;
47. Planetary Health Annual Meeting and Festival – 2021;
48. X Simpósio Internacional Multidisciplinar de Câncer de Mama – 2021;
49. I Simpósio de Física Aplicada a Medicina – UFU – 2021;
50. I Encontro de Extensão Universitária do IBB – UNESP – 2022;
51. I Simpósio de Radioproteção e Qualidade de Imagem do HCFMB – 2022;
52. XIII Congresso Internacional de Uro-oncologia / VIII Simpósio Multiprofissional – 2022
53. Best Practices in Breast Oncology BPBO – 2022;
54. V Simpósio Internacional de Onco-Hematologia – SINTOMA – 2022;
55. V Simpósio Nacional EVA de Oncologia Ginecológica – 2022;
56. Algoritmos Globais em Oncologia e Hematologia – 2022;
57. 7º Simpósio Internacional de Tumores Gastrointestinais – 2022;
58. 10º Simpósio Internacional Oncoclínicas e Dana-Farber Cancer Institute – 2022;
59. Simpósio Anual do Programa de Pós-Graduação em Biologia Geral e Aplicada – 2022;
60. 7° Workshop de Biotecnologia – 2022;
61. International Sirius Workshop on Heterogeneous and Hierarchical Materials (H2Mat) – 2022;
62. Congresso Internacional de Ciência, Tecnologia e Desenvolvimento – 2022;
63. XI Proteomics Workshop – 2022;
64. VI Simpósio Internacional GU - Review e IV Simpósio Multiprofissional – LACOG – 2022;
65. Congresso de Ciência e Tecnologia dos Biomateriais – BIOMAT22 – 2022;

66. 1st International Symposium in Bioscience and Biotechnology: Innovations and Trends – 2022;
67. II Simpósio de Física Aplicada à Medicina – SIFAM – 2022;
68. I Congresso Brasileiro em Biociências Aplicadas à Saúde – 2023;
69. Journées de la recheche de la Faculté de médecine et de ses centres de recherche affiliés – 2023;
70. VIII Workshop de Biotecnologia – 2023;
71. Algoritmos Globais e Controvérsias 2ª edição – 2023;
72. XII Congresso de Biociências – 2023;
73. XXXV Congresso de Iniciação Científica da Unesp – 2023;

Palestra Ministrada

Palestra "O Papel do Físico Médico na Medicina Nuclear e na Pesquisa: da clínica para a academia", organizada pela Liga Acadêmica de Física Médica - LiFiM do Instituto de Biociências de Botucatu – 2022.

Resumos em eventos

1. Efeitos metabólicos do meio enriquecido com Co-Cr no acoplamento de células endoteliais submetidas a shear-stress e osteoblastos, de autoria de ***Almeida, G.S***.; Fernandes, C.J.C.; Pinto, T.S.; Bezerra, F.J.; Zambuzzi, W.F., no I Simpósio Digital de Genética e Biotecnologia da UFJF (I SDGB) - 2020
2. Coupling of shear-stressed endothelial cell and osteoblasts in responding to Co-Cr-enriched medium. ***Gerson Santos de Almeida***, Célio Junior da Costa Fernandes, Thaís Silva Pinto, Fábio José Bezerra, Willian Fernando Zambuzzi, no XX Congress of the Brazilian Society for Cell Biology - 2021.
3. Meio enriquecido com hidroxiapatita altera a expressão de genes relacionados ao fenótipo osteoblástico de células MG63. ***Gerson Santos de Almeida***, Marcel Rodrigues Ferreira, Célio Junior da Costa Fernandes, Willian Fernando Zambuzzi – II CDNB – 2021
4. Hipóxia induzida por hidroxiapatita dopada com cobalto modula a expressão de genes de diferenciação osteoblástica, ***Almeida. G.S****.;* Moraes. J.F.; Ferreira, M.R.; Fernandes, C.J.C; Feltran, G.S.; Pinto, T.S; Morais, P.B; Zambuzzi. W.F. – VI Workbiotec - 2021
5. Avaliação da resposta de osteoblastos ao meio enriquecido com titânio, Morais, P. B.; Fernandes, C. J.C.; ***Almeida, G. S***.; Zambuzzi, W. F. – V Workbiotec - 2021
6. Cellular response of MG-63 cells in Hydroxyapatite/TCP enriched medium with different thermal treatments, ***Gerson Santos de Almeida***, Marcel Rodrigues Ferreira, Célio Junior

da Costa Fernandes, Carlos Alberto Oliveira de Biagi Junior, Willian Fernando Zambuzzi - XIX SBPMat - 2021

7. Effect of the Niobium Substitutional Element on the Mechanical Properties and Biocompatibility of Ti-25Ta-Nb Alloys, Fernanda de Freitas Quadros, Célio Junior da Costa Fernandes, ***Gerson Santos de Almeida***, Willian Fernando Zambuzzi, Carlos Roberto Grandini – XIX SBPMat - 2021
8. Cytotoxicity of new Ti-based alloys aiming at biomedical applications, Dante Oliver Guim Corrêa, Fernanda de Freitas Quadros, Giovana Collombaro Cardoso, ***Gerson Santos de Almeida***, Willian Fernando Zambuzzi, Carlos Roberto Grandini - XIX SBPMat – 2021
9. Síntese e caracterização do filme de Hidroxiapatita, depositado sobre titânio recoberto com titanato de cálcio, Maria Gabriela Jacheto Carra, João Ícaro Miranda Morais Garcia, ***Gerson Santos de Almeida***, Margarida Juri Saeki - XXXIII Congresso de Iniciação Científica da Unesp – 2021
10. Efeito do meio condicionado por células endoteliais HUVEC e cloreto de cobalto na diferenciação de células mesenquimais: Um olhar aos lncRNAs HOTAIR e HOTTIP, Aron Roger de Oliveira, ***Gerson Santos de Almeida***, Marcel Rodrigues Ferreira, Georgia da Silva Feltran, Willian Fernando Zambuzzi - XXXIII Congresso de Iniciação Científica da Unesp – 2021
11. Avaliação da citotoxicidade de novas ligas de titânio para uso biomédico, Dante Oliver Guim Corrêa, ***Gerson Santos de Almeida***, Carlos Roberto Grandini - XXXIII Congresso de Iniciação Científica da Unesp – 2021
12. Efeito do meio enriquecido com hidroxiapatita dopada com cobalto em células osteoblásticas, Luísa Camilo Suter, ***Gerson Santos de Almeida***, Marcel Rodrigues Ferreira, Julia Ferreira de Morais, Willian Fernando Zambuzzi, Congrebio – 2021;
13. Effect of heat treatments on some properties of Ti-10Mo-Mn for biomedical applications, Mariana Luna Lourenço, Dante Oliver, ***Gerson Santos de Almeida***, Carlos Roberto Grandini, XI Latin American Congress of Artificial Organs and Biomaterials – 2021;
14. Chemical, biological and mechanical characterization of Zr-25Ta-5Ti Alloy, Edriely Saraiva, Dante Oliver, Pedro Akira Bazaglia Kuroda, ***Gerson Santos de Almeida***, Carlos Roberto Grandini, XI Latin American Congress of Artificial Organs and Biomaterials – 2021;
15. New alloys of the Ti-5Mo-Nb system, with low elastic modulus, for biomedical applications, Giovana Collombaro Cardoso, Dante Oliver, ***Gerson Santos de Almeida***, Carlos Roberto Grandini, XI Latin American Congress of Artificial Organs and Biomaterials – 2021;

16. Study of new titanium-based alloys as biomaterials and their cytotoxic potentials, Dante Oliver, ***Gerson Santos De Almeida***, Carlos Roberto Grandini, XI Latin American Congress of Artificial Organs and Biomaterials – 2021;
17. Deposição de hidroxiapatita sobre titânio recoberto com titanato de cálcio: caracterização e ensaio biológico, Carra, M.G.J.; Garcia, J.I.M.M.; ***Almeida, G.S.***; Zambuzzi, W.F.; Saeki, M.J. Congresso Brasileiro de Cerâmica (65-66 CBC) – 2022;
18. Design and characterization of TiZrNbTaMo/Mn HEAs for potential use as orthopedical implants, Jhuliene Elen Torrento, Tiago Santos Pereira de Sousa, Conrado Ramos Moreira Afonso, Carlos Roberto Grandini, ***Gerson Santos de Almeida***, Willian Fernando Zambuzzi and Diego Rafael Nespeque Correa. XX B-MRS Meeting – 2022;
19. Síntese e caracterização de fosfatos de cálcio bifásico (BCP) composto por monetita (CaP) e fosfato tricálcico (β-TCP), Luisa Camilo Suter, ***Gerson Santos de Almeida***, Marcel Rodrigues Ferreira, Geórgia da Silva Feltran, Maria Gabriela Jacheto Carra e Willian Fernando Zambuzzi. 7° Workshop de Biotecnologia – 2022;
20. Desenvolvimento de um modelo de scaffolds ósseo a base de hidrogéis poliméricos naturais, Julia F. Moraes, Marcel R. Ferreira, Geórgia S. Feltran, ***Gerson S. Almeida*** e Willian F. Zambuzzi, 7° Workshop de Biotecnologia – 2022;
21. Construção e caracterização de um modelo de *scaffolds* ósseos a base de hidrogéis, Julia F. Moraes, Marcel R. Ferreira, Guilherme S. Sousa, Geórgia S. Feltran, ***Gerson S. Almeida*** e Willian F. Zambuzzi, 11º Congresso de Biociências – 2022;
22. Construção e caracterização de um modelo de esferoide ósseo a base de hidrogéis, Júlia F.Moraes. Marcel R. Ferreira, ***Gerson S. Almeida***, Geórgia S. Feltran, Willian F. Zambuzzi, XXXIV Congresso de Iniciação Científica da UNESP – 2022;
23. Síntese e caracterização físico-química de Fosfato de Cálcio Bifásico (BCP) dopado com cobalto (Co), Luisa Camilo Suter, ***Gerson Santos de Almeida***, Marcel Rodrigues Ferreira, Geórgia da Silva Feltran, Maria Gabriela Jacheto Carra e Willian Fernando Zambuzzi XXXIV Congresso de Iniciação Científica da UNESP – 1ª e 2ª fase – 2022;
24. Desenvolvimento e caracterização de novas ligas de Ti-Mo-Nb para aplicações biomédicas, Giovana Collombaro Cardoso, ***Gerson Santos de Almeida***, Dante Oliver Guim Corrêa, Willian Fernando Zambuzzi e Carlos Roberto Grandini, Congresso de Biomateriais – 2022;
25. Síntese e caracterização de fosfato de cálcio bifásico (BCP) dopado com cobalto para aplicação biotecnológica, Luisa Camilo Suter, ***Gerson Santos de Almeida***, Marcel Rodrigues Ferreira, Margarida Juri Saeki, Willian Fernando Zambuzzi, XXXV Congresso de Iniciação Científica da Unesp – 2023;

26. Constituição de Unidades Biomiméticas com Perspectiva de Regeneração do Tecido Ósseo, Júlia Ferreira de Moraes, Marcel Rodrigues Ferreira, ***Gerson Santos de Almeida***, Geórgia da Silva Feltran, Anderson Moreira Gomes, Willian Fernando Zambuzzi, XXXV Congresso de Iniciação Científica da Unesp – 2023;
27. Titanium surface modified by oxide films containing calcium and apatite to improve bone integration, João Ícaro Miranda Morais Garcia, Maria Gabriela Jacheto Carra, Diego Rafael Nespeque Correa, Nilson C. Cruz, ***Gerson Santos de Almeida***, Vicente Amigó Borrás e Margarida Juri Saeki - XXI B-MRS Meeting – 2023;
28. Effects of CoCr-enriched medium on shear-stressed endothelial cell and osteoblasts, ***Gerson Santos de Almeida***, Maria Gabriela Jacheto Carra, Célio Junior da Costa Fernandes, Thaís Silva Pinto e Willian Fernando Zambuzzi, XXI B-MRS Meeting – 2023;

Artigos Submetidos e em Revisão

1. Influence of Nb and Zr additions on microstructure, elastic modulus, and cytotoxicity of β-Ti-25Ta alloys for biomedical applications. Pedro Akira Bazaglia Kuroda, Rafael Formenton Macedo dos Santos, ***Gerson Santos de Almeida***, Willian Fernando Zambuzzi, Carlos Roberto Grandini and Conrado Ramos Moreira Afonso;
2. Influence of Zr addition in βTi-25Ta-xZr alloys on oxide formation by MAO-treatment. Pedro Akira Bazaglia Kuroda[a], Rafael Formenton Macedo dos Santos[b], Mariana Rossi Correa[a], ***Gerson Santos de Almeida***[c], Willian Fernando Zambuzzi[c], Diego Rafael Nespeque Correa[d], Carlos Roberto Grandini[e] and Conrado Ramos Moreira Afonso[a];
3. Gamma-oryzanol (γOz) rich rice bran promotes osteogenic phenotype of bone marrow-obtained stromal cells. Thaís Silva Pinto, Jéssica Leite Garcia, Anderson Moreira Gomes, Amanda Fantini de Camargo Andrade, ***Gerson Santos de Almeida***, Camila Renata Correa, Willian Fernando Zambuzzi;
4. Preparation and characterization of TI-10Mo-5Mm-Ag alloys for biomedical applications, Melissa Daniela de Almeida Nespeque[1], Mariana Rocha Correa[1], Dante Oliver Guim Corrêa[1], Mariana Luna Lourenço[1], ***Gerson Santos de Almeida***[2], Willian Fernando Zambuzzi[2], Marília Afonso Rabelo Buzalaf[3], James Venturini[4], Diego Rafael Nespeque Correa[1], Carlos Roberto Grandini[1];
5. Development of Novel β-type Zr-25Ta-5Ti Alloy for Biomedical Applications. Edriely de Oliveira Saraiva[1], ***Gerson Santos de Almeida***[2], Willian Fernando Zambuzzi[2], Pedro Akira Bazaglia Kuroda[3], Carlos Roberto Grandini[1].
6. Modulation of HIF-1α and TNF-α in pre-osteoblasts treated with alcohol extract of propolis: implications for cellular response and signaling pathways. Paula Bertin de Morais, ***Gerson***

Santos de Almeida, Amanda Fantini de Camargo Andrade, Ricardo de Oliveira Orsi, Willian Fernando Zambuzzi, Célio Jr. Da Costa Fernandes.

7. Synthesis of apatite-$CaTiO_3$ bilayer films on cp-Ti by sol-gel/dip-coating and plasma electrolytic oxidation and its effects on mechanical, electrochemical, and biological properties - João Miranda Morais Garcia, Maria Jacheto Carra, Diego N Correa, **Gerson Almeida**, Geórgia Feltran, Paula Chiachia Pasta, Gustavo Rocha de Castro, Elidiane Cipriano Rangel, Nilson Cristiano Cruz, Willian Fernando Zambuzzi, Vicente Amigó Borás, Margarida Juri Saeki.
8. Cobalt-doped monetite induces biomimetic hypoxia and rapidly camouflages bone healing environment - ***Gerson Santos de Almeida***[1], Thais Silva Pinto[1], Luísa Camilo Suter[1], Geórgia da Silva Feltran[1], Maria Gabriela Jacheto Carra[1], Paula Bertin de Morais[1], Diego Rafael Nespeque Corrêa[2], Margarida Juri Saeki[1], Paulo Noronha Lisboa Filho3, Willian Fernando Zambuzzi[1].
9. The biological properties of Co-doped monetite are influenced by thermal treatment - ***Gerson Santos de Almeida***[1], Luisa Camilo Suter[1], Thais Silva Pinto[1], Géorgia da Silva Feltran[1], Maria Gabriela Jacheto Carra[2], Diego Rafael Nespeque Corrêa[3], Margarida Juri Saeki[2], Paulo Noronha Lisboa-Filho[4], Willian Fernando Zambuzzi[1]
10. Optimizing titanium osseointegration using thermally modified Co-doped monetite coatings - ***Gerson Santos de Almeida***[1]*, Maria Gabriela Jacheto Carra[2]*, Luisa Camilo Suter[1], Julia Bucci[2], Diego Rafael Nespeque Corrêa[3], Margarida Juri Saeki[2], Willian Fernando Zambuzzi[1].

Artigos publicados

1. 2020 - GSVA score reveals molecular signatures from transcriptome for biomaterials comparison. Ferreira MR[1]; ***Almeida GS[1]***; Biagi CA[2]; Silva WA jr[2]; Zambuzzi WF[1] - DOI:10.1002/jbm.a.37090
2. 2021 - Metabolic effects of CoCr-enriched medium on shear-stressed endothelial cell and osteoblasts: a possible mechanism involving a hypoxic condition on bone healing. Célio Junior da Costa Fernandes, ***Gerson Santos de Almeida***, Thais Silva Pinto, Fábio J Bezerra, Willian Zambuzzi - DOI: 10.1016/j.msec.2021.112353
3. 2022 - Preparation and characterization of novel as-cast Ti-Mo-Nb alloys for biomedical applications. Giovana Collombaro Cardoso, ***Gerson Santos de Almeida***, Dante Oliver Guim Corrêa, Willian Fernando Zambuzzi, Marília Afonso Rabelo Buzalaf, Diego Rafael Nespeque Correa, Carlos Roberto Grandini – DOI:10.1038/s41598-022-14820-8

4. 2022 - Development of non-equiatomic Bio-HEAs based on TiZrNbTa - (Mo and Mn). Jhuliene Elen Torrento, Tiago dos Santos Pereira de Sousa, Nilson Cristino da Cruz, ***Gerson Santos de Almeida***, Willian Fernando Zambuzzi, Carlos Roberto Grandini, Diego Rafael Nespeque Correa - DOI: 10.1063/5.0100465
5. 2023 - Epigenetic Differences Arise in Endothelial Cells Responding to Cobalt–Chromium. Célio Júnior Fernandes, Rodrigo A. Da Silva, ***Gerson Santos de Almeida***, Marcel Ferreira Rodrigues, Paula Bertin De Morais, Fábio Bezerra, Willian Fernando Zambuzzi – DOI: 10.3390/jfb14030127
6. 2023 - Titanium-Enriched Medium Promotes Environment-Induced Epigenetic Machinery Changes in Human Endothelial Cells. Célio Júnior da C. Fernandes; Rodrigo A. da Silva; Patrícia F. Wood; Marcel Rodrigues Ferreira; ***Gerson Santos de Almeida;*** Julia Ferreira de Moraes; Fábio Bezerra; Willian F. Zambuzzi – DOI: 10.3390/jfb14030131
7. 2023 - The Action of Angiocrine Molecules Sourced from Mechanotransduction-Related Endothelial Cell Partially Explain the Successful of Titanium in Osseointegration. Patrícia Fretes Wood, Célio Junior da Costa Fernandes; ***Gerson Santos de Almeida***, Luísa Camilo Suter, João Paulo Ruiz Lucio de Lima Parra; Fábio J Bezerra; Willian Fernando Zambuzzi – DOI: 10.3390/jfb2301533
8. 2023 - Synthesis and characterization of different Cobalt (Co)-doped monetites for bone regeneration, ***Gerson Santos de Almeida***[1], Marcel Rodrigues Ferreira[1], Célio Junior da Costa Fernandes[1], Luísa Camilo Surter[1], Maria Gabriela Jacheto Carra[1], Diego Rafael Nespeque Correa[2], Elidiane Cipriano Rangel[3], Margarida Juri Saeki[1], Willian Fernando Zambuzzi[1] - DOI: 10.1002/jbm.b.35319
9. 2023 - Mechanosignaling-related angiocrine factors drive osteoblastic phenotype in response to zirconia, Célio Junior da Costa Fernandes; ***Gerson Santos de Almeida;*** Patrícia Fretes; Anderson M. Gomes; Fabio Bezerra; José C. S. Vieira; Pedro M. Padilha; Willian Fernando Zambuzzi – DOI: 10.1016/j.jtemb.2023.127337
10. 2024 - Obtaining of Antibacterial Nanoporous Layer on Ti7.5Mo Alloy Surface Combining Alkaline Treatment and Silver: In Vitro Studies, Barbara Lois Mathias de Souza, Ana Lúcia do Amaral Escada, Célio Junior da Costa Fernandes, ***Gerson Santos de Almeida***, Willian Fernando Zambuzzi, Patrícia Capellato, Daniela Sachs, Ana Paula Rosifini Alves Claro – DOI: 10.3390/coatings14010052;
11. 2024 - Combination of in silico and cell culture strategies to predict biomaterial performance: effects of sintering temperature on the biological properties of hydroxyapatite. ***Gerson Santos de Almeida***; Marcel Rodrigues Ferreira; Célio Junior da Costa Fernandes; Carlos Alberto Oliveira de Biagi Junior; Wilson Araújo Silva Júnior;

Elidiane Cipriano Rangel; Paulo Noronha Lisboa Filho; Willian Fernando Zambuzzi – DOI: 10.1002/jbm.b.35389

Membro de Órgão Colegiado

1. Membro discente titular do Conselho do Departamento de Ciências Químicas e Biológicas (mandato 2021 – 2022), e membro discente suplente (mandato 2022 - 2023);
2. Membro discente do Conselho do Programa de Biologia Geral e Aplicada (mandato 2021 a 2022).

Atuação como Revisor em Periódicos, Comissão Julgadora e Bancas, e Avaliador em eventos

1. Revisor no periódico **Materials & Design** (ISSN: 0264-1275);
2. Revisor no periódico **Revista Brasileira de Pesquisa em Saúde/Brazilian Journal of Health Research** (ISSN - 2446-5410);
3. Membro da banca avaliadora do Trabalho de Conclusão de Curso de Luisa Camilo Suter, Curso de Engenharia de Bioprocessos de Biotecnologia – FCA/Botucatu – 2023;
4. Membro da banca avaliadora do Trabalho de Conclusão de Curso de Carla Cristina Albertini, Curso de Engenharia de Bioprocessos de Biotecnologia – FCA/Botucatu – 2023;
5. Membro da banca avaliadora do Trabalho de Conclusão de Curso de Julia Ferreira de Moraes, Curso de Física Médica - IBB – 2023;
6. Membro da banca avaliadora do Trabalho de Conclusão de Curso de Julia Bucci, Curso de Física Médica do IBB – 2023;
7. Avaliador de trabalhos no "**XX Congress of the Brazilian Society for Cell Biology**";
8. Avaliador dos trabalhos no **XXXIII Congresso de Iniciação Científica da Unesp** - IB/Botucatu;

Doutorado no exterior (doutorado sanduiche)

Período de doutorado sanduiche com bolsa CapesPrInt, realizado no LBB: Laboratoire de biomatériaux et de bioingénierie da Universidade de Laval - Quebec - Canadá, sob a supervisão do Prof. Dr. Diego Mantovani, de setembro de 2022 a agosto de 2023.

Organização de eventos

Membro da Comissão Organizadora do Simpósio Anual do Programa de Pós-Graduação em Biologia Geral e Aplicada – 2022.

Prêmios e indicações

Certificado de "***Top Cited Article 2021-2022***", do artigo "GSVA score reveals molecular signatures from transcriptomes for biomaterials comparison" como um dos artigos mais citados do "*Journal of Biomedical Materials Research Part A*";

Artigo "Titanium-Enriched Medium Promotes Environment-Induced Epigenetic Machinery Changes in Human Endothelial Cells" selecionado como "***Editor's Choice Articles***", no *Journal of Functional Biomaterials* da MDPI – 2023.